

Luís Miguel da Luz Caixinha Duarte

IN VIVO AUTOMATIC CATARACT DETECTION AND CLASSIFICATION USING THE ULTRASOUND TECHNIQUE

Doctoral Thesis in Biomedical Engineering, Supervised by Jaime Baptista dos Santos and António Miguel Lino Santos
Morgado and presented in the Faculty of Sciences and Technology of the University of Coimbra

September 2016



UNIVERSIDADE DE COIMBRA

In vivo Automatic Cataract Detection and Classification using the Ultrasound Technique

Doctoral Thesis in Biomedical Engineering

Luís Miguel da Luz Caixinha Duarte

Supervisors

Jaime Baptista dos Santos, Ph.D.

António Miguel Lino Santos Morgado, Ph.D.

Faculty of Sciences and Technology

University of Coimbra

September 2016

Cover image: image of a lens slice acquired in this work

For my wife, my love, Sandrina...

Forever thank you!

É com um enorme sentimento de gratidão que quero dizer aos meus queridos pais, que a verdadeira génese deste trabalho está na oportunidade que com esforço, carinho e afeto, incondicionalmente me deram, e que nunca puderam ter; a oportunidade de aprender...

É a educação e o amor o vosso legado, será esse tesouro que farei tudo para deixar a quem educar.

Para sempre obrigado!

Miguel.

I want to thank to my little daughter, Joana da Luz, having kept me awake with its beautiful cry, the precious nights I needed to finish my thesis.

Thank you my sweet...

*I want to thank my sister, my brother in law and friend, and my nieces, their support, care and encouragement during all these years.
All of you are an inspiration for me.*

Thank you.

ACKNOWLEDGMENTS

I would like to express my sincere gratitude to my supervisors for believing in the idea of this project, and for their support making possible its successful achievement. I also want to thank all the technical and scientific support and the high critical thinking with which they guided my work.

Thank you dear professors.

I want to thank the DEEC - Department of Electrical and Computer Engineering, where this work was developed. In particular I want to thank the people with whom I had the pleasure of working. Special thanks to Professor Mário Santos, Professor Fernando Perdigão, Professor Marco Gomes and Eng. João Amaro. All made these years of work a very pleasant experience.

I want to thank the IBILI - Institute for Biomedical Imaging and Life Sciences and CEMUC - Centre for Mechanical Engineering of the University of Coimbra, for providing me the access to the research facilities to conduct part of this work.

Finally I want to thank the Foundation for Science and Technology (Fundação para a Ciência e Tecnologia – FCT) for the financial support (grant PTDC/DTP-PIC/0419/2012).

RESUMO

A catarata é uma condição associada à perda da normal transparência do cristalino. A sua progressão pode resultar na perda parcial ou total da visão. O processo de formação da catarata resulta no aumento do número de dispersores de luz no cristalino, na sua opacificação e no aumento da sua dureza. Atualmente, a catarata não tem prevenção ou tratamento farmacológico, pelo que a única terapêutica eficaz para recuperação da visão é a remoção cirúrgica da catarata com substituição do cristalino por uma lente intraocular. A facoemulsificação é a técnica cirúrgica mais usada. A detecção precoce da catarata, a classificação da sua severidade, bem como a estimação da sua dureza, constituem aspetos clínicos relevantes. A estimação da dureza da catarata é importante para a seleção adequada dos níveis de energia de facoemulsificação e consequente diminuição das complicações cirúrgicas.

Este trabalho tinha por objetivo a deteção precoce e caracterização da catarata, nomeadamente a estimação da sua dureza, recorrendo a métodos por ultrassons, bem como a sua classificação automática usando técnicas de “*machine learning*”. De modo a demonstrar a aplicabilidade e utilidade dos ultrassons na caracterização não invasiva da catarata, foi realizado, inicialmente, um estudo *ex vivo* de prova de conceito em olhos de suíno, induzindo nestes catarata por imersão dos cristalinos numa solução de etanol:2.propanol:formalina. A aquisição dos sinais acústicos foi realizada com um transdutor ultrassónico de 25 MHz, funcionando em modo pulso-eco, tendo sido extraídos os parâmetros velocidade e atenuação. De modo a visualizar e caracterizar a catarata, foram construídas imagens B-scan e do parâmetro m de Nakagami, com base nos sinais de *backscattering*. Foram extraídas 97 *features*, para a classificação automática dos graus de severidade da catarata, usando os classificadores de Naive Bayes, *K-Nearest-Neighbours*, *Fisher Linear Discriminant* e *Support Vector Machine (SVM)*.

A distribuição espacial dos agregados proteicos e a compactação de fibras para os diferentes graus de severidade da catarata foram analisadas com base em imagens histológicas dos cristalinos obtidas nas regiões do córtex e do núcleo.

O estudo *ex vivo* demonstrou que a dureza da catarata pode ser estimada de forma não invasiva e o grau de severidade da catarata pode ser classificado automaticamente com técnicas de *machine learning*. Verificou-se que os parâmetros acústicos, velocidade e atenuação, aumentam significativamente com a progressão da catarata. Constatou-se, também, que a intensidade média do brilho das imagens de B-scan e o valor médio do parâmetro m de Nakagami, aumentam significativamente com a progressão da catarata, como resultado do aumento das regiões de alta concentração de dispersores (*scatterers*). As abordagens de *machine learning* usadas, obtiveram um bom desempenho na classificação da catarata ($F\text{-measure} \geq 0,725$), confirmando a existência de uma associação entre os parâmetros acústicos e o grau de severidade da catarata.

No estudo realizado *in vivo*, foi desenvolvido um modelo animal para catarata nuclear do qual resultaram doze ratos Wistar com catarata incipiente, treze com catarata moderada e onze com catarata severa. Os sinais acústicos foram adquiridos com uma sonda oftalmológica de ultrassons de 20 MHz. A identificação dos sinais referentes às interfaces do globo ocular, requereu o desenvolvimento de um algoritmo que foi capaz de localizar o eco da cápsula posterior, de difícil detecção. Foram extraídas 27 *features* para detecção e classificação automática da catarata, usando os classificadores SVM, Naive Bayes, *Multilayer Perceptron* e *Random Forest*. As durezas do núcleo e do córtex do cristalino foram medidas e a respectiva elasticidade estimada em cristalinos de 12 ratos, por técnicas de nanoindentação.

Demonstrou-se que a velocidade, atenuação e o desvio de frequência (*downshift*) aumentam significativamente com a progressão da catarata ($p < 0,001$).

O classificador SVM apresentou o melhor desempenho na classificação automática do grau de severidade da catarata, com uma precisão, sensibilidade e especificidade de 0,997, e um erro absoluto relativo de 0,4%.

Foi observada uma diferença estatisticamente significativa para os valores da dureza entre os diferentes graus de severidade da catarata ($p = 0,016$). O núcleo apresentou o maior aumento da dureza com a progressão da catarata ($p = 0,049$). Foi obtida uma correlação moderada a boa entre a dureza do núcleo e 23 das 27 *features* analisadas. Foi encontrada uma forte correlação entre o módulo de Young e a dureza do cristalino ($r = 0,953$, para o núcleo e $r = 0,701$ para o córtex, $p < 0,001$).

A metodologia desenvolvida permitiu detectar a catarata nuclear *in vivo* em estádios iniciais, classificar automaticamente o seu grau de severidade e estimar a sua dureza de modo não invasivo.

Com base nos estudos realizados, foi desenvolvido um protótipo (ESUS - *Eye Scan Ultrasound System*), para a detecção precoce e classificação automática da catarata, bem como para a estimação da sua dureza em tempo real. Este protótipo está protegido por um Pedido Provisório de Patente PPP108836 (2015).

Palavras Chave: Catarata; Ultrassons; Classificação Automática; Dureza

ABSTRACT

Cataract is a condition associated with the loss of the normal transparency of the crystalline lens. Its progression may result in partial or total vision loss. The cataract formation process is a result of fibrosis and protein aggregation within the lens. Fiber compaction and proteins aggregation have the effect of increasing the light scattering, lens opacity and hardness, leading to visual acuity loss.

Currently, cataract has no pharmacological treatment or prevention and the only effective therapy to restore vision is the cataract surgical removal, replacing the natural lens by an artificial intraocular lens. The phacoemulsification is the most widely used surgical technique for cataract removal.

For diagnosis and therapeutic purposes it is of major importance to identify the cataract in its early stage, and accurately determine its type and severity. The early cataract detection, the correct classification, and its hardness estimation are key factors for clinical cataract management. In particular, the cataract hardness estimation plays an important role in the optimal phacoemulsification energy level selection, which results in less surgical complications and higher safety levels.

This work aims to *in vivo* characterize the cataract based on ultrasound techniques, namely, to early detect cataract formation, estimate its hardness, and automatically classify its severity level using machine learning. A prototype, to be validated in the future in clinical studies, was developed and tested in this work in small animals (*Wistar* rats).

Before conducting *in vivo* experiments in an animal model for nuclear cataract, a proof-of-concept study was conducted *ex vivo* in porcine lenses.

The proof-of-concept study was conducted to validate the experimental setup and to demonstrate the feasibility of the ultrasound technique for the cataract characterization noninvasively (without lens destruction). In that study the cataract was induced by lens immersion in a ethanol:2-propanol:formalin solution. A 25 MHz ultrasound transducer with a 25 mm focus and 5 mm active diameter was used to collect the acoustical parameters (velocity and attenuation), and backscattering signals. In order to visualize and characterize cataract B-scan and Nakagami *m* parameter images were constructed. Ninety-seven features were extracted and subjected to a Principal Component Analysis. Naive Bayes, K-Nearest-Neighbours, Fisher Linear Discriminant and Support Vector Machine (SVM) classifiers were used to automatically

classify the cataract severity. The spatial distribution of protein aggregates and the fiber compaction for the different cataract degrees was also analysed based on histological slices' images obtained in the nucleus and cortex regions.

This study showed that the cataract hardness can be noninvasively estimated and the cataract severity automatically classified with machine learning techniques, using the acoustical parameters, B-scan and Nakagami parametric images, and the backscattering signals. It was observed that the acoustical parameters (velocity and attenuation) increased significantly with the cataract progression. Also, the mean brightness of the B-scan images and the mean value of the Nakagami m parameter showed an increase over the cataract progression, as a result of the increased region of high scatterers concentration. Finally, the used machine learning techniques presented a good performance for cataract classification (F-measure ≥ 0.725) confirming the existence of an association between the ultrasound parameters and cataract severity.

For the *in vivo* study, fifty rats were used: fourteen as control and thirty-six as study group. First, an animal model for nuclear cataract was developed, which provided 12 rats with incipient, 13 with moderate, and 11 with severe cataract. Then, a 20 MHz ophthalmic ultrasound probe with a focal length of 8.9 mm, and active diameter of 3 mm was used for signals collection. An algorithm was developed to identify all pulses associated to the eye boundaries, in particular the posterior capsule echo, which in general has small amplitude. Next, twenty-seven features in time and frequency domain were extracted for cataract detection and automatic classification by using SVM, Naive Bayes, Multilayer Perceptron and Random Forest classifiers.

The hardness of the nucleus and the cortex regions of the lens were also objectively measured in 12 rats using the NanoTestTM, and the respective elasticity estimated.

It was shown that the velocity, attenuation and frequency downshift significantly increased with cataract progression ($p < 0.001$). The SVM classifier showed the higher performance for the automatic classification of cataract severity, with a precision, sensitivity and specificity of 0.997, with a relative absolute error of 0.4%. A statistically significant difference was found for the hardness of the different cataract degrees ($p = 0.016$). The nucleus showed a higher hardness increase with cataract progression ($p = 0.049$). A moderate to good correlation between the features and the nucleus hardness was found in 23 out of the 27 features. A strong correlation was found between the Young's modulus and the lens hardness ($r = 0.953$, for the nucleus and $r = 0.701$ for the cortex, $p < 0.001$).

The methodology developed in this study allows detecting the nuclear cataract *in vivo* in early stages, classifying automatically its severity degree and estimating its hardness noninvasively.

Following the obtained results a prototype called Eye Scan Ultrasound System (ESUS) was developed for early and automatic cataract detection and classification in real time. This prototype is currently protected under provisional patent application PPP108836 (Santos *et al.* 2015).

Keywords: Cataract; Ultrasounds; Automatic Classification; hardness

Abbreviations

AG	Aminoguanidine
ALARA	As Low As Reasonably Achievable
app	Application
AREDS	Age-Related Eye Disease Study
ARM	Advanced RISC (Reduced Instruction Set Computing) Machine
C	Cortical (used for cortical cataract classification)
CAD	Computer Assisted Diagnosis
cDNA	Coding Deoxyribonucleic Acid
CRT	Classification and Regression Tree
CT	Computed Tomography
DFT	Discrete Fourier Transform
DGAV	Direção Geral de Alimentação e Veterinária
DMEM	Dulbecco's Modified Eagle Medium
DNA	Deoxyribonucleic Acid
ESUS	Eye Scan Ultrasound System
FCT	Fundação para a Ciência e Tecnologia
FDA	Food and Drug Administration
FLD	Fisher Linear Discriminant
FPGA	Field Programmable Gate Array
GLCM	Grey Level Co-occurrence Matrix
GLNU	Grey Level Non-Uniformity
GLRLM	Grey Level Run Length Matrix
GMM	Gaussian Mixture Models
H ₂ O ₂	Hydrogen Peroxide
HDD	Hard Disk Drive
HGLRE	High Grey Level Run Emphasis
IEEE	Institute of Electrical and Electronics Engineers
ISO	International Organization for Standardization
KNN	K Nearest Neighbour
LGLRE	Low Grey Level Run Emphasis
LOCS	Lens Opacity Classification System

LRE	Long Run Emphasis
MI	Mechanical Index
MR	Magnetic Resonance
MSE	Mean Square Error
N	Nuclear (used for nuclear cataract classification)
Na ₂ SeO ₃	Sodium Selenite
NC	Nuclear Cataract (used for nuclear cataract classification)
NICE	National Institute for Health and care Excellence
NO	Nuclear Opalescence (used for opalescence of the nuclear cataract classification)
P	Posterior (used for posterior subcapsular cataract classification)
PCA	Principal Component Analysis
PMN-PT	Magnesium Niobate-Lead Titanate
Q _L	Lens Quality
ODS	Output Display Standards
PL	Programmable Logic
PS	Processor Subsystem
RAM	Random Access Memory
RF	Radio Frequency
RISC	Reduced Instruction Set Computing
RLNU	Run Length Non-Uniformity
RMS	Root Mean Square
ROI	Region Of Interest
RP	Run Percentage
RT-PCR	Reverse Transcription - Polymerase Chain Reaction
SAM	Scanning Acoustic Microscope
SFM	Spectral Flatness Measure
SNR	Signal to Noise Ratio
SoC	System-on-Chip
SPPA	Spatial Peak Pulse Average Intensity
SPTA	Spatial Peak Temporal Average
SRE	Short Run Emphasis
SVM	Support Vector Machine
TI	Thermal Index
UBM	Ultrasound Biomicroscopy

UK	United Kingdom
USA	United States of America
WCGS	Wisconsin Cataract Grading System
WHO	World Health Organization

Figures

Figure 2-1. Illustration of the most common types of cataract (adapted from (Beebe <i>et al.</i> 2010)).....	8
Figure 2-2. Standard images for LOCS III classification system (adapted from (Chylack <i>et al.</i> 1993)).....	14
Figure 2-3. General mechanisms of the cataract formation.	17
Figure 2-4. Biochemical process of the selenite-induced cataract (adapted from (Shearer <i>et al.</i> 1997)).	17
Figure 3-1. Illustration of a pulse-echo transducer.	23
Figure 3-2. Illustration of the pulse-echo mode.	23
Figure 3-3. A-scan signal obtained <i>in vivo</i> in a rat's eye.	26
Figure 3-4. B-scan obtained <i>ex vivo</i> in a rat's eye.	26
Figure 4-1. Echoes obtained <i>in vivo</i> in a rat's eye.	32
Figure 4.2. Setup for the ultrasound velocity calculation based on equation (4-3).....	34
Figure 4.3. Setup for the frequency-dependent attenuation calculation based on the anterior and posterior lens capsule echoes.....	35
Figure 4.4. Setup for the frequency-dependent attenuation calculation making use of a planar reflector.....	36
Figure 4-5. B-scan images: (a) for a lens without cataract; (b) and for a lens with induced cataract (Caixinha <i>et al.</i> 2014a).....	40
Figure 4-6. Illustration of the pre-Rayleigh, Rayleigh and post-Rayleigh distributions, and m parameter values (adapted from (Ho <i>et al.</i> 2013)).	42
Figure 4-7. Nakagami distribution for different values of the m parameter.	43
Figure 4-8. Nakagami images representing the scatterers distribution for a lens without cataract (a) and for a lens with induced cataract (b) (Caixinha <i>et al.</i> 2014a).....	44
Figure 5-1. Lens extraction procedure ((a) enucleated porcine eye; (b) lens enucleation; and (c) lens cleaned from iris remains and adhering vitreous) (Caixinha 2012).	45
Figure 5-2. Porcine lenses: normal lens and lenses with induced cataract obtained after 60 and 180 minutes of immersion in the ethanol:2-propanol:formalin solution.	46
Figure 5-3. Experimental setup (schematic – left; and photograph – right).	46
Figure 5-4. Ultrasound velocity mean values <i>versus</i> lens immersion time by using equation (4-2) and equation (4-3), (mean difference between methods: 29.2 m/s (Confidence Interval: 23.3 to 35.2); Limits of agreement: -46.8 to 105.3) (Caixinha 2012; Jesus <i>et al.</i> 2012).....	48

Figure 5-5. Echoes spectrum amplitude for the different immersion times: (a) anterior capsule; (b) posterior capsule, mean values (Caixinha 2012).....49

Figure 5-6. Echoes spectrum amplitude for the different immersion times using a planar reflector, mean values (Caixinha 2012).....49

Figure 5-7. Frequency-dependent attenuation mean values obtained by equations (4-5) and (4-7), for 10 MHz (mean difference between methods: 0.036 dB/mm (Confidence Interval: 0.026 to 0.046); Limits of agreement: -0.094 to 0.166) (Caixinha 2012; Jesus *et al.* 2012).....50

Figure 5-8. Centre frequency downshift *versus* depth in the lenses with total cataract (180 minutes of immersion time), mean values (Caixinha 2012; Jesus *et al.* 2013).....51

Figure 5-9. Linear fit of the mean centre frequency downshift *versus* depth, in lenses with different degrees of cataract (from 20 to 180 minutes of immersion time) (Caixinha 2012; Jesus *et al.* 2013).....51

Figure 5-10. Nakagami *m* parameter as function of immersion time, mean values (Caixinha 2012; Jesus *et al.* 2013).....52

Figure 5-11. Nakagami scale parameter Ω as function of immersion time, mean values (Caixinha 2012; Jesus *et al.* 2013).....52

Figure 6-1. Number of lenses used in the proof-of-concept study, for the different experiments. *lenses with total cataract were not considered because it was found in analysis 1 that the acoustical parameters, B-scan and Nakagami images, does not discriminate advanced from total cataract.....58

Figure 6-2. transducer pulse shape using a plane reflector in water.59

Figure 6-3. Flowchart for B-scan and Nakagami images construction.....61

Figure 6-4. ROI used to extract textural features from the B-scan and Nakagami images (Caixinha *et al.* 2014a; Caixinha *et al.* 2015a).63

Figure 6-5. Leica Microsystems CM3350S cryostat.....64

Figure 6-6. Acoustical parameters for the different immersion times (a) velocity and (b) frequency-dependent attenuation, (mean \pm 1SD) (Caixinha *et al.* 2014a).68

Figure 6-7. B-scan images for lenses: (a) without cataract; (b) 60 minutes; (c) 120 minutes; (d) and 180 minutes of immersion time (Caixinha *et al.* 2014a).....69

Figure 6-8. Mean B-scan brightness for the different immersion times, (mean \pm 1SD) (Caixinha *et al.* 2014a).69

Figure 6-9. Nakagami images for lenses: (a) without cataract; (b) 60 minutes; (c) 120 minutes; and (d) 180 minutes of immersion time (Caixinha *et al.* 2014a).....70

Figure 6-10. Mean Nakagami *m* parameter for the different immersion times, (mean \pm 1SD) (Caixinha *et al.* 2014a).....70

Figure 6-11. Microscopy image of a transversal slice of the nucleo-cortex region (Caixinha *et al.* 2014a). ..71

Figure 6-12. Microscopy images of the lenses' slices over the different immersion times ((a) and (b) 0 minutes; (c) and (d) 60 minutes; (e) and (f) 120 minutes; and (g) and (h) 180 minutes of immersion time) (Caixinha <i>et al.</i> 2014a).....	72
Figure 6-13. Slices' images mean brightness for the cortex and the nucleus regions for different immersion times, mean values (Caixinha <i>et al.</i> 2014a).....	72
Figure 6-14. Mean Nakagami m parameter <i>versus</i> cortex images mean brightness (for the different immersion times), mean values (Caixinha <i>et al.</i> 2014a).....	72
Figure 6-15. Principal nodes of the CRT for cataract characterization (Caixinha <i>et al.</i> 2014a).....	73
Figure 6-16. p -values for the 97 extracted features from the A-scan and backscattering signals (statistically significant features had a p -value < 0.05) (Caixinha <i>et al.</i> 2015a).....	75
Figure 6-17. Average F-measure of the 4 classifiers for the first 20 components obtained by PCA (Caixinha <i>et al.</i> 2015a).....	75
Figure 6-18. F-measure of the multiclass classifier for the first 20 components obtained by PCA.....	76
Figure 7-1. Number of rats used in the <i>in vivo</i> study.....	81
Figure 7-2. Micro Materials Ltd Wrexham, U.K. NanoTest™.....	82
Figure 7-3. Illustration of the nanoindentation test (h_{\max} : sample thickness; h_c : contact depth; and h_{final} : residual indentation depth).....	83
Figure 7-4. Image of an indent left by a Berkovich tip in the nucleus region of a rat's lens.....	83
Figure 7-5. Load-displacement curves for a nanoindentation test with 6 indentations in the cortex region of a healthy rat's lens.....	84
Figure 7-6. <i>In vivo</i> and <i>post mortem</i> acquisitions (Caixinha <i>et al.</i> 2016).....	87
Figure 7-7. <i>Ex vivo</i> acquisitions (Caixinha <i>et al.</i> 2016).....	87
Figure 7-8. Setup for data acquisition (Tx: Transmit; Rx: Receive; HDD: Hard Disk Drive; RAM: Random Access Memory) (Caixinha <i>et al.</i> 2016).....	88
Figure 7-9. Illustration of an A-scan signal for a cataractous lens.....	88
Figure 7-10. Procedure for automatic detection of ocular interfaces (Caixinha <i>et al.</i> 2016).....	90
Figure 7-11. Temporal features extraction from a lens echo signal. The signal in red indicates the presence of cataract. The labels f_i indicate features listed in Table 7-4 (Caixinha <i>et al.</i> 2016).....	94
Figure 7-12. Illustration of the final extracted feature vector (A_i : A-scan; A_{mean} : mean of 20 A-scans; fv_i : feature vectors; and FV_{median} : median of the feature vectors).....	94
Figure 7-13. Degrees of nuclear cataract severity obtained with the animal model. (a) Incipient; (b) Moderate; and (c) Severe (Caixinha <i>et al.</i> 2016).....	96
Figure 7-14. Number of rats with the different degrees of nuclear cataract (Incipient; Moderate, and Severe).....	96

Figure 7-15. Lens thickness *versus* age.....97

Figure 7-16. Slice images of lenses with severe cataract. The arrows identify the indentation locations (Caixinha *et al.* 2016).....98

Figure 7-17. Indentation curves for a lens with severe cataract.....98

Figure 7-18. Lens hardness in GPa for healthy lenses and for different degrees of cataract severity measured by NanoTest™, mean values.....99

Figure 7-19. Lens hardness increase in the cortex and nucleus regions with cataract severity measured by NanoTest™, mean values.99

Figure 7-20. Lens Young’s modulus in GPa for healthy lenses and for different degrees of cataract severity measured by NanoTest™, mean values.100

Figure 7-21. Increase of the lens Young’s modulus in GPa in the cortex and nucleus regions with cataract severity measured by NanoTest™, mean values.....100

Figure 7-22. ICC values between *in vivo* and *post mortem* acquisitions and between *in vivo* and *ex vivo* acquisitions for the 27 extracted features (below 0.400 the agreement is poor, dashed line).....101

Figure 7-23. time of flight in healthy lenses and with different cataract degrees (mean±1SD) (Caixinha *et al.* 2016).....102

Figure 7-24. Ultrasound attenuation coefficient for 10 MHz for the different cataract degrees (mean±1SD) (Caixinha *et al.* 2016).....102

Figure 7-25. Frequency downshift for the different cataract degrees (mean±1SD) (Caixinha *et al.* 2016). .102

Figure 7-26. Transfer function for the different cataract severities.102

Figure 7-27. Correlation coefficient between the nucleus hardness and the extracted features *in vivo* (below 0.400 the correlation is weak, dashed line) (Caixinha *et al.* 2016).103

Figure 7-28. Scree plot for the PCA of the 27 extracted features.103

Figure 7-29. Cumulative variance explained by the 12 extracted components.103

Figure 7-30. ESUS key components blocks.....110

Figure 7-31. ESUS block diagram.112

Figure 7-32. Scheme of the ESUS prototype (a B-scan for a rat’ lens is shown based on *ex vivo* acquisitions).
.....113

Figure 7-33. Layout of the ESUS prototype (a B-scan for a rat’s lens is shown based on *ex vivo* acquisitions).
.....114

Tables

Table 2-1. Simplified LOCS system for nuclear, cortical and subcapsular cataracts grading (adapted from (American Optometric Association 2004)).	15
Table 4-1. Techniques used for ultrasound visualization and/or characterization of ocular structures.	31
Table 4-2. n-parameter for human ocular tissues (de Korte <i>et al.</i> 1994).	34
Table 4-3. Values published for the ultrasound velocity and attenuation in lenses without and with cataract.	38
Table 5-1. Lens propagation velocity results (n=20).	48
Table 5-2. Attenuation coefficient in the porcine lenses for 10 MHz (n=20).	52
Table 6-1. Transducer characteristics.	59
Table 6-2. Ninety-seven (97) features extracted from the ultrasound signals.	65
Table 6-3. Classification of lenses with or without cataract (Caixinha <i>et al.</i> 2014a).	74
Table 6-4. Classification of severe (advanced and total) or incipient cataract (Caixinha <i>et al.</i> 2014a).	74
Table 6-5. Classifiers performance for the classification into healthy or cataractous lenses using 2 components (Caixinha <i>et al.</i> 2015a).	76
Table 6-6. Classifiers performance for the classification into incipient or advanced cataractous lenses using 9 components (Caixinha <i>et al.</i> 2015b).	76
Table 6-7. Average performance for the multiclass SVM classification using 15 components (Caixinha <i>et al.</i> 2014b).	77
Table 7-1. Classification criteria for the 3 levels of cataract severity.	82
Table 7-2. Poisson's ratio measured in the human eye.	85
Table 7-3. Transducer characteristics (Imasonic, SAS, France).	87
Table 7-4. Extracted features (Caixinha <i>et al.</i> 2016).	93
Table 7-5. Rat's eye dimensions.	97
Table 7-6. Hardness measured by NanoTest TM (Caixinha <i>et al.</i> 2016).	99
Table 7-7. Young's modulus computed based on the reduced Young's modulus measured by NanoTest TM .	100
Table 7-8. Description of the 12 components obtained by PCA (coefficients lower than 0.1 are not presented).	104
Table 7-9. Performance of the different classifiers using the 27 selected features (RAE – relative absolute error) (Caixinha <i>et al.</i> 2016).	105

Table 7-10. Performance of the different classifiers using the 12 components obtained by PCA (RAE – relative absolute error) (Caixinha *et al.* 2016).105

Table 7-11. Accuracy of the SVM classifier for the 27 features considering different optimization parameters (* values chosen for the C and Gamma parameters).....106

Table 7-12. Accuracy of the SVM classifier for the 12 components obtained by PCA considering different optimization parameters (* values chosen for the C and Gamma parameters).106

Table of Contents

1	INTRODUCTION	1
1.1	MOTIVATION	1
1.2	OBJECTIVES	3
1.3	CONTRIBUTION AND RELEVANCE	3
1.4	THESIS ORGANIZATION	6
2	OVERVIEW ON CATARACT RESEARCH AND CLINICAL MANAGEMENT	7
2.1	INTRODUCTION	7
2.2	PREVALENCE OF THE CATARACT	9
2.3	CLINICAL CATARACT MANAGEMENT	10
2.4	CLINICAL METHODS FOR CATARACT CHARACTERIZATION AND CLASSIFICATION	12
2.4.1	METHODS FOR CATARACT VISUALIZATION AND CHARACTERIZATION	12
2.4.2	CATARACT CLASSIFICATION	13
2.5	ANIMAL MODELS FOR CATARACT INDUCTION	15
2.5.1	INDUCTION PROCESSES	16
2.5.2	<i>IN VIVO</i> STUDIES	18
3	ULTRASOUNDS	21
3.1	INTRODUCTION	21
3.2	ULTRASOUND CONCEPTS	22
3.3	THERMAL EFFECTS	24
3.4	NON-THERMAL EFFECTS	24
3.5	SAFETY	25
3.6	ULTRASOUND A-SCAN AND B-SCAN MODES	26
4	CHARACTERIZATION OF THE CRYSTALLINE LENS BY ULTRASOUNDS	29
4.1	INTRODUCTION	29
4.2	ACOUSTICAL PROPERTIES OF CRYSTALLINE LENS	30

4.2.1	ULTRASOUND VELOCITY	33
4.2.2	FREQUENCY-DEPENDENT ATTENUATION	34
4.2.3	EVALUATION OF THE ACOUSTICAL PARAMETERS IN THE CRYSTALLINE LENS	36
4.3	CATARACT IMAGING	39
4.3.1	B-SCAN IMAGING	39
4.3.2	NAKAGAMI PARAMETRIC IMAGING	40
5	<i>EX VIVO</i> CATARACT CHARACTERIZATION: EXPLORATORY STUDY	45
5.1	OBJECTIVE	45
5.2	MATERIALS AND METHODS	45
5.2.1	LENSES PREPARATION AND CATARACT INDUCTION	45
5.2.2	EXPERIMENTAL SETUP FOR LENSES SIGNAL ACQUISITION	46
5.2.3	STATISTICAL ANALYSIS	47
5.3	RESULTS	47
5.3.1	ULTRASOUND VELOCITY	47
5.3.2	ULTRASOUND FREQUENCY-DEPENDENT ATTENUATION	48
5.3.3	NAKAGAMI M AND Ω PARAMETERS	52
5.4	DISCUSSION	53
5.5	RESULTING PUBLICATIONS	54
6	<i>EX VIVO</i> CATARACT CHARACTERIZATION	57
6.1	OBJECTIVE	57
6.2	MATERIALS AND METHODS	57
6.2.1	SAMPLE SIZE AND CATARACT INDUCTION	57
6.2.2	EXPERIMENTAL SETUP	59
6.2.3	DATA ACQUISITION	60
6.2.4	FEATURES EXTRACTION	62
6.2.5	NUCLEUS AND CORTEX HISTOLOGICAL SLICES	63
6.2.6	DATA ANALYSIS	64
6.3	RESULTS	68
6.3.1	ULTRASOUND VELOCITY AND FREQUENCY-DEPENDENT ATTENUATION	68
6.3.2	B-SCAN IMAGING	69
6.3.3	NAKAGAMI PARAMETRIC IMAGING	70

6.3.4	HISTOLOGICAL SLICES' IMAGES	71
6.3.5	PREDICTIVE FEATURES FOR CATARACT SEVERITY	73
6.3.6	AUTOMATIC CATARACT CLASSIFICATION	74
6.4	CONCLUSIONS	77
6.4.1	CHARACTERIZATION OF THE CATARACTOUS LENS	77
6.4.2	AUTOMATIC CATARACT CLASSIFICATION BASED ON THE EXTRACTED FEATURES	78
6.5	RESULTING PUBLICATIONS	78
7	<u>IN VIVO CATARACT DETECTION, AUTOMATIC CLASSIFICATION AND HARDNESS ESTIMATION</u>	79
7.1	OBJECTIVE AND STUDY DESCRIPTION	79
7.2	MATERIALS AND METHODS	80
7.2.1	ANIMAL MODEL FOR NUCLEAR CATARACT	80
7.2.2	EXPERIMENTAL PROCEDURES	81
7.2.3	MACHINE LEARNING TECHNIQUES FOR AUTOMATIC CATARACT CLASSIFICATION	95
7.3	RESULTS	96
7.3.1	ANIMAL MODEL AND LENS CHARACTERIZATION	96
7.3.2	FEATURES ANALYSIS	101
7.3.3	AUTOMATIC CLASSIFICATION OF CATARACT SEVERITY	105
7.4	DISCUSSION AND CONCLUSIONS	106
7.4.1	ANIMAL MODEL AND LENS CHARACTERIZATION	106
7.4.2	AUTOMATIC DETECTION OF OCULAR INTERFACES	108
7.4.3	AGREEMENT BETWEEN <i>IN VIVO</i> , <i>EX VIVO</i> AND <i>POST MORTEM</i> ACQUISITIONS	108
7.4.4	<i>IN VIVO</i> FEATURES EXTRACTION	109
7.4.5	AUTOMATIC CATARACT CLASSIFICATION	109
7.5	EYE SCAN ULTRASOUND SYSTEM (ESUS)	109
7.5.1	ESUS DESCRIPTION	110
7.5.2	ESUS PROTOTYPE	113
7.6	RESULTING PUBLICATIONS	115
8	<u>CONCLUSIONS AND FUTURE WORKS</u>	117
8.1	CONCLUSIONS	117
8.2	FUTURE WORKS	119

REFERENCES **121**

PUBLICATIONS **145**

<i>EX VIVO</i> EXPLORATORY STUDY	145
<i>EX VIVO</i> STUDY	145
<i>IN VIVO</i> STUDY	146

1 INTRODUCTION

1.1 Motivation

Cataract is a condition associated with the loss of the normal transparency of the crystalline lens. Its progression may result in partial or total vision loss. Cataract is due to several factors, mainly the process of cellular aging, oxidative and photo-oxidative damages, and heredity (Beebe *et al.* 2010; Berthoud and Beyer 2009; Hashim and Zarina 2012; Kruk *et al.* 2015; Michael and Bron 2011; Phaniendra *et al.* 2015; Wormstone and Wride 2011). The cataract formation process comprises fibrosis and protein aggregation within the lens (Beebe *et al.* 2010; Kanski and Bowling 2006; Kruk *et al.* 2015; Prokofyeva *et al.* 2013; Tabandeh *et al.* 2000). Fiber compaction and the lens proteins aggregation and insolubilization have the effect of increasing the light scattering, lens' opacity and hardness, which results in visual acuity loss (Beebe *et al.* 2010). Although some cellular and molecular mechanisms involved in the process of cataractogenesis are already identified, the complete mechanism of the disease is still under investigation (Beebe *et al.* 2010).

Currently, cataract has no pharmacological treatment or prevention (Abdelkader *et al.* 2015; Babizhayev *et al.* 2014; Babizhayev and Yegorov 2014; Babizhayev and Yegorov 2016; Hejtmancik 2015; Njie-Mbye *et al.* 2013); the only effective therapy to restore vision is the cataract surgical removal and lens replacement by an artificial intraocular lens. The phacoemulsification is the most widely used surgical technique for cataract removal (Lundström *et al.* 2012; The Royal College of Ophthalmologists 2015). The knowledge on the appropriate energy levels to be used in this type of surgery is essential for the preservation of the posterior lens capsule integrity, for avoiding corneal endothelial cells loss, and for the preservation of the structures adjacent to the surgical area (American Academy of Ophthalmology 2011; The Royal College of Ophthalmologists 2010; The Royal College of Ophthalmologists 2015). So, the correct cataract location, degree of severity, and specially its hardness are relevant aspects to consider in the surgery planning in order to minimize surgical risks and post-operative complications (Alió and Kady 2010; Hayashi *et al.* 1996).

The search for high safety levels in the phacoemulsification cataract surgery has made the hardness of the cataractous lens a relevant aspect (Paunksnis *et al.* 2007). Lens hardness may depend on many factors such as aging; degree and extent of cataract, which are connected with changes in the lens proteins nature; compactness of the lens fibers; and other biochemical changes (Keenan *et al.* 2008; Tabandeh *et al.* 2000). The accurate estimation of the cataractous lens hardness is important for the optimal selection of the ultrasound energy level to be used for the cataract surgical extraction. Currently, the selection of the ultrasound phacoemulsification energy level is based on a subjective assessment of the cataract hardness. The energy levels to be used in the phacoemulsification for the different types of cataract are not well referenced in the literature. Since they vary from equipment to equipment and depend on its technical specifications, it is not possible to establish reliable reference levels (Fine *et al.* 2001; Gupta *et al.* 2013; Malhotra 2008). In a study encompassing 200 cataract surgeries performed by the same surgeon, using two different types of phacoemulsification devices, Schafer and Arbisser showed that the ultrasound energy levels used in phacoemulsification increased exponentially with cataract severity, ranging from 0.01 Joules for less dense cataracts to 0.3 Joules for dense cataracts, for frequencies ranging from 28 kHz to 50 kHz (Schafer and Arbisser 2004). In that study, it was also shown that when providing additional information to the surgeons on the ultrasonic pulsing regime and energy for the different grades of cataract, the energy level can be reduced by 20% without compromising the clinical effectiveness of the cataract surgery, improving therefore patients' outcomes. Therefore, the cataract hardness estimation can be a relevant information to support the decision about the optimal phacoemulsification or phaco-LASER (Light Amplification by Stimulated Emission of Radiation) energy levels to select.

Ultrasounds can be used for the characterization and visualization of the ocular structures due to its safe nature when used for diagnostics (Pavlin and Foster 2012; Silverman 2009; U *et al.* 2008; WHO Study Group 1998), and easy propagation in opaque structures. The echo signals reflected from a cataractous lens differ from the ones reflected from a lens without cataract. That is due to the microstructural changing of the cataractous lens (Coleman *et al.* 1975; de Korte *et al.* 1994; Paunksnis *et al.* 2007). Since ultrasound waves are largely influenced by the presence of high-molecular-weight compounds and by tissue density the ultrasound parameters have been shown to be related with cataract hardness (El-Brawany 2009; Huang *et al.* 2007a; Huang *et al.* 2009b; Tabandeh *et al.* 2000; Tsui *et al.* 2011). In cataractous lens, the increased protein aggregation and fiber compaction contribute to the lens hardening, which consequently influences the lens tissue echogenicity. Previous works showed that cataractous lenses present higher ultrasound attenuation values, (Huang *et al.* 2007a; Huang *et al.* 2007b; Tabandeh *et al.* 2000) than lenses without cataract. The results obtained for the ultrasound velocity are still under discussion. Huang *et al.* found a velocity increase with cataract progression (Huang *et al.* 2007a; Huang *et al.* 2007b) and Tabandeh *et al.* found no association between ultrasound velocity and cataract progression (Tabandeh *et al.* 2000).

In this context, ultrasound techniques can be used to obtain *in vivo* the lens acoustical parameters, such as the propagation velocity, attenuation, and the backscattering of the ultrasound waves, which can be used for cataract characterization, and particularly for its hardness estimation. Ultrasound techniques are proposed in this thesis as a noninvasive technique for cataract characterization and hardness estimation.

1.2 Objectives

The purpose of this work was to develop a prototype based on the noninvasive ultrasound technique for early cataract detection, automatic classification and hardness estimation *in vivo*. It was expected that the obtained results could contribute with additional and objective information for a sustained decision concerning the optimal energy level to be used in the cataract surgery.

To demonstrate that the ultrasound technique can be used for the noninvasive characterization of the cataractous lens, *ex vivo* studies were first performed in porcine lenses, which are easier to handle (lenses size with 9-10 mm *versus* 4-5mm for the rats), and easily obtained from slaughterhouses.

An exploratory study was first performed to test the feasibility of using the ultrasound technique for the objective cataract characterization, in porcine lenses with different induced cataract degrees. Based on the obtained results a proof-of-concept study was thereafter implemented to validate the experimental setup and to demonstrate that the ultrasound technique can be used to characterize and visualize the cataractous lens, and to estimate noninvasively its hardness. An extensive extraction and selection of features was made to classify automatically the cataract severity, based on the acoustical parameters and backscattering signals. Histological slices from the nucleus and cortex regions were obtained and analysed to show that the used method for cataract induction leads to an increase of lens' fibers compaction and proteins aggregation, and consequently to an hardness increase over the cataract progression. Correlations were made between the slice image characteristics and the extracted features, to characterize the cataract hardness.

After validating the experimental setup, an *in vivo* study was performed for early cataract detection, automatic classification and hardness estimation. One of the challenges was to demonstrate that the tissue structural changes induced by the cataractogenic process promote tissue hardness. Two important biomechanical tissue properties were objectively determined: the hardness and the elasticity. This step was essential to noninvasively estimate the lens hardness, by correlating the acoustical parameters and the extracted features, with the hardness and the elasticity of healthy lenses and lenses with different cataract severity degrees. Moreover, an animal model was created to obtain *in vivo* cataractous lenses with different severity and hardness levels. This cataract model aimed to mimic what happens in humans for the most common type of cataract: the age-related cataract.

1.3 Contribution and relevance

This work was carried out under the project “Development of new methodologies based on ultrasounds for *in vivo* cataract characterization”, funded by the Foundation for Science and Technology (Fundação para a Ciência e Tecnologia – FCT) (grant PTDC/DTP-PIC/0419/2012). The project final evaluation was excellent.

The exploratory results of this work, obtained *ex vivo*, were presented in the PhD proposal (Caixinha 2012), and presented and published as proceedings in two meetings of the Institute of Electrical and Electronics Engineers (IEEE):

- Caixinha M. Técnicas não Invasivas por Ultrassons para Visualização e Caracterização Objetiva da Catarata. Determinação da Energia Ótima para Facoemulsificação. Proposta de Tese de Doutoramento em Engenharia Biomédica. Departamento de Física e Departamento de Engenharia Electrotécnica e de Computadores da Faculdade de Ciências e Tecnologia, e IBILI – Instituto Biomédico de Investigação em Luz e Imagem da Faculdade de Medicina; Universidade de Coimbra (2012).
- Jesus, D.; Caixinha, M.; Santos, M.; Santos, J. Ultrasound techniques for lens hardness characterization: A comparison study. IEEE International Ultrasonics Symposium (IUS). Dresden, Germany. 2012; 2376-2379 (DOI: 10.1109/ ULTSYM.2012.0594).
- Jesus, D.; Velte, E.; Caixinha, M.; Santos, M.; Santos, J. Using of the ultrasound frequency-dependent attenuation and Nakagami distribution for cataract evaluation. Bioengineering (ENBENG), IEEE 3rd Portuguese Meeting. Braga, Portugal. 2013; 1-4 (DOI: 10.1109/ ENBENG.2013.6518388).

The *ex vivo* and *in vivo* results of this work were presented and published as conference papers in three international meetings on biomedical engineering and ultrasounds.

- Caixinha, M.; Jesus, D.; Santos, M.; Santos, J.; Velte, E. Characterization of scatterers concentration in cataractous lens using Nakagami distribution by ultrasounds. IEEE International Ultrasonics Symposium (IUS). Prague, Czech Republic. 2013; 425-428 (DOI: 10.1109/ ULTSYM.2013.0110).
- Caixinha, M.; Velte, E.; Santos, M.; Santos, J. New approach for objective cataract classification based on ultrasound techniques using multiclass SVM classifiers. IEEE International Ultrasonics Symposium (IUS). Chicago, United States of America (USA). 2014; 2402-2405 (DOI: 10.1109/ULTSYM.2014.0599).
- Caixinha, M.; Velte, E.; Santos, M.; Perdigão, F.; Amaro, J.; Gomes M.; Santos, J. Automatic Cataract Classification based on Ultrasound Techniques using Machine Learning: A comparative Study. International Congress on Ultrasonics (ICU). Metz, France. 2015; Physics Procedia vol. 70 p. 1221-1224 (DOI:10.1016/j.phpro.2015.08.263).

The *ex vivo* and *in vivo* results were also published in the IEEE Transaction on Biomedical Engineering journal and Ultrasound in Medicine and Biology journal:

- Caixinha, M.; Jesus, D.; Velte, E.; Santos, M.; Santos, J. Using ultrasound backscattering signals and Nakagami statistical distribution to assess regional cataract hardness. IEEE Transactions on Biomedical Engineering. 2014; 61(12): 2921-2929 (DOI: 10.1109/ TBME.2014.2335739).
- Caixinha, M.; Santos, M.; Santos J. Automatic cataract hardness classification *ex vivo* by ultrasound techniques. Ultrasound in Medicine and Biology. 2015; 1-10 (DOI: 10.1016/j.ultrasmedbio.2015.11.021).

-
- Caixinha, M.; Amaro, J.; Santos, M.; Perdigão, F.; Gomes, M.; Santos, J. *In vivo* Automatic Nuclear Cataract Detection and Classification in an Animal Model by Ultrasounds. IEEE Transactions on Biomedical Engineering. 2016; 63(11): 2326-2335 (DOI: 10.1109/TBME.2016.2527787).

A review on machine learning techniques was also published in the journal Current Eye Research:

- Caixinha M. and Nunes S. Machine Learning Techniques in Clinical Vision Sciences. Current Eye Research. 2016; (DOI: 10.1080/02713683.2016.1175019)

A prototype named ESUS – Eye Scan Ultrasound System for *in vivo* acquisitions was developed and registered under the patent provisional application PPP108836, which is described in section 7.5.

The prototype is composed by an ophthalmic ultrasound probe, an ultrasonic compact pulser/receiver, an analog-to-digital acquisition board and a low-cost system-on-chip (SoC) platform for signal processing and for the detection and classification of the cataract. An android application (app) was also developed to visualize in real time the produced results enabling the use of unwired devices such as tablets. The ESUS was designed to be user-friendly in order to be used in clinical practice. Several options are made available such as the visualization of the acquired A-scan signals, the B-scans images, and ultrasound features.

Registered patent:

- J. Santos, M. Gomes, M. Santos, F. Perdigão, A. Morgado, L. Duarte (M. Caixinha), J. Amaro and J. Ferreira, "ESUS – Eye Scan Ultrasound System", Pedido Provisório de Patente PPP108836, September, 2015.

The prototype was presented in the TECHDAYS meeting in Aveiro, Portugal (17 – 18 September 2015).

All publications are provided in the respective section.

The relevance of this work can be considered in two major aspects, scientific and clinical.

The scientific publications contributed for the state-of-the-art concerning to the eye lens tissue characterization by the ultrasound technique.

The developed methodology that was tested and validated *in vivo* in an animal model, allowed the implementation of the referred prototype for the automatic cataract classification and early detection in order to improve the clinical cataract diagnosis and management; a disease that is the most common cause of avoidable blindness in the world. Concerning to the clinical cataract therapeutic (phacoemulsification cataract surgery), the development of a medical device based on the prototype (ESUS), has the potential to provide important information about the optimal phacoemulsification energy levels, and this way reduce the surgical complications associated with the extraction of dense cataracts. The optimization of the surgical procedure may have a positive socio-economic impact.

1.4 Thesis organization

This thesis is composed by 8 chapters, including the introduction (chapter 1), where the motivation, objectives, contribution and relevance of this work are presented.

The state-of-the-art on cataract clinical epidemiology, cataract formation, management and induction in animal models is presented in chapter 2.

The theoretical background on ultrasounds, the pulse-echo mode, the transducer design, the thermal and non-thermal effects of ultrasounds in biological tissues, and the safety aspects are presented in chapter 3.

Chapter 4 focus on the ultrasound technique applied to the crystalline lens characterization. The acoustical parameters, such as velocity and frequency-dependent attenuation, and the B-scan and Nakagami m parametric imaging techniques are described in the context of cataract characterization and visualization.

Chapters 5, 6 and 7 present the experimental results obtained in this work.

In chapter 5, the exploratory results obtained *ex vivo* in porcine lenses are presented. These experiments were used to design the *ex vivo* proof-of-concept study and the *in vivo* study. The obtained results were presented in the thesis project presented in 2012 in the University of Coimbra (Caixinha 2012) and were used when submitting this work for financial support to the national Foundation for Science and Technology (Fundação para a Ciência e Tecnologia – FCT), which financial support was granted.

In chapter 6, the proof-of-concept study conducted *ex vivo* in porcine lenses is presented.

In chapter 7, the *in vivo* study for early cataract detection, automatic classification and hardness estimation is presented.

The final conclusions, contributions and suggestions for future works are presented in chapter 8.

The scientific contributions of this work are listed at the end of each chapter.

2 OVERVIEW ON CATARACT RESEARCH AND CLINICAL MANAGEMENT

2.1 Introduction

Cataract is a clouding or opacity in the crystalline lens of the eye, and is considered to be a natural consequence of aging. The cataract may progress slowly from slight to complete opacity, leading to vision loss (Beebe *et al.* 2010; World Health Organization 2013). The crystalline lens opacity results from the accumulation of oxidative damages that are a consequence of the cellular ageing process, the protein aggregation, and the disturbance of the regular alignment or packing of the lens fibers, leading to increased light scattering and decreased light transmission, causing opacity and hardening, especially in the lens nucleus (Beebe *et al.* 2010). The oxidative damages are the major cause of cortical and nuclear cataract. The three main types of age-related cataract are associated with the lens regions where the opacities have origin: the nucleus, cortex and the posterior pole (close to the posterior capsule), resulting in nuclear, cortical or posterior subcapsular cataracts, respectively (Figure 2-1). The cataract may also be congenital or may develop secondary to drug, due to trauma, eye injuries, intraocular inflammation, exposure to ionizing radiation and other eye diseases (Beebe *et al.* 2010; Berthoud and Beyer 2009; Hashim and Zarina 2012; Kruk *et al.* 2015; Michael and Bron 2011; Phaniendra *et al.* 2015; Wormstone and Wride 2011)

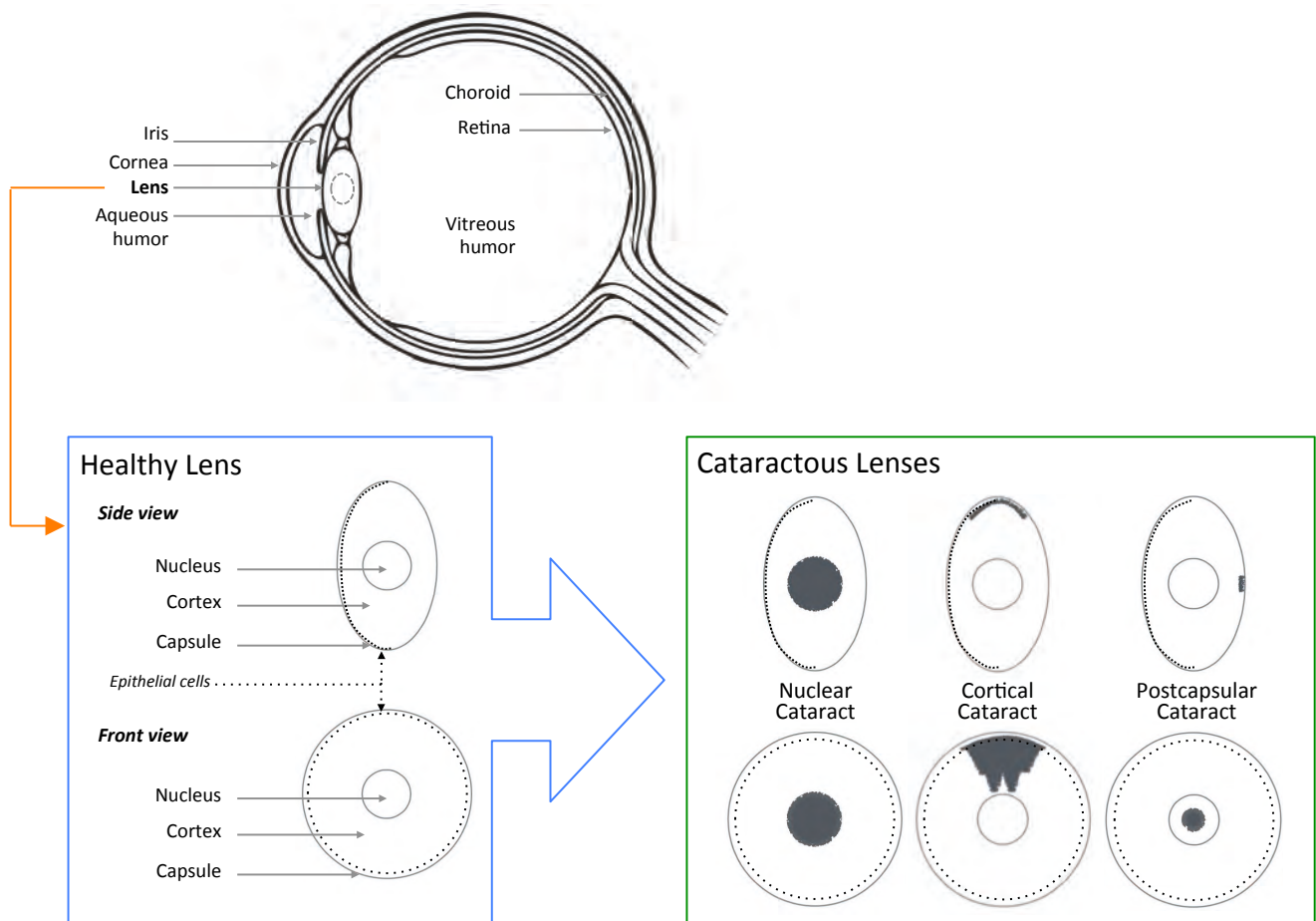


FIGURE 2-1. ILLUSTRATION OF THE MOST COMMON TYPES OF CATARACT (ADAPTED FROM (Beebe *et al.* 2010)).

Although significant progress has been made toward identifying risk factors for cataract development, there is no primary prevention or medical treatment (Abdelkader *et al.* 2015; Babizhayev *et al.* 2014; Babizhayev and Yegorov 2014; Babizhayev and Yegorov 2016; Hejtmancik 2015; Njie-Mbye *et al.* 2013). Cataract surgical removal remains the only successful therapy for vision restoration in over 90% of patients without other complications (Lundström *et al.* 2012; The Royal College of Ophthalmologists 2015). However, even where surgical services are available, low vision secondary to cataract may remain prevalent, as a result of several surgical constraints such as the access to comprehensive eye care integrated into healthcare systems (World Health Organization 2013).

The mechanisms that could prevent age-related cataract are not known yet since ageing is the cumulative effect of the complex interaction of exposure to many factors over time contributing to the development of the cataract. Some of the environmental factors involved in the cataractogenic process are well known, while others are not yet identified or confirmed. Reducing smoking (Cumming and Mitchell 1997; Klein *et al.* 1993; Solberg *et al.* 1998), ocular exposure to ultraviolet-B (UV-B) radiation (Bochow *et al.* 1989; McCarty *et al.* 1999; Taylor *et al.* 1988; West *et al.* 1998; World Health Organization 1994), and alcohol consumption (Cumming and Mitchell 1997; Harding and van

Heyningen 1988; Muñoz *et al.* 1993), may prevent or delay the development of cataract. Diabetes mellitus (Ederer *et al.* 1981; West and Valmadrid), hypertension and high body mass index are other identified risk factors for cataract development (Cumming *et al.* 1997; Garbe *et al.* 1998; Hodge *et al.* 1995; Kanski and Bowling 2006; Taylor 1999).

Studies in cataract epidemiology identified a strong genetic component. Studies performed in twins showed that more than half of the cortical and nuclear cataracts are heritable (Hammond *et al.* 2000; Hammond *et al.* 2001; Heiba *et al.* 1993; Heiba *et al.* 1995; McCarty *et al.* 1999). However, at this stage, nothing can be done at genetic level to prevent or delay cataract development.

Studies based on the cellular and molecular mechanisms associated with the cataractogenesis process open new perspectives for the prevention and/or delay of the cataract formation. With the exception of the antioxidant vitamins A, C, and E (Taylor *et al.* 1995), no other protective pharmaceutical components has emerged. However, the challenge for the identification of an effective preventive drug is still kept.

Advances in cataract research must follow in the prevention direction, focused on identifying genetic and molecular mechanisms involved in the process of cataract development (Abdelkader *et al.* 2015; Babizhayev *et al.* 2014; Babizhayev and Yegorov 2014; Babizhayev and Yegorov 2016; Christopher *et al.* 2014; Hejtmancik 2015; Njie-Mbye *et al.* 2013). Pharmacological means of preventing the disease are needed to reduce the number of patients needing cataract surgery. Although cataract surgery is safe, there are still complications that may lead to vision loss (Lundström *et al.* 2012; The Royal College of Ophthalmologists 2015). Therefore, the surgical treatment should move towards to less invasive and safer surgical methods, since the surgical technique itself is related to the fragmentation of the cataract for later removal.

The development of new techniques that can be applied during the surgical process, giving more information and safety to the surgeons, remains a scientific and technological challenge. When providing surgeons with real time and objective information about the patient-cataract properties, the surgery settings can be optimized, making the surgical procedure safer, then reducing the surgical complications, particularly in the case of dense nuclear cataracts that require higher phacoemulsification energy (Abell *et al.* 2015; Schafer and Arbisser 2004; Tabandeh *et al.* 1994).

2.2 Prevalence of the cataract

According to the World Health Organization (WHO), age-related cataract is responsible for 33% of the avoidable blindness in the world, representing about 20 million people (World Health Organization 2013). Cataract is now the most frequent cause of blindness in the world (Boyers *et al.* 2015; World Health Organization 2005; World Health Organization 2013). It is estimated that over the next 10 to 20 years the world's population will increase by about one third, doubling the number of people over 65 years. If that increase in the elderly population is confirmed, the number of cases with reduced vision (lower than 3/60) or blindness secondary to cataract will double, reaching

approximately 40 million people by the year 2020 (Bourne *et al.* 2014; Boyers *et al.* 2015; Lundström *et al.* 2012; The Royal College of Ophthalmologists 2015; World Health Organization 2005; World Health Organization 2013). The epidemiological studies on cataract (*i.e.*, surveys carried out to assess the prevalence and/or incidence of cataract by age, sex and geographic distribution of the population) show that about 10% of the active population in Europe has age-related cataract (Prokofyeva *et al.* 2013). The prevalence of cataract increases with age from 5% for ages ranging from 52 to 62 years to 64% for the ages above 70 years (Prokofyeva *et al.* 2013).

2.3 Clinical cataract management

Several guidelines are available for clinical cataract management (American Academy of Ophthalmology 2011; American Optometric Association 2004; The Royal College of Ophthalmologists 2010; The Royal College of Ophthalmologists 2015). The National Institute for Health and Care Excellence (NICE)¹ is currently developing an evidence-based guideline for the diagnosis and management of cataracts². That guideline, planned for April 2018, is expected to be used as a reference guideline in Europe.

The clinical cataract management depends on the cataract type and the resulting visual disability, which includes the effects of cataract on the visual function, lifestyle and daily activities (The Royal College of Ophthalmologists 2015). Cataracts may be classified into several types based on their appearance and origin. According to the latest version of the International Statistical Classification of Diseases and Related Health Problems 10th Revision (ICD-10)³, lens disorders related with cataract are classified as: senile cataract (code H25); other cataracts (code H26); other lens disorders (code H27); cataract and other lens disorders in diseases classified elsewhere (code H28); and congenital lens malformations (code Q12).

Different symptoms may therefore result from the different cataract types. The cataract characteristic symptoms are the decrease on visual acuity and increased light scattering, and as a direct consequence, increased glare, and contrast sensitivity reduction (The Royal College of Ophthalmologists 2015). Myopia can also arise as a consequence of changes in the lens refractive index, reducing by this way the visual acuity. Nuclear cataract, for example, is characterized by distance vision impairment, while cortical and posterior subcapsular cataract is characterized by disabling glare, even before visual acuity impairment. Patients with cataract should be informed of possible changes in vision such as reduced visual acuity or contrast sensitivity or even the possibility of seeing multiple images (polyopia), which may be permanent or occurring only under certain conditions. The patient should also be informed that the presence of an opacity in the crystalline lens does not necessarily require a surgical intervention.

¹ NICE is an European institute that provides evidence-based guidance to inform decision making in healthcare.

² <http://www.nice.org.uk/guidance/indevelopment/gid-cgwave0741> (accessed on February 26th 2016).

³ International Statistical Classification of Diseases and Related Health Problems 10th Revision (ICD-10) (<http://apps.who.int/classifications/icd10>, accessed on July 20th 2014).

When vision loss affects the ability to make the daily life normal activities, the cataract surgical removal should be considered (The Royal College of Ophthalmologists 2015).

The phacoemulsification is the standard surgical technique for cataract removal and vision recovery, being used in more than 99.5% of the cases (Lundström *et al.* 2012). The cataract surgery improves visual function, namely visual acuity, contrast sensitivity, depth perception, activity, anxiety, depression, visual disability, and quality of life (The Royal College of Ophthalmologists 2015). This surgical procedure uses an ultrasonic device that is inserted into the lens through a small puncture to fragment the cataract into small pieces, which are then aspirated (Abell *et al.* 2014; Huang *et al.* 2007b; Wilson *et al.* 2005). After aspiration, an intraocular lens is placed into the capsular bag replacing the natural lens. Currently, there are two main types of surgical procedures of common use, the extracapsular cataract surgery and the extracapsular surgery with small incision. In both techniques, the posterior lens capsule remains intact to sustain the intraocular lens to be implanted and prevent the invasion of surgical material into the vitreous, avoiding the risk of surgical complications (American Academy of Ophthalmology 2011; American Optometric Association 2004; Coombes and Gartry 2003; Haripriya *et al.* 2012; Lundström *et al.* 2012; Pershing and Kumar 2011; Tabin *et al.* 2008; Zhang *et al.* 2013). Thus, the lens capsule integrity is essential for reducing the risk of surgical complications and subsequent vision loss.

Surgical complications leading to permanent vision loss are rare (American Academy of Ophthalmology 2011; Lundström *et al.* 2012; The Royal College of Ophthalmologists 2015). The main complications potentially harmful include corneal endothelium damage, infectious endophthalmitis, expulsive intraoperative hemorrhage, cystoid macular edema, retinal detachment, corneal edema, and intraocular lens luxation. Less common complications but equally harmful, include secondary glaucoma, displacement of the choroid, and vitreous hemorrhage (hemovitreal). Less serious complications include poor closure of the surgical incision, sterile hypopyon, iris lesion, posterior capsular rupture, vitreous loss, and iritis (inflammation of the iris), (American Academy of Ophthalmology 2011).

Recently, new phacoemulsification approaches based on LASER technology have emerged. Those techniques, called phaco-LASER, allow for more accurate and minimal corneal incision and anterior capsulotomy, and require lower energy levels for cataract emulsification by using pulsed LASER. Despite reducing corneal damages by thermal effects, phaco-LASER techniques have some disadvantages, namely limited efficiency for nuclear cataract extraction, low effectiveness to fragment dense cataracts, and increased surgical time (Fine *et al.* 2004; Fine *et al.* 2002; Yeoh 2014). A recent study performed in 4080 eyes compared the safety of the phaco-LASER with the traditional phacoemulsification techniques (Abell *et al.* 2015). In both techniques the energy levels used to fragment the cataract were chosen by the surgeon based on the lens appearance (cataract density). This study concluded that the safety and the posterior capsule complications are equal between both techniques. The development of surgical methods safer and less invasive that use reduced phacoemulsification energy, and reducing consequently the damages caused by the associated thermal effects, remains a scientific challenge (Abell *et al.* 2015; Donaldson *et al.* 2013; Fine *et al.* 2004).

In the surgery of dense cataracts, particularly for the case of nuclear cataract extraction, the risks of surgical complications by posterior lens capsule rupture, and corneal endothelial cells loss are still considerable (Artzén *et al.* 2009; Fine *et al.* 2002; Ilavska and Kardos 2010; Kim 2009; The Royal College of Ophthalmologists 2010). Nuclear cataract is the type of cataract with higher hardness (Hatch *et al.* 2015; Tabandeh *et al.* 1994; The Royal College of Ophthalmologists 2010). This type of cataract requires higher ultrasound or LASER radiation energy levels to be fragmented, and consequently is associated to higher percentages of surgical complications (Johansson *et al.* 2009; Muhtaseb *et al.* 2004). It is well established that the phacoemulsification energy levels are directly related with the cataract hardness (Fine *et al.* 2004; Fine *et al.* 2002; Venkatesh *et al.* 2010). An inappropriate selection of the phacoemulsification energy level underlies the main surgical complications (Smadja and Krueger 2013). It is therefore, important to estimate the cataract hardness in order to minimize the surgical complications, namely in dense or nuclear cataracts (Davison and Chylack 2003; Fine *et al.* 2001; Leon *et al.* 2016). The major post-surgical complications associated with this type of surgery as result of the energy overestimation, represents 5 to 10% of the total complications, where the more frequent are the corneal endothelial cells loss (Boyd *et al.* 2012; Chen *et al.* 2015; Dick *et al.* 1996; Dick 2010; Fakhry and El Shazly 2011; Hayashi *et al.* 1994; Hayashi *et al.* 1996; Liu *et al.* 2007; Walkow *et al.* 2000) and the posterior lens' capsule rupture (American Academy of Ophthalmology 2011; American Optometric Association 2004; Johansson *et al.* 2009; Smadja and Krueger 2013; Yap and Heng 1999). About 3% of these complications result in total vision loss (American Optometric Association 2004).

2.4 Clinical methods for cataract characterization and classification

2.4.1 Methods for cataract visualization and characterization

The currently available methods for the visualization and evaluation of cataracts are (Camparini *et al.* 2000; Datiles *et al.* 1987; Malhotra 2008; Smith *et al.* 2001):

- Slit Lamp Biomicroscopy;
- Scanning LASER Slit Lamp Photography;
- Scheimpflug Slit Lamp Photography;
- Retroillumination Slit Lamp Photography;
- Quasi-Elastic LASER Light Scattering Spectroscopy;
- Magnetic Resonance Imaging.

The current guidelines for clinical cataract management recommended the slit lamp for cataract visualization and characterization (Datiles and Ansari 2006; The Royal College of Ophthalmologists 2010). This method consists of a high intensity light source, focused in the eye with a shape of a slit of light, and a biomicroscope, that allows a magnified visualization of the eye anterior segment. In the presence of extensive opacities, this method cannot allow the correct visualization of the areas behind the lens, and methods such as the retroillumination slit lamp or Scheimpflug slit lamp photography can be used (Datiles and Ansari 2006). In the retroillumination method the

images are obtained by light reflected by the retina. The Scheimpflug photography is based on the Scheimpflug principle, and allows obtaining a focused image even if the lens plane and image plane are not parallel. This technique requires multiple images of different meridians to assess the extent of the cataract opacity.

2.4.2 Cataract classification

Several cataract classification systems based on standard images have been developed to document and monitor cataract formation, progression or regression, (Datiles *et al.* 1987; Wong *et al.* 2013). Classification systems for cataract are of major importance in clinical research because they allow the semi-objective assessment of drug effect during the development and/or progression of cataract (Datiles *et al.* 1987; Magno *et al.* 1993; Wong *et al.* 2013).

The severity degree of cataracts is classified based on the visual evaluation of the lens opacity, or based on alternative classification systems that compare the obtained images with standard images of the crystalline lens.

The nuclear cataract is usually classified based on the colour and opalescence of the nucleus using standard images obtained by a slit lamp, while the cortical and posterior subcapsular cataracts, are usually classified by using images obtained with standard retroillumination (Bencić *et al.* 2005).

There are several international cataract classification systems that are based on the lens shape and colour. The most commonly used are: Oxford Clinical Cataract Classification and Grading System (Sparrow *et al.* 1986), Johns Hopkins System (West *et al.* 1988), Wisconsin Cataract Grading System (WCGS) (Klein *et al.* 1989; Klein *et al.* 1992), the modified system WCGS - Age-Related Eye Disease Study (AREDS) Lens Opacity Grading Protocol (Klein *et al.* 1992; Thylefors *et al.* 2002), and the Lens Opacity Classification System (LOCS versions I, II, and III) (Chylack *et al.* 1989; Chylack *et al.* 1993; Davison and Chylack 2003; Leske *et al.* 1988).

The LOCS classification system, introduced in 1988 by Leske (Chylack *et al.* 1989; Chylack *et al.* 1993; Leske *et al.* 1988) is still the classification system frequently used for cataract severity degree evaluation. Beside its use in clinical research, it is also widely used to monitor the cataract progression in clinical studies, especially the senile cataract (Magno *et al.* 1993).

The cataract degree classification, according to the LOCS III system is obtained by comparing the cataractous lens with a set of sixteen standard photographs: six reference photographs for nuclear cataract (N), five reference photographs for cortical cataract (C) and five reference photographs for the posterior subcapsular cataract (P) (Figure 2-2). A severity level ranging from 1 to 6 is used for the opalescence of the nuclear cataract (NO) (NO1 to NO6) and for its colour (NC) (NC1 to NC6). For the cortical cataract (C) and posterior subcapsular cataract (P) a severity level ranging from 1 to 5 is used (C1 to C5 and P1 to P5, respectively).

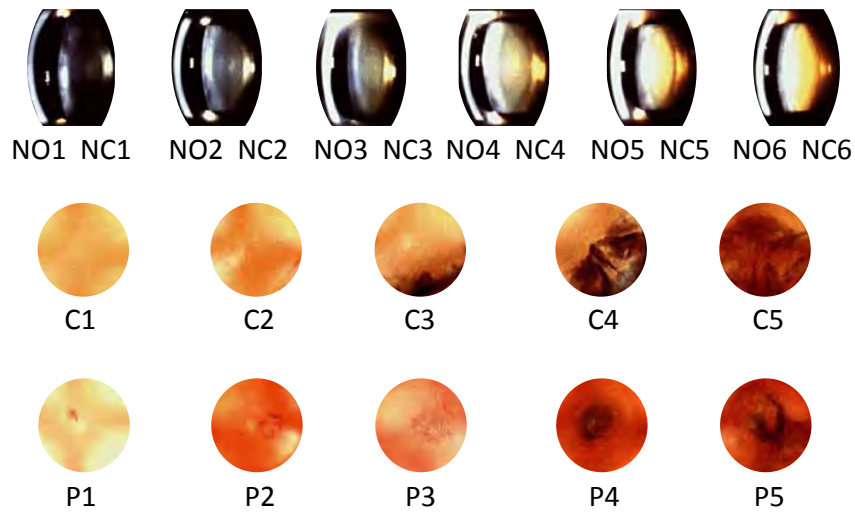


FIGURE 2-2. STANDARD IMAGES FOR LOCS III CLASSIFICATION SYSTEM (ADAPTED FROM (Chylack *et al.* 1993)).

A relationship between the nuclear cataract severity assessed using the LOCS III and the energy level used for the phacoemulsification was already established. Higher phacoemulsification energy levels (time and power) are required as the NC and NO increase (Bencić *et al.* 2005; Davison and Chylack 2003; Filgueira *et al.* 2016; Gupta *et al.* 2013; Magalhães *et al.* 2011). The LOCS III is a useful cataract classification system for the lens opacity evaluation, either for clinical practice or for surgeries allowing the phacoemulsification energy level estimation (Bencić *et al.* 2005; Filgueira *et al.* 2016). However, this type of classification system, like the other systems for cataract classification (Chylack *et al.* 1989; Chylack *et al.* 1993; Klein *et al.* 1989; Klein *et al.* 1992; Leske *et al.* 1988; Sparrow *et al.* 1986; Thylefors *et al.* 2002; West *et al.* 1988), rely on a subjective evaluation that depends on the exam settings, and the examiners expertise (Davison and Chylack 2003; Gao *et al.* 2013; Kirwan *et al.* 2003; Panchapakesan *et al.* 1997). Some approaches have been used for the automatic classification of the cataract severity, however those approaches rely also on retroillumination and/or slit lamp images depending therefore on the exam settings (Camparini *et al.* 2000; Cheung *et al.* 2011; Datiles *et al.* 1987; Gao *et al.* 2013; Kolhe and Guru 2015; Magno *et al.* 1993; Xu *et al.* 2013).

In clinical practice a simplified LOCS system is usually used for monitoring the progression of nuclear, cortical, and posterior subcapsular cataracts (Table 2-1).

TABLE 2-1. SIMPLIFIED LOCS SYSTEM FOR NUCLEAR, CORTICAL AND SUBCAPSULAR CATARACTS GRADING (ADAPTED FROM (American Optometric Association 2004)).

	Level 1	Level 2	Level 3	Level 4
<i>Nuclear Cataract</i>				
Yellowing and sclerosis of the lens nucleus	Mild	Moderate	Pronounced	Severe
<i>Cortical Cataract</i>				
Percentage of the intrapupillary space occupied by opacity	10%	10%-50%	50%-90%	> 90%
<i>Posterior Subcapsular Cataract</i>				
Percentage of the posterior capsular area occupied by opacity	3%	30%	50%	> 50%

While the LOCS system allows the classification of the cataract severity and for the detection of changes of the cataract progression in a short period of time, even when the crystalline presents only moderate opacities (Magno *et al.* 1993), it does not allow the estimation of the lens hardness. The extraction of objective and quantitative parameters that correlate with the lens hardness was first studied by Smith (Smith *et al.* 2002). The author established *ex vivo* in human crystallines, a relationship between the mechanical parameters of the lens (degree of compressibility) and its visual appearance (opacity). Smith found a strong correlation between the progression of the cataracts and the colour of the nucleo-cortex of the lens. The work of Smith suggests that the progression of the cataracts can be estimated based on intrinsic parameters of the crystalline lens that can be measured objectively.

In the last years the applicability of ultrasounds to the cataractous lenses characterization has been studied (He and Liu 2009; He and Liu 2011; Huang *et al.* 2007a; Huang *et al.* 2007b; Huang *et al.* 2009a; Tsui *et al.* 2011; Wang *et al.* 2011). In cataractous lenses, regions of higher opacity are associated with stronger echoes due to impedances mismatching verified in the interface between normal tissue and cataract. So, the signature of the echo signal from a lens with cataract differs from the one of a lens without cataract (Tsui *et al.* 2007; Tsui *et al.* 2011; Tsui and Chang 2007). The ultrasounds appear as a powerful noninvasive and less expensive technique, working as an alternative for objective cataract characterization and classification (Caixinha *et al.* 2014a; Huang *et al.* 2007a).

2.5 Animal models for Cataract induction

The use of rats as models for the study of human disease has a long history, extending back to the last century. Animal models are frequently used in the early stages of clinical research to study biological and molecular processes that occur in humans. Those models are used for testing and visualization of hypotheses *in vitro* and *in vivo* that will be tested and verified in humans, in the latest stages of the research. The knowledge of the human and rat's genomes has lead to the development of new animal models based on the controlled alteration of the animals' genetic code. Currently available genetic variants of rats' models include a wide spectrum of human ocular diseases (Smith *et al.*

2001) including glaucoma (Anderson *et al.* 2002; Chang *et al.* 1999), retinal and macular degeneration (Hawes *et al.* 2000; Ikeda *et al.* 2000; Kedzierski *et al.* 2001), cataracts (Ai *et al.* 2000; Smith *et al.* 1997), retinoblastoma (Windle *et al.* 1990), and intraocular tumours (Anand *et al.* 1994; Syed *et al.* 1998). The genetic imprint of disease is often superimposed on the complex molecular expression patterns that accompany the normal development. Thus, understanding the regulation and controlling mechanisms of the normal development, it is expected to create knowledge of major importance for the interpretations of disease stages.

2.5.1 Induction processes

The eye is constantly exposed to the external atmospheric agents and it has been shown that the oxygen-derived free radicals are involved in some ocular diseases such as cataracts (Manikandan and Thiagarajan 2009; Santosa and Jones 2005).

The hydrogen peroxide (H₂O₂) is an oxidant intermediate that is present in the anterior and posterior eye segments being involved in the pathophysiological changes of the eye (Li *et al.* 2010; Manikandan and Thiagarajan 2009; Nakajima *et al.* 2002). By regulating the free radicals in the eye the disease onset can be delayed (Berthoud and Beyer 2009; Goswami *et al.* 2003; Jin *et al.* 2010; Santosa and Jones 2005). Some of the biochemical processes that occur in the cataract formation, in particular cataract mediated by selenite are already identified in animal models. These mechanisms are: alteration in the metabolism of cell membrane, intracellular accumulation of calcium-induced calpain proteolysis, cytoskeletal loss and precipitation of the crystalline proteins (Li *et al.* 2010; Manikandan and Thiagarajan 2009; Nakajima *et al.* 2002).

The human eye has several endogenous defence mechanisms that are capable of protecting the lens of the photo-oxidative and oxidative damage. Selenite-induced oxidative stress mediated cataractogenesis has been shown to be prevented by antioxidative agents. Selenite is an essential trace element in the eye since it induces oxidative stress and, at the same time, forms an important part of biological defence as a key component of selenoproteins, protecting against cadmium-mediated apoptosis by regulating reactive oxygen species generation. However, in amounts considered toxic it is able to significantly induce oxidative stress by formation of reactive oxygen species (Manikandan and Thiagarajan 2009).

Figure 2-3 illustrates the general mechanisms of the cataract formation and Figure 2-4 illustrates the biochemical process of the selenite-induced cataract.

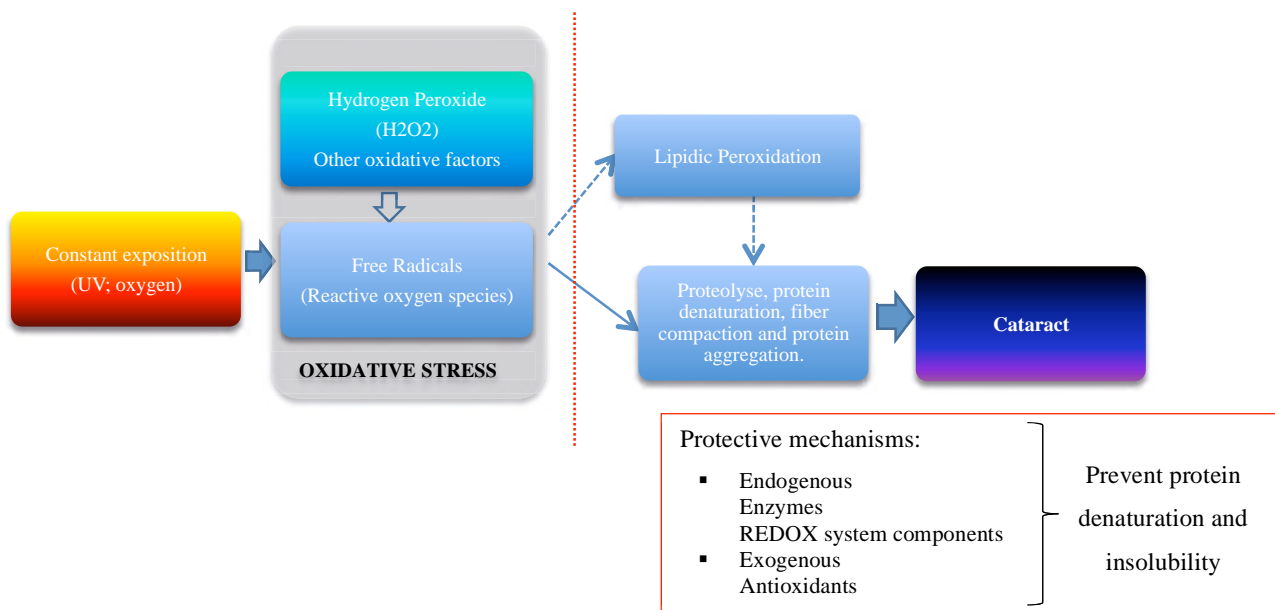


FIGURE 2-3. GENERAL MECHANISMS OF THE CATARACT FORMATION.

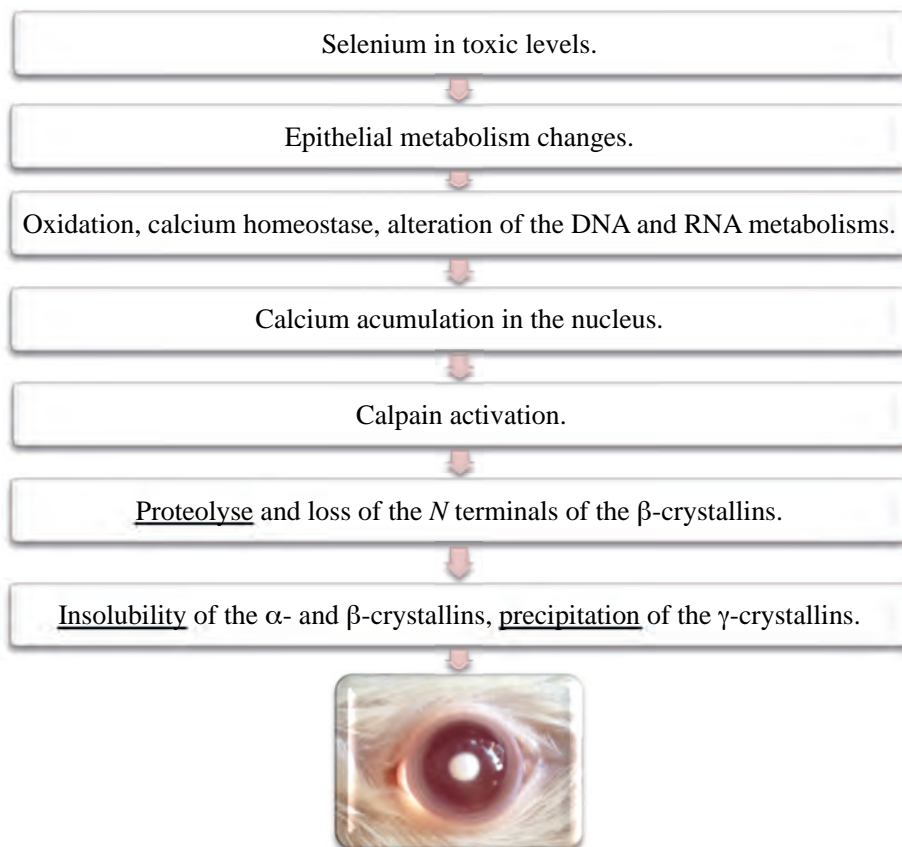


FIGURE 2-4. BIOCHEMICAL PROCESS OF THE SELENITE-INDUCED CATARACT (ADAPTED FROM (Shearer *et al.* 1997)).

The ability of selenite to cause cataracts was first described in 1977 by Ošťádalová (Ošťádalová *et al.* 1977). Cataract by selenite-overdose is an extremely rapid and convenient model for nuclear cataract (Shearer *et al.* 1997). Shearer *et al.* used the animal model of selenite-induced cataract in order to identify molecular mechanisms involved in the process of cataractogenesis (Shearer *et al.* 1997). In this animal model cataract is produced in suckling rat pups by an overdose of the essential trace mineral selenite, usually by a subcutaneous injection of 19-30 μ moles/kg body weight of sodium selenite (Na₂SeO₃) into rats of 10-14 days of age, since selenite is cataractogenic only when administered in rats before completion of the critical maturation period of the lens, *i.e.*, approximately 16 days of age.

Within 4-6 days severe bilateral nuclear cataracts are present.

The current state-of-the-art on age-related cataract prevention shows that the research is performed predominantly in rats' selenite cataract models (Kyselova 2010). Even though selenite was shown to induce oxidative stress in lens tissue, its exact mode of action is still unclear, needing further investigation.

For *ex vivo* studies other animal models can be used. For phacoemulsification training, Sugiura *et al.* (Sugiura *et al.* 1999) created an *ex vivo* animal model in porcine eyes, by injecting into the lens a formalin and alcohol solution (ethanol, 2-propanol, or both). With this solution the authors intended producing a cataract similar to the human cataract, *i.e.*, a cataract with a uniform and reproducible nucleus hardness and an anterior capsule with a viscosity and elasticity similar to the human cataractous lens' capsule.

Formalin was used to harden the lens nucleus and reduce the lens capsule's viscosity and elasticity. Formalin fixes proteins and tissues (including connective tissue and lipids) when the amino group of the proteins reacts with the aldehyde group by cross-linkage. However, because formalin alone results only in a partial nucleus hardening, it was combined with an alcohol (ethanol and/or 2-propanol). Alcohols have a strong affinity with both water and formalin, and the formaldehyde molecules, dissolved in alcohol to form hydrogen bonds with alcohol molecules, can uniformly permeate the lens. The most effective solution to create a nuclear cataract in porcine lenses was the solution ethanol:2-propanol:formalin in a ratio of 3:3:4 (Sugiura *et al.* 1999).

2.5.2 *In vivo* studies

Many medical imaging technologies developed for humans are now being scaled down for small animals allowing to study diseases such as cataract (Langner *et al.* 2010; Needles *et al.* 2010; van Oterendorp *et al.* 2011). Imaging techniques applied to animal's models not only permit the observation *in vivo* of the functional and morphologic changes resulting from the genetic alteration but also allow longitudinal studies under carefully controlled conditions. Microimaging technologies, such as fundus photography, fluorescein angiography, and gonioscopy⁴, have been adapted to the rat with some difficulty. Scaled versions of ultrasound, magnetic resonance (MR), and computed tomography (CT) imaging have also been adapted to the rat (Foster *et al.* 2003; Needles *et al.* 2010; Zhang *et al.*

⁴ Gonioscopy: method for evaluating the iridocorneal angle.

2011). Whereas micro-MR and -CT approaches have largely concentrated on imaging of embryonic rat development after death, ultrasounds (ultrasonic biomicroscopy – UBM), has been used for *in vivo* imaging of the rat's lens (Foster *et al.* 2003). To study the normal embryonic development of the mouse eye Foster *et al.* (Foster *et al.* 2003) used an UBM with a 40 MHz probe. Sixty-five (65) embryonic eyes were analysed at different development stages. The morphogenesis of the ocular tissues, *e.g.*, retina, lens, and cornea, was revealed from the earliest stages of embryonic development. Using UBM the authors were able to assess *in vivo* the ocular morphogenesis and to compute the relative growth rates of different ocular structures, *i.e.*, globe and lens.

In this thesis a 20 MHz ophthalmic ultrasound probe was used for *in vivo* ultrasound signals collection in an animal model for nuclear cataract. The work developed, presented in chapter 7, demonstrated that the use of high frequency ultrasounds allows obtaining biometry of the ocular interfaces, and also automatic nuclear cataract detection and classification.

3 ULTRASOUNDS

3.1 Introduction

Ultrasounds are characterized as mechanical waves propagating with frequencies higher than the upper audible limit of human hearing, which is approximately 20 kHz in healthy young adults. Since the mechanical wave propagation is a result of particles vibration, ultrasounds only exist in material media. Thus, it is expected that the ultrasound waves are greatly influenced by the medium in which they travel. As the ultrasound waves propagate they suffer attenuation (Cobbold 2006). This attenuation is a result of absorption, when the acoustical energy is transferred to the medium and converted into heat; or scattering, when the incident ultrasound wave interacts with the medium microstructural composition generating secondary waves.

The ultrasound wave intensity at a depth x ($I(x)$), for a plane wave and for an incident wave (at the transducer surface) with intensity (I_0), can be written as,

$$I(x) = I_0 e^{-\alpha x} \quad (3-1)$$

where α is the frequency-dependent attenuation coefficient in the tissue.

Essentially two wave modes can occur as the ultrasound waves propagate: longitudinal (compressional) wave mode, if the particles vibration is in the same direction as the ultrasound wavefront propagation; and transverse (or Shear) wave mode, if the particles vibration is normal to the direction of the wave propagation. Shear waves have little relevance in soft tissues evaluation (British Institute of Radiology 2000). The longitudinal waves are the most commonly used in medical applications.

Ultrasounds are considered safe and effective for *in vivo* imaging (WHO Study Group 1998). The ultrasound application in the biological tissue characterization has been extensively studied in recent years and implemented into many important imaging medical tools for diagnosis.

The first applications of ultrasound methodologies for eye imaging originated in the 50's decade of the previous century with the work of Mundt and Hughes (Mundt and Hughes 1956) and Baum and Greenwood (Baum and Greenwood 1958). Due to the eye's properties, namely their aqueous components and structure, ultrasounds are suitable for imaging, allowing to study the ocular pathologies and anatomy (Chaudhari *et al.* 2013). Compared to other imaging modalities used in ophthalmology, ultrasounds are safe and noninvasive allowing to visualize structures even in the presence of obscuring lesions, such as vitreous hemorrhage, or in the presence of opacities, such as cataracts (Lizzi and Coleman 2004; Pavlin and Foster 2012). Currently, the technique is widely used in clinical practice for the biometry of the ocular structures, in particular to measure the globe length, to estimate the corrective lens power, detect and measure ocular tumors, including choroidal melanomas, visualize lens dislocation, and to detect retinal abnormalities, including retinal detachment.

The centre frequency used for ocular biometry and diagnosis is usually in the order of 10 MHz, except for the UBM systems that use higher frequencies, typically between 35 and 50 MHz, allowing higher resolutions in the detection of the eye anterior segment structures (Konstantopoulos *et al.* 2007; Silverman 2009). The frequency selection is a trade-off between the spatial resolution of the image and the penetration depth. Thus, lower frequencies produce lower resolutions but deeper eye regions can be imaged. High frequencies cannot penetrate deeply into tissue, but provide high-resolution images. For instance, a 2 MHz probe will produce low-resolution images of internal organs such as the liver, while a 50 MHz probe will produce high-resolution images of superficial tissues as cornea (He and Liu 2009; He and Liu 2011; Realini and Lovelace 2003).

3.2 Ultrasound concepts

Ultrasounds are generated by a piezoelectric effect transducer, or probe. The transducer consists of an active element (ceramic material), which has the ability to operate both as a transmitter and a receiver of mechanical waves. The transducer active element converts electrical signals into acoustical waves that propagate through the medium and converts the echo signals from the tissue boundaries into electrical ones. A matching layer is also used to allow maximum energy transfer to the medium as well as a backing material (damping material) to avoid multiple reflections in the opposite face of the active element. Figure 3-1 illustrates an ultrasound transducer.

In general, the matching layer can be composed by several layers with different acoustical impedances in order that the layer directly contacting the tissue has approximately the same impedance of it. The layers' thickness corresponds to one quarter-wavelength. The acoustical impedance is denominated by Z and is given by,

$$Z = \rho v \tag{3-2}$$

where ρ is the tissue mass density and v is the wave propagation velocity. Reflections can occur in the tissue interfaces, whenever the media present different acoustical impedances. For instance, an interface made of soft

tissue-bone, produces a high reflection coefficient, which is characterized by a bright region on the ultrasound image (Haar 2011).

The transducer can be focused to enhance the lateral resolution and increase the acoustical power at the focus region. The lateral resolution is given by,

$$\text{Lateral Resolution} = f_{number}\lambda \quad (3-3)$$

where f_{number} is the transducer f -number, given by the ratio between the transducer focal length (L) and aperture (D), and λ is the ultrasound wavelength. The axial resolution is given by,

$$\text{Axial Resolution} = vt_{pulse}/2 \quad (3-4)$$

where v is the ultrasound velocity and t_{pulse} is the pulse period (Silverman 2009).

The pulse-echo mode is the diagnostic method essentially used in medicine. In this mode, a single probe is used for two important functions: acoustical signal transmission and echoes receiving (Figure 3-2). This approach was used in the present work for *ex vivo* and *in vivo* signal acquisitions.

For diagnostic use, the total acoustic power emitted by the transducer, *i.e.*, the rate at which energy is emitted by the transducer to the biological tissue, should be below several hundred milliwatts in order to avoid thermal and non-thermal effects (British Institute of Radiology 2000). These effects depend on ultrasound exposure duration, intensity, frequency, emission mode (pulsed or continuous) and acoustic power.

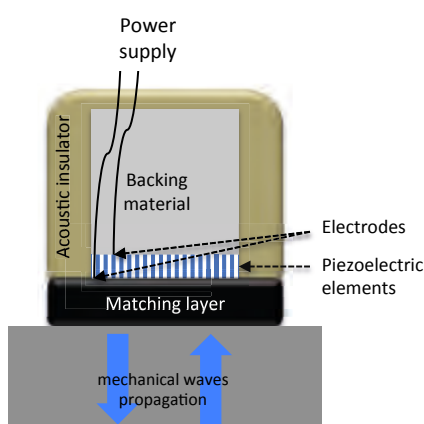


FIGURE 3-1. ILLUSTRATION OF A PULSE-ECHO TRANSDUCER.

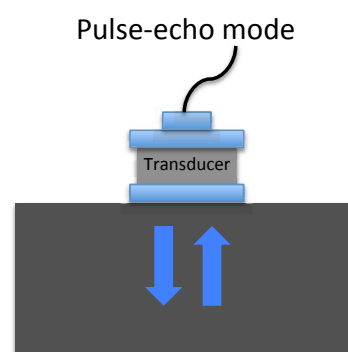


FIGURE 3-2. ILLUSTRATION OF THE PULSE-ECHO MODE.

3.3 Thermal effects

The absorption of acoustical energy within tissue causes a temperature increase. The amount of heat depends on the intensity of the ultrasound wave (I), the time of exposure, and the absorption characteristics of the tissue.

The rate of heat per unit volume (\dot{Q}) is given by the expression,

$$\dot{Q} = \alpha I \quad (3-5)$$

where α is the attenuation coefficient. If there is no heat loss by conduction, convection or radiation, (Haar 2011), we have,

$$\dot{Q} = \rho C dT/dt \quad (3-6)$$

where ρ is the tissue density, C is the heat capacity of the tissue, and dT/dt is the rate of temperature change with time. The maximum possible rate of temperature increase for different modes of ultrasound is estimated from $\alpha I/\rho C$. Therefore, to prevent thermal injury the time of exposure should be minimized (Deane and Lees 2000). The emission mode and the beam width should also be considered since pulsed waves and/or wider beams can reduce temperature increase (British Institute of Radiology 2000; Shankar and Pagel 2011).

Factors related with the biological tissue characteristics, such as: the tissue protein content (absorption coefficients are directly related to tissue protein content, (Shankar and Pagel 2011)) and the tissue perfusion (that allows heat dissipation by convection, (Horder *et al.* 1998)) should also be considered to prevent thermal injury.

3.4 Non-thermal effects

Acoustical energy creates also mechanical, or non-thermal effects, such as, cavitation, torque forces, oscillatory shear, pressure and acoustic streaming.

Cavitation is produced by the interaction of ultrasound with gas bubbles. This process may increase temperature and pressure within the bubble and cause mechanical stress on surrounding tissues, (Dalecki 2004). Biological structures containing gas, such as lungs or intestines, are prone to cavitation effects.

For ultrasound imaging, that uses frequencies higher than 1 MHz, the cavitation effect is unlikely (Leong *et al.* 2011).

3.5 Safety

Ultrasounds produce thermal and non-thermal effects in biological tissue (British Institute of Radiology 2000; Haar 2011; Shankar and Pagel 2011; U.S Department of Health and Human Services *et al.* 2008). In Europe, ultrasound imaging devices must comply with the essential requirements for safety and effectiveness laydown in the Medical Devices Directive 93/42/EEC (European Union) and the international standards IEC 60601 and 61157 (International Electrotechnical Commission 1992; International Electrotechnical Commission 2005).

Two indices, derived from the acoustic power output, are usually provided to the users to monitor patient's safety during patients' examination: the thermal index (TI) and the mechanical index (MI). The users should monitor both indices during ultrasound acquisitions and adjust the ultrasound imaging devices settings to keep these indices as low as reasonably achievable (ALARA principle⁵) (Hlinomazová and Hrazdira 2005) without compromising the diagnostic value of the examination.

The mechanical index (MI) is an indicator of the potential effect by cavitation, being defined as (Haar 2011), p_r/\sqrt{f} , where f is the pulse centre frequency and p_r is the maximum value of peak negative pressure (anywhere in the ultrasound field).

The thermal index (TI) is defined as the ratio of the total acoustical power (W) to the acoustical power required to raise the tissue temperature by 1 °C (W_{deg}).

Three different TIs are defined: TIS , that assumes that only soft tissues are being analysed by ultrasounds; TIB , that assumes that bone is present at the focus; and TIC , that assumes that bone is very close to the probe. TIs calculation depends on the emission mode and the beam aperture (Output Display Standards – ODS, (American Institute for Ultrasound in Medicine - AIUM and National Electrical Manufacturers Association - NEMA 2010)).

When MI and TI are not available to the user, the worst case should be considered for the particular probe, emission mode and case under analysis, *i.e.*, MI should be set to MI_{max} and TI should be set for the maximal temperature increase ($0.5\Delta T_{max}$) (Palte *et al.* 2012).

The eye is a sensory organ particularly vulnerable to thermal injury since the lens and the aqueous and vitreous humours have no vascular blood supply and therefore no blood flow in the exposed volume that can act as a cooling mechanism (Church and Barnett 2000). The maximum permissible acoustical output exposure levels for ocular applications, denominated as maximum permitted spatial peak temporal average intensity (I_{SPTA}) and maximum permitted spatial peak pulse average intensity (I_{SPPA}), are set to $I_{SPTA} \leq 50 \text{ mW/cm}^2$ and $I_{SPPA} \leq 28 \text{ W/cm}^2$ (Lee and Garra 2004; U.S Department of Health and Human Services *et al.* 2008). For ocular ultrasound medical imaging TI should be lower than 1.0 (Herman and Harris 1999; U.S Department of Health and Human Services *et al.* 2008),

⁵ ALARA is an acronym for As Low As Reasonably Achievable. The ALARA principle is a safety principle for diagnostic methods to minimize interaction of physical energy with biological tissues.

and MI should be lower than 0.23 (American Institute of Ultrasound in Medicine (AIUM) 1993; U.S Department of Health and Human Services *et al.* 2008).

In this work, the transducer was of low acoustic power, in order to ensure safety when used in humans.

3.6 Ultrasound A-scan and B-scan modes

The A-Scan and B-scan ultrasound modes were used in this work.

In the A-scan mode the received signal amplitude is represented along one axis (usually the y-axis) and the travel time of the ultrasonic pulse is represented as a displacement along the other axis (usually the x-axis), as illustrated in Figure 3-3. Most commercial equipments represent the received signal amplitude *versus* propagation distance (depth). In this work, an ultrasound wave propagated through the eye interfaces and the produced echoes were collected and analyzed. The amplitude of the obtained echoes depends on several factors such as: the tissue properties at the interfaces; the incidence angle of acoustical waves; the flatness and smoothness of the interfaces; and the eye layers' density. The eye layers' thickness and the eye axial length were obtained by measuring the propagation time between specific amplitude peaks in the A-scan signals.

The B-scans are brightness images obtained from the received A-scan signals. The brightness is proportional to the echoes amplitude with the echoes of high amplitude appearing as hyperechoic (white), and the absence of signal represented as anechoic (black), (Figure 3-4). The B-scan images of the eye allow visualizing the ocular lesions, including anatomic location, shape, borders, and size. They can also be used for the detection of pathological structures such as retinal or choroidal detachment, foreign bodies, or tumors. Combining A-scan and B-scan modes can contribute for better characterization of the ocular tissues.

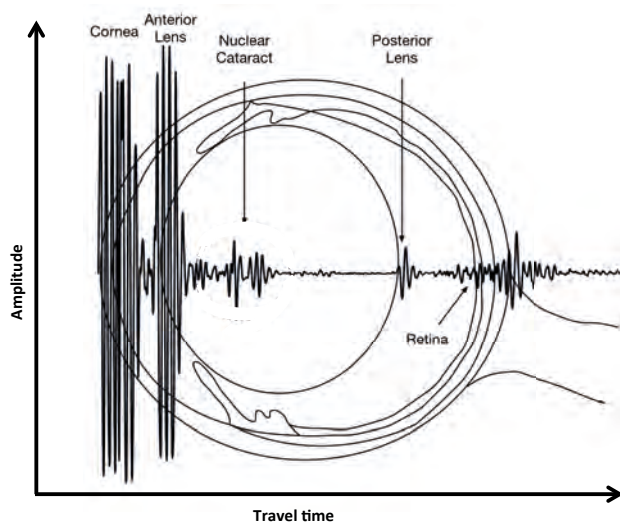


FIGURE 3-3. A-SCAN SIGNAL OBTAINED *IN VIVO* IN A RAT'S EYE.

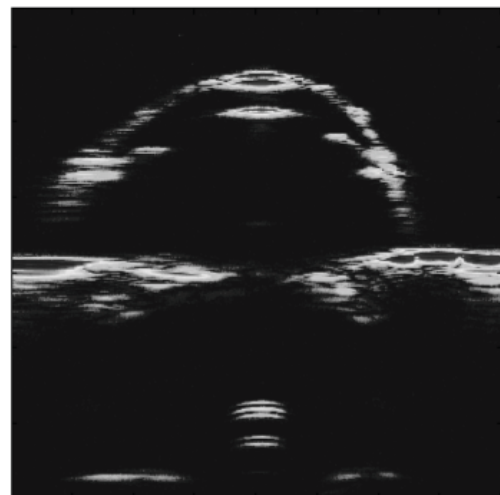


FIGURE 3-4. B-SCAN OBTAINED *EX VIVO* IN A RAT'S EYE.

Due to the different tissue interfaces in the eye and echogenicity of the biological structures, ultrasound image processing encompasses not only the echoes generated by the tissue structures, but also the echoes that are generated by the tissue scatterers and are obtained from the combination of constructive and destructive interference, when the sound waves propagate back to the transducer. Those echoes are called speckle and do not correspond to underlying structure, but reflect the local echogenicity of the underlying scatterers (too small to be individually resolved in the ultrasound image). In most of the cases, those echoes are considered noise, downgrading the ultrasound image quality. However, they can provide valuable information about the tissue characteristics since the statistics of those signals depends on the scatterers' density (Christensen 1988; Dantas *et al.* 2005). Speckle is dependent on the bandwidth, frequency of the transducer, and the geometry and size of the tissue structure.

4 CHARACTERIZATION OF THE CRYSTALLINE LENS BY ULTRASOUNDS

4.1 Introduction

The ultrasounds application in ophthalmology is widespread. In eye examinations the most common probes use ultrasound frequencies ranging from 10 to 50 MHz, for biometry and pachymetry, respectively, and generate very short pulses that enable the eye layers' discrimination. These pulses propagate through the ocular tissues with a speed that is directly proportional to the density and elasticity of the tissue. Discontinuities in density and/or compressibility of the structures in the path create a reflected echo, the amplitude of which is proportional to the differences in the values of the density or compressibility. Ultrasound pulses are attenuated, mainly as a result of the absorption and scattering as they propagate through the tissue. The rate of attenuation depends on the density (molecular weight and size), tissue structure, and ultrasound wave frequency.

The crystalline proteins (α , β and γ) constitute the main structure of the human lens, representing approximately 90% of its composition. Their structural function is to assist in maintaining the appropriate refractive index of the lens and its transparency. Their molecular weights are: α -crystallins 600-900 kDa; β -crystallins 50-250 kDa; and γ -crystallins about 20 kDa (Horwitz *et al.* 1999; Michael and Bron 2011; Paunksnis *et al.* 2003). During the cataract formation the lens' proteins aggregation, mainly due to the oxidative damage, result in protein density changes which contribute for lens opacification. The protein aggregation, that is randomly distributed, produces high molecular weight aggregates that promote ultrasound scattering (Boscia *et al.* 2000; Dierks *et al.* 1998). The ultrasound techniques may provide useful information about crystalline lens tissue. Density and hardness of the crystalline lens can be evaluated from measurements of tissue lens acoustic characteristics namely by the evaluation of ultrasound velocity and frequency-dependent attenuation (El-Brawany 2009; Huang *et al.* 2007a; Huang *et al.* 2007b).

4.2 Acoustical properties of crystalline lens

Currently, the ultrasounds are used in clinical practice of ophthalmology for the objective assessment of the biometric parameters of the anterior segment of the eye, including the biometric parameters of the lens with dense nuclear and/or posterior subcapsular cataract (using 10 to 15 MHz), (Findl 2005; Lenhart *et al.* 2010; Moeini and Eslami 2008), and for B-scan imaging of the anterior segment of the eye with UBM (Aptel *et al.* 2011; Piñero *et al.* 2008) (Table 4-1).

The features extracted from the ultrasound A-scan biometry as the first peak to last peak ratio and time of flight of the ultrasound signal between peaks, were used by El-Brawany (El-Brawany 2009) to evaluate noninvasively the hardness of human cataract. El-Brawany performed biometry on 16 patients undergoing standard extracapsular cataract extraction pre- and post-operatively. Preoperative hardness of the lens was assessed *in vivo* based on 5 A-scans obtained with a commercial ultrasound “A” scanner (Allergan Humphrey Model 8ZU), while post-operative hardness was assessed *in vitro* using an ultrasound scanning acoustic microscope (SAM). Pre- and post-operative results were found to be correlated, indicating that A-scan signals can be used as an indicator of the lens hardness.

Ultrasound methods can also be used for cataractous lens characterization, as demonstrated recently in *ex vivo* studies (He and Liu 2009; Huang *et al.* 2007a; Huang *et al.* 2007b; Zhang *et al.* 2011), by evaluating the acoustical properties of different cataract types (He and Liu 2011; Huang *et al.* 2007a; Huang *et al.* 2007b).

Table 4-1 presents some studies conducted in humans and in animals with ultrasounds, for the visualization and/or characterization of the ocular structures.

TABLE 4-1. TECHNIQUES USED FOR ULTRASOUND VISUALIZATION AND/OR CHARACTERIZATION OF OCULAR STRUCTURES.

Authors	Used frequency	Purpose/Details
HUMANS		
Aptel, 2011 (Aptel <i>et al.</i> 2011)	50 MHz	- UBM was used to visualize and characterize the eye anterior segment structure in 12 patients with refractory glaucoma subjected to insonification using a ring-shaped probe containing 6 miniaturized high-frequency transducers operating at 21 MHz.
El-Einen, 2011 (Abu El Einen <i>et al.</i> 2011)	10 MHz	- Immersion B-guided biometry was compared to contact A-mode biometry in 60 eyes with intraocular lenses for axial length and intraocular lens power measurements. A-scan biometry was compared to B-scan.
Siddiqui, 2011 (Siddiqui <i>et al.</i> 2011)	5 MHz	- To evaluate the impact of ocular tamponade agents when measuring the axial length and refraction with ultrasound biometry, the ultrasound velocity in heavier ocular tamponade agents was measured <i>in vitro</i> .
El-Brawany, 2009 (El-Brawany 2009)	5 MHz	- To assess the feasibility of features extracted from ultrasound A-scan biometry to evaluate the hardness of human cataract noninvasively in 16 lens from patients that performed standard extracapsular cataract extraction.
Zeng, 2009 (Zeng <i>et al.</i> 2009)	10 MHz	- To compare lens thickness measured with anterior segment optical coherence tomography and with A-scan biometry in 66 eyes from phakic patients.
Piñero, 2008 (Piñero <i>et al.</i> 2008)	50 MHz	- To compare anterior chamber depth, central corneal thickness, angle-to-angle distance, and the iridocorneal angle size measured with UBM and optical coherence tomography in 20 eyes without pathology or previous surgery.
Paunksnis, 2007 (Paunksnis <i>et al.</i> 2007)	7 MHz	- To improve early cataract detection and quantitative evaluation of maturity using a commercial A/B-scan ultrasonic system. The backscattered signals from 228 eyes were digitized, recorded and processed.
Tabandeh, 2000 (Tabandeh <i>et al.</i> 2000)	1-20 MHz	- To evaluate the relationship between hardness of the human crystalline lens and its acoustic characteristics (velocity and attenuation) measured with a scanning acoustic microscope using the pulse transmission reflection method in 37 lenses from patients who had extracapsular cataract surgery.
MICE		
Zhang, 2011 (Zhang <i>et al.</i> 2011)	40 MHz	- To evaluate the utility of <i>in vivo</i> imaging of uveal melanoma in mice with high-frequency contrast-enhanced ultrasound in 14 female mice 12-week-old.
Foster, 2003 (Foster <i>et al.</i> 2003)	40 MHz	- To study normal embryonic development in 65 mouse' eyes with UBM.
CANINE		
He, 2010 (He and Liu 2011)	11 MHz	- To examine the correlation between corneal acoustic impedance and Young's modulus in 20 canine' eyes.
PORCINE		
Huang, 2009 (Huang <i>et al.</i> 2009a)	47 MHz	- To explore the use of an ultrasound needle transducer for invasive measurements of ultrasound attenuation coefficient to evaluate the hardness of the cataract lens in 30 porcine lenses.
He, 2009 (He and Liu 2009)	11 MHz	- To describe a quantitative ultrasonic spectroscopy technique for the noninvasive characterization of corneal biomechanical properties in 20 porcine corneas.
Huang, 2007 (Huang <i>et al.</i> 2007a)	35 MHz	- To measure ultrasound velocity and frequency-dependent attenuation in 50 porcine cataractous lenses.
Tsui, 2007 (Tsui <i>et al.</i> 2007)	35 MHz	- To explore the feasibility of using an ultrasonic parametric image based on the Nakagami distribution to quantify the lens hardness in 5 porcine cataractous lenses with an ultrasound needle transducer.
Tsui, 2011 (Tsui <i>et al.</i> 2011)	45 MHz	- To apply an ultrasonic needle transducer to estimate the Nakagami parameter as an alternative for characterizing the cataract lens in 28 porcine cataractous lenses.
Huang, 2007 (Huang <i>et al.</i> 2007b)	46 MHz	- To measure ultrasound velocity and frequency-dependent attenuation coefficient with an ultrasound needle transducer in 30 porcine cataractous lenses.

The characterization of the cataractous lens by ultrasounds can therefore be achieved noninvasively, since most acoustic properties associated with changes in the lens tissue can be measured without loss of the original physiological information (Moeini and Eslami 2008).

It has been established that the ultrasound parameters, namely the ultrasound velocity and frequency-dependent attenuation can be used to estimate the hardness of the cataract (Huang *et al.* 2007a; Huang *et al.* 2007b), since the acoustical waves are influenced by microstructural changes. In cataractous lenses, there is an increase of protein aggregation and fibers compaction, which contributes to the increase in hardness. These changes in the lens tissue structure lead to alterations in the lens acoustical properties.

The normal crystalline structure presents a signature characterized by clear A-scan signals with well-defined interfaces and without backscattering. On the other hand, the cataractous lens is characterized by the presence of a large number of protein aggregates, which act as micro-scatterers of the ultrasound waves. As a consequence, the lens A-scan signals show a noisy aspect. The cataractous lens structure has a stochastic behaviour in terms of the interpretation of the reflected signal. The analysis of the resultant signals (backscattering) associated with the acoustical parameters calculation can provide important information for the characterization of the different cataract types. Figure 4-1 shows the anterior and posterior lens boundaries echo signals obtained *in vivo* in a rat's eye, whose amplitudes are directly related to the reflection coefficients between the aqueous humour and the anterior lens capsule, and between the posterior lens capsule and the vitreous, respectively.

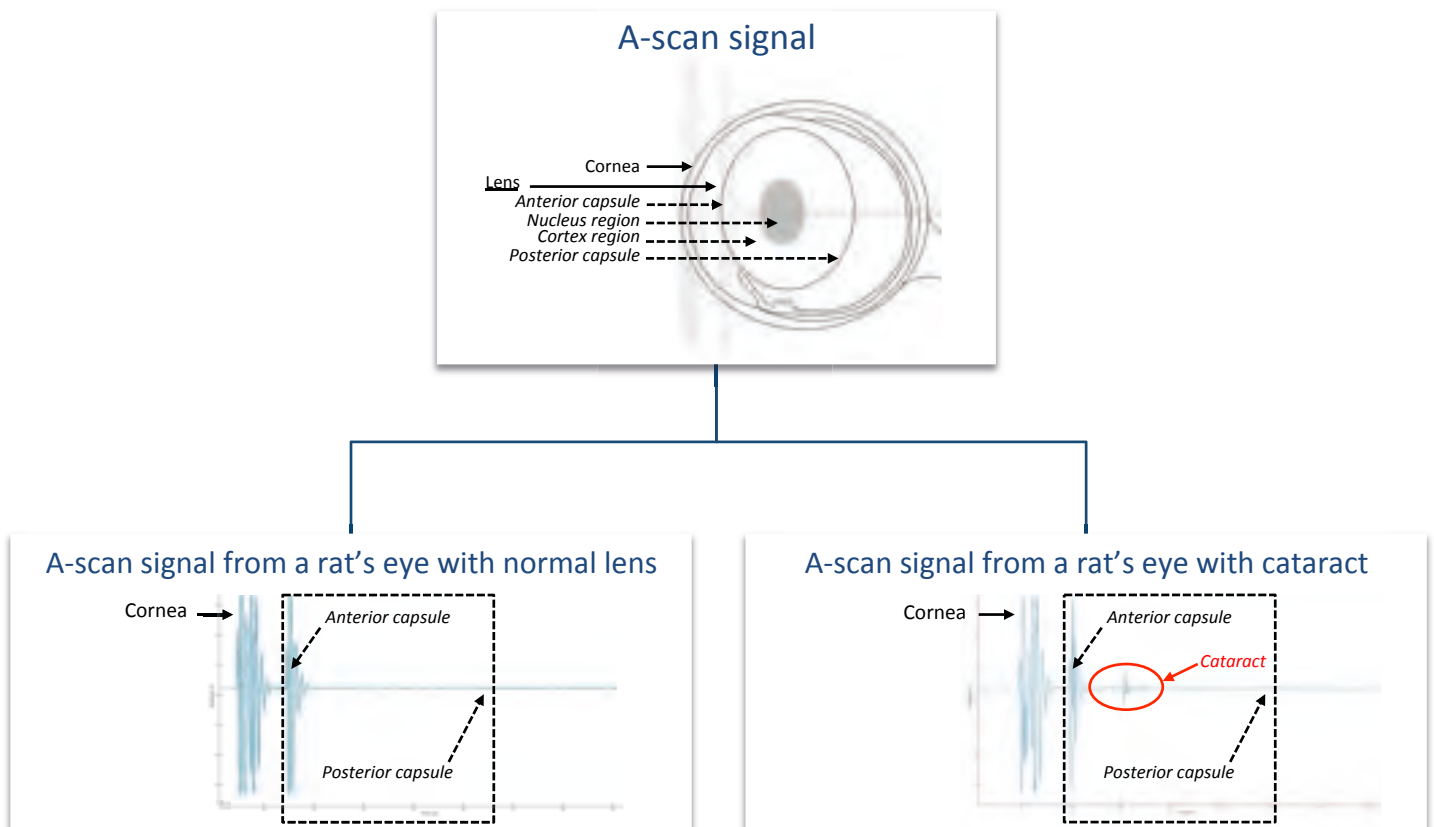


FIGURE 4-1. ECHOES OBTAINED *IN VIVO* IN A RAT'S EYE.

4.2.1 Ultrasound velocity

The ultrasound propagation velocity has been widely used for the characterization of healthy and cataractous lenses since its behaviour depends on the tissue properties, namely on the density. Thus, the ultrasound velocity presents higher values for solid media than for liquid media (O'Brien 2007).

The ultrasound velocity can be computed based on:

1. the propagation time through the lens;
2. the amplitude spectrum of the anterior and posterior lens boundary signals.

By measuring the wave propagation time (Δt), between the anterior and posterior lens capsule echoes, the ultrasound velocity (V) is given by,

$$V = 2d/\Delta t \quad (4-1)$$

where d is the lens thickness.

Alternatively, using the amplitude spectrum method, the ultrasound velocity (V) can be calculated by,

$$V = 2d \Delta f \quad (4-2)$$

where Δf is the frequency variation between two successive maxima (minima) of the signal spectrum.

In both approaches the lens thickness, d can be measured by a calliper. Since the lens is a soft tissue some inaccuracy may occur in the measurements, affecting therefore the velocity estimation. An alternative expression for velocity calculation that does not require the lens thickness knowledge, is (Sugata *et al.* 1992),

$$V = c \left(\frac{t_s - t_c}{t_b - t_a} + 1 \right) \quad (4-3)$$

where c is the ultrasound velocity in the solution where the lens is immersed, t_c and t_s are the propagation times for the path between the transducer and a reflector with and without the lens inserted, respectively, and t_a and t_b are the propagation times for the pulses travelling from the transducer to the anterior and posterior surfaces of the lens, respectively (Figure 4.2). Although independent of the lens thickness, this approach is not feasible in *in vivo* experiments.

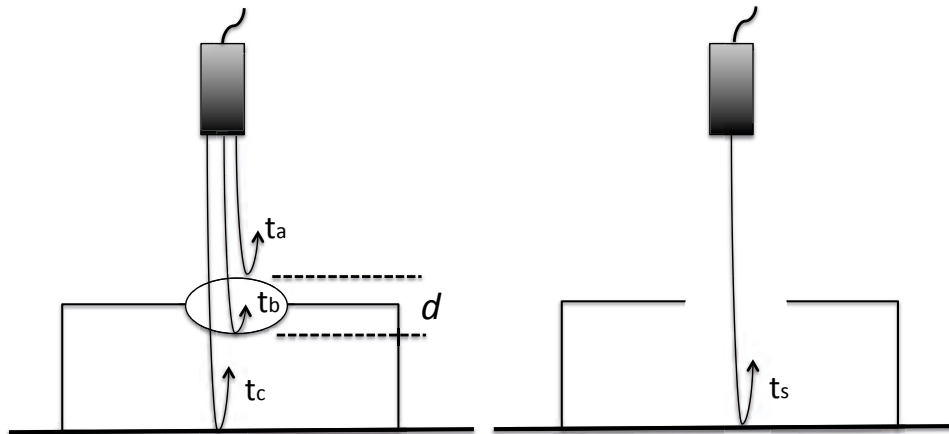


FIGURE 4.2. SETUP FOR THE ULTRASOUND VELOCITY CALCULATION BASED ON EQUATION (4-3).

4.2.2 Frequency-dependent attenuation

As already referred, an ultrasound wave suffers frequency-dependent attenuation when propagating along the lens tissue (Mamou and Oelze 2013; Narayana and Ophir 1983; Oelze and O'Brien 2002). In most tissues, the frequency-dependent attenuation coefficient is given by the expression,

$$\alpha(f) = \beta f^n \tag{4-4}$$

where α is the attenuation coefficient, f is the frequency, and β and n are the parameters that characterize the attenuation of the medium. It is assumed for biological tissues that the dependence of the attenuation with frequency is linear. However, according to the published experimental results (Nakajima *et al.* 1999; Narayana and Ophir 1983; Parker *et al.* 1988; Ray and Behari 1987) the factor n can vary between 0.7 to 2 in biological tissues. Some of the n values for human ocular tissues are presented in Table 4-2.

TABLE 4-2. n -PARAMETER FOR HUMAN OCULAR TISSUES (de Korte *et al.* 1994).

Tissue	n
Cornea	1.56
Lens	1.87
Retina	0.86
Choroid	2.13
Sclera	1.49

The frequency-dependent attenuation $\alpha(f)$ can be evaluated by two different methodologies:

1. Energy loss analysis in the path between the anterior and posterior lens capsule, using only the respective reflection signals.
2. Energy loss analysis in the path between the anterior and posterior lens capsule making use of a planar reflector.

The approach using only the anterior and posterior capsule echoes is shown in Figure 4.3. The frequency-dependent attenuation is expressed as (Huang *et al.* 2007b),

$$\alpha(f) = \frac{20}{2d} \log_{10} \left(\frac{A_1(f) R_2}{A_2(f) R_1} T_{12} T_{21} \right) \quad (4-5)$$

where $A_1(f)$ and $A_2(f)$ are respectively the amplitude spectra of the anterior and posterior lens capsule echoes, R_1 and R_2 are the reflection coefficients in the lens boundaries, and T_{12} and T_{21} are the transmission coefficients,

$$T_{12} T_{21} = \frac{4Z_2 Z_1}{(Z_2 + Z_1)^2} \quad (4-6)$$

where Z_1 and Z_2 are the acoustical impedances of the solution and the lens, respectively, (Figure 4.3).

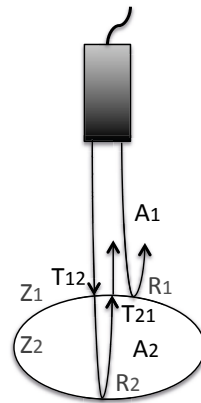


FIGURE 4.3. SETUP FOR THE FREQUENCY-DEPENDENT ATTENUATION CALCULATION BASED ON THE ANTERIOR AND POSTERIOR LENS CAPSULE ECHOES.

The frequency-dependent attenuation calculation using a planar reflector makes use of the configuration illustrated in Figure 4.4, resulting the following expression,

$$\alpha(f) = \frac{20}{2d} \log_{10} \left(\frac{A_1(f)}{A_2(f)} (T_{12} T_{21})^2 \right) - \alpha_s \quad (4-7)$$

where $A_1(f)$ and $A_2(f)$ are the amplitude spectra of the echoes from the reflector without and with the lens inserted in the solution, respectively, and α_s is the attenuation in the solution path corresponding to the lens thickness.

The transmission and reflection coefficients as well as the α_s factor are attenuation correction parameters that are generally neglected (Huang *et al.* 2007a).

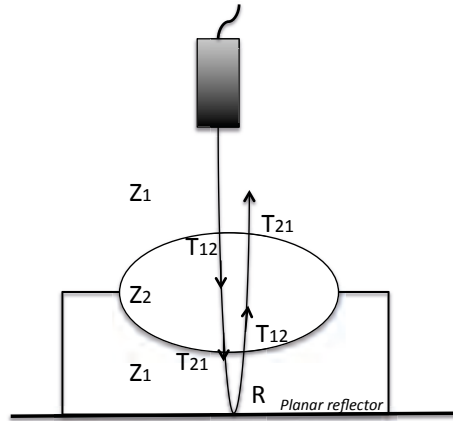


FIGURE 4.4. SETUP FOR THE FREQUENCY-DEPENDENT ATTENUATION CALCULATION MAKING USE OF A PLANAR REFLECTOR.

The attenuation by dispersion was calculated by analysing the frequency downshift from the backscattering signals along the lens depth. As the higher frequency components suffer greater attenuation than the lower ones, the centre frequency of the backscattering signals tends to evolve towards the low frequencies along the lens depth. Since it is assumed that the attenuation increases linearly with frequency, the slope of the centre frequency downshift *versus* depth is proportional to the attenuation coefficient. Therefore, assuming that the pulse along the lens has a Gaussian shape, when analysing the frequency downshift from the backscattering signals the attenuation parameter (β) is given by (Huang *et al.* 2009a),

$$\beta = \frac{\Delta f(z)}{\Delta z 4 \sigma^2} \quad (4-8)$$

where $\Delta f(z)$ is the centre frequency at a particular depth z in the lens and therefore, $\Delta f(z)/\Delta z$ represents the slope of the linear fitting applied to the centre frequencies plot of the backscattered echoes *versus* depth z , and σ is the Gaussian bandwidth of the pulse.

4.2.3 Evaluation of the acoustical parameters in the crystalline lens

The first works to evaluate the acoustical parameters in the eye were done in the 1950's by Oksala *et al.* (Oksala and Lehtinen 1958). They found that the ultrasound waves propagate with an average speed of 1640.5 m/s in the normal lens and 1532.0 m/s in the aqueous and vitreous humours. They also concluded that the ultrasound propagation was

not influenced significantly by the cornea and sclera structures, but was significantly influenced when propagating in the crystalline lens. Later Oguchi *et al.* also studied how the ultrasound propagation was influenced by the crystalline lens, demonstrating, for the first time, that the waves suffered absorption, scattering and dispersion effects (Oguchi *et al.* 1975).

To assess *ex vivo* the hardness of cataractous lenses, Huang *et al.* used an ultrasonic transducer with a centre frequency of 35 MHz to measure the propagation velocity and the frequency-dependent attenuation (in a range of 25-45 MHz) on 50 porcine lenses without and with cataract, induced by immersion over 3 hours in an ethanol:2-propanol:formalin solution, (Huang *et al.* 2007a). In this study phacoemulsification was performed in the cataractous lenses with different energy levels to evaluate the feasibility of using the ultrasound parameters to assess the lenses hardness. The authors found an attenuation coefficient of 4.49 ± 0.05 dB/mm at 30 MHz and 6.32 ± 0.04 dB/mm at 40 MHz, for the normal porcine lenses. For the cataractous lenses, the attenuation coefficient and the ultrasound velocity were found to increase with the cataract progression. The attenuation coefficient increased from 7.36 ± 0.25 dB/mm to 11.1 ± 0.92 dB/mm at 30 and 40 MHz respectively, and for an immersion time of 180 minutes (corresponding to an increase from 2.6 to 101.2 kPa in the Young's modulus⁶), while the ultrasound velocity increased from 1639.8 ± 4.2 in normal lenses to 1735.6 ± 10.4 m/s after 180 minutes of immersion time. The authors calculated the Young's modulus by compressing the lens, measuring their deformation in the horizontal plane. The attenuation coefficient and the ultrasound velocity were found to be linearly correlated with the phacoemulsification energy level ($r = 0.941$ and $r = 0.915$, respectively), showing that the ultrasound parameters can be useful to select the optimal phacoemulsification energy level.

Additionally, based on their previous results, Huang *et al.* (Huang *et al.* 2007b) developed a 46 MHz ultrasonic needle transducer to assess the anterior-to-posterior profiles of the ultrasound parameters, invasively (Huang *et al.* 2007b). The 46 MHz needle transducer, composed by a lead magnesium niobate-lead titanate (PMN-PT) single crystal with 0.4 mm of aperture and 0.9 mm in diameter was inserted into the lens to acquire signals at specific depths and to evaluate the respective velocity and frequency-dependent attenuation parameters. The study was carried out in 30 porcine lenses without and with induced nuclear and cortical cataract. The authors found that the velocity and attenuation coefficient were not spatially constant within the lenses and that they correlated with the different types of cataract. For cortical cataract the velocity and the attenuation coefficient increased 3.1% and 41.0%, respectively at the centre of the lens.

Some values published for the ultrasound velocity and attenuation in lenses without and with cataract are presented in Table 4-3.

⁶ Young's modulus or modulus of elasticity is a mechanical property of a material that defines the relationship between stress (force per unit area) and strain (proportional deformation).

TABLE 4-3. VALUES PUBLISHED FOR THE ULTRASOUND VELOCITY AND ATTENUATION IN LENSES WITHOUT AND WITH CATARACT.

Authors	Lenses number	Transducer centre frequency	Lenses without Cataract	Lenses with Cataract	Used method
<i>Velocity (m/s)</i>					
<i>Porcine lenses</i>					
Huang, 2007 (Huang <i>et al.</i> 2007a)	50	35 MHz	1639.8 ± 4.2	1735.6 ± 10.4	Without lens thickness
Huang, 2007 (Huang <i>et al.</i> 2007b)	30	46 MHz	1704.4 ± 4.2	1759.2 ± 5.6	Time of flight ⁷
<i>Attenuation coefficient and Frequency-dependent attenuation</i>					
<i>Porcine lenses</i>					
Huang, 2007 (Huang <i>et al.</i> 2007a)	50	35 MHz	4.49 ± 0.05 dB/mm 6.32 ± 0.04 dB/mm	7.36 ± 0.25 dB/mm 11.10 ± 0.92 dB/mm	Using a planar reflector values at 30 MHz and at 40 MHz
Huang, 2007 (Huang <i>et al.</i> 2007b)	30	46 MHz	10.00 ± 0.35 dB/mm	14.10 ± 0.68 dB/mm	Using a planar reflector
Huang, 2009 (Huang <i>et al.</i> 2009b)	30	47 MHz	0.048 ± 0.02 dB/mm MHz	0.52 ± 0.06 dB/mm MHz	Based on the backscattering signals
<i>Human lenses</i>					
Sugata, 1992 (Sugata <i>et al.</i> 1992)	7	10 MHz	0.07 to 0.92 dB/cm MHz	1.6 to 7.3 dB/cm MHz	Using the anterior and posterior capsule echoes
El Brawany, 2009 (El-Brawany 2009)	13	5 MHz	---	3.4 to 6.6 dB/cm	Using the anterior and posterior capsule echoes at 5 MHz

The results presented in Table 4-3 show that the cataract hardness produces higher increase in the attenuation than in the velocity.

Similar results were found by Tabandeh *et al.*, who assessed the human crystalline lens ultrasound properties and hardness in 37 cataractous lens from 37 patients planned for extracapsular cataract surgery, (Tabandeh, 2000). The cataractous lenses were analysed *in vitro* by scanning acoustic microscope using the pulse-echo mode, in order to calculate the ultrasound velocity and attenuation. The hardness was measured based on the force required to bisect the lens using an automated guillotine. The authors found a statistically significant correlation between the lens hardness and the attenuation of the ultrasound waves ($r = 0.65$, $p < 0.001$). However no significant correlation was found for the ultrasound velocity, $r = 0.22$, $p < 0.200$.

⁷Values obtained in the nucleus of the lens with a needle transducer.

A quantitative method for cataract classification based on ultrasonography was presented by Paunksnis *et al.*, (Paunksnis *et al.* 2007). The authors proposed a new parameter for cataractous lens classification, analysing the echo-signal energy characteristics. This parameter named lens quality, Q_L , is a function of the ultrasound wave spectral average slope in dB/MHz and the echo-signal energy from the lens nucleus, and reflects the ultrasound interaction with the lens tissue (attenuation) and the scattering phenomena. Using an ultrasonic echoscope (Mentor A/B) with a 7 MHz probe, they obtained signals from 228 eyes with different lens conditions, which were captured, digitized, recorded and processed to compute Q_L . Five lens' categories were considered: phantom signals; normal (healthy eyes); incipient cataract; immature cataract and mature cataract. The Q_L values were found to be different for the 5 lens' categories, discriminating lenses into healthy lenses ($Q_L > 50$), incipient or immature cataract ($Q_L = 2 - 20$) and mature cataract ($Q_L < 1$).

4.3 Cataract imaging

In cataractous lenses, regions of higher opacity give rise to strong echoes due to the large impedance gradient verified in the interface between the normal tissue and cataract. Then, it is expected that A-scan signals from a lens with cataract differ from the ones obtained in lenses without cataract (Tsui *et al.* 2007; Tsui *et al.* 2011; Tsui and Chang 2007). A brightness image of the lens (B-scan) can be constructed by using the A-scan signals amplitude. This image corresponds to a two-dimensional plane, which is parallel to the ultrasound waves propagation direction, allowing for a qualitative characterization of the lens structure.

However, this conventional brightness image cannot be used as a quantitative indicator of lens hardness, since the signals amplitude is dependent on the system settings (such as the gain or the dynamic range), the acquisition mode (angle of incidence of the ultrasound), and the user experience (Tsui and Chang 2007; Tsui *et al.* 2008).

4.3.1 B-scan imaging

Although A-scan signals contain a large amount of information they are difficult to interpret and therefore, the ultrasound data are usually presented as brightness-modulated images (B-scan). The construction of these images encompasses the envelope detection of the A-scan signals using the Hilbert transform (Lizzi *et al.* 2003; Noble and Wells 2010), followed by a logarithmic compression. Then, the amplitudes are converted to a scale of 256 grey levels for posterior image construction by mapping of all grey levels in the correct position of the two-dimensional plane of the tissue.

Figure 4-5 shows two B-scan images obtained using the procedure described above, being visible an increase of the brightness with the cataract progression.

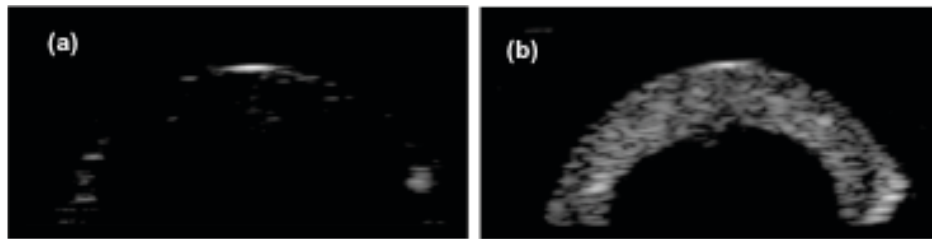


FIGURE 4-5. B-SCAN IMAGES: (a) FOR A LENS WITHOUT CATARACT; (b) AND FOR A LENS WITH INDUCED CATARACT (Caixinha *et al.* 2014a).

For *in vivo* eye imaging with a free-hand scanning probe, the B-scan image construction presents some limitations. Contrarily to mechanical built-in probes, as the one used for *ex vivo* studies, free-hand imaging can address a large variety of clinical applications. However the construction of the B-scan images is challenging. The sparsity of data is the main difficulty to transform a non-uniform distributed set of A-scans into a consistent B-scan image.

A tracking system is needed to continuously record the A-scans position and orientation for the correct construction of the B-scan images, without geometrical artefacts or image distortions. This tracking system will allow to correctly co-register the acquired A-scans regarding to eye movements and shape (correcting possible probe misalignments).

4.3.2 Nakagami parametric imaging

The lens scatterers density can be characterized using techniques that use the distribution of ultrasound backscattered signal envelope, which depends on the properties of tissue microstructure. These techniques make use of backscattering signals according to a statistical approach for tissue characterization (Bouhleb *et al.* 2006; Shankar 2000).

Statistical models are generally used to describe the backscattering signal envelope. These models are based on statistical distributions that depend on the size and density of the scattering particles present in the tissue (scatterers), and the scattering amplitude and reflection originated in these particles by the incident ultrasound wave.

Wagner *et al.* proposed three statistical distributions for the tissue backscattered signal envelope based on the properties of the backscattering signals, in particular on the signal to noise ratio (SNR) (Wagner *et al.* 1983):

- the pre-Rayleigh distribution, when the resolution cell of the transducer⁸ contains scatterers randomly distributed and with varying scattering cross-sections (Figure 4-6);
- the Rayleigh distribution, when the resolution cell of the transducer contains a large number of randomly distributed scatterers (Figure 4-6); and
- the post-Rayleigh distribution, when the resolution cell of the transducer contains scatterers randomly distributed and periodically located⁹ (Figure 4-6).

⁸ The transducer resolution cell is defined as the volume given by the axial and lateral resolutions.

These models have the advantage of having a simple mathematical treatment, but do not discriminate accurately the different regions of the tissues, which often preclude the differentiation of healthy from pathologic tissue (Shankar 2000). Therefore, to describe backscattering signals the K statistical distribution¹⁰ was thereafter proposed by Shankar (Shankar 2000). The two parameters of the K distribution (the effective number of scatterers and the micro-scale parameter), allow obtaining information about the number and density of micro-scatterers; the amplitude variation of scattering within a selected interval (window), as well as the mean scattering amplitude in these intervals (Bouhleb *et al.* 2006; Shankar 2000). When analysing media with a high-density of scatterers, the K and the Rayleigh distributions have a similar behaviour.

Although in some cases the K distribution allows a better tissue characterization, it is computationally complex, especially when dealing with a large number of scatterers (Shankar 2000). Therefore, to characterize backscattering signal, Shankar proposed a simpler model, which is based on the Nakagami distribution (Shankar 2000). The Nakagami distribution allows the characterization of the scattering amplitude and density of scatterers in the tissue. The detailed description of the Nakagami distribution¹¹ can be found in (Shankar 2000). The probability density function of the backscattered signal envelope (r), given by the Nakagami distribution (Figure 4-7) is expressed by, (Shankar 2000),

$$f(r; m, \Omega) = \frac{2}{\Gamma(m)} \left(\frac{m}{\Omega}\right)^m r^{2m-1} e^{-\frac{m}{\Omega}r^2} U(r) \quad (4-9)$$

where $\Gamma(\cdot)$ is the Gamma function, $U(\cdot)$ is the unit step function, and m and Ω are the Nakagami distribution's parameters. The m parameter is the shape parameter and Ω is the scale parameter of the distribution. They are expressed as,

$$m = \frac{[E\{r^2\}]^2}{E\{[r^2 - E\{r^2\}]^2\}} \quad (4-10)$$

$$\Omega = E\{r^2\} \quad (4-11)$$

where $E\{\cdot\}$ denotes the expected value. The m parameter is the ratio between the square of the mean and the variance of r^2 .

Figure 4-6 illustrates the physical meaning of the m parameter value in the characterization of tissue scatterers.

⁹The Rayleigh distribution is the distribution of the magnitude of a vector which Cartesian components are normally distributed with zero mean and equal variance.

¹⁰The K distribution arises by compounding two gamma distributions.

¹¹ The Nakagami distribution is the distribution of the random variable r when r^2 follows the Gamma distribution.

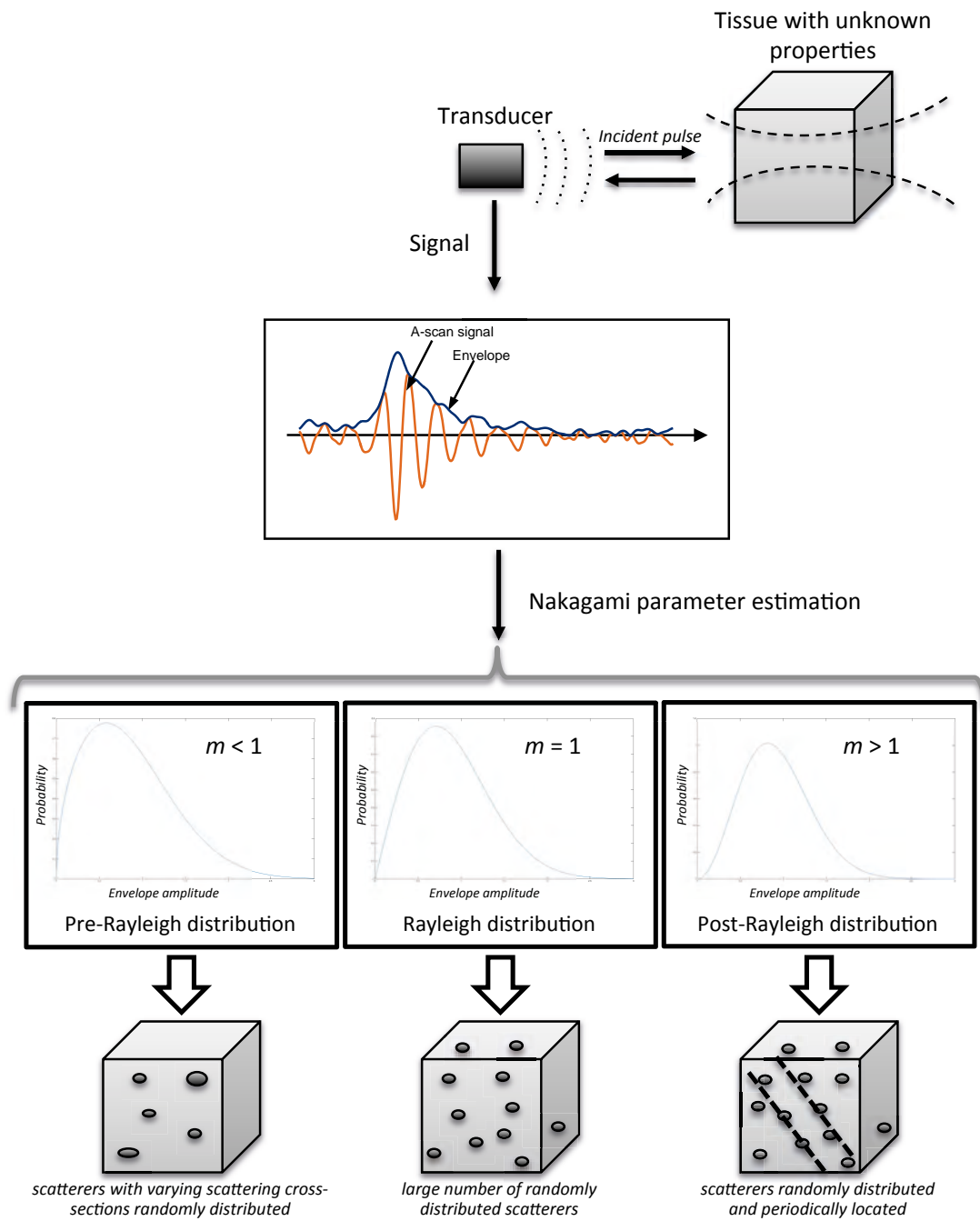


FIGURE 4-6. ILLUSTRATION OF THE PRE-RAYLEIGH, RAYLEIGH AND POST-RAYLEIGH DISTRIBUTIONS, AND m PARAMETER VALUES (ADAPTED FROM (Ho *et al.* 2013)).

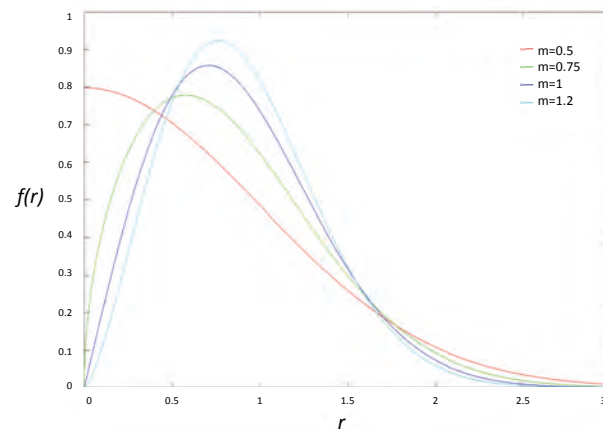


FIGURE 4-7. NAKAGAMI DISTRIBUTION FOR DIFFERENT VALUES OF THE m PARAMETER.

The backscattered envelope statistics change from a pre-Rayleigh to a Rayleigh distribution as the m parameter varies from 0 to 1 (a m parameter >1 means that the backscattered envelope statistics follows a post-Rayleigh distribution, Figure 4-6). The Nakagami m parameter allows therefore for tissue characterization by estimating scatterers' distribution. For this reason, the images composed by the local m parameters, the Nakagami images, represent an attractive statistical model-based parametric imaging technique for the visualization of the changes in the backscattering envelope statistics, improving tissue characterization. This technique has been used in different clinical areas, such as nephrology (Ho *et al.* 2012; Ho *et al.* 2013; Tsui *et al.* 2009; Tsui *et al.* 2014), oncology (Liao *et al.* 2012; Shankar *et al.* 2001; Shankar *et al.* 2003; Tsui *et al.* 2010b; Yang *et al.* 2015), dermatology (Lin *et al.* 2011), cardiology (Yu and Lee 2014), and ophthalmology (Tsui *et al.* 2007; Tsui *et al.* 2011). As the statistics of the backscattered echoes vary with the scatter concentration, the Nakagami image can be used to identify the scatter concentrations in the crystalline lens (Shankar 2000; Tsui *et al.* 2007). Although Nakagami images can be seen as a reliable tool to complement B-scan images, problems have to be solved to make it effective, namely the artefacts generated by the noise in the anechoic areas of the lenses. In order to reduce noise, appropriate local estimation of the m parameter is required.

As said, the Nakagami parametric image is constructed based on the B-mode image, and corresponds to a two-dimensional representation of the m parameter values. The image construction process encompasses a sliding window, whose width is selected to provide good resolution. Small windows improve the resolution, but result in fewer envelope points, which can lead to bad estimations of the m parameter. Large windows improve the m parameter estimation and the image smoothness, but compromise the image resolution (Tsui *et al.* 2006). The size of the window is therefore a trade-off between the image resolution and the m parameter estimation.

The sliding window is moved over the envelope of the backscattering signals to estimate the local Nakagami m parameters for imaging (Davignon *et al.* 2005; Tsui and Chang 2007; Tsui *et al.* 2014). To construct a Nakagami image and to simultaneously estimate accurately the m parameter, ensuring a reliable tissue characterization, a

window larger than at least one spatial resolution of the B-scan image is usually used (Tsui and Chang 2007; Wang *et al.* 2013; Yang *et al.* 2014).

The algorithm used to construct the Nakagami m parametric images encompasses the following steps:

1. The A-scan lines collected from longitudinal positions (x) are demodulated to obtain the envelope of all signals in a matrix \mathbf{R} with N_y rows and N_x columns. Each column has N_y points of the corresponding A-scan envelope and each row encompasses N_x different A-scans.
2. A $l \times k$ size window is used around each point (i, j) of the matrix \mathbf{R} in order to estimate the m parameter of the Nakagami distribution for that pixel. This estimate is the maximum likelihood estimate of the parameter m (Kolar *et al.* 2004).
3. The Nakagami m parametric image \mathbf{M} is built with all the estimates.

Figure 4-8 show two Nakagami images obtained according to the procedure described above, representing the areas of scatterers concentrations.

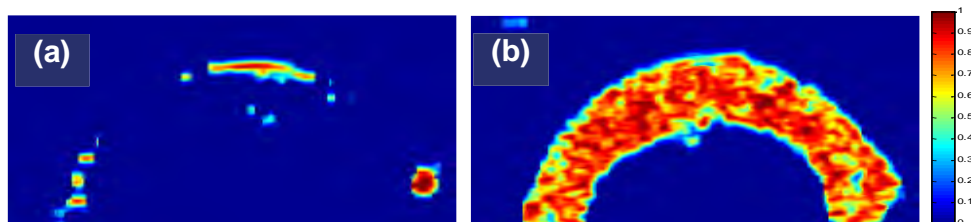


FIGURE 4-8. NAKAGAMI IMAGES REPRESENTING THE SCATTERERS DISTRIBUTION FOR A LENS WITHOUT CATARACT (a) AND FOR A LENS WITH INDUCED CATARACT (b) (Caixinha *et al.* 2014a).

The Nakagami distribution has been widely used for regional characterization of the crystalline lens hardness (Tsui *et al.* 2006; Tsui *et al.* 2007; Tsui *et al.* 2009; Tsui *et al.* 2008). This methodology provides good correlation with the hardness of the lens in its different regions and appears itself as a complementary image of the B-scan acquisition mode (Tsui *et al.* 2007). However, like the previous Rayleigh and K distributions, Nakagami distribution does not allow properly to describe the tissue anisotropy (Bouhleb *et al.* 2006). So new approaches are being developed that still need validation (Tsui *et al.* 2009; Zhou *et al.* 2014).

5 EX VIVO CATARACT CHARACTERIZATION: EXPLORATORY STUDY

5.1 Objective

To test the feasibility of using the ultrasound technique for the objective characterization of the cataractous lens, an exploratory study was conducted *ex vivo* in porcine lenses with different induced cataract degrees. The results were presented in (Caixinha 2012), and published afterwards in two proceedings (Jesus *et al.* 2012; Jesus *et al.* 2013). This work is described in the next sections.

5.2 Materials and methods

5.2.1 Lenses preparation and cataract induction

Twenty-five (25) porcine eyes collected in a slaughterhouse were used. The lenses were enucleated with a surgical scalpel, and carefully prepared in order to remove iris remains and adhering vitreous, preserving the lens capsule (Figure 5-1). The lenses average anteroposterior diameter, measured with a calliper, was 8.3 ± 0.4 mm.

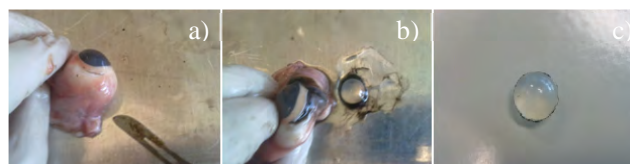


FIGURE 5-1. LENS EXTRACTION PROCEDURE ((a) ENUCLEATED PORCINE EYE; (b) LENS ENUCLEATION; AND (C) LENS CLEANED FROM IRIS REMAINS AND ADHERING VITREOUS) (Caixinha 2012).

The lenses were examined with an adapted slit lamp to reject lenses with any type of opacity. Twenty lenses without opacities were kept in DMEM solution before being used (the DMEM solution allows to preserve the crystalline lens for 72 hours without loss of its physiological properties) (Manikandan and Thiagarajan 2009).

Cataract was induced by lenses immersion in an ethanol:2-propanol:formalin solution at a ratio of 3:3:4, to increase the cataract hardness (Sugiura *et al.* 1999). This cataract induction process has the advantage of rapidly inducing opacity in the lenses. The cataract formation process and the data acquisition were performed simultaneously, *i.e.*, while cataract was induced by increasing the immersion time in the solution, the corresponding acoustical signals were continuously acquired at 20 minutes intervals, from 0 to 180 minutes (Figure 5-2).

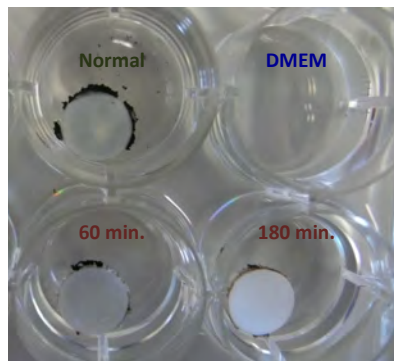


FIGURE 5-2. PORCINE LENSES: NORMAL LENS AND LENSES WITH INDUCED CATARACT OBTAINED AFTER 60 AND 180 MINUTES OF IMMERSION IN THE ETHANOL:2-PROPANOL:FORMALIN SOLUTION.

5.2.2 Experimental setup for lenses signal acquisition

The setup shown in Figure 5-3 was used to obtain the lens acoustical parameters, as propagation velocity and frequency-dependent attenuation, and to analyse the backscattering lens signals.

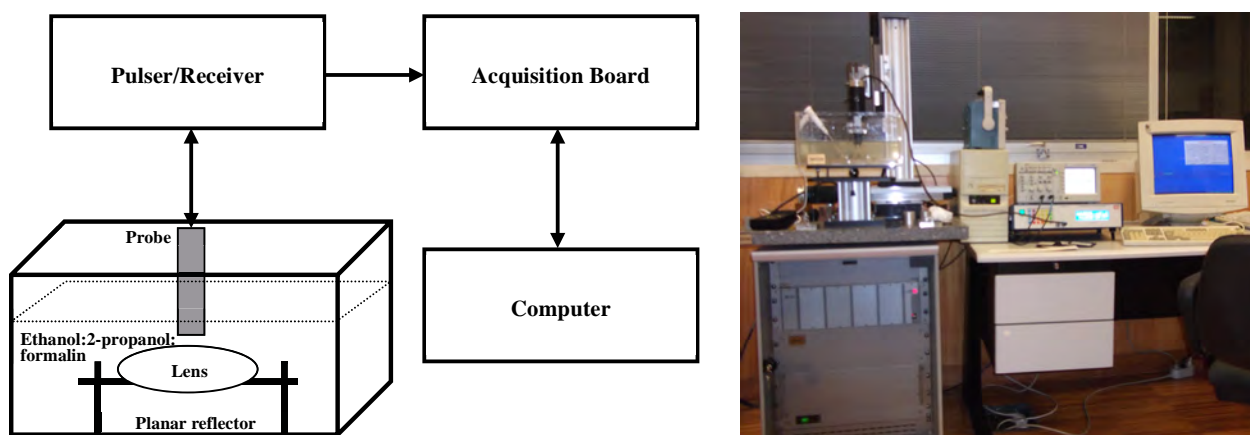


FIGURE 5-3. EXPERIMENTAL SETUP (SCHEMATIC – LEFT; AND PHOTOGRAPH – RIGHT).

A 25 MHz transducer (model IAP-F25.3.1, Krautkramer, NSW, Australia) with a 25 mm focus, 5 mm active diameter and a pulse length of 0.13 μ s at -6 dB, was used (the transducer characteristics are shown in Table 6-1). The lenses were placed on a stainless steel holder having a machined hole matched to the lens. During data collection, the

solution temperature was kept constant at $28.0 \pm 0.5^\circ\text{C}$. A 35 MHz bandwidth pulser/receiver (model PR5800, Olympus NDT Inc., Waltham, MA, Unites States of America – USA) was used in a pulse-echo configuration. The echo signals were recorded and digitized by using a 14 bits, 200 MHz ADLINK DAQ PCIe board (model PCIe-9842, ADLINK Technology Inc., Taipe, Taiwan). The transducer was moved using a computer-controlled micro-positioning system.

5.2.3 Statistical analysis

To compare the ultrasound parameters obtained from lens without and with induced cataract (*i.e.* with different lens hardness), the non-parametric Kruskal-Wallis and Wilcoxon tests were used (Spurrier 2003; Tournoy *et al.* 2010). Also, to evaluate the agreement between the different approaches used to estimate the ultrasound velocity and frequency-dependent attenuation, the Intraclass Correlation Coefficient (ICC) was calculated. When required, the limits of agreement were computed using the Bland and Altman method (Bland and Altman 1986). The commercial software SPSS, version 17.0 (SPSS Inc., Chicago, IL, USA) was used. Statistical values were considered significant for $p \leq 0.05$.

5.3 Results

5.3.1 Ultrasound velocity

A good agreement was found between the three approaches used for the propagation velocity assessment (equations (4-1), (4-2) and (4-3)), (ICC > 0.700; $p < 0.001$). The use of the time-of-flight and the amplitude spectra approaches led to the higher agreement (ICC = 0.946, $p < 0.001$), since they are conceptually identical, changing only the processing domain. For the three methods a statistically significant increase with the lens immersion time (*i.e.*, lens hardness) was found for the velocity ($p < 0.001$; Figure 5-4).

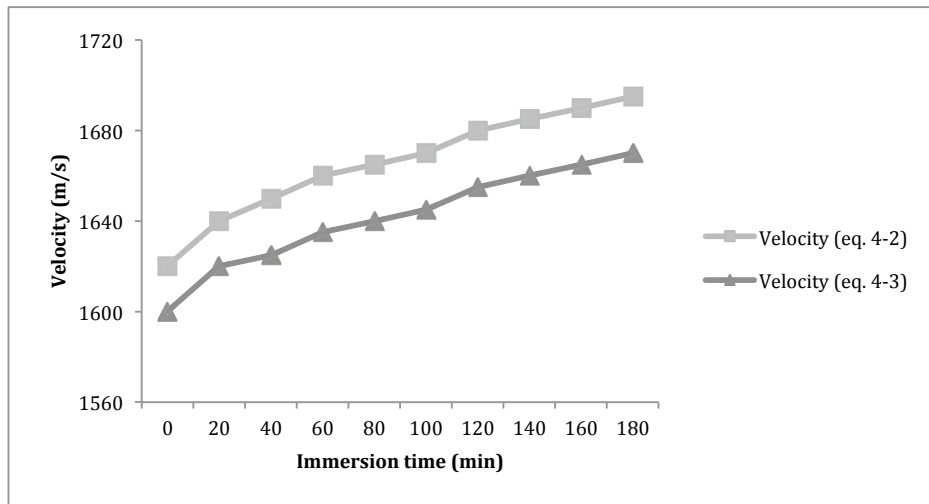


FIGURE 5-4. ULTRASOUND VELOCITY MEAN VALUES *VERSUS* LENS IMMERSION TIME BY USING EQUATION (4-2) AND EQUATION (4-3), (MEAN DIFFERENCE BETWEEN METHODS: 29.2 m/s (CONFIDENCE INTERVAL: 23.3 TO 35.2); LIMITS OF AGREEMENT: -46.8 TO 105.3) (Caixinha 2012; Jesus *et al.* 2012).

The alternative method (equation 4-3), although in agreement with the first two, cannot be used in *in vivo* measurements since it requires a reference signal from a planar reflector.

The velocity results for all studied lenses, with and without cataract, are presented in Table 5-1.

TABLE 5-1. LENS PROPAGATION VELOCITY RESULTS (N=20).

Ultrasound velocity	Without Cataract	With Total Cataract (immersion time = 180 minutes)	<i>p</i>
Time-of-flight method (equation (4-1))	1617 ± 36 m/s	1694 ± 31 m/s	< 0.001
Amplitude spectrum method (equation (4-2))	1619 ± 39 m/s	1692 ± 38 m/s	< 0.001
Alternative method: use of a planar reflector. No lens thickness knowledge (equation (4-3)).	1597 ± 37 m/s	1670 ± 32 m/s	< 0.001

5.3.2 Ultrasound frequency-dependent attenuation

A clear downshift of the centre frequency of the posterior and anterior capsule echoes is observed for the different lens immersion times (Figure 5-5). The centre frequency of the anterior capsule echo remained constant (Figure 5-5 (a)) while the posterior capsule echo centre frequency decreased 28% over the immersion time (Figure 5-5 (b)). As expected, the echoes amplitude of the anterior capsule increases with cataract progression (Figure 5-5 (a)) while the posterior capsule echoes amplitude decreases (Figure 5-5 (b)).

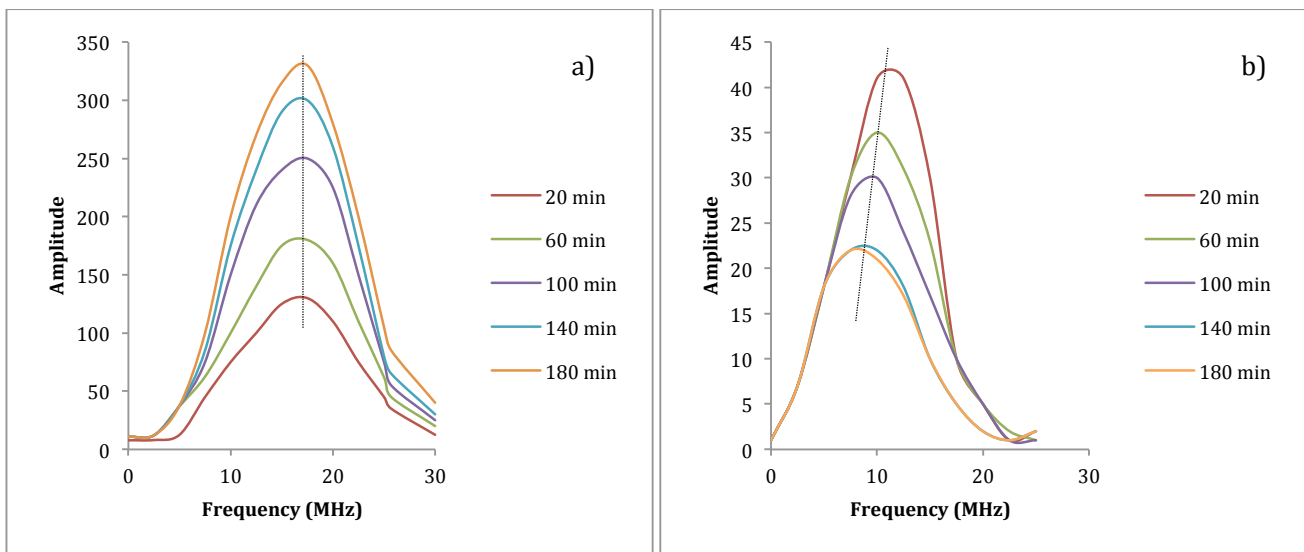


FIGURE 5-5. ECHOES SPECTRUM AMPLITUDE FOR THE DIFFERENT IMMERSION TIMES: (a) ANTERIOR CAPSULE; (b) POSTERIOR CAPSULE, MEAN VALUES (Caixinha 2012).

When using the alternative method, making use of a planar reflector, a downshift of 17% is observed in the centre frequency over the immersion time, for the echoes coming from the reflector with the lens inserted (Figure 5-6).

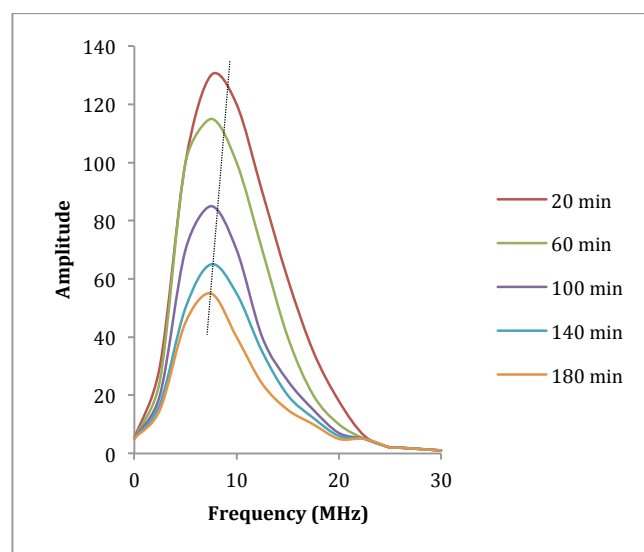


FIGURE 5-6. ECHOES SPECTRUM AMPLITUDE FOR THE DIFFERENT IMMERSION TIMES USING A PLANAR REFLECTOR, MEAN VALUES (Caixinha 2012).

The frequency-dependent attenuation obtained by equations (4-5) and (4-7) clearly increases with the immersion time ($p < 0.001$), *i.e.*, with the lens hardness increase, as shown in (Figure 5-7).

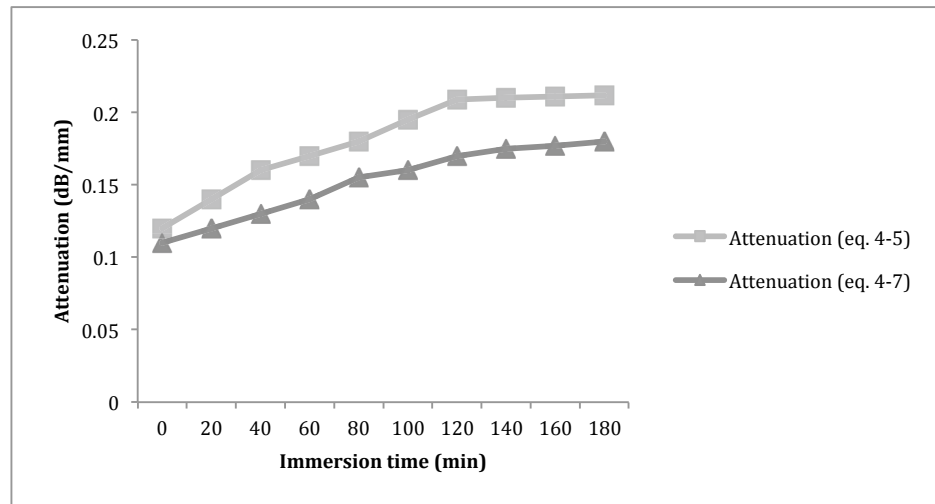


FIGURE 5-7. FREQUENCY-DEPENDENT ATTENUATION MEAN VALUES OBTAINED BY EQUATIONS (4-5) AND (4-7), FOR 10 MHz (MEAN DIFFERENCE BETWEEN METHODS: 0.036 dB/mm (CONFIDENCE INTERVAL: 0.026 TO 0.046); LIMITS OF AGREEMENT: -0.094 TO 0.166) (Caixinha 2012; Jesus *et al.* 2012).

No significant effect of the correction factors *i.e.*, transmission and reflection coefficients, was found in the frequency-dependent attenuation estimation by equation (4-5). Both approaches allow obtaining the attenuation value consistently over the immersion time (ICC = 0.984, $p < 0.001$).

The effect of the correction factors for the frequency-dependent attenuation estimation using equation (4-7) was analysed considering the following approaches: (i) without corrections; (ii) considering the transmission coefficients; (iii) considering the attenuation correction α_s ; and (iv) considering both transmission coefficients and α_s ($\alpha_s = 2.3 \times 10^{-3}$ dB/mm MHz at 20 °C (Cameron 1991)). These four approaches showed an excellent agreement for the estimation of the frequency-dependent attenuation (ICC = 0.997, $p < 0.001$).

The frequency-dependent attenuation coefficients obtained by equations (4-5) and (4-7), showed similar results over immersion time (ICC = 0.717, $p < 0.001$). The frequency-dependent attenuation is almost constant above 120 minutes of immersion time, as shown in Figure 5-7. The correction effect to account for energy loss due to reflections/transmissions at the lens - solution boundaries showed small changes in the frequency-dependent attenuation. The effect of the setup geometry, considering the attenuation in the solution path occupied by the lens, showed also small changes in the frequency-dependent attenuation coefficients. The errors resulting from neglecting the correction factors are therefore meaningless.

When analysing the attenuation *versus* frequency using equation (4-7), for different immersion times, a significant attenuation increase was observed as the hardness increase ($p < 0.001$). As the higher frequency signal components suffer increased attenuation, the spectrum centre frequency of the backscattering signal is shifted to lower

frequencies with depth. That was proved by calculating the attenuation coefficient according to equation (4-8) in a region of the lens with 3 mm in depth, starting in the anterior capsule and corresponding to the higher intensity region of the backscattering signals. Small signal frames, whose size was set equal to the length of incident pulse of the backscattered signal, were processed using a Hanning window, with a 50% window overlap. Each frame was afterwards processed by Fourier transform to extract its spectrum, followed by filtering using a Gaussian bandpass filter, whose cut-off frequencies were set at 5 MHz and 25 MHz.

Figure 5-8 illustrates the centre frequency decrease with depth, for a total cataract, and Figure 5-9 shows the linear fit of the centre frequency downshift *versus* depth, for all immersion times. A clear slope increase is observed from 20 to 180 minutes.

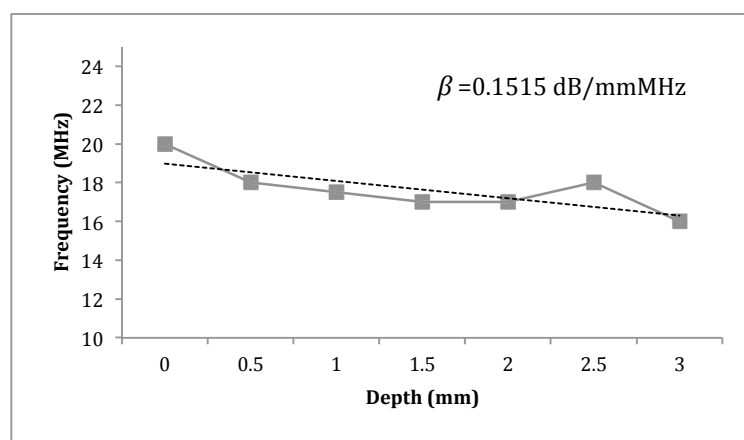


FIGURE 5-8. CENTRE FREQUENCY DOWNSHIFT *VERSUS* DEPTH IN THE LENSES WITH TOTAL CATARACT (180 MINUTES OF IMMERSION TIME), MEAN VALUES (Caixinha 2012; Jesus *et al.* 2013).

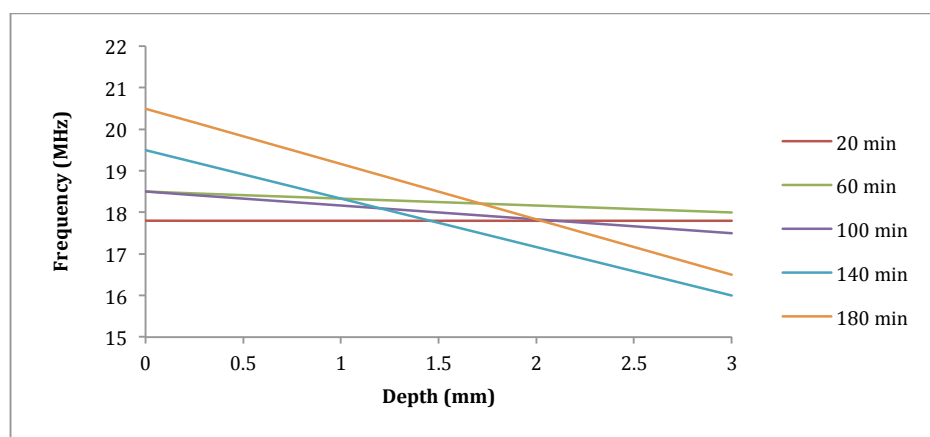


FIGURE 5-9. LINEAR FIT OF THE MEAN CENTRE FREQUENCY DOWNSHIFT *VERSUS* DEPTH, IN LENSES WITH DIFFERENT DEGREES OF CATARACT (FROM 20 TO 180 MINUTES OF IMMERSION TIME) (Caixinha 2012; Jesus *et al.* 2013).

The frequency-dependent attenuation measured in porcine lenses with and without cataract is presented in Table 5-2.

TABLE 5-2. ATTENUATION COEFFICIENT IN THE PORCINE LENSES FOR 10 MHz (N=20).

Attenuation coefficient	Without Cataract	With Total Cataract (180 min. of immersion time)	<i>p</i>
Using equation (4-5)	0.117 ± 0.020 dB/mm	0.212 ± 0.030 dB/mm	< 0.001
Using a planar reflector (equation (4-7))	0.111 ± 0.010 dB/mm	0.180 ± 0.020 dB/mm	< 0.001

5.3.3 Nakagami *m* and Ω parameters

The mean Nakagami *m* parameter, obtained by equation (4-10) and based on 10 A-scan lines acquired in the central portion of the lens, increased from 0.63 to 0.88 for the immersion time range, corresponding to an increase of 0.0013 per minute (Figure 5-10).

The Nakagami scaling parameter Ω , describing how the backscattering intensity values changed with cataract progression, varied with the immersion time only in the early stages of cataract formation, *i.e.*, from 0 to 40 minutes (Figure 5-11).

The results showed that the backscattered statistics progress from a pre-Rayleigh (*i.e.*, $m < 1$) to a Rayleigh distribution (*i.e.*, $m \approx 1$), suggesting that protein aggregation and fiber compaction increase with cataract progression.

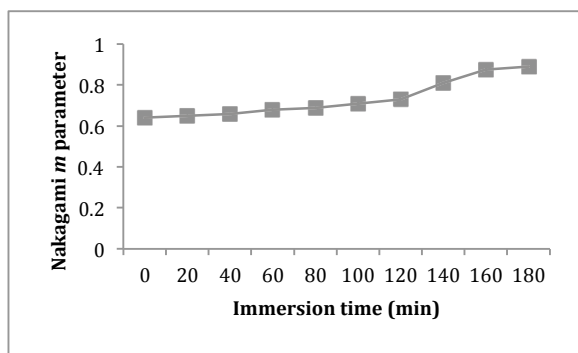


FIGURE 5-10. NAKAGAMI *m* PARAMETER AS FUNCTION OF IMMERSION TIME, MEAN VALUES (Caixinha 2012; Jesus *et al.* 2013).

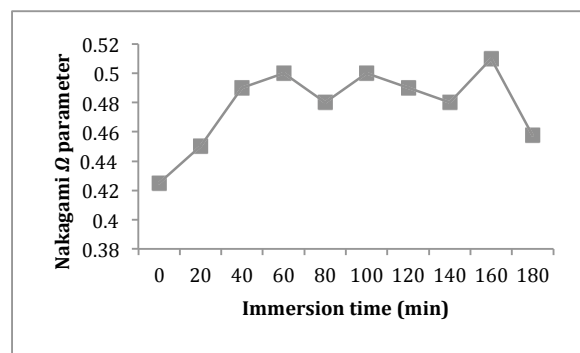


FIGURE 5-11. NAKAGAMI SCALE PARAMETER Ω AS FUNCTION OF IMMERSION TIME, MEAN VALUES (Caixinha 2012; Jesus *et al.* 2013).

5.4 Discussion

The *in vitro* results using porcine lenses are consistent with the results published by other authors. The obtained results confirm that the ultrasound velocity and frequency-dependent attenuation increases significantly with cataract progression (*i.e.*, lens hardness, $p < 0.001$) and that cataract progression produces a higher increase in the attenuation than in velocity.

In this exploratory study, velocities of 1597-1619 m/s and 1670-1694 m/s were found in normal and cataractous porcine lenses, respectively, being in agreement with the results published by Oksala *et al.* (Oksala and Lehtinen 1958) and Huang *et al.* (Huang *et al.* 2007a; Huang *et al.* 2007b). Oksala *et al.* (Oksala and Lehtinen 1958) found an average velocity of 1640.5 m/s in normal human lenses. Huang *et al.* found, in normal porcine lenses, a mean velocity of 1639.8 m/s and, for cataractous lenses, 1735.6 m/s, when using a 35 MHz transducer (Huang *et al.* 2007a). In a second work using a 46 MHz needle transducer, Huang *et al.* found in normal porcine lenses a mean velocity of 1704.4 m/s and for cataractous lenses a mean velocity of 1759.2 m/s, when using a (Huang *et al.* 2007b). Attenuation coefficients of 0.111-0.117 dB/mm and 0.180-0.212 dB/mm were found in normal and cataractous porcine lenses, respectively. The increase of the frequency-dependent attenuation, obtained with a 25 MHz transducer from 62.1% to 81.2%, considering the two different methods used, is in agreement with the results published by Huang *et al.* (Huang *et al.* 2007a) with a 35 MHz transducer. Huang *et al.* found an attenuation coefficient increase of 64.6% at 30 MHz (from 4.49 ± 0.05 dB/mm for normal lenses to 7.36 ± 0.25 dB/mm for cataractous lenses), and 75.6% at 40 MHz (from 6.32 ± 0.04 dB/mm for normal lenses to 11.1 ± 0.92 dB/mm for cataractous lenses) (Huang *et al.* 2007a).

Huang *et al.* showed (Huang *et al.* 2007a) that both acoustic parameters, velocity and frequency-dependent attenuation, are positively correlated with the lens Young's modulus and with the phacoemulsification energy level, concluding that the ultrasound parameters can be useful to select the optimal phacoemulsification energy level. In human lenses a similar result was found by Tabandeh *et al.* (Tabandeh *et al.* 2000), where a positive correlation between the frequency-dependent attenuation and the lens hardness was found.

The centre frequency downshift measurement approach was also used in this exploratory study, providing the attenuation coefficient calculation along the transducer beam in the lens. A clear centre frequency downshift was observed with cataract progression. The centre frequency of the anterior capsule echo remains constant while the posterior capsule echo centre frequency decrease 28% with cataract progression. When using the planar reflector method, a downshift of 17% is observed in the centre frequency. As the higher frequency signal components suffer increased attenuation, with cataract progression the spectrum centre frequency of the backscattering signal is shifted to lower frequencies with depth.

It was shown that the different approaches used to estimate the ultrasound velocity and the frequency-dependent attenuation produces similar results ($ICC \geq 0.717$). A good agreement was found between the three different approaches used for the propagation velocity calculation. The time-of-flight and the amplitude spectra approaches led

to the higher agreement since they are conceptually identical. The alternative method, that does not require the lens' thickness knowledge, although in agreement with the first two, cannot be used *in vivo* since it requires a reference signal from a planar reflector. A good agreement was also found between the two different approaches used for the frequency-dependent attenuation. For both approaches no significant effect of the correction factors was found, and therefore, the transmission and reflection coefficients, as well as the α_s factor can be neglected when estimating the frequency-dependent attenuation (Huang *et al.* 2007a).

The backscattering signals were also analysed through the Nakagami m and Ω parameters. The Nakagami m parameter reflected changes in the arrangement, distribution and concentration of scatterers in the lens through cataract formation. The results showed that the statistics of the backscattered envelope varied from a pre-Rayleigh to a Rayleigh distribution as the immersion time increased; *i.e.*, with the cataract progression. The Nakagami m parameter increasing demonstrates an increase of the scatterers concentration over the cataract formation, suggesting that protein aggregation and fiber compaction increase with cataract progression. The scaling parameter Ω did not show a consistent variation with the cataract progression process, varying significantly only in the early stages of the cataract formation.

The results of the exploratory study show that the ultrasound technique can be used to characterize the cataractous lens. By using the acoustical parameters, velocity and frequency-dependent attenuation, and the backscattering signals, namely the Nakagami m parameter, the cataract formation can be objectively and noninvasively characterized.

5.5 Resulting publications

The following thesis project was elaborated:

- Caixinha, M., 2012. Técnicas não Invasivas por Ultrassons para Visualização e Caracterização Objetiva da Catarata. Determinação da Energia Ótima para Facoemulsificação. Universidade de Coimbra.

The following papers were published (section PUBLICATIONS):

- Ultrasound techniques for lens hardness characterization: A comparison study. Jesus, D.; Caixinha, M.; Santos, M.; Santos, J. IEEE 2012 International Ultrasonics Symposium (IUS). 2012; 2376-2379 (DOI: 10.1109/ULTSYM.2012.0594).

- Using of the ultrasound frequency-dependent attenuation and Nakagami distribution for cataract evaluation
Jesus, D.; Velte, E.; Caixinha, M.; Santos, M.; Santos, J. Bioengineering (ENBENG), 2013 IEEE 3rd Portuguese Meeting. 2013; 1-4 (DOI: 10.1109/ENBENG.2013.6518388).

6 EX VIVO CATARACT CHARACTERIZATION

6.1 Objective

To validate the experimental setup and to demonstrate that the ultrasound technique can be used to characterize cataract and estimate its hardness *in vivo* a proof-of-concept study was performed *ex vivo* in porcine lenses.

For this purpose an extensive extraction and selection of features based on the acoustical parameters and backscattering signals, was made to automatically classify the cataract severity and to characterize noninvasively the cataract hardness. B-scan and Nakagami m parametric images were also produced.

Additionally, to prove that the used method for cataract induction (described in Chapter 5) leads to an increase of fibers compaction and proteins aggregation, and consequently to a hardness increase over the cataract progression, histological slices from the nucleus and cortex regions were obtained and analysed. To characterize the cataract hardness, correlations were made between the slice images characteristics, and the extracted ultrasound features.

6.2 Materials and methods

6.2.1 Sample size and cataract induction

The sample size estimation depends on the nature of the study and the analyses to be performed. The sample size is usually estimated for a desired statistical power considering the planned analysis and the expected result, or effect size. Higher desired statistical power or smaller expected effect size, require a larger number of cases. In studies where there is no *prior* knowledge on the final effect size and where machine learning techniques are used to explore the data, the sample size is based on simulations or on rules-of-thumb (Siddiqui 2013).

The sample size for this study, *i.e.*, the number of lenses needed for the proof-of-concept, was estimated based on the guidelines provided in the literature describing the appropriate sample size for multivariate statistical techniques (Fan *et al.* 1999; Meyers *et al.* 2006). According to these guidelines a sample size of 200 lenses is considered fair when using 10 features, maximum (Siddiqui 2013). For a higher number of features the sample size should also be higher (Siddiqui 2013).

Two different analyses were carried out in this study: (1) cataract characterization; and (2) automatic classification of the cataract severity (Figure 6-1). A minimum of 200 lenses was considered for the two analyses. In order to not compromise the statistical power, a data dimensionality reduction was performed in the second analysis.

A total of 262 lenses from porcine eyes were therefore collected in a slaughterhouse. The lenses were carefully extracted in order to preserve the capsule. The remaining iris and adherent aqueous and vitreous humour, resulting from the enucleation process, were thoroughly cleaned, to avoid unwanted pulses in the A-Scan acquisitions. Ten lenses were excluded due to the presence of opacities. The lens mean anteroposterior and equatorial diameters were 8.2 ± 0.2 mm and 12.3 ± 0.2 mm, respectively, and the mean weight was 0.42 ± 0.01 g.

Cataract was induced in 177 lenses using the method described in Chapter 5 (section 5.2.1). To obtain different cataract degrees, the lenses were immersed in the solution over 60, 120 and 180 minutes. The number of lenses used in the proof-of-concept study, for the different experiments, is illustrated in Figure 6-1.

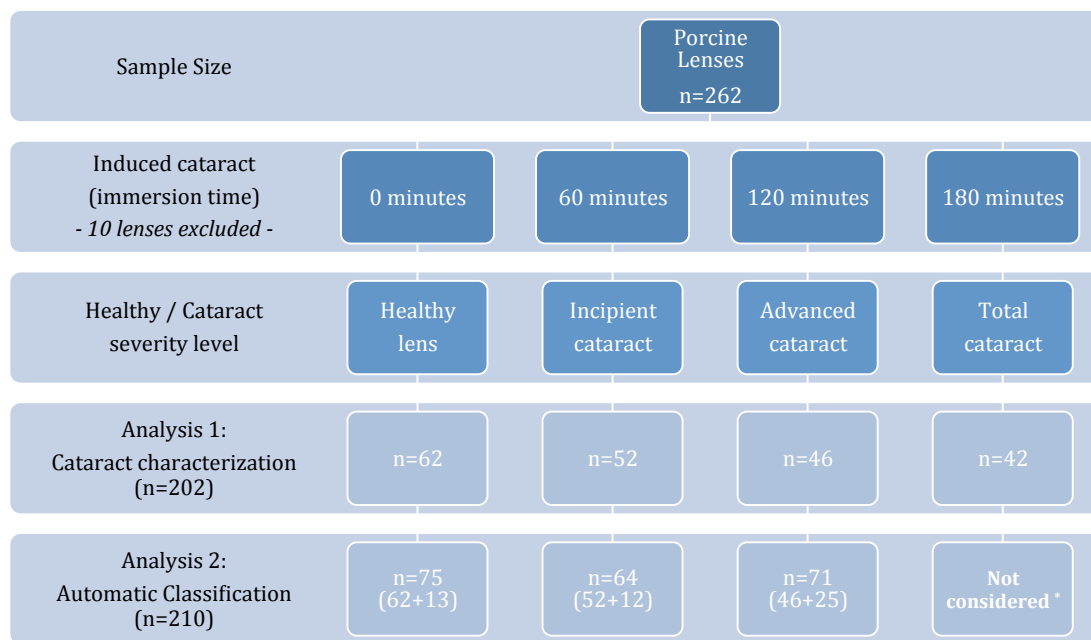


FIGURE 6-1. NUMBER OF LENSES USED IN THE PROOF-OF-CONCEPT STUDY, FOR THE DIFFERENT EXPERIMENTS.

*LENSES WITH TOTAL CATARACT WERE NOT CONSIDERED BECAUSE IT WAS FOUND IN ANALYSIS 1 THAT THE ACOUSTICAL PARAMETERS, B-SCAN AND NAKAGAMI IMAGES, DOES NOT DISCRIMINATE ADVANCED FROM TOTAL CATARACT.

6.2.2 Experimental setup

The ultrasound parameters, velocity, frequency-dependent attenuation, and the backscattering signals were obtained, using the setup shown in Figure 5-3.

The transducer characteristics were described in Chapter 5 (section 5.2.2) and are summarized in Table 6-1. A typical pulse obtained by the transducer, collected from a plane reflector is shown in Figure 5-3. The transducer excitation and signals acquisition were made using the same pulser-receiver and acquisition board described in Chapter 5 (section 5.2.2).

TABLE 6-1. TRANSDUCER CHARACTERISTICS.

Probe characteristics	
Type	IAP-F25.3.1
Active element size	Ø 5 mm
Centre frequency	25 MHz
Bandwidth	> 80% at -6 dB
Focal distance	25 mm in water
Focal diameter	0.3 mm
Pulse length	0.13 µs at -6 dB
Axial resolution	104 µm
Lateral resolution	320 µm

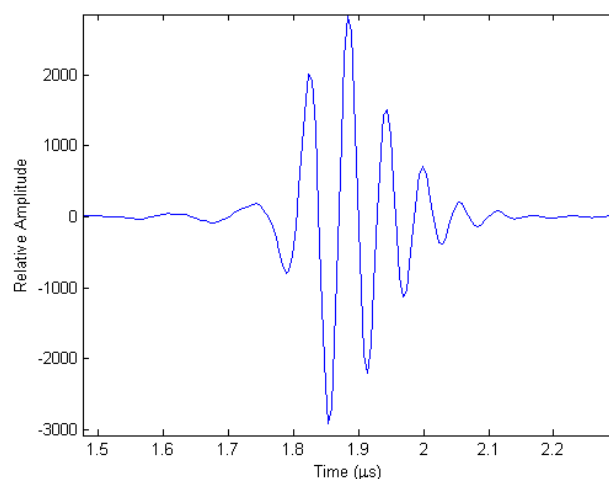


FIGURE 6-2. TRANSDUCER PULSE SHAPE USING A PLANE REFLECTOR IN WATER.

6.2.3 Data acquisition

6.2.3.1 Ultrasound velocity and frequency-dependent attenuation

The propagation velocity was calculated considering the average propagation time of ten A-scan signals obtained over the central portion of the lenses, according to equation (4-1). The attenuation coefficient was calculated using equation (4-5), considering also the average of ten A-scan signals.

6.2.3.2 B-scan imaging

As stated in Chapter 4, the B-scan image encompasses the signal envelope detection followed by a logarithmic compression. The backscattering signals envelope is obtained using the Hilbert transform considering a dynamic range of 40 dB. For the image construction, we used 15000 A-scan lines, sampled at a 200 MHz rate and spaced by 0.001 mm. A flowchart for the brightness image construction is shown in Figure 6-3.

6.2.3.3 Nakagami imaging

The Nakagami parametric images were made based on the B-scan images, and correspond to a two-dimensional representation of the m parameter values (*i.e.*, the Nakagami shape parameter). The image construction process encompassed a sliding window selected to provide good spatial resolution. A small window improves the resolution but, on the other hand, gives rise to few envelope points, which can lead to bad estimations of the m parameter (Tsui *et al.* 2006). A sliding window with a length equal to three times the transducer pulse length (0.39 μ s) was considered in order to simultaneously provide good image resolution and stable Nakagami m parameter estimation (Tsui and Chang 2007). Taking into account the sampling frequency of 200 MHz and 99% of overlapping, the window had a size of 78 samples.

To reduce noise and improve the Nakagami m parameter performance, a noise-assisted Nakagami m parameter approach was used, *i.e.*, an adaptive threshold filter was applied to the backscattered signals before the construction of the Nakagami parametric image (Tsui *et al.* 2009; Tsui *et al.* 2010a). Since the noise level corresponded to a SNR of 17 dB, the adaptive threshold filter was based on noise-assisted empirical mode decomposition. Two other filtering techniques were tested, namely noise-assisted correlation algorithm (Tsui *et al.* 2012), and wavelet-based image denoising (Thakur and Anand 2005). The results obtained were very similar to the noise-assisted empirical mode decomposition technique, whose performance is similar to the conventional thresholding technique based on applying a threshold for rejecting small echoes.

A colour scale was used for the Nakagami images to ease the visualization and interpretation. The colour scale ranges from blue to red as the m parameter values increase from 0 to 1, corresponding to backscattered signal envelopes changing from a pre-Rayleigh to a Rayleigh statistical distribution (Figure 6-3).

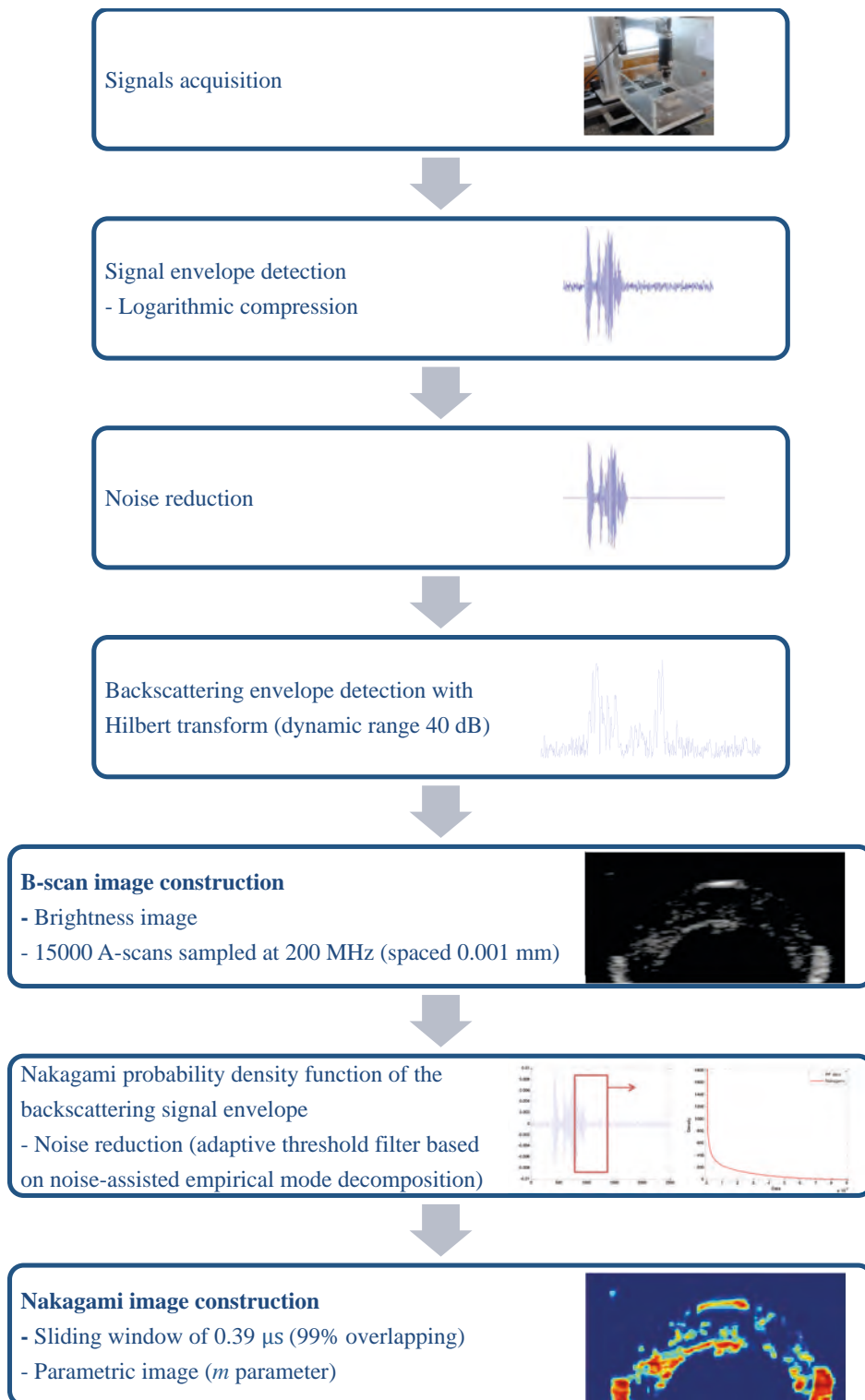


FIGURE 6-3. FLOWCHART FOR B-SCAN AND NAKAGAMI IMAGES CONSTRUCTION.

6.2.4 Features extraction

6.2.4.1 A-scan signals

The following features were extracted from the A-scan signals: the mean and variance values of the velocity and attenuation coefficient; the slope, intercept, and mid-band, extracted from the Hilbert and Fourier spectra by linear regression techniques (Kalisz 1997); and the mean frequency, frequency downshift, frequency at maximal amplitude and the backscattering coefficient.

The spectral slope is affected by attenuation and is related to the effective size of tissue scatterers. The spectral intercept is unaffected by attenuation (that is linearly dependent on frequency), and is related to the effective sizes concentrations and relative acoustical impedances of the tissue scatterers. The mid-band fit is affected by attenuation and is related to the above tissue properties (Kalisz 1997).

6.2.4.2 Backscattering signals

Two approaches were used for the backscattering signals: statistical distributions modelling and spectral analysis (Brand *et al.* 2008; Machado *et al.* 2006; Smolíková *et al.* 2004).

The amplitude of the backscattering signal envelope was modelled by the Nakagami statistical distribution. The parameters of this distribution provide information on the scatterers' density (the number of scatterers within the resolution cell of the transducer) and size, which is related to the amplitude (Smolíková *et al.* 2004). The following features were extracted from the Nakagami distribution: Nakagami shape parameter (m), and scale parameter (Ω).

The spectral analysis of the backscattering signals can provide useful information about acoustical and structural properties of the tissue microstructure (Brand *et al.* 2008; Machado *et al.* 2006). Thus, the following features were extracted: the predominant and global periodicity, the predominant and global orientation, the variance of the periodicity function, the variance of the orientation function and the amplitude of the Discrete Fourier Transform (DFT) spectra.

Features were also extracted from the B-scan and Nakagami images by textural analysis (Brand *et al.* 2008; Machado *et al.* 2006; Smolíková *et al.* 2004) performed on a region of interest (ROI) with 4.5 mm in width and 1.5 mm in depth, whose size was defined to include only the anterior lens hemisphere (excluding the anterior capsule and including only regions containing protein aggregates and collagen fibers), as shown in Figure 6-4 (a). To exclude any contribution of the external region to the lens, a mask with its shape was also used, as shown in Figure 6-4 (b). Textural analysis allows the interpretation of the tissue appearance based on the obtained medical image, which is usually described in terms of the image smoothness, grain, regularity and/or homogeneity. The extracted features from textural analysis are based on the variations of the image intensity, which represent the tissue echogenicity. The following parameters were extracted from the B-scan and Nakagami images:

- First order statistic parameters from the image histogram, *i.e.* mean, variance, kurtosis, skewness, standard deviation, mode and median.
- Grey Level Co-occurrence Matrix (GLCM) parameters for 0°, 45°, 90° and 135°, *i.e.*, energy, inertia, entropy, correlation and homogeneity, (Bankman 2000; Haralick *et al.* 1973).

- Grey Level Run Length Matrix (GLRLM) parameters, *i.e.*, Short and Long Run Emphasis (SRE and LRE), Grey Level Non-Uniformity (GLNU), Run Percentage (RP), Run Length Non-Uniformity (RLNU), and Low and High Grey Level Run Emphasis (LGLRE and HGLRE), (Bankman 2000; Haidekker 2011; Haralick *et al.* 1973; Tang 1998).
- Fractal dimension (Hausdorff dimension) (Bankman 2000).

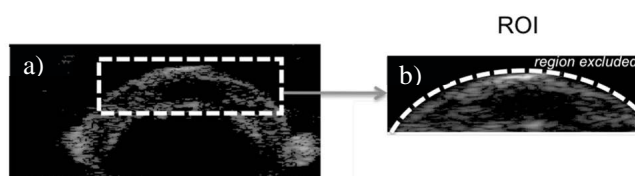


FIGURE 6-4. ROI USED TO EXTRACT TEXTURAL FEATURES FROM THE B-SCAN AND NAKAGAMI IMAGES (Caixinha *et al.* 2014a; Caixinha *et al.* 2015a).

Data processing was performed in Matlab (MathWorks Inc., MA, USA).

6.2.5 Nucleus and cortex histological slices

Slices with 50 μm in thickness were obtained from 15 lenses, in the cortex and the nucleus regions (5 healthy lenses, 5 lenses with initial cataract and 5 with severe cataract) to prove that the used cataract induction method promotes an increase in protein aggregation and fiber compaction, and also to correlate the lens hardness increase with the extracted features from the B-scan and the Nakagami images.

The lenses were first frozen at $-40\text{ }^{\circ}\text{C}$ in an embedding resin, Cryomatrix Shandon medium (Thermo Scientific Shandon Ltd, WA, USA), and then the slices were made transversally, with a glass knife using a Leica Microsystems CM3350S cryostat (Leica Microsystems, Wetzlar, Germany, Figure 6-5). The Hematoxylin and Eosin (H&E) staining protocol was used (Cardiff *et al.* 2014; Fischer *et al.* 2008) to stain the lens proteins nonspecifically, and the connective tissue and collagen. The stained slices from the nucleus and the cortex were imaged using an inverted microscope with a digital image capture system. The images were acquired with the same magnification (40x for the slices in the cortex and the nucleus regions, and 4x for the slices of the nucleo-cortex region), illumination intensity and exposure time. In accordance with the conditions of image acquisition and with the staining protocol, the darker areas in the microscopy image are associated with a higher concentration of protein aggregates and fibers compaction. To compare the amount of proteins and collagen fibers in the different lens regions, and to compare between healthy and cataractous lenses, the mean brightness of each image was computed. The mean brightness obtained in those images was correlated with the mean brightness of the B-scan images as well as with the mean Nakagami m parameter.

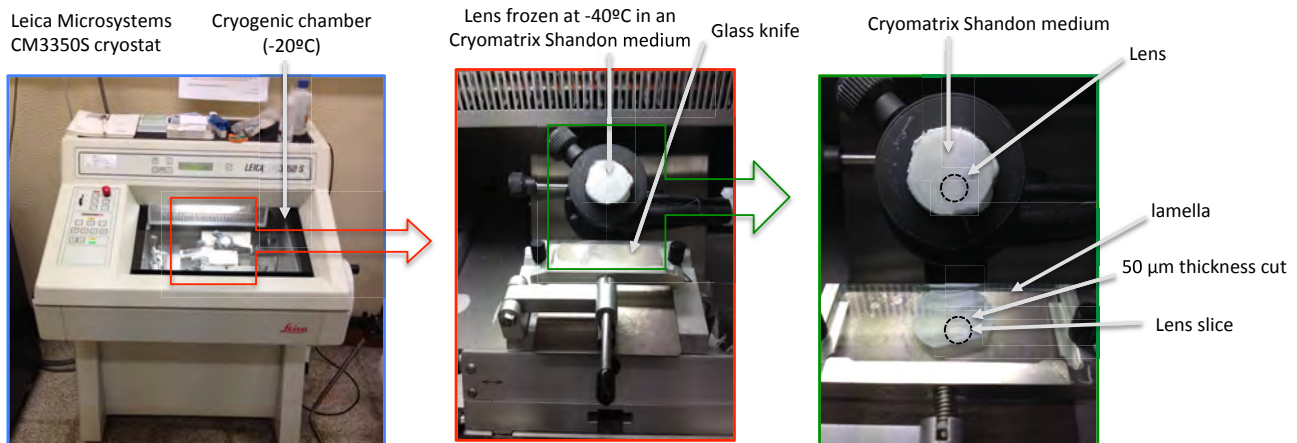


FIGURE 6-5. LEICA MICROSYSTEMS CM3350S CRYOSTAT.

6.2.6 Data analysis

6.2.6.1 Statistical analysis

For the ultrasound velocity, attenuation, mean brightness of the B-scan images, mean Nakagami m parameter and mean brightness of the slices' images, statistically significant differences between lenses with and without cataract were tested using ANOVA test with Bonferroni *post hoc* test for multiple comparisons, and correlations between the different parameters were tested using the Spearman correlation coefficient. The commercial statistical software IBM SPSS Statistics version 20 was used (IBM Corp., NY, USA). Statistical values were considered significant for p -values lower than 0.05.

6.2.6.2 Cataract characterization

A classification and regression tree (CRT) with a 10-fold cross validation was performed, to verify whether the acoustical parameters (velocity and attenuation), the mean and variance brightness in the B-scan images, and the mean and variance of the m parameter in the Nakagami images, can predict cataract.

Classification and regression trees (CRT) are a supervised learning technique that creates rules to classify elements according to predefined categories (Quinlan J 1996; Rokach and Maimon 2005). CRT are classifiers with a tree-like structure that splits recursively the input dataset until each data subset consists completely (or predominantly) of elements from one category. The tree grows from the parent (root) to the child nodes (leaves) and in each node a test is performed on one or more attributes to decide how the data should be split. Data partitioning is completed when the data subset at a node is either "pure" (*i.e.*, all cases within the node has the same target variable value) or sufficiently small (as set by the user, *a priori*). CRT uses an algorithm where data partitioning is based on the maximization of the within node homogeneity, *i.e.*, the minimization of the number of cases with different membership in each node of the tree (minimization of the node impurity) (Rokach and Maimon 2005). Furthermore, to reduce overfitting risk, and to create a more accurate CRT, the initial tree is pruned, that is the small and/or deep nodes of the tree are removed.

The CRT was performed using the commercial statistical software IBM SPSS Statistics version 20 (IBM Corp., NY, USA).

6.2.6.3 Automatic cataract classification

Ninety-seven (97) features were extracted from the acquired signals (18 from the A-scan signals and 79 from the backscattering signals, Table 6-2), in order to automatically classify the cataract severity using machine learning techniques (Caixinha and Nunes 2016). Two approaches were used, one using a 2-step binary classifier for the classification into healthy or cataractous lenses, as well as for the classification into incipient or advanced cataract; and another using a multiclass classifier for the classification into healthy, incipient or advanced cataract.

TABLE 6-2. NINETY-SEVEN (97) FEATURES EXTRACTED FROM THE ULTRASOUND SIGNALS.

Features	Number	Features extracted	
<i>1 to 4</i>	<i>4</i>	<i>Ultrasound velocity and attenuation</i>	Mean and variance values of the ultrasound velocity and attenuation coefficient.
<i>5 to 18</i>	<i>14</i>	<i>A-scan features</i>	For Hilbert and Fourier spectra the following features were extracted using linear regression techniques: spectral slope; intercept; and midband fit. The mean frequency; frequency downshift; frequency at maximal amplitude; and backscattering coefficient were also extracted.
<i>19 to 60</i>	<i>42</i>	<i>B-scan features</i>	-
	7	two dimensional DFT	For the DFT the following spectral measures were extracted: predominant periodicity; global periodicity; predominant orientation; global orientation; variance of the periodicity function; variance of the orientation function; and amplitude of the DFT spectra.
	7	1 st order statistics	First order statistics from the image histogram: mean; variance; skewness; kurtosis; standard-deviation; mode; and median.
	20	GLCM	For 0°, 45°, 90° and 135°: energy; inertia; entropy; correlation; and homogeneity
	7	GLRLM	SRE; LRE; GLNU; RP; RLNU; LGLRE; and HGLRE
	1	Fractal dimension	Hausdorff dimension
<i>61 to 97</i>	<i>37</i>	<i>Nakagami features</i>	-
	2	Nakagami distribution	<i>m</i> and <i>Q</i> parameters
	7	1 st order statistics	First order statistics from the image histogram: mean; variance; skewness; kurtosis; standard-deviation; mode; and median.
	20	GLCM	For 0°, 45°, 90° and 135°: energy; inertia; entropy; correlation; and homogeneity
	7	GLRLM	SRE; LRE; GLNU; RP; RLNU; LGLRE; and HGLRE
	1	Fractal dimension	Hausdorff dimension

In order to obtain a parsimonious description of the multivariate data, reducing or eliminating statistically correlated data, obtaining a compact, accurate, and representative sample of the data, a dimensionality reduction was performed (Jain *et al.* 2000; Kambhatla and Leen 1997). To reduce the features number to 20 maximum (considering the 210 lenses and the 97 features under analysis), a principal component analysis (PCA) was performed (Guyon and Elisseeff 2003; Kambhatla and Leen 1997; Sajda 2006; Shin and Markey 2006). PCA is a multivariate statistical method that generates a new set of features, which is a linear combination of the original features. The composition of each new component is determined by the information provided by each feature and by its correlation with the other features. Mathematically, the principal components are found by calculating the eigenvectors and eigenvalues¹² of the covariance matrix¹³. This is equivalent to finding the axis system in which the covariance matrix is diagonal. The eigenvector with the largest eigenvalue corresponds to the vector with the higher variation in the dataset, and the eigenvector with the second largest eigenvalue corresponds to the vector (orthogonal) with the next highest variation in the dataset (Kambhatla and Leen 1997; Sajda 2006; Shin and Markey 2006). The graphical representation of the eigenvalues associated with the extracted components (called scree plot) allows to visually assess the components that explain most of the variation in the data. The components can also be represented as a function of the cumulative variance of the data. In this study, a stepwise approach was used to select the best set of components provided by the PCA. The selected number of components was based on the set of components that achieved the highest average F-measure value, given by:

$$F - measure = 2 \frac{Precision \times Sensitivity}{Precision + Sensitivity} \quad (6-1)$$

where the precision is,

$$Precision = \frac{\sum True\ Positive}{\sum Test\ outcome\ Positive} \quad (6-2)$$

and the sensitivity is,

¹² Eigenvectors (or characteristic vectors) and eigenvalues (or characteristic values) are a special set of vectors and scalars, respectively, associated with a linear system of equations. Let A be a square matrix ($n \times n$). A non-zero vector V is called an eigenvector of A if and only if there is a number (real or complex) such that $AV = \lambda V$. In this case, the vector V is called an eigenvector of A corresponding to λ .

¹³ The variance-covariance matrix is a square matrix that contains the variances and covariances associated with the different features. The diagonal elements of the matrix contain the variances of the features and the off-diagonal elements contain the covariances between all possible pairs of features.

$$Sensitivity = \frac{\sum True\ Positive}{\sum Condition\ Positive} \quad (6-3)$$

The selected components from the PCA, *i.e.*, the features combinations that simultaneously reduce the data dimensionally and explain the variance observed in the data, were used to train and test the classifiers.

For the 2-step binary classification, four different classifiers were considered: two classifiers based on a probabilistic approach, Naive Bayes and K Nearest-Neighbour (KNN), and two others based on the construction of decision boundaries, Fisher Linear Discriminant (FLD) and Support Vector Machines (SVM) (Jain *et al.* 2000). A Radial Basis Function¹⁴ (RBF) kernel (Chang and Lin 2011a; Chang and Lin 2011b) was used for the SVM classifiers.

Bayes classifiers use the Bayes' theorem that assumes a strong independence between the features, and assigns data to the class with the maximum *posteriori* probability, minimizing the probability of misclassification. KNN classifiers are nonparametric decision rules that, based on a training data set, compute for each class the distances between data ("neighbour") and then classify new cases based on the distances between these cases and the nearest neighbours.

FLD classifiers create discriminant functions, *i.e.*, linear combinations of the features that minimize the Mean Square Error (MSE) between the classification results and the true class. New cases are classified based on the value of these functions. SVM classifiers classify data by finding the best hyperplanes that separates data from different classes. The best hyperplane for an SVM is the one with the largest margin between two classes and without data inside (El-Naqa *et al.* 2002; Kim *et al.* 2013).

The SVM classifier was used for multiclass classification. The one-against-all approach was used to classify the features into one of the three lens categories, *i.e.*, healthy lens, incipient cataract and advanced cataract.

A RBF kernel (Chang and Lin 2011a; Chang and Lin 2011b) was used for the SVM classifiers. An optimization algorithm was used to optimize simultaneously the cost function¹⁵ C and the RBF Gamma (γ) parameter.

A k -fold cross-validation was performed with $k = 10$, where the classifiers are trained with $k-1$ samples selected randomly and tested with the remaining sample. The performance of the different classifiers was calculated considering the average performance of each fold and using the following measures: F-measure; accuracy; precision; sensitivity and specificity, where the specificity and the accuracy are given by,

$$Specificity = \frac{\sum True\ Negative}{\sum Condition\ Negative} \quad (6-4)$$

¹⁴ Radial basis functions allow approximating multivariate functions by linear combinations of terms based on single univariate functions.

¹⁵ The cost function is a function that attributes a cost, or risk number, for the classification in each category.

$$Accuracy = \frac{\sum True\ Positive + \sum True\ Negative}{\sum Total\ Sample} \quad (6-5)$$

The classification process was performed in Matlab (MathWorks Inc., MA, USA). The Optimization Toolbox was used to optimize the SVM C and γ parameters.

6.3 Results

6.3.1 Ultrasound velocity and frequency-dependent attenuation

Both acoustical parameters, velocity and frequency-dependent attenuation, showed a statistically significant increase with cataract progression ($p < 0.001$) as shown in Figure 6-6. This increase was statistically significant for all immersion times except from 120 to 180 minutes, corresponding to advanced and total cataract, respectively ($p = 0.834$).

The velocity increased from 1585.0 ± 31.7 m/s in healthy lenses to 1652.7 ± 27.8 m/s in lenses with total cataract (Figure 6-6 (a)). The frequency-dependent attenuation increased from 0.406 ± 0.028 dB/mm MHz in healthy lenses to 0.444 ± 0.037 dB/mm MHz in lenses with total cataract (Figure 6-6 (b)).

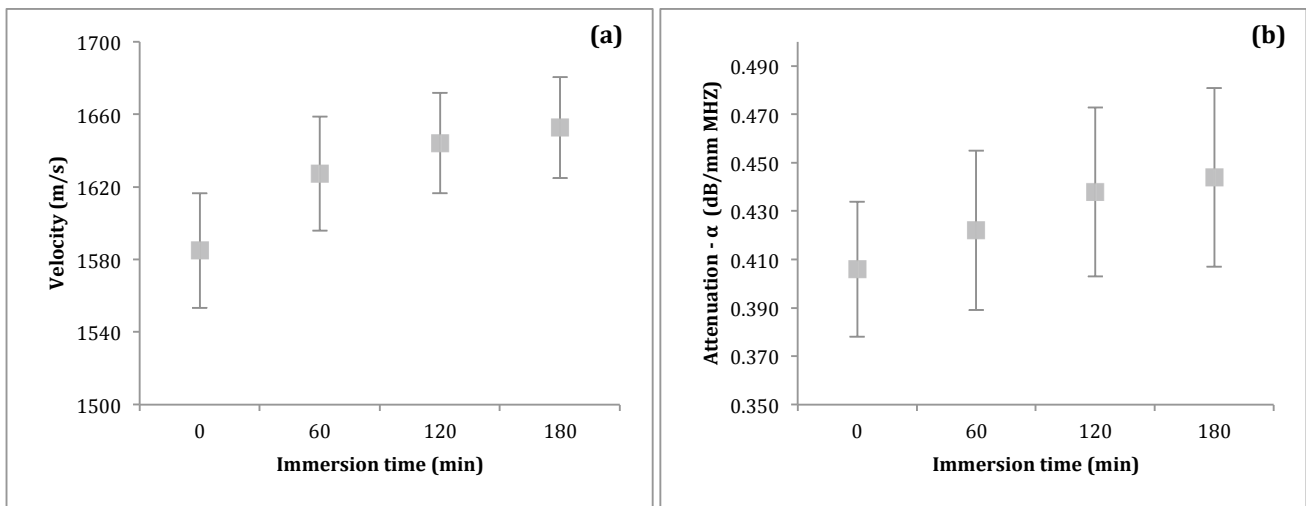


FIGURE 6-6. ACOUSTICAL PARAMETERS FOR THE DIFFERENT IMMERSION TIMES (a) VELOCITY AND (b) FREQUENCY-DEPENDENT ATTENUATION, (MEAN \pm 1SD) (Caixinha *et al.* 2014a).

6.3.2 B-scan imaging

The B-scan image brightness increased with the cataract progression as shown in Figure 6-7. The cataract progression pattern, observed in the B-scan images is a result of the method used for cataract induction. The mean brightness (normalized values¹⁶) in the defined ROI, increased from 0.239 ± 0.094 for lenses without cataract to 0.753 ± 0.222 for lenses with total cataract (Figure 6-8). A statistically significant increase was found with cataract progression, over and between the different immersion times ($p < 0.01$). Moreover, the mean brightness showed a good correlation with the ultrasound velocity ($r = 0.605$, $p < 0.001$) and a moderate correlation with the attenuation ($r = 0.529$, $p < 0.001$).

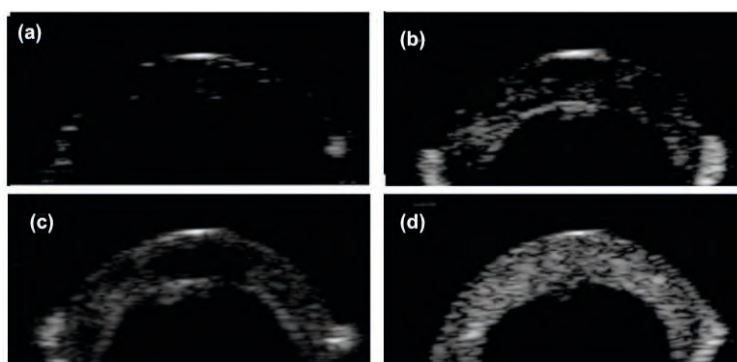


FIGURE 6-7. B-SCAN IMAGES FOR LENSES: (a) WITHOUT CATARACT; (b) 60 MINUTES; (c) 120 MINUTES; (d) AND 180 MINUTES OF IMMERSION TIME (Caixinha *et al.* 2014a).

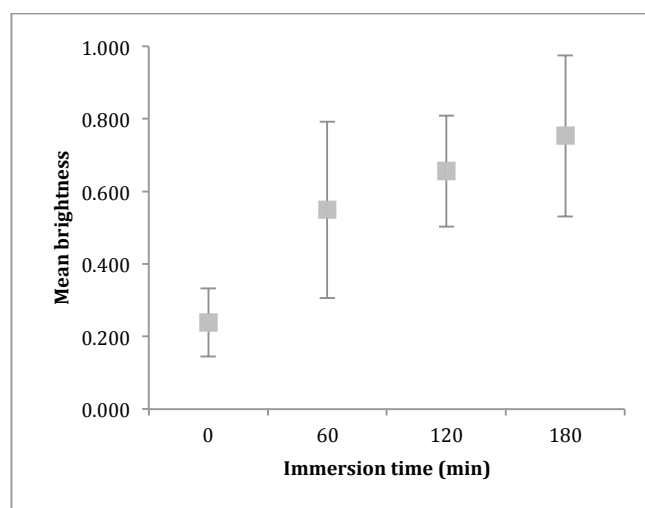


FIGURE 6-8. MEAN B-SCAN BRIGHTNESS FOR THE DIFFERENT IMMERSION TIMES, (MEAN \pm 1SD) (Caixinha *et al.* 2014a).

¹⁶ The B-scan image brightness, originally in a scale ranging from 0 to 255 (eight bits of resolution), was normalized to a scale ranging from 0 to 1.

6.3.3 Nakagami parametric imaging

The Nakagami m parameter also showed an increase with cataract progression from the cortex to the nucleus, as shown in the Nakagami images, Figure 6-9. The mean value of the m parameter, obtained in the defined ROI changed from 0.272 ± 0.076 for lenses without cataract to 0.554 ± 0.166 , for lenses with total cataract (Figure 6-10). Also a statistically significant increase was found with cataract progression ($p < 0.01$). Besides, the mean Nakagami m parameter showed a good correlation with the velocity ($r = 0.657, p < 0.001$) and a moderate correlation with the attenuation ($r = 0.471, p < 0.001$).

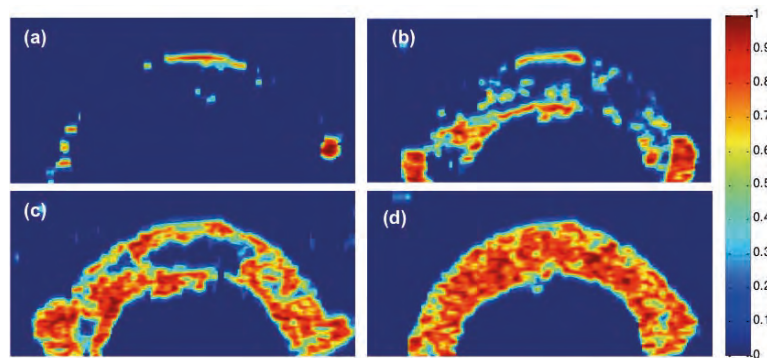


FIGURE 6-9. NAKAGAMI IMAGES FOR LENSES: (a) WITHOUT CATARACT; (b) 60 MINUTES; (c) 120 MINUTES; AND (d) 180 MINUTES OF IMMERSION TIME (Caixinha *et al.* 2014a).

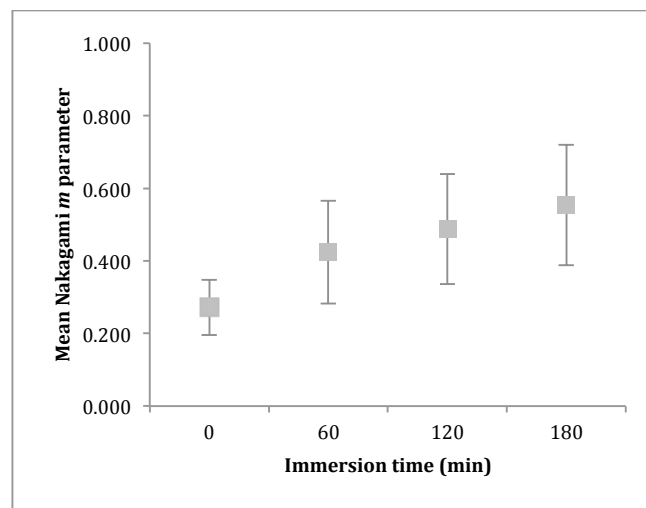


FIGURE 6-10. MEAN NAKAGAMI m PARAMETER FOR THE DIFFERENT IMMERSION TIMES, (MEAN \pm 1SD) (Caixinha *et al.* 2014a).

It can be observed that, in healthy lenses, the m parameter values are close to 0 (Figure 6-9 (a)), while for lenses with total cataract the m parameter values are close to 1 (Figure 6-9 (d)). The m parameter behaviour indicates that the scatterers distribution evolves from a pre-Rayleigh to a Rayleigh distribution as the cataract progresses from incipient

to total cataract. These findings are in agreement with the works of Shankar and Tsui *et al.* (Shankar 2000; Tsui *et al.* 2006). Also, with cataract progression the m parameter increases deeper in the cortex region, revealing the presence of a larger number of scatterers from the cortex to the nucleus (Figure 6-9).

It should be noticed that the Nakagami m parameter estimation is affected by two components: the hardness of the tissue and the scatterers' concentration (Tsui *et al.* 2013). In cataract formation, where the increase of the hardness is related to the increase of fiber compaction and scatterers' concentration, the separation between these two components is difficult for the used cataract induction model.

6.3.4 Histological slices' images

The difference in protein aggregate's concentration and fiber compaction, in the nucleus and cortex regions of a cataractous lens, can be observed in microscopy images of transversal slices of the nucleo-cortex region (Figure 6-11).

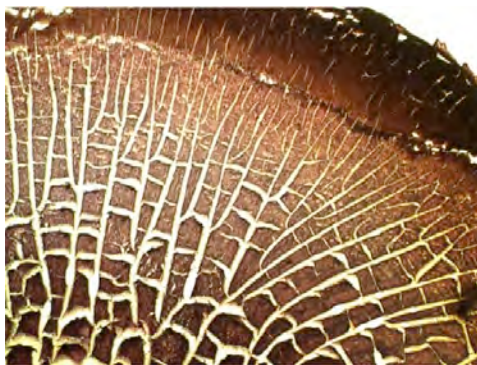


FIGURE 6-11. MICROSCOPY IMAGE OF A TRANSVERSAL SLICE OF THE NUCLEO-CORTEX REGION (Caixinha *et al.* 2014a).

Microscopy images for the nucleus and the cortex regions over the specified immersion times are shown in Figure 6-12. More pronounced dyeing was observed along the different immersion times, denoting a clear increase in protein aggregates and fiber compaction during the process of cataract formation. Such is in agreement with the decrease of images' brightness (normalized values¹⁷) observed for the different immersion times, in both cortex and nucleus regions (Figure 6-13). Moreover, for all immersion times the nucleus region showed a higher dyeing than the cortex region, indicating the presence of more protein aggregates and fiber compaction in this region of the lens. The results obtained with the microscopy images are in agreement with the ones obtained with the Nakagami images for different cataract degrees. A strong correlation was found between the mean brightness of the slices' images and the mean Nakagami m parameter in the cortex region ($r = -0.943$; $p = 0.029$) (Figure 6-14). No correlation was made for the nucleus due to the absence of backscattering signals for the whole extension of this region of the lens. Regarding

¹⁷ The brightness of the slices' images, originally in a scale ranging from 0 to 255 (eight bits of resolution), was normalized to a scale ranging from 0 to 1.

the mean brightness of the B-scan images, a statistically significant correlation was also found with the mean brightness of the slices' images ($r = -0.922$; $p = 0.039$).

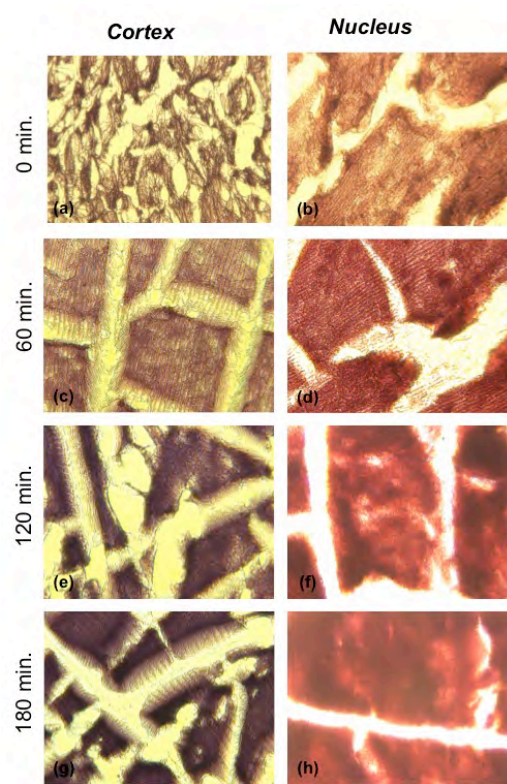


FIGURE 6-12. MICROSCOPY IMAGES OF THE LENSES' SLICES OVER THE DIFFERENT IMMERSION TIMES ((a) AND (b) 0 MINUTES; (c) AND (d) 60 MINUTES; (e) AND (f) 120 MINUTES; AND (g) AND (h) 180 MINUTES OF IMMERSION TIME) (Caixinha *et al.* 2014a).

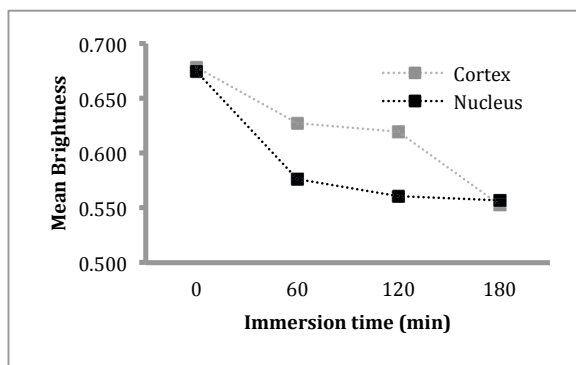


FIGURE 6-13. SLICES' IMAGES MEAN BRIGHTNESS FOR THE CORTEX AND THE NUCLEUS REGIONS FOR DIFFERENT IMMERSION TIMES, MEAN VALUES (Caixinha *et al.* 2014a).

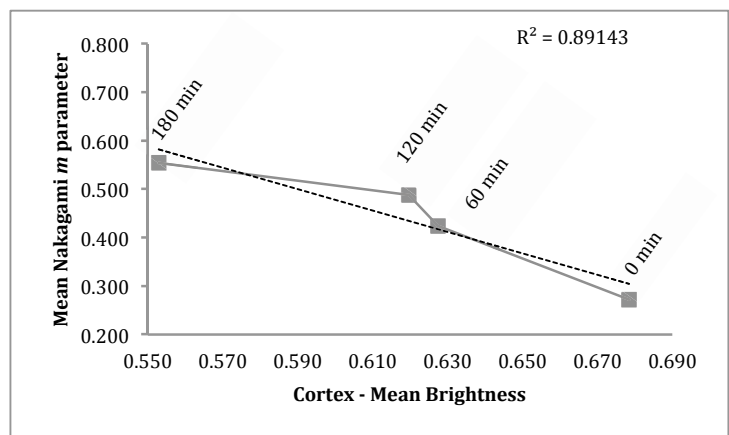


FIGURE 6-14. MEAN NAKAGAMI m PARAMETER VERSUS CORTEX IMAGES MEAN BRIGHTNESS (FOR THE DIFFERENT IMMERSION TIMES), MEAN VALUES (Caixinha *et al.* 2014a).

6.3.5 Predictive features for cataract severity

The CRT was performed considering the two acoustical parameters (velocity and attenuation), the B-scan mean brightness and the mean Nakagami m parameter. Additionally, to account for the dispersion of the brightness values in the B-scan image and the spreading of the m parameter values in the Nakagami image, the variance of the brightness and the variance of the m parameter for the same ROI were considered.

Eighty-seven percent (87.1%) of the lenses were correctly predicted by the CRT, with a risk estimate¹⁸ of 25.2% (Figure 6-15). A good discrimination was found between lenses without cataract and lenses with cataract. Seventy-three percent (72.6%) of the lenses without cataract are characterized by a mean brightness of the B-scan images ≤ 0.351 , a variance of the brightness of the B-scan images ≤ 0.070 , a velocity ≤ 1625 m/s and an attenuation ≤ 0.415 dB/mm MHz. Lenses with cataract are characterized by a mean brightness of the B-scan images > 0.351 , being the remaining discriminating factors the variance and the mean value of the Nakagami m parameter. Lenses with incipient cataract are characterized by a variance of the m parameter in the Nakagami image > 0.110 , or when the variance is lower than 0.110, by a mean value of the m parameter ≤ 0.374 . Lenses with advanced cataract are characterized by a value of the variance of the Nakagami m parameter lower than 0.110 and a mean value of the m parameter higher than 0.374.

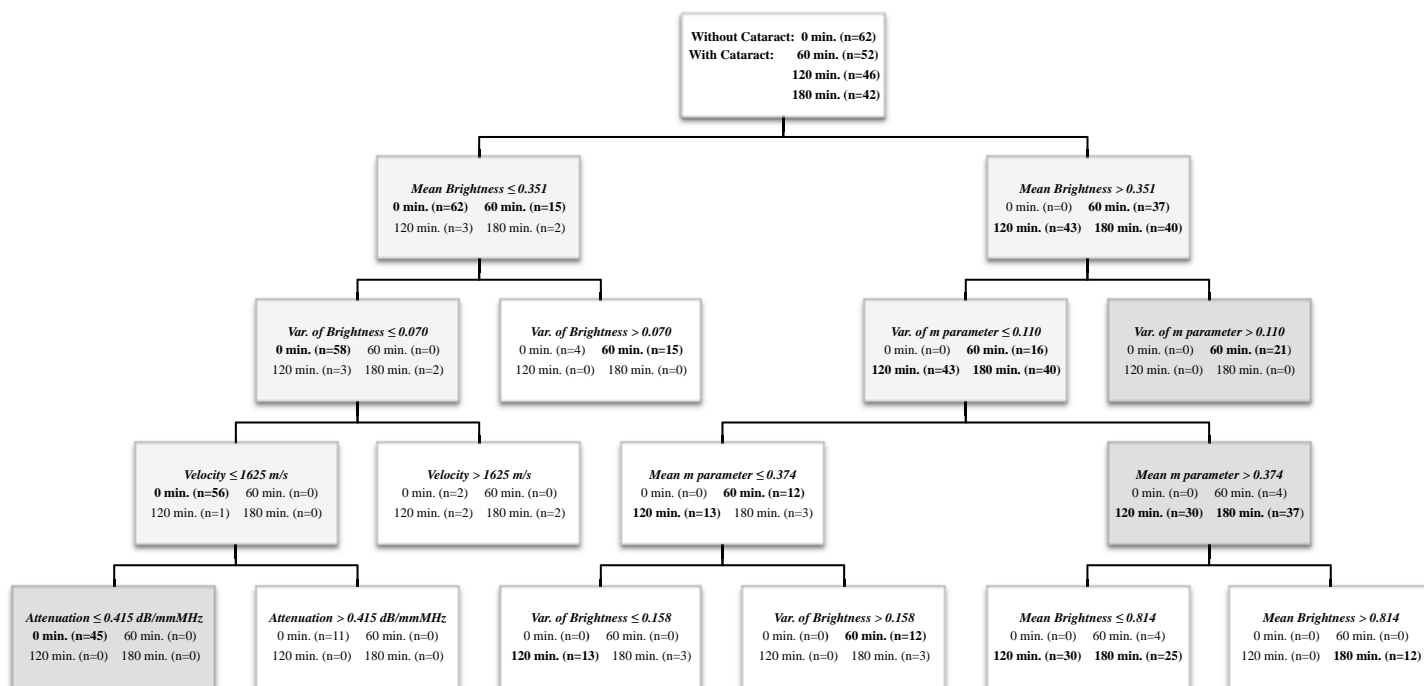


FIGURE 6-15. PRINCIPAL NODES OF THE CRT FOR CATARACT CHARACTERIZATION (Caixinha *et al.* 2014a).

¹⁸ The risk estimate is a measure of accuracy. For the CRT the risk estimate is the proportion of cases incorrectly classified after adjustment for *prior* probabilities and misclassification costs.

The cut-off values obtained by the CRT for the characterization of the lenses without cataract, classify 157 lenses with cataract and 45 lenses without cataract (Table 6-3). The mean and variance of the B-scan brightness, and the velocity and/or the attenuation values allow for a sensitivity of 1.000 for the presence of cataract (all the lenses with cataract are correctly classified) and a specificity of 0.726 (*i.e.*, for the classification of lenses without cataract). The low mean value and the lower variance of the m parameter for lenses without cataract is due to the absence of scatters in lenses without cataract and therefore the m parameter does not appear as a discriminating factor for lenses without cataract.

TABLE 6-3. CLASSIFICATION OF LENSES WITH OR WITHOUT CATARACT (Caixinha *et al.* 2014a).

	Cataract	No Cataract	TOTAL
Lenses with cataract (60, 120 or 180 minutes of immersion time)	<u>140</u>	0	140
Lenses without cataract (0 minutes)	17	<u>45</u>	62
TOTAL	157	45	202

A variance of the m parameter > 0.110 and a mean value of the m parameter > 0.374 allowed discriminating lenses with cataract with a sensitivity of 0.784, for the more severe stages of cataract formation, and a specificity of 0.865, for the incipient stages of cataract formation (Table 6-4).

TABLE 6-4. CLASSIFICATION OF SEVERE (ADVANCED AND TOTAL) OR INCIPIENT CATARACT (Caixinha *et al.* 2014a).

	Severe Cataract	Incipient Cataract	TOTAL
Lenses with severe cataract (advanced and total cataract, 120 and 180 minutes of immersion time, respectively)	<u>69</u>	19	88
Lenses with incipient cataract (60 minutes of immersion time)	7	<u>45</u>	52
TOTAL	64	76	140

6.3.6 Automatic cataract classification

6.3.6.1 Extracted features significance

Considering the 97 extracted features, the univariate analysis showed that most of the extracted features from the A-scan and backscattering signals were statistically different between healthy and cataractous lenses and between incipient and advanced cataract (p -values, Figure 6-16).

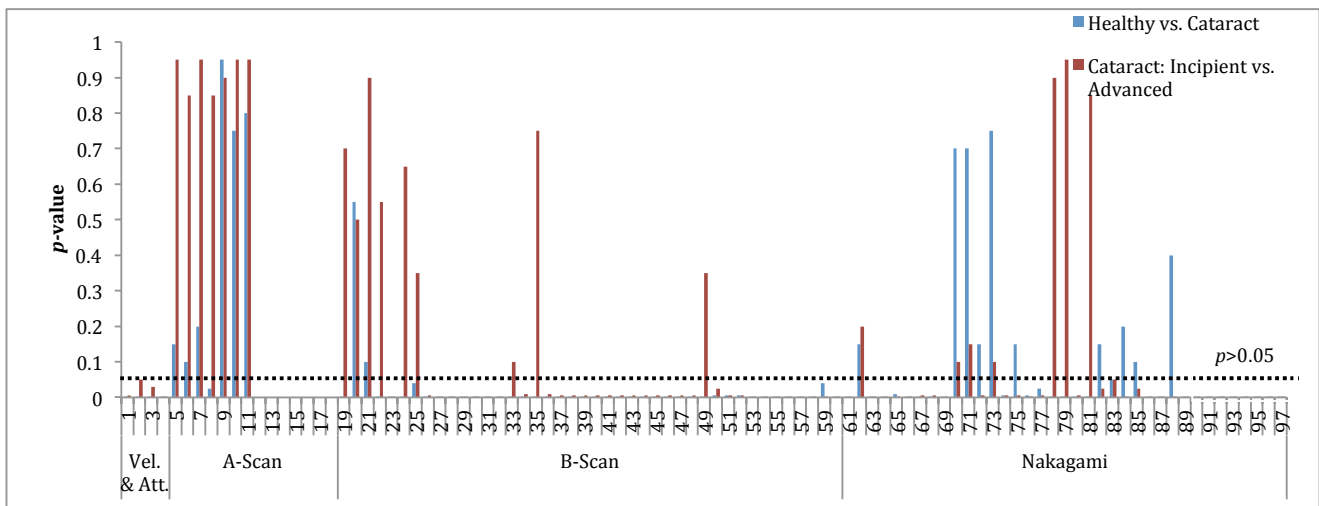


FIGURE 6-16. P-VALUES FOR THE 97 EXTRACTED FEATURES FROM THE A-SCAN AND BACKSCATTERING SIGNALS (STATISTICALLY SIGNIFICANT FEATURES HAD A P-VALUE < 0.05) (Caixinha *et al.* 2015a).

6.3.6.2 Binary classification

The average F-measure for the different classifiers (Naive Bayes, KNN, FLD and SVM) shows that 2 components obtained by PCA allow the highest discrimination between healthy and cataractous lenses (F-measure = 0.950), while 9 components are needed to achieve the highest discrimination between incipient and advanced cataract (F-measure = 0.912) (Figure 6-17).

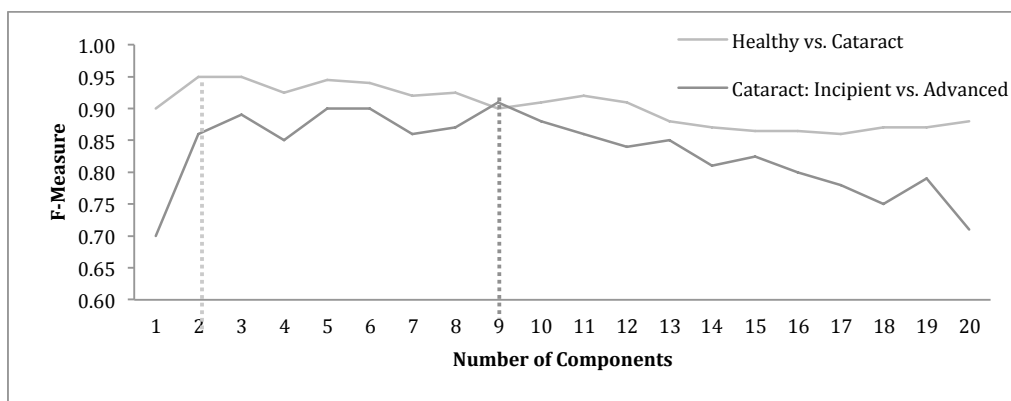


FIGURE 6-17. AVERAGE F-MEASURE OF THE 4 CLASSIFIERS FOR THE FIRST 20 COMPONENTS OBTAINED BY PCA (Caixinha *et al.* 2015a).

All the classifiers showed a good performance for the classification into healthy or cataractous lenses (F-measure \geq 0.927, Table 6-5). Higher sensitivity was found for the KNN and SVM classifiers (0.957 and 0.950, respectively), while higher specificity was found for the KNN and FLD classifiers (0.855 and 0.851, respectively).

For the classification into incipient and advanced cataract, only the SVM classifier achieved a good performance (F-measure = 0.906, Table 6-6), with a sensitivity and specificity of 0.983 and 0.806, respectively. For the remaining

classifiers (Naive Bayes, KNN and FLD), the performance was lower than 0.798 (FLD), being the sensitivities and specificities lower than 0.814 and 0.783 (FLD).

TABLE 6-5. CLASSIFIERS PERFORMANCE FOR THE CLASSIFICATION INTO HEALTHY OR CATARACTOUS LENSES USING 2 COMPONENTS (Caixinha *et al.* 2015a).

	Precision	Specificity	Sensitivity	Accuracy	F-Measure
Naive Bayes	0.924	0.761	0.940	0.896	0.932
KNN	0.953	0.855	0.957	0.932	0.955
FLD	0.949	0.851	0.906	0.892	0.927
SVM	0.932	0.787	0.950	0.910	0.941

TABLE 6-6. CLASSIFIERS PERFORMANCE FOR THE CLASSIFICATION INTO INCIPIENT OR ADVANCED CATARACTOUS LENSES USING 9 COMPONENTS (Caixinha *et al.* 2015b).

	Precision	Specificity	Sensitivity	Accuracy	F-Measure
Naive Bayes	0.712	0.711	0.737	0.724	0.725
KNN	0.701	0.690	0.752	0.721	0.756
FLD	0.783	0.783	0.814	0.798	0.798
SVM	0.840	0.806	0.983	0.896	0.906

6.3.6.3 Multiclass classification

The highest F-measure was found for 15 components obtained by PCA (F-measure = 0.950, Figure 6-18).

The average performance of the multiclass SVM was of 0.845 (F-measure, Table 6-7). The average sensitivity and specificity were 0.846 and 0.923, respectively.

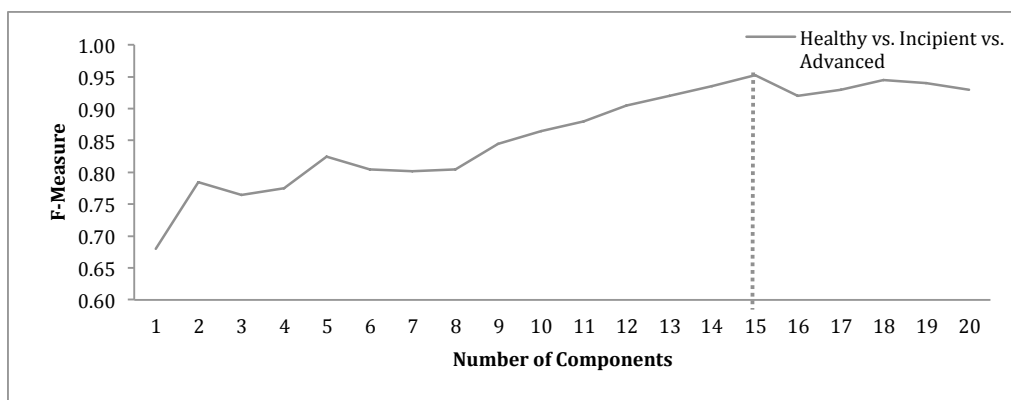


FIGURE 6-18. F-MEASURE OF THE MULTICLASS CLASSIFIER FOR THE FIRST 20 COMPONENTS OBTAINED BY PCA.

Ninety-two percent (91.8%) of the extracted features from healthy lenses were correctly classified (the sensitivity was 0.864 and the specificity 0.948, Table 6-7). Ninety-two percent (92.2%) of the extracted features from lenses with incipient cataract were correctly classified (the sensitivity was 0.891 and the specificity 0.935, Table 6-7). Eighty-five percent (85.1%) of the extracted features from lenses with advanced cataract were correctly classified (the sensitivity was 0.785 and the specificity 0.885, Table 6-7).

TABLE 6-7. AVERAGE PERFORMANCE FOR THE MULTICLASS SVM CLASSIFICATION USING 15 COMPONENTS (Caixinha *et al.* 2014b).

	Precision	Specificity	Sensitivity	Accuracy	F-Measure
Healthy lenses	0.902	0.948	0.864	0.918	0.882
Incipient cataract	0.858	0.935	0.891	0.922	0.874
Advanced cataract	0.778	0.885	0.785	0.851	0.781
Weighted average	0.847	0.923	0.846	0.897	0.845

6.4 Conclusions

6.4.1 Characterization of the cataractous lens

This study aimed to understand how acoustical parameters as the propagation velocity and frequency-dependent attenuation changed with the cataract progression. In addition, to visualize the cataract progression, B-scan and Nakagami images were constructed by analyzing the lens backscattering signals, and, to provide a classification of the cataract severity, several features were extracted from the lens collected signals and classified using Naive Bayes, KNN, FLD and SVM classifiers.

It was shown in this work that the velocity and frequency-dependent attenuation increase significantly with the cataract progression. The B-scan images presented more brightness areas with cataract progression as a result of the increased scatterers concentration from the cortex to the nucleus, which is responsible for lens opacity. This was also demonstrated by analysing the Nakagami images, where the m parameter increased over the cataract progression. The cataract progression pattern, observed in the B-scan and Nakagami images is a result of the used method for cataract induction. The m parameter behaviour indicated that the scatterers distribution evolves from a pre-Rayleigh to a Rayleigh distribution as the cataract progresses from incipient to total. Also, with cataract progression the m parameter increased deeper in the cortex region, revealing the presence of a larger number of scatterers from the cortex to the nucleus.

6.4.2 Automatic cataract classification based on the extracted features

It was shown that machine learning techniques can be useful for the automatic classification of the cataract severity, based on the features extracted from the ultrasound signals.

Concerning the used classifiers, the results showed that the multiclass SVM presented the best performance for the cataract classification, providing an objective discrimination of the cataract severity levels. Thus, the results of using classifiers, in particular the multiclass SVM, proved that the ultrasound velocity and attenuation combined with the backscattering signal analysis, characterized in terms of the B-scan and Nakagami imaging allow for a good discrimination of the different cataract degrees and appear as a good alternative to the clinical classification systems currently used.

6.5 Resulting publications

The following papers were published (section PUBLICATIONS):

- Characterization of scatterers concentration in cataractous lens using Nakagami distribution by ultrasounds. Caixinha, M.; Jesus, D.; Santos, M.; Santos, J.; Velte, E. 2013 IEEE International Ultrasonics Symposium (IUS). 2013; 425-428 (DOI: 10.1109/ULTSYM.2013.0110).
- Using ultrasound backscattering signals and Nakagami statistical distribution to assess regional cataract hardness. Caixinha, M.; Jesus, D.; Velte, E.; Santos, M.; Santos, J. IEEE Transactions on Biomedical Engineering. 2014; 61(12): 2921-2929 (DOI: 10.1109/TBME.2014.2335739).
- New approach for objective cataract classification based on ultrasound techniques using multiclass SVM classifiers. Caixinha, M.; Velte, E.; Santos, M.; Santos, J. 2014 IEEE International Ultrasonics Symposium (IUS). 2014; 2402-2405 (DOI: 10.1109/ULTSYM.2014.0599).
- Automatic cataract classification based on ultrasound techniques using machine learning: A comparative Study. Caixinha, M.; Velte, E.; Santos, M.; Perdigão, F.; Amaro, J.; Gomes M.; Santos, J. 2015 ICU International Congress on Ultrasonics, Abstract Book.
- Automatic cataract hardness classification *ex vivo* by ultrasound techniques. Caixinha, M.; Santos, M.; Santos J. Ultrasound in Medicine and Biology. 2015; 1-10 (DOI: 10.1016/j.ultrasmedbio.2015.11.021).
- Machine learning techniques in clinical vision sciences. Caixinha M. and Nunes S. Current Eye Research. 2016; (DOI: 10.1080/02713683.2016.1175019).

7 *IN VIVO* CATARACT DETECTION, AUTOMATIC CLASSIFICATION AND HARDNESS ESTIMATION

7.1 Objective and study description

After the *ex vivo* analysis, this study aimed to demonstrate that the ultrasound technique can be used to early detect nuclear cataract *in vivo*, classify its severity, and estimate its hardness.

A 20 MHz ophthalmic single element transducer was used to acquire acoustical signals (A-scan) in rats' eyes with different nuclear cataract severity levels. For this purpose, an animal model for nuclear cataract that mimics what happens in human age-related cataract was developed.

Three different approaches for signals collection were considered to validate the setup for *in vivo* cataract detection and classification: *in vivo*, *post mortem* and *ex vivo*, to demonstrate that the eye movements' *in vivo* and the eventual probe misalignment with the free-hand acquisition mode would not affect the classification results.

In order to classify the different cataract severity levels, algorithms were first developed for automatic detection of ocular boundaries and for early cataract detection, using the signals collected from the eyes. Then, 27 features in time and frequency domain, were extracted from the rats' eyes A-scan signals, and used to train and test different classifiers, in order to identify healthy and cataractous lenses, as well as automatically classify nuclear cataract according to the following degrees: incipient (early stage), moderate, and severe.

To correlate the extracted features with the lens hardness and to demonstrate that the hardness can be noninvasively estimated, the hardness of the nucleus and cortex regions was objectively measured in 12 rats, using the NanoTestTM technology. The lens elasticity was also obtained.

The developed animal model and the defined methodology were used to study *in vivo* the nuclear cataract with different degrees of severity, and estimate its hardness using the ultrasound technique. As the B-scan and Nakagami images are difficult to construct *in vivo* with a free-hand acquisition (as explained in the B-scan image section 4.3.1), they were not considered in this study.

This work also led to the development of a medical device prototype for the automatic cataract detection and classification, and its hardness estimation. The prototype, when applied to humans could be a useful tool to support cataract surgery and clinical practice.

7.2 Materials and methods

7.2.1 Animal model for nuclear cataract

Wistar rats were used for nuclear cataract induction by sodium selenite (Na_2SeO_3) overdose. This animal model is an extremely rapid and convenient model for nuclear cataract, being currently used in cataract research since that type of induced cataract mimics well the human age-related cataract (Kyselova 2010; Shearer *et al.* 1997).

In order to obtain different nuclear cataract degrees, the animal model created by Oštádalová *et al.* (Oštádalová *et al.* 1977) was modified in this work, and a pilot study in six rats was conducted. The rats were injected with three different concentrations of sodium selenite at two different periods of eyes' maturation, namely before and after eyes opening, at day 11 and day 15, respectively. All the rats were followed weekly and after the 4th month the rats were examined with a modified slit-lamp, for observing the different cataract severity levels. A minimum follow-up period of 4 months was considered.

7.2.1.1 Sample size

The sample size for this study was estimated based on the results obtained in the proof-of-concept study for the ultrasound velocity and frequency-dependent attenuation. The G*Power software version 3.1 was used (Faul *et al.* 2007; Faul *et al.* 2009).

Considering the mean values found for the ultrasound velocity and frequency-dependent attenuation for healthy and incipient cataractous lenses, a sample size of 12 lenses per group was estimated for a statistical power of 90%, an alpha-level of 0.05, and an effect size (*i.e.*, the difference between the mean values of the healthy and the incipient cataractous lenses, divided by the standard deviation) of 1.4 and 1.6, respectively. A minimum of 12 rats for the healthy lens group and 36 for the cataractous lenses group (incipient, moderate and severe cataract) was therefore considered.

7.2.1.2 Animals' ethical considerations

All the experiments of this study were carried out in accordance with the European regulation on the protection of animals used for scientific purposes (Directive 2010/63/EU). The experiments were approved by the National Directorate General of Food and Veterinary Medicine (Direção-Geral de Alimentação e Veterinária – DGVA), and by the Animal Welfare Office of the University of Coimbra (Órgão para o Bem Estar Animal – ORBEA). The animal experiments were made in order to minimize its suffering.

7.2.2 Experimental procedures

7.2.2.1 Animal model

Fifty (50) rats, males and females, with ages ranging from 4 to 10 months (mean age of 4.8 ± 2.5 months), were used in this study. Fourteen (14) were used as control and 36 as study group. Eighteen rats were injected at day 11 (before eyes opening) and 18 rats were injected at day 15 (after eyes opening). Then, the rats were divided in subgroups of 6 rats, each group was injected with 20, 25 and 30 $\mu\text{mol/kg}$ of sodium selenite, respectively (Figure 7-1).

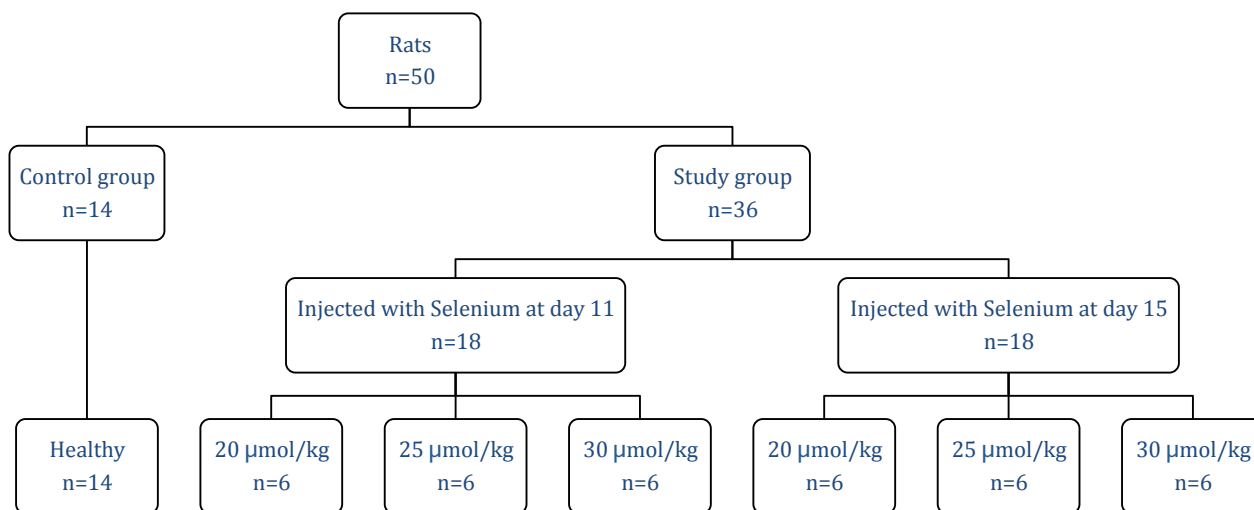
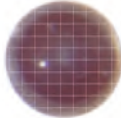
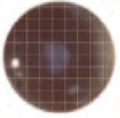
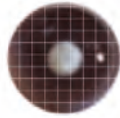


FIGURE 7-1. NUMBER OF RATS USED IN THE *IN VIVO* STUDY.

The rats' eyes were analysed with a modified slit lamp, in order to identify possible changes in the transparent media, and to detect other type of lens' opacities. The images from the cataract were acquired with a digital camera keeping the magnification and the focal length fixed. Since there is no image database for rats to classify the cataract severity according to the classification system LOCS III, a standardized grid was projected onto the acquired digital images to assist the manual classification (Table 7-1). The cataract severity was thereafter classified in 3 types, according to the transparency and the area occupied by the opacity in the entire lens (in accordance with the LOCS III that is based on the opalescence of the nuclear cataract). The approach consisted of counting the squares occupied by the opacity. Thus, based on the area, appearance and shape of the opacity, the cataract was labelled as incipient, when a small and diffuse opacity was observed; moderate, when a diffuse opacity with well-defined borders occupying approximately half of the lens was observed; and severe, when a well-defined opacity, occupying approximately half of the lens was observed. Table 7-1 illustrates the three cataract severity levels.

TABLE 7-1. CLASSIFICATION CRITERIA FOR THE 3 LEVELS OF CATARACT SEVERITY.

Incipient cataract	Moderate cataract	Severe cataract
		
Small and diffuse opacity	Diffuse opacity with well-defined borders occupying approximately half of the lens	Well-defined opacity, occupying approximately half of the lens

7.2.2.2 Hardness and elasticity measurements

The hardness is an important biomechanical property of a tissue. It measures the resistance of a tissue when a compressive force is applied and can be measured by indentation hardness techniques.

The nanoindentation hardness is a technique used to measure hardness in small volumes. In this work the NanoTest™ (Micro Materials Ltd, Wrexham, UK, Figure 7-2) was used to measure two important biomechanical properties of the crystalline lens, the hardness and the Young’s modulus (elasticity) (Beake *et al.* 2002).

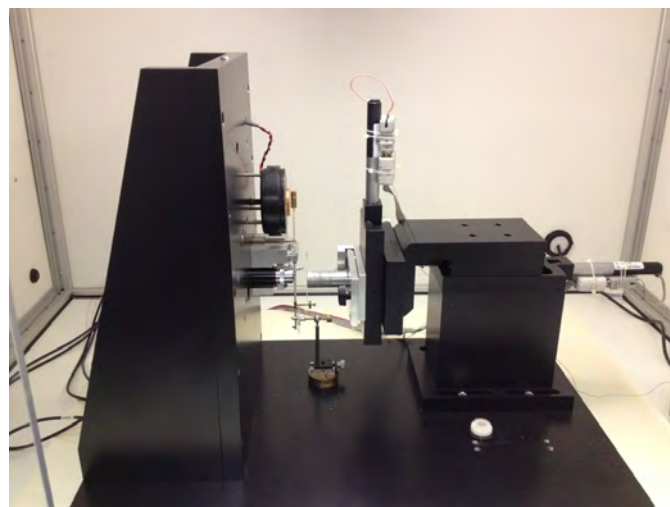


FIGURE 7-2. MICRO MATERIALS LDT WREXHAM, U.K. NANOTEST™.

The nanoindentation technique uses a hard tip (indenter) with known mechanical properties that is pressed into the sample whose properties are unknown (in this work the hard tip was of diamond). The load placed on the indenter tip is increased as the tip penetrates further into the sample until a predefined value, or until reaching its maximum, where the load may be constant or removed (Figure 7-3) (de la Rosa-Fox *et al.* 2007; Fischer-Cripps 2011; Panich and Yong 2005). In this study, the maximum loading was used. Nanoindentation allows indenting on the nanoscale with a very precise tip shape and high spatial resolutions in placing the indents. Small loads and tip sizes are used,

and the indentation area is a few square micrometres or even nanometres.

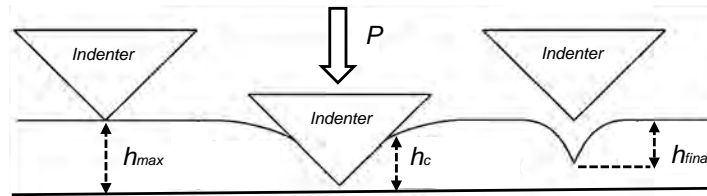


FIGURE 7-3. ILLUSTRATION OF THE NANOINDENTATION TEST (h_{max} : SAMPLE THICKNESS; h_c : CONTACT DEPTH; AND h_{final} : RESIDUAL INDENTATION DEPTH).

The area of the residual indentation in the sample is measured and the hardness, H , is defined as the maximum load, P_{max} , divided by the residual indentation area, A_r ,

$$H = \frac{P_{max}}{A_r} \quad (7-1)$$

An indenter with a known geometry is used to estimate the indentation area. In this work, a Berkovich tip was used, with a three-side pyramid geometry, as shown in Figure 7-4.



FIGURE 7-4. IMAGE OF AN INDENT LEFT BY A BERKOVICH TIP IN THE NUCLEUS REGION OF A RAT'S LENS.

During the nanoindentation test, the load and depth of penetration are recorded and the indentation area is determined using the known geometry of the indentation tip. The load-displacement curve (Figure 7-5) is then used to extract the biomechanical properties of the tissue as the hardness and the reduced Young's modulus.

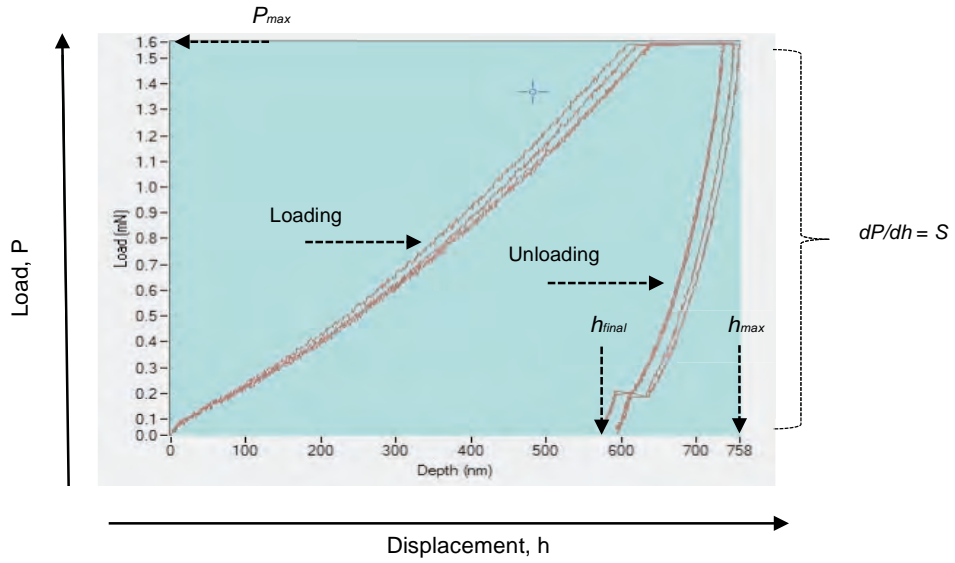


FIGURE 7-5. LOAD-DISPLACEMENT CURVES FOR A NANOINDENTATION TEST WITH 6 INDENTATIONS IN THE CORTEX REGION OF A HEALTHY RAT’S LENS.

The slope of the unloading curve, dP/dh , is the stiffness, S , of the tissue (*i.e.*, the extent to which the tissue resists in response to the applied force). For a pyramidal analysis (Berkovich tip) the depth *versus* the unloading curve is fitted by a known power law fit (Oliver and Pharr 1992).

The stiffness, which includes the contribution from both the tissue being tested and the response of the test device itself, is used to calculate the reduced Young's modulus, E_r , using the following expression,

$$E_r = \frac{1}{B} \frac{\sqrt{\pi}}{2} \frac{S}{\sqrt{A_p(h_c)}} \tag{7-2}$$

where $A_p(h_c)$ is the projected area of the indentation at the contact depth h_c , and B is a geometrical constant of unity order. In this work, $A_p(h_c)$ was approximated by a polynomial fitting for the Berkovich tip (Beake *et al.* 2002).

If the sample’s Poisson’s ratio is known, the reduced modulus, E_r , can be converted to the Young’s modulus of the test sample (lens tissue, E_{lens}) by using the following expression (Beake *et al.* 2002),

$$\frac{1}{E_r} = \frac{(1 - \nu_{lens}^2)}{E_{lens}} + \frac{(1 - \nu_{indenter}^2)}{E_{indenter}} \tag{7-3}$$

where: $\nu_{indenter}$ is the indenter Poisson’s ratio (for a diamond indenter tip, $\nu_{indenter} = 0.07$); $E_{indenter}$ is the indenter Young’s modulus (for a diamond indenter tip, $E_{indenter} = 1141 \text{ GPa}$); ν_{lens} is the lens Poisson’s ratio; and

E_{lens} is the lens Young's modulus. Given the indenter parameters, the Young's modulus for the crystalline lenses is given by,

$$E_{lens} = \frac{(1 - \nu_{lens}^2)}{\left(\frac{1}{E_r} - \frac{(1 - 0.07^2)}{1141}\right)} \quad (7-4)$$

The Poisson ratio (ν), or coefficient of expansion, is the expansion fraction divided by the compression fraction when a tissue is compressed in one direction. For stable, isotropic and linear elastic tissues the Poisson's ratio ranges from 0 to 0.5 (in some materials that shrink in the transverse direction when compressed, negative values may occur). For soft tissues the Poisson's ratio ranges from 0.45 to 0.49 (Chen *et al.* 1996). A perfectly incompressible tissue deformed elastically at small strains will have a Poisson's ratio of 0.5, while a tissue showing very little lateral expansion when compressed will have a Poisson's ratio close to 0.

Due to the complexity of the experimental measurements in tissues, there are few publications on soft tissue properties. So, for soft tissues, namely for the crystalline lens, a linear elastic and isotropic material model is considered in the literature, with a Poisson's ratio close to 0.5, *i.e.*, a nearly incompressible tissue due to the water content that is predominant. The following works in biological soft tissues were found in the literature (Battaglioli and Kamm 1984; Bocskai and Bojtár 2013; Burd *et al.* 2002; Fisher 1969; Fisher 1971; Gefen *et al.* 2009; Hermans *et al.* 2007; Hermans *et al.* 2008; Hollman *et al.* 2007; Hozic *et al.* 2012; McKee *et al.* 2011; Uchio *et al.* 1999; Weeber *et al.* 2005; Weeber *et al.* 2007; Weeber and van der Heijde 2008). The few experimental measurements available in the literature demonstrated that the eye Poisson's ratio is near to 0.5, ranging from 0.42 to 0.48 (Table 7-2).

TABLE 7-2. POISSON'S RATIO MEASURED IN THE HUMAN EYE.

Eye structure	Poisson's ratio [mean (minimum; maximum)]	Author
Cornea	0.42 (0.395; 0.445)	Uchio <i>et al.</i> (Uchio <i>et al.</i> 1999)
Sclera	0.47 (0.455; 0.480)	Uchio <i>et al.</i> (Uchio <i>et al.</i> 1999)
	0.478 (0.460; 0.500)	Battaglioli and Kamm (Battaglioli and Kamm 1984)
Lens Capsule	0.47	Fisher (Fisher 1969)

In this work, Poisson's ratios of 0.49 for both the cortex and nucleus were considered (Burd *et al.* 2002; Schumacher *et al.* 2007).

To demonstrate that the different induced cataract have different hardnesses, 12 lenses (3 without cataract, 3 with incipient cataract, 3 with moderate cataract, and 3 with severe cataract), were submitted to hardness tests, using

nanindentation technique (NanoTest™ from Micro Materials Ltd, Wrexham, United Kingdom – UK) (Panich and Yong 2005). For the samples preparation, the lenses were first frozen at -40 °C in an embedding resin, Cryomatrix Shandon medium (Thermo Scientific Shandon Ltd, WA, USA) and then cut transversally with a glass knife using a Leica Microsystems CM3350S cryostat (Leica Microsystems, Wetzlar, Germany). The sample nanohardness measurement requires that the tissue has a regular surface and a thickness such that the penetration depth of the indentation does not have a radius less than 10% of the total tissue thickness to avoid the substrate effect (Fischer-Cripps 2011). Experimentally, and after analysing the samples with an optical microscope, it was found that the most regular surfaces of the lens tissue were obtained when cuts were made with 50 µm in thickness at -20 °C. Based on this result, several slices were made in two regions of the lens (cortex and nucleus). Six indentations were performed in each analysed region and the average value was considered as the mean hardness of the lens in that region¹⁹. The NanoTest™ data analysis software produced automatically the hardness and the reduced Young's modulus of the lens tissue in the nucleus and cortex (Beake *et al.* 2002).

7.2.2.3 Ultrasound signal acquisition

Three different approaches for ultrasound signal collection were considered: *in vivo*, *post mortem* and *ex vivo*, as shown in Figure 7-6 and Figure 7-7. The objective was to demonstrate that the eye movements, and the eventual probe misalignment in relation to the ocular surface that can happen *in vivo*, do not affect the classification results.

Before the *in vivo* acquisition, the rats were anesthetized with an intraperitoneal ketamine hydrochloride injection (75 mg/kg), and their pupils were dilated with 10% phenylephrine hydrochloride eye drops. After the *in vivo* acquisition, the rats were sacrificed by cervical dislocation, and their eyes were enucleated. The eye axial length, and the lens anteroposterior and equatorial diameters were measured using a calliper.

One eye per rat was selected randomly for the *in vivo*, *post mortem* and *ex vivo* ultrasound signal acquisitions, and the other eye was used for the NanoTest™ measurements.

A 20 MHz single element ophthalmic probe (Imasonic, SAS, France), complying with the essential requirements for safety and effectiveness laid down in the Medical Devices Directive 93/42/EEC (European Union) and the international standards IEC 60601 and 61157 (International Electrotechnical Commission 1992; International Electrotechnical Commission 2005) was used. The probe had a focal length of 8.9 mm and an active diameter of 3 mm and was excited using a pulser/receiver (model Compact Pulser, Ultratek, CA, USA) with a 1 kHz pulse repetition frequency (PRF) and a bandwidth of 100 MHz. The probe characteristics are summarized in Table 7-3. The A-scan signals were collected and sampled using the same acquisition board described in Chapter 5 (section 5.2.2). A digital oscilloscope (model TDS 3032, Tektronix Inc., TX, USA) was used to display the signals during the acquisitions. The experimental setup is shown in Figure 7-8. Signal processing was carried out in Matlab (MathWorks Inc., MA, USA).

¹⁹ For statistical purposes it is recommended to acquire between 5 to 10 indentation curves under the same parameters (Beake *et al.* 2002).

TABLE 7-3. TRANSDUCER CHARACTERISTICS (IMASONIC, SAS, FRANCE).

Probe characteristics	
Type	Ophthalmic probe
Active element (piezocomposite material)	⊙ 3.2 mm
Frequency	20 MHz
Bandwidth	15.8 MHz ($\geq 55\%$ at -6 dB)
Focal length	8.9 mm
Pulse length	61.4 ns at -6 dB
Axial resolution	4.9 μm
Lateral resolution	224 μm

On the *in vivo* and *post mortem* acquisitions, a custom-made buffer, filled with an isotonic PBS solution, was used for eye-probe coupling, as shown in Figure 7-6. On the *ex vivo* acquisitions, the eyes were enucleated from the orbital cavity and placed on a holder, with a machined hole matched to the lens, immersed in the PBS solution with the temperature kept constant (at $28.0 \pm 0.5^\circ\text{C}$). The probe was attached to a micropositioning system, allowing its precise positioning over the eye surface, therefore improving the collected signals (Figure 7-7).



FIGURE 7-6. *IN VIVO* AND *POST MORTEM* ACQUISITIONS (Caixinha *et al.* 2016).

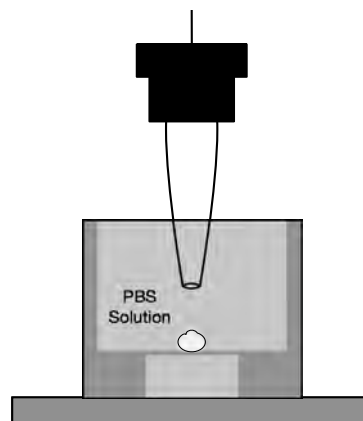


FIGURE 7-7. *EX VIVO* ACQUISITIONS (Caixinha *et al.* 2016).

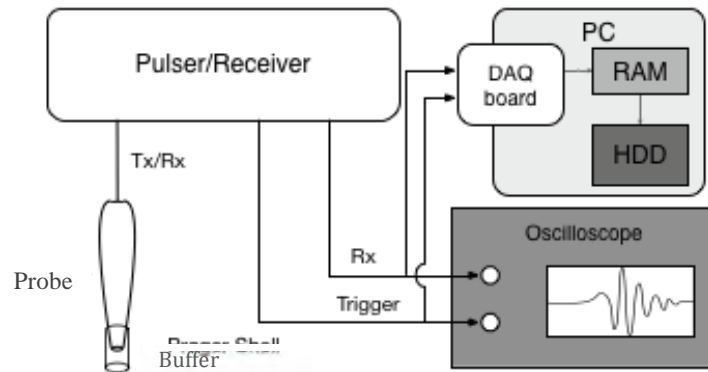


FIGURE 7-8. SETUP FOR DATA ACQUISITION (T_x : TRANSMIT; R_x : RECEIVE; HDD: HARD DISK DRIVE; RAM: RANDOM ACCESS MEMORY) (Caixinha *et al.* 2016).

An A-scan signal, illustrating the ultrasound propagation over the ocular boundaries, is shown in Figure 7-9. High amplitude reflections are observed at the anterior and posterior corneal surfaces as well as at the anterior lens capsule. A strong echo is also observed when cataract is present. The echo originating from the posterior lens capsule has low amplitude as the ones from retina, choroid and periorbital fat.

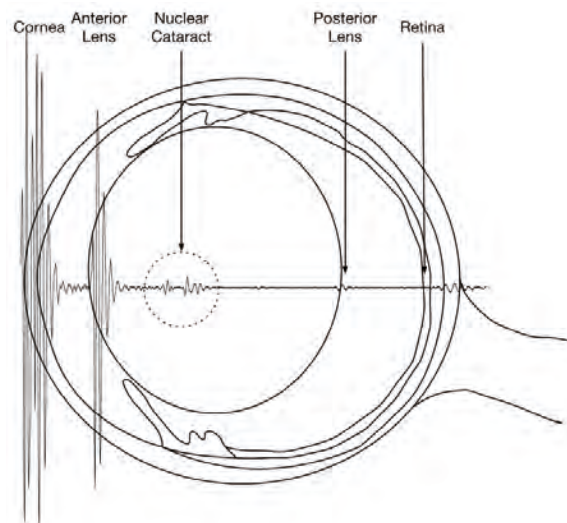


FIGURE 7-9. ILLUSTRATION OF AN A-SCAN SIGNAL FOR A CATARACTOUS LENS.

7.2.2.4 Signal Processing

7.2.2.4.1 Automatic detection of ocular interfaces

Signal conditioning and denoising was carried out before the detection of the ocular interfaces. A linear phase passband filter with cut-off frequencies of 1 MHz and 50 MHz was applied to the signal, in order to select the frequencies of interest and minimize the noise. Then, to improve the signal-to-noise ratio (SNR), 20 A-scans were averaged, corresponding to an averaging period of 20 ms (according to the PRF).

Several algorithms were developed for the automatic detection of the ocular interfaces. They are described in pseudo-code in Figure 7-10, along with illustrations of their implementation over the signal waveform. The propagation time was used for the definition of the different regions of the ocular interfaces searching process. It was assumed that the distances between the corneal and lens interfaces are known (Hughes 1979), and considered a mean propagation velocity of 1600 m/s and 1650 m/s, for healthy and cataractous lenses, respectively (Caixinha *et al.* 2014a). The t_c time, corresponding to the anterior cornea interface, whose calculation is illustrated in Figure 7-10, is used as a relative reference for the determination of the time position of the remaining ocular interface occurrences.

In order to find t_c , a search window over the entire A-scan signal was considered, taking as reference the emission pulse, t_p . This is located in the time instant corresponding to highest absolute amplitude value of the A-scan. The search region for t_c starts at $t_p + 3 \mu\text{s}$ (with $3 \mu\text{s}$ being a safe margin to avoid any disturbance by the emission pulse), enabling successful detection for both approaches of Figure 7-6 and Figure 7-7. The anterior cornea interface detection comprises two steps: first, the position of the maximum absolute value of the signal in the search region is located, max_pos ; second, starting at the sample $\text{max_pos}-20$ (20 samples correspond to $0.1 \mu\text{s}$, *i.e.*, the average duration of the corneal echo), the first sample above a threshold, defined as the signal's standard deviation (std), is searched.

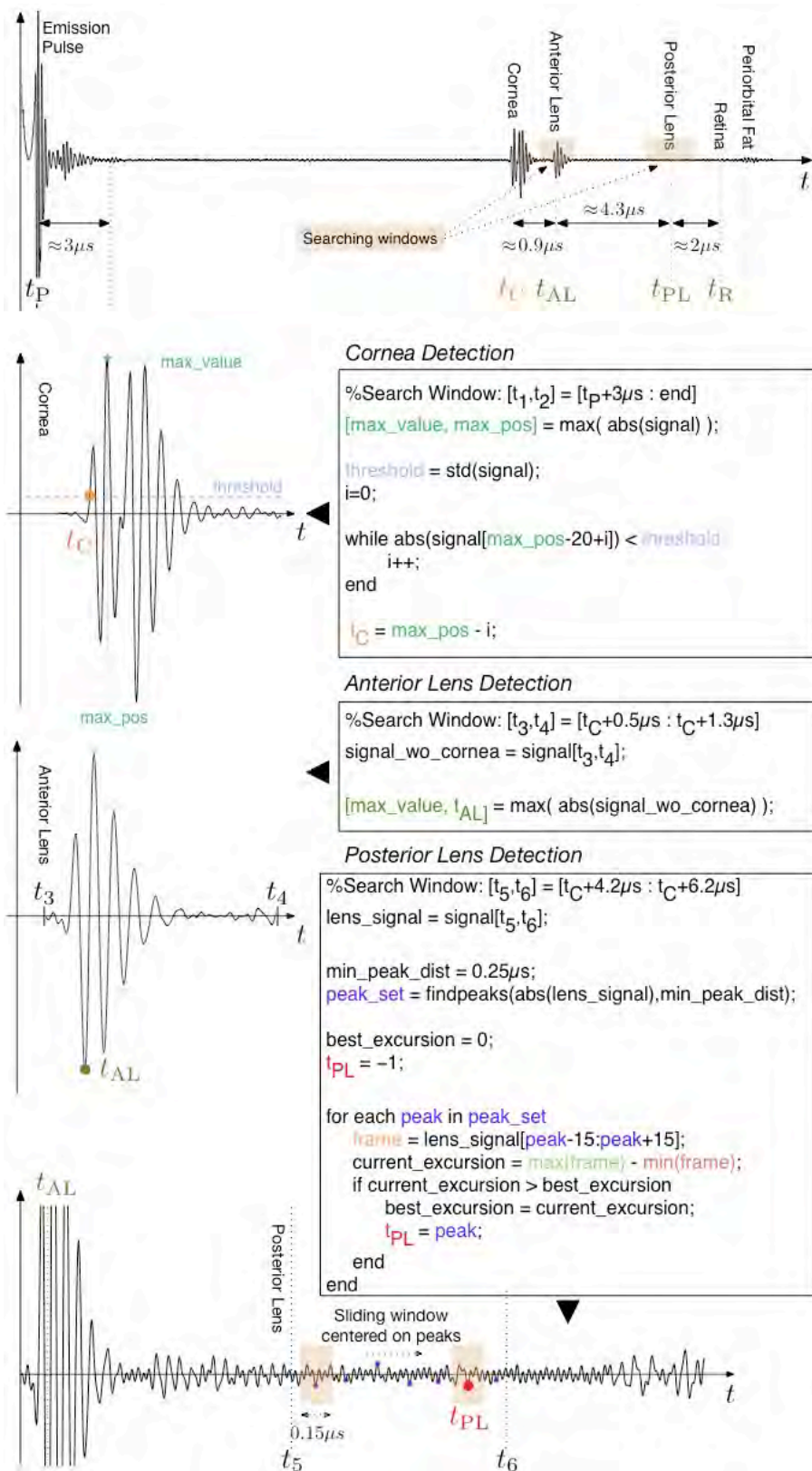


FIGURE 7-10. PROCEDURE FOR AUTOMATIC DETECTION OF OCULAR INTERFACES (Caixinha *et al.* 2016).

Taking t_C , the anterior lens interface detection is straightforward, being defined by the position of the maximum absolute value of the signal in the region $[t_C + 0.5 \mu\text{s}; t_C + 1.3 \mu\text{s}]$, which corresponds to a range of $0.9 \pm 0.4 \mu\text{s}$ (Figure 7-10).

The posterior lens capsule echo presented low amplitude mainly due to attenuation. In fact, in some cases this amplitude is of the same order of the noise magnitude. Therefore, a more elaborated searching method was developed. Thus, considering the search window $[t_C + 4.2 \mu\text{s}; t_C + 6.2 \mu\text{s}]$, defined according to (Caixinha *et al.* 2014a) and (Hughes 1979), the signal peaks spaced at least by $0.25 \mu\text{s}$ were determined. The time interval of $0.25 \mu\text{s}$ relates to the length of the echo pulses, which are characterized by 5 cycles (20 MHz excitation signal). To apply this constraint, the `findpeaks` function, (MathWorks Inc 2015) chooses the taller peak (absolute value) of the search window and eliminates all peaks over $0.25 \mu\text{s}$. Then, the function repeats the procedure for the tallest remaining peak and iterates until it runs out of peaks to consider. Next, a window with $0.15 \mu\text{s}$ (corresponding to 30 samples of the digitized A-scan signal) centred in each peak is set, and the signal excursion (difference between maximum and minimum) inside the window is calculated. The peak position whose window presents the highest signal excursion provides good estimation of the posterior lens capsule location. The algorithm here proposed to automatically detect the low amplitude echoes of the posterior lens capsule addresses the challenge reported by several authors in the literature (Guggenheim *et al.* 2004; Lozano and Twa 2013; Paunksnis *et al.* 2007).

The developed methods allow the estimation of the corneal thickness, anterior and vitreous chamber axial lengths, and lens thickness. The echoes originating from retina, choroid, and periorbital fat can be used to assess the eyeball axial length.

7.2.2.4.2 Features extraction

After signal filtering and automatic detection of the ocular interfaces, 27 features were extracted from the A-scan signals for each acquisition approach, in order to identify the presence of cataract, classify its severity, and estimate its hardness.

Three types of features were extracted (listed in Table 7-4): time domain features (f1 to f10); statistical time domain features (f11 to f19) and frequency derived features (f20 to f27).

The time domain features were extracted directly from the A-scan signal and are explained in Figure 7-11 and Table 7-4.

The statistical time domain features were extracted by applying a sliding rectangular window of $0.30 \mu\text{s}$ (60 samples) to the lens signal. The sliding window procedure was applied throughout the entire lens signal, excluding the anterior and posterior lens echoes (variable running time, depending on lens size). Some measures, such as energy (f14), sample standard deviation (f15), Root Mean Square (RMS) (f16), and Spectral Flatness Measure (SFM; the ratio of the geometric mean to the arithmetic mean of the frame samples), (f19), are taken from the signal frame that has the highest amplitude excursion, characterized by feature f12.

The spectral centroid (f21) and 95% roll-off (f20) are measures usually taken for audio signals (Eyben *et al.* 2010) and are evaluated through a DFT of a frame. They represent the centre of the spectral samples distribution, and the

frequency below which 95% of the magnitude distribution is concentrated, respectively. The frequency downshift (f22) and feature f27 are standard in ultrasound quantitative evaluation (Santos 1998). For their evaluation, the DFT was applied to the anterior and posterior lens frames and their peak spectral frequencies (f_{CA} and f_{CP} , respectively) were extracted. The frequency downshift is the difference of the peak values ($f_{CA} - f_{CP}$). To account for variations in lens size, feature f23 represents the frequency downshift (f22) divided by the lens propagation time (f1). The ratio of the anterior and posterior lens spectra represents the transfer function, from which the linear and quadratic fitting parameters (f24 to f26) are extracted. From the linear fitted slope, the attenuation (f27) can be computed according to (Santos 1998).

The ratios described in f18-f21 are taken from the highest excursion frames in the anterior and posterior lens reflections.

Feature vectors were produced from each 20 averaged A-scans ($A_{i\text{ mean}}$) to classify the cataract severity levels based on the 27 extracted features. Fifty feature vectors (fv_i) were obtained during a one second acquisition. The final feature vector was computed by calculating the median value of the 50 feature vectors (FV_{median}), as illustrated in Figure 7-12.

TABLE 7-4. EXTRACTED FEATURES (Caixinha *et al.* 2016).

f1.	Propagation time in the lens path, (<i>d5</i>).
f2.	Maximum absolute amplitude of the signal inside the lens, (<i>global_lens_max</i>).
f3.	Propagation time until maximum absolute amplitude (f2) signal inside the lens, (<i>max_idx</i>).
f4.	Normalized propagation time, $f3/f1$, (<i>max_idx_nor</i>).
f5.	Decaying time with a threshold of 80% of maximum amplitude, (<i>last_idx_abv_thr</i>).
f6.	Maximum duration of an excursion of the absolute amplitude above the threshold, (<i>longest_seq_abv_thr</i>).
f7.	The starting instant where feature f6 occurs, (<i>idx_longest_seq_abv_thr</i>).
f8.	The cumulative duration of all excursions above the threshold, f6 included, (<i>total_abv_thr</i>).
f9.	The area of the envelope above the threshold, (<i>area_abv_thr</i>).
f10.	Maximum excursion of the signal inside the lens, (<i>global_lens_minmax</i>).
f11.	Ratio of the standard deviation of the absolute value of the signal inside the lens by the standard deviation of the absolute value of the anterior lens reflection, (<i>global_lens_std</i>).
f12.	Maximum signal excursion of the signal of all frames along the lens, (<i>max_lens_minmax</i>).
f13.	Initial position (time) of the frame where f12 occurs, (<i>max_lens_frame_bg</i>).
f14.	Energy of the frame where f12 occurs, (<i>max_lens_energy</i>).
f15.	Standard deviation of the frame where f12 occurs, (<i>max_lens_standard_deviation</i>).
f16.	Root-mean-square value of the frame where f12 occurs, (<i>max_lens_RMS</i>).
f17.	The anterior to posterior lens amplitude ratio ($ a_1/a_2 $, Figure 7-11), (<i>Maximum_Lens_Amplitude_Ratio</i>).
f18.	The ratio of kurtosis coefficients of the anterior and posterior lens reflections, (<i>KC_Ratio</i>).
f19.	The ratio of spectral flatness measures of the posterior and anterior lens, (<i>SFM_Ratio</i>).
f20.	The ratio of roll-off 95% bandwidths of the anterior and posterior lens reflections, (<i>RO95_ratio</i>).
f21.	The ratio of spectral centroids of the anterior and posterior lens reflections, (<i>Spectral_centroid_Ratio</i>).
f22.	Frequency downshift from anterior to posterior lens reflections, (<i>Frequency_Downshift</i>).
f23.	Centre frequency deviation ($f22/f1$). This normalization factor eliminates the variations in the downshift induced by the natural variability in lens sizes, (<i>Norm_Freq_downshift</i>).
f24.	The y-intercept value of the linear fitted transfer function, (<i>Linear_Fitting_Coefficient_a0</i>).
f25.	The slope of the linear fitted transfer function, (<i>Linear_Fitting_Coefficient_a1</i>).
f26.	Quadratic fitting coefficient (second order coefficient of the quadratic fitting of the transfer function), (<i>Quadratic_Fit_Coef_b2</i>).
f27.	Attenuation coefficient value in the lens for 10 MHz, calculated according to the method defined in (Santos 1998), (<i>Attenuation_db_mm_10MHz</i>).

7.2.3 Machine learning techniques for automatic cataract classification

7.2.3.1 Dimensionality Reduction

In order to optimize the classification performance, the extracted features were subjected to a PCA (Guyon and Elisseeff 2003) (section 6.2.6.3). PCA was also performed to verify that the high number of features (27), compared with the sample size (50), did not compromise the classification performance (Siddiqui 2013). The number of generated components was defined such that 95% of the original data variance was explained.

7.2.3.2 Classifiers

The 27 extracted features were used to train and test different classifiers in order to classify cataract into healthy, incipient, moderate, and severe. The following classifiers were tested: Naive Bayes (Bouckaert 2004), Multilayer Perceptron (Neural Network) (Pal and Mitra 1992), SVM with a RBF kernel (Chang and Lin 2011b), and Random Forest (Jain *et al.* 2000). For the SVM classifier, a grid-search approach was used to optimize simultaneously the cost function C and the RBF Gamma (γ) parameter, establishing a trade-off between the accuracy and the total number of support vectors (Hsu *et al.* 2010). This approach consists of assessing the SVM accuracy for different values of the C and Gamma parameters. The combination of lower C and Gamma values resulting in the highest accuracy was chosen in this work.

For the classifiers training, a k -fold cross-validation was used with $k = 10$. The performance of the classifiers was calculated taking the average performance of each fold. The metrics used to assess classifiers performance were the F-measure, accuracy, precision, sensitivity and specificity.

7.2.3.3 Data Analysis

The Spearman correlation was used to test for correlations between the lens thickness and the rats' age, since an association between lens thickness and rats' age (over 2 months) was proposed by (Lozano and Twa 2013), and for correlations between the lens hardness and the extracted features.

To assess the agreement between acquisitions performed *in vivo*, *post mortem*, and *ex vivo*, the ICC between these three acquisitions was computed for the extracted features.

Statistically significant differences between lenses without cataract (controls), and lenses with cataract (incipient, moderate and severe) were tested for the extracted features using ANOVA with Bonferroni *post hoc* test for multiple comparisons. The Kruskal-Wallis test was used for testing statistically significant differences between the lens hardness and Young's modulus (Panich and Yong 2005) and the cataract severity.

PCA and classification were performed with the Waikato Environment for Knowledge Analysis (WEKA) software (Hall *et al.* 2009), and the statistical analyses were performed using the IBM SPSS Statistics version 22.0 (IBM Corp. in Armonk, NY, USA).

Results were considered statistically significant for p -values < 0.05 .

7.3 Results

7.3.1 Animal model and lens characterization

7.3.1.1 Animal model for nuclear cataract

Although the three nuclear cataract degrees (incipient, moderate, and severe, Figure 7-13) were observed in the 36 rats injected before eyes opening, most of them developed moderate or severe cataract (Figure 7-14). Only incipient and moderate cataracts were observed in the rats injected after eyes opening (Figure 7-14).

The used cataract induction model produced 12 rats with incipient cataract, 13 rats with moderate cataract, and 11 rats with severe cataract.

No statistically significant differences were found between the different cataract degrees and age ($p = 0.050$).

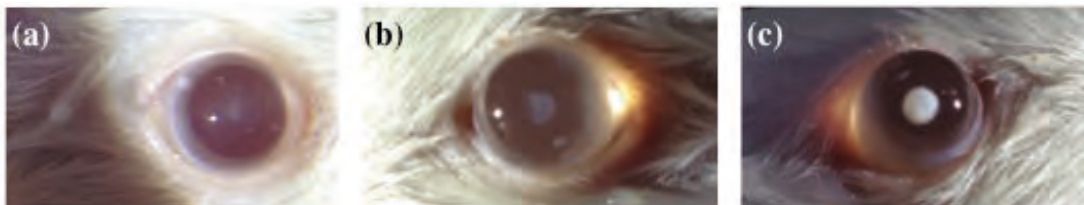


FIGURE 7-13. DEGREES OF NUCLEAR CATARACT SEVERITY OBTAINED WITH THE ANIMAL MODEL. (a) INCIPIENT; (b) MODERATE; AND (c) SEVERE (Caixinha *et al.* 2016).

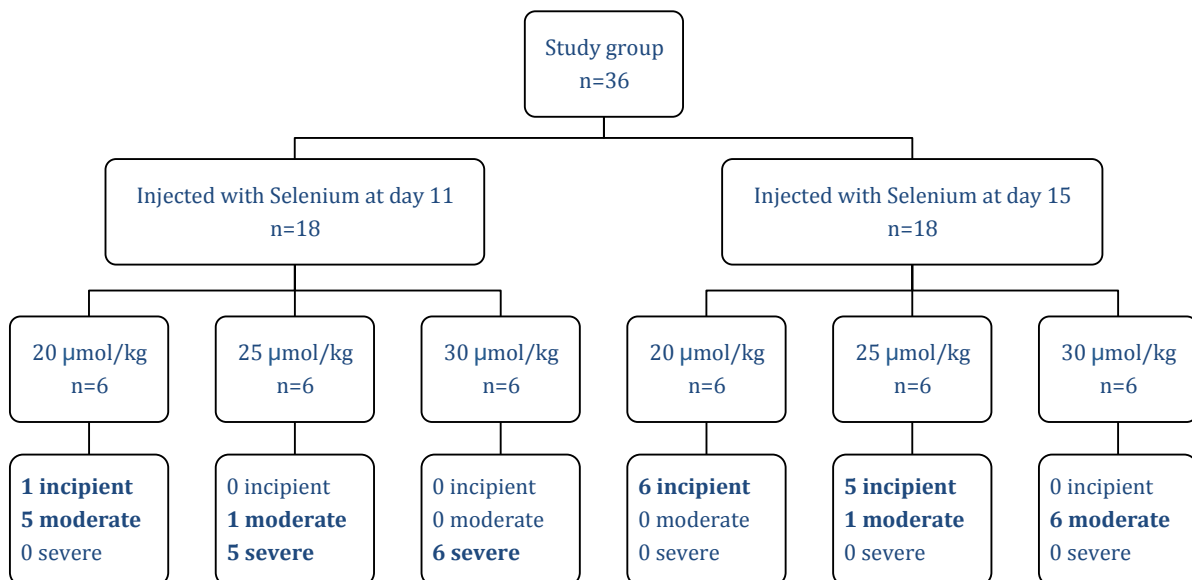


FIGURE 7-14. NUMBER OF RATS WITH THE DIFFERENT DEGREES OF NUCLEAR CATARACT (INCIPIENT; MODERATE, AND SEVERE).

7.3.1.2 Rats' eye characterization

For the 50 rats (14 healthy and 36 with nuclear cataract) the lens thickness measured with a calliper, ranged from 3.06 mm to 4.28 mm (mean \pm standard-deviation: 3.52 ± 0.49 , Table 7-5), which is in accordance with the results found in the literature (Hughes 1979), where a 3.71 mm mean value was proposed for rats with a mean age of 4.2 months. An association between lens thickness and rats' age over 2 months was proposed by (Lozano and Twa 2013). In our study, only a weak correlation was found between the lens thickness and the rats' age ($r = 0.397$; $p < 0.001$, Figure 7-15).

The rat's eye axial length, corneal thickness, anterior and vitreous chambers' axial lengths and lens thickness were estimated *in vivo* using the ultrasound pulse-echo mode. A mean velocity of 1600 m/s for healthy lenses and 1650 m/s for cataractous lenses was considered, based on the results obtained in porcine eyes by Caixinha *et al.*, (Caixinha *et al.* 2014a). The results for the eye axial length measured *ex vivo* and estimated *in vivo*, using the propagation time and the considered velocities, are presented in Table 7-5. No accurate measurements could be obtained *ex vivo* for the corneal thickness, as well as for the anterior and vitreous chambers' axial lengths, (values missing in Table 7-5).

TABLE 7-5. RAT'S EYE DIMENSIONS.

	Measured <i>ex vivo</i>	Estimated <i>in vivo</i>	Hughes (Hughes 1979)	Massof (Massof and Chang 1972)
Corneal thickness (mm)	-	0.20 \pm 0.02	0.26 \pm 0.002	0.25
Lens thickness (mm)	3.52 \pm 0.49	3.54 \pm 0.01	3.71 \pm 0.05	3.87 \pm 0.19
<i>Axial length (mm)</i>				
- Anterior chamber	-	0.74 \pm 0.09	0.62	0.87 \pm 0.15
- Vitreous chamber	-	1.69 \pm 0.19	1.39	1.51 \pm 0.29
- Eye	5.88 \pm 0.45	6.23 \pm 0.20	6.29 \pm 0.04	5.89 \pm 0.47

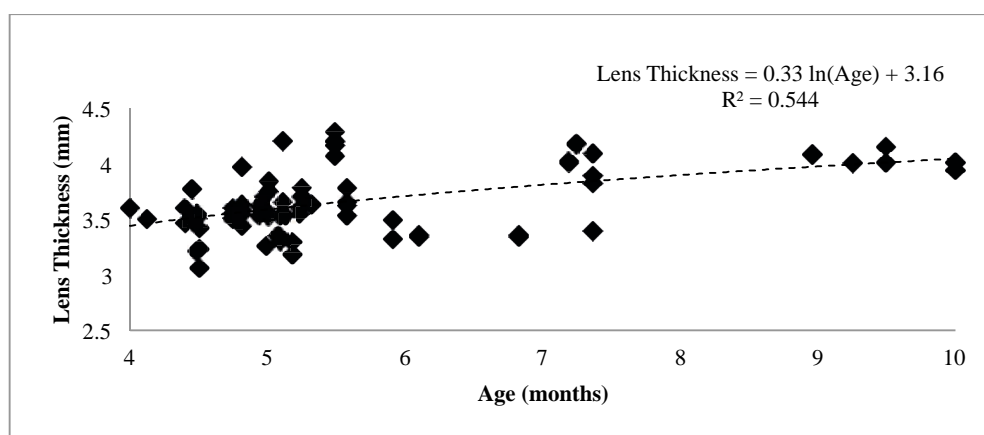


FIGURE 7-15. LENS THICKNESS VERSUS AGE.

7.3.1.3 Lens hardness and elasticity measurements

The hardness of the cortex and nucleus regions was measured for healthy lenses and for lenses with different cataract degrees using the NanoTest™. Each slice was observed with optical microscopy (model Leica DM400 M LED, Leica Microsystems CMS GmbH, Germany) to confirm that the indentations were carried out in the correct region of the lens. After the hardness tests, the indentation images were acquired with the same equipment. The indentations marks can be seen in Figure 7-16, and the regular indentation curves are shown in Figure 7-17, where the ordinate represents the exerted force by the indenter in the tissue, expressed in millinewton, and the abscissa represents the indentation depth in nanometres.

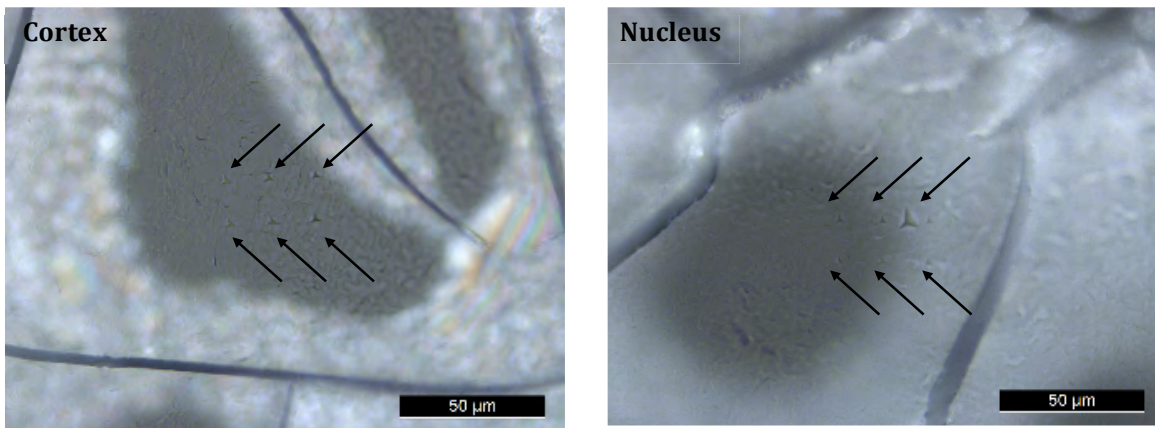


FIGURE 7-16. SLICE IMAGES OF LENSES WITH SEVERE CATARACT. THE ARROWS IDENTIFY THE INDENTATION LOCATIONS (Caixinha *et al.* 2016).

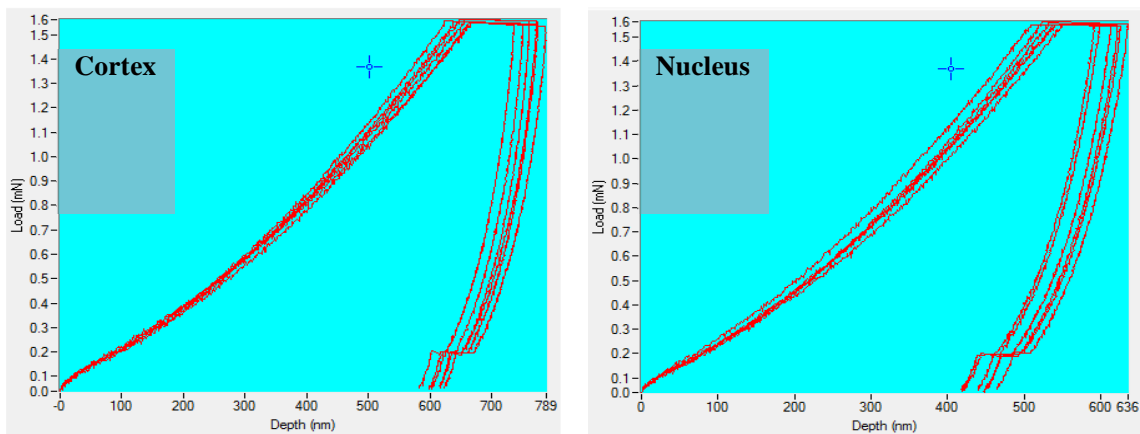


FIGURE 7-17. INDENTATION CURVES FOR A LENS WITH SEVERE CATARACT.

The hardness values for the different cataract severity levels in the two considered regions are presented in Table 7-6 and Figure 7-18. A statistically significant difference was found for the hardness of the different nuclear cataract severity levels, in the cortex and nucleus regions ($p = 0.016$). The results showed a lens hardness increase with cataract progression in the cortex and nucleus regions. As expected, the nucleus region presented higher hardness

than the cortex region and showed a higher hardness increase with the cataract severity ($p = 0.049$, Figure 7-19). Moreover, even for the healthy lenses (without cataract), the nucleus region presented a higher hardness than the cortex (Table 7-6 and Figure 7-18).

A moderate correlation was found between the lens hardness and the rats' mean age ($r = 0.597$, $p = 0.003$ for the nucleus, and $r = 0.474$, $p = 0.022$ for the cortex).

TABLE 7-6. HARDNESS MEASURED BY NANOTEST™ (Caixinha *et al.* 2016).

	Cortex	Nucleus
Healthy lenses (GPa)	0.136 ± 0.003	0.156 ± 0.005
Incipient cataract (GPa)	0.159 ± 0.004	0.195 ± 0.009
Moderate cataract (GPa)	0.183 ± 0.004	0.228 ± 0.014
Severe cataract (GPa)	0.199 ± 0.004	0.264 ± 0.009

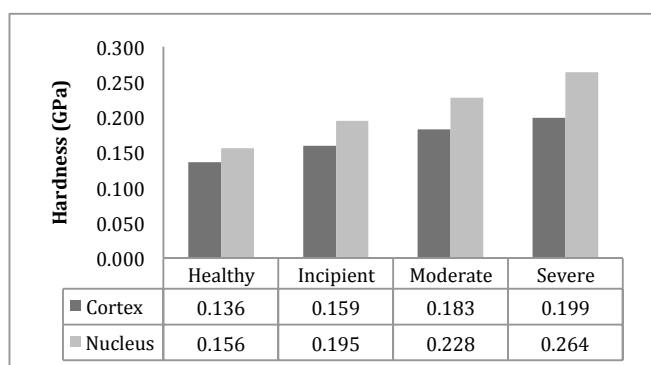


FIGURE 7-18. LENS HARDNESS IN GPA FOR HEALTHY LENSES AND FOR DIFFERENT DEGREES OF CATARACT SEVERITY MEASURED BY NANOTEST™, MEAN VALUES.

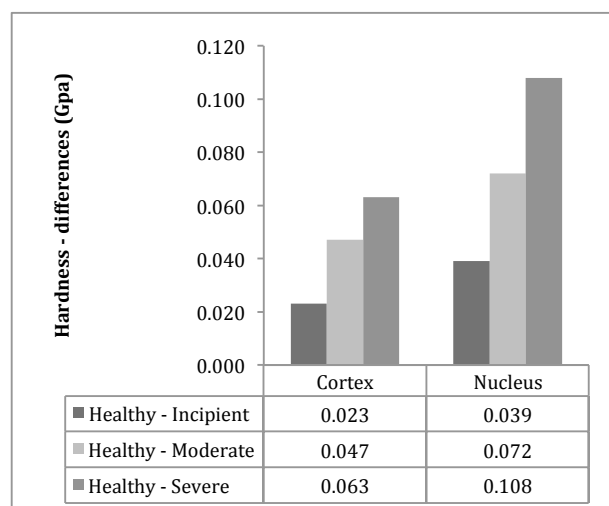


FIGURE 7-19. LENS HARDNESS INCREASE IN THE CORTEX AND NUCLEUS REGIONS WITH CATARACT SEVERITY MEASURED BY NANOTEST™, MEAN VALUES.

A strong correlation was found between the Young's modulus and the lens hardness ($r = 0.953$, for the nucleus and $r = 0.701$ for the cortex, $p < 0.001$). The results showed an increase of the lens Young's modulus with cataract progression in both regions of the lens, cortex and nucleus. However, no statistically significant difference was found for the Young's modulus between the different nuclear cataract severity levels, in both regions of the lens ($p = 0.065$;

Table 7-7 and Figure 7-20). From healthy to incipient cataractous lenses, only the nucleus region showed a statistically significant increase of the Young's modulus ($p = 0.001$ for the nucleus and $p = 0.069$ for the cortex). From incipient to moderate and from moderate to severe, the Young's modulus increase was not statistically significant in both regions of the lens ($p = 1.00$ for the nucleus and $P > 0.103$ for the cortex, Figure 7-21). The increase of the Young's modulus was only statistically significant in both regions of the lens between healthy and moderate cataract ($p = 0.022$) and between healthy and severe cataract ($p = 0.004$). For healthy and severe cataractous lenses, the Young's modulus was higher in the cortex, while for the incipient and moderate cataractous lenses, the Young's modulus was higher in the nucleus.

Also, a correlation was found between the lens Young's modulus and the rats' mean age ($r = 0.487$, $p = 0.030$ for the nucleus, and $r = 0.362$, $p = 0.020$ for the cortex).

TABLE 7-7. YOUNG'S MODULUS COMPUTED BASED ON THE REDUCED YOUNG'S MODULUS MEASURED BY NANOTEST™.

	Cortex	Nucleus
Healthy (GPa)	3.438 ± 0.058	3.391 ± 0.148
Incipient cataract (GPa)	3.465 ± 0.068	3.739 ± 0.130
Moderate cataract (GPa)	3.607 ± 0.060	3.781 ± 0.113
Severe cataract (GPa)	3.963 ± 0.065	3.848 ± 0.110

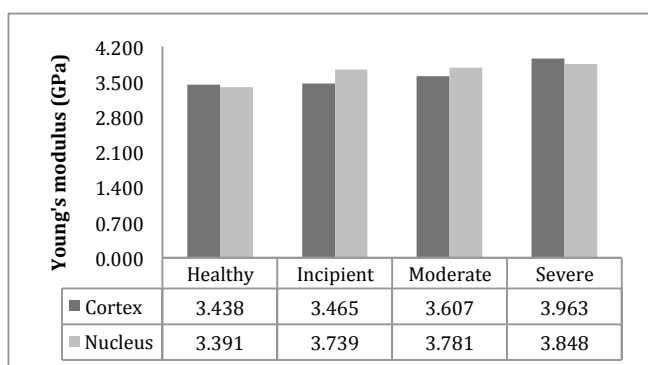


FIGURE 7-20. LENS YOUNG'S MODULUS IN GPA FOR HEALTHY LENSES AND FOR DIFFERENT DEGREES OF CATARACT SEVERITY MEASURED BY NANOTEST™, MEAN VALUES.

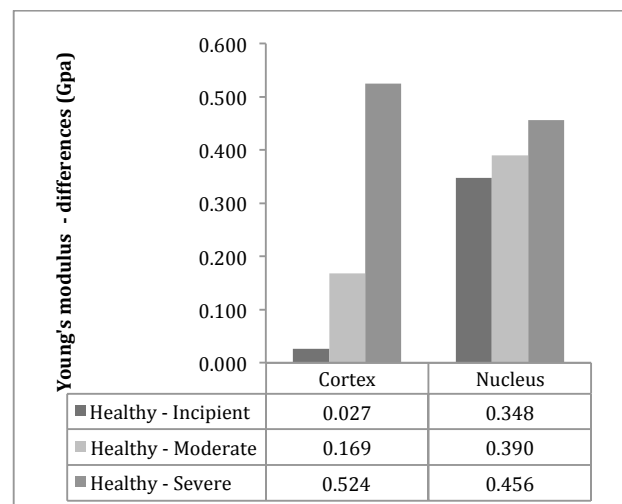


FIGURE 7-21. INCREASE OF THE LENS YOUNG'S MODULUS IN GPA IN THE CORTEX AND NUCLEUS REGIONS WITH CATARACT SEVERITY MEASURED BY NANOTEST™, MEAN VALUES.

7.3.2 Features analysis

7.3.2.1 Agreement between acquisitions

Overall, a good agreement was found between the extracted features obtained *in vivo*, *post mortem* and *ex vivo* as shown in Figure 7-22. Twenty-six out of the 27 features showed a fair to excellent agreement ($ICC \geq 0.400$) between the *in vivo* and *post mortem* acquisitions. The agreement between the *in vivo* and *ex vivo* extracted features was fair to excellent ($ICC \geq 0.400$) in 24 out of the 27 features. Since the eye movement and probe misalignment do not significantly affect the extracted features *in vivo*, only the *in vivo* results are presented hereinafter.

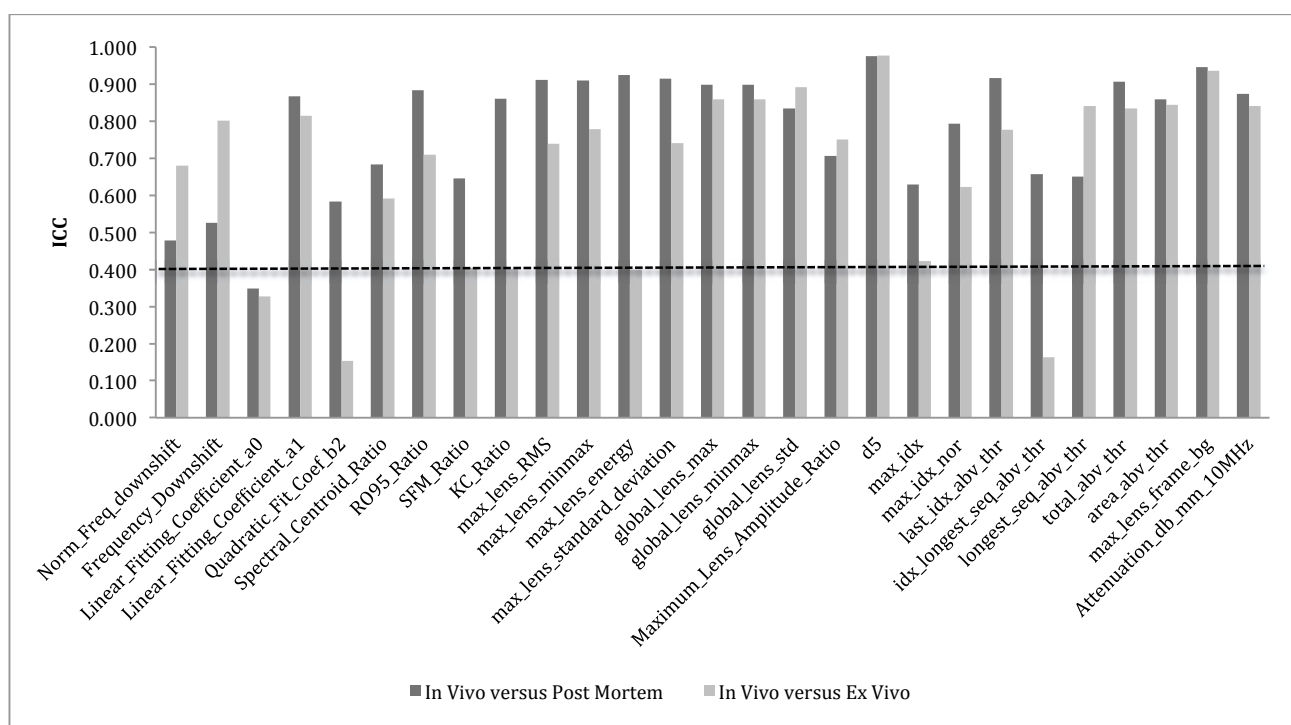


FIGURE 7-22. ICC VALUES BETWEEN *IN VIVO* AND *POST MORTEM* ACQUISITIONS AND BETWEEN *IN VIVO* AND *EX VIVO* ACQUISITIONS FOR THE 27 EXTRACTED FEATURES (BELOW 0.400 THE AGREEMENT IS POOR, DASHED LINE).

7.3.2.2 *In vivo* results

All the 27 features extracted *in vivo* showed a statistically significant difference between healthy and cataractous lenses and between the different cataract degrees (incipient, moderate and severe cataract), ($p < 0.01$).

In particular, for the acoustical parameters frequently used in tissue characterization, as the propagation velocity and attenuation (Huang *et al.* 2007a; Huang *et al.* 2007b; Paunksnis *et al.* 2007; Raitelaitienè and Paunksnis 2005; Tabandeh *et al.* 2000), it was verified that the wave propagation time decreased from $4.31 \pm 0.02 \mu\text{s}$ for healthy to $3.93 \pm 0.11 \mu\text{s}$ for severe cataractous lenses ($p < 0.001$; Figure 7-23), meaning that the velocity increases with the cataract severity, in spite of the lens thickness variation ($3.52 \pm 0.49 \text{ mm}$). Concerning to the attenuation, an increase from $2.78 \pm 0.60 \text{ dB/mm}$ in healthy lenses to $5.50 \pm 2.25 \text{ dB/mm}$ in severe cataractous lenses was found ($p < 0.001$; Figure 7-24).

The observed increase in the propagation velocity and attenuation with the cataract severity is in accordance with the results obtained in the proof-of-concept study carried out in porcine lenses (Caixinha *et al.* 2014a).

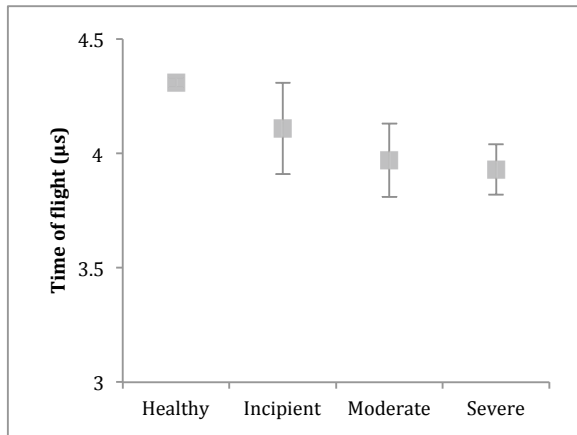


FIGURE 7-23. TIME OF FLIGHT IN HEALTHY LENSES AND WITH DIFFERENT CATARACT DEGREES (MEAN±1SD) (Caixinha *et al.* 2016).

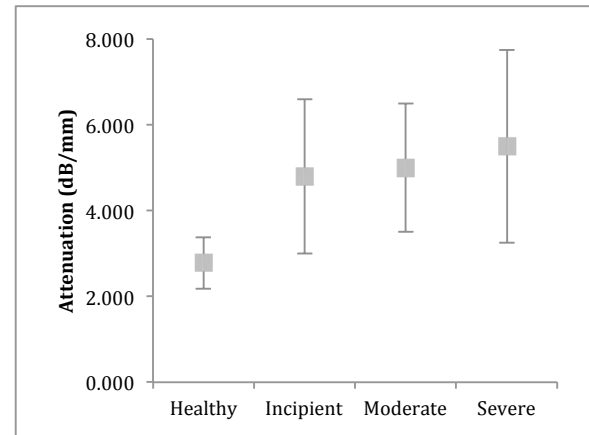


FIGURE 7-24. ULTRASOUND ATTENUATION COEFFICIENT FOR 10 MHz FOR THE DIFFERENT CATARACT DEGREES (MEAN±1SD) (Caixinha *et al.* 2016).

The frequency downshift is another useful parameter to infer about the tissue microstructure. It was observed a frequency shifting, corresponding to the difference between the anterior and posterior lens capsule spectra centre frequency, whose value was 1.04 ± 0.51 MHz for the healthy lenses and 1.97 ± 0.62 MHz for the lenses with severe cataract ($p < 0.001$; Figure 7-25). Thus, the frequency downshift was of 0.93 MHz corresponding to 89.4% of variation from healthy to severe cataract. Moreover, an increase of the transfer function slope with cataract severity, calculated as the ratio of the anterior and posterior lens capsule spectra, was also observed, which indicates that the high frequencies are attenuated with cataract progression (Figure 7-26).

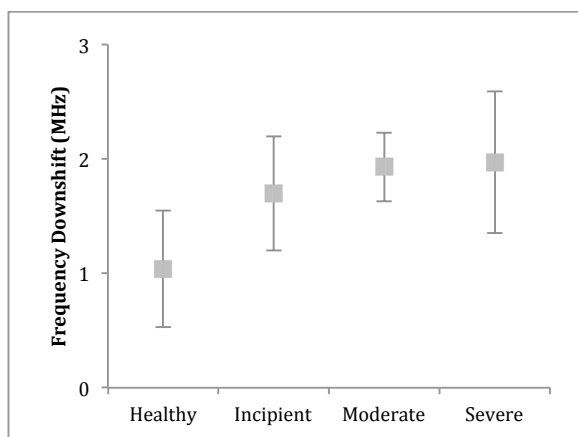


FIGURE 7-25. FREQUENCY DOWNSHIFT FOR THE DIFFERENT CATARACT DEGREES (MEAN±1SD) (Caixinha *et al.* 2016).

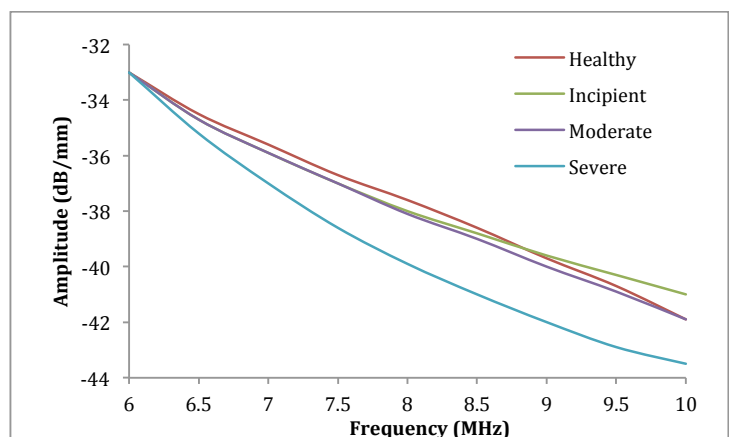


FIGURE 7-26. TRANSFER FUNCTION FOR THE DIFFERENT CATARACT SEVERITIES.

Considering the 27 extracted features, a moderate to good correlation between the features and the nucleus hardness, for the different cataract severity levels, was found in 23 out of the 27 features, as shown in Figure 7-27.

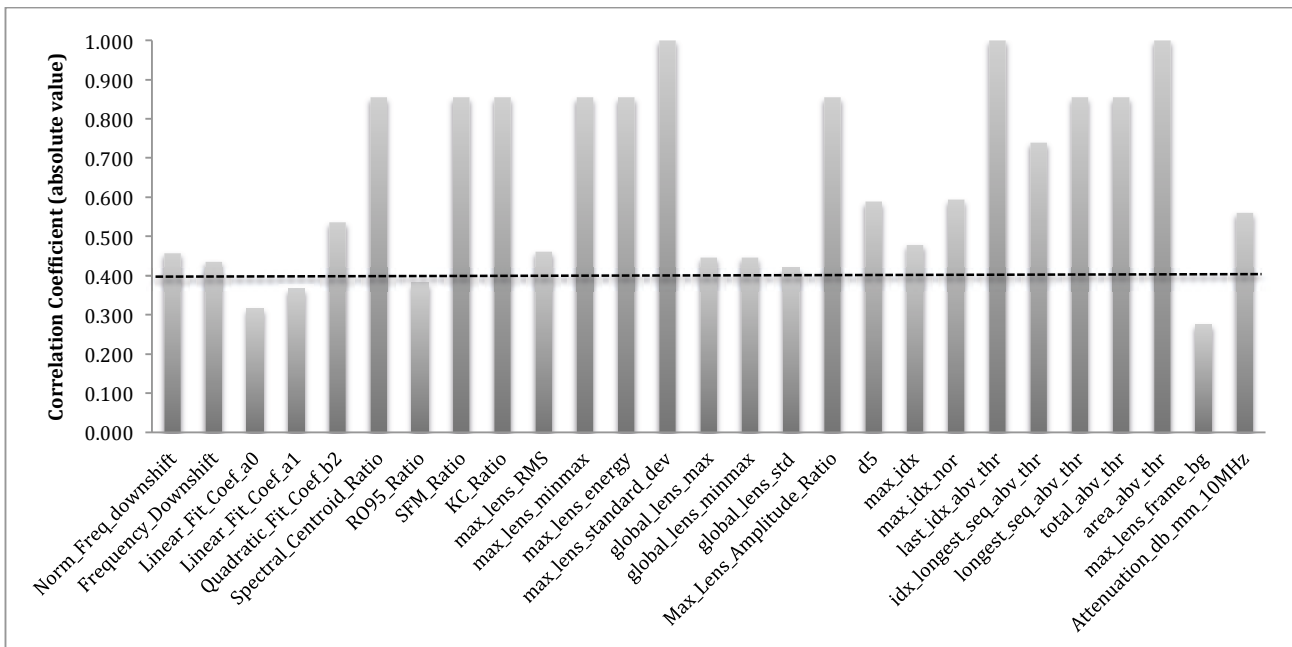


FIGURE 7-27. CORRELATION COEFFICIENT BETWEEN THE NUCLEUS HARDNESS AND THE EXTRACTED FEATURES *IN VIVO* (BELOW 0.400 THE CORRELATION IS WEAK, DASHED LINE) (Caixinha *et al.* 2016).

After using these 27 features in a PCA, 12 components were obtained, that accounted for 95.1% of the cumulative variance of the 27 extracted features (Figure 7-28 and Figure 7-29).

The description of each component is presented in Table 7-8. Each component is composed by 8 to 18 features with a coefficient equal or higher than 0.1, indicating the absence of a specific association between the extracted features.

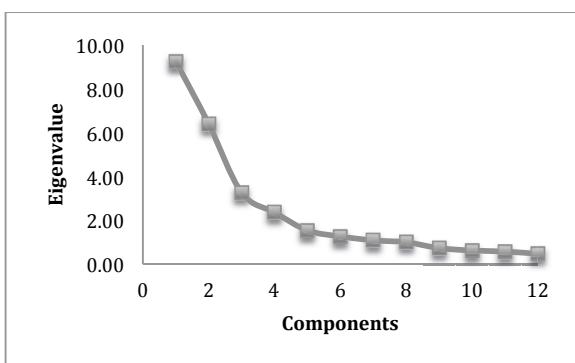


FIGURE 7-28. SCREE PLOT FOR THE PCA OF THE 27 EXTRACTED FEATURES.

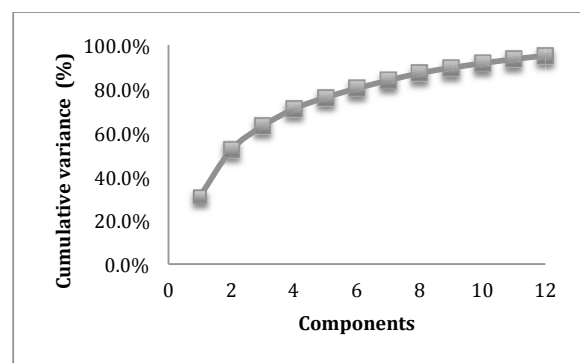


FIGURE 7-29. CUMULATIVE VARIANCE EXPLAINED BY THE 12 EXTRACTED COMPONENTS.

TABLE 7-8. DESCRIPTION OF THE 12 COMPONENTS OBTAINED BY PCA (COEFFICIENTS LOWER THAN 0.1 ARE NOT PRESENTED).

Features	Components											
	C1	C2	C3	C4	C5	C6	C7	C8	C9	C10	C11	C12
<i>Normalized_Frequency_downshift</i>	-0.240	0.127	-0.331	-0.331	0.340	0.340	0.177	-0.218	0.177			-0.212
<i>Frequency_Downshift</i>	-0.255	0.140	-0.323	-0.323	0.304	0.304	0.136	-0.228	0.136			-0.142
<i>Linear_Fitting_Coefficient_a0</i>	-0.307		0.126	-0.129								
<i>Linear_Fitting_Coefficient_a1</i>	0.302	-0.135	0.162							0.392	0.545	
<i>Quadratic_Fitting_Coefficient_b2</i>	-0.217	0.138	-0.213	-0.486	-0.166	-0.184	0.171					
<i>Spectral_Centroid_Ratio</i>	0.206	-0.163	-0.163	-0.315	0.208	-0.236	-0.153					
<i>RO95_Ratio</i>	0.132	-0.239	-0.120	-0.167	0.208	-0.236	-0.153					
<i>SFM_Ratio</i>	-0.207	0.125	0.124	0.444	-0.169	0.217						
<i>KC_Ratio</i>	-0.250	0.183	0.126	0.178	-0.509	0.356	0.155	-0.368				
<i>max_lens_RMS</i>	0.348	-0.256	-0.156								0.131	
<i>max_lens_minmax</i>	0.345	-0.212	-0.123									
<i>max_lens_energy</i>	0.293	-0.339	-0.205	-0.177	0.104	0.212	0.190					
<i>max_lens_standard_deviation</i>	0.347	-0.261	-0.153									
<i>global_lens_max</i>	-0.238	-0.348	0.120	0.107	0.108	-0.104						
<i>global_lens_minmax</i>	-0.238	-0.348	0.120	0.107	0.108	-0.104						
<i>global_lens_std</i>	-0.223	-0.362	-0.178								-0.103	
<i>Maximum_Lens_Amplitude_Ratio</i>	-0.191	0.186	0.115	-0.207	-0.388	-0.116	-0.430					
<i>d5</i>	-0.176	0.101	0.285	-0.421	0.229	0.404	0.453	-0.237				
<i>max_idx</i>	0.140	0.196	0.380	0.114	0.203	0.296	0.179					
<i>max_idx_nor</i>	0.240	0.334	0.336	-0.264	0.105	0.221						
<i>last_idx_abv_thr</i>	0.190	0.270	-0.122	-0.211	0.157	0.311	-0.248	-0.232				
<i>idx_longest_seq_abv_thr</i>	0.145	0.254	0.228	0.550	-0.572	0.100						
<i>longest_seq_abv_thr</i>	0.232	0.232	-0.201	-0.647	-0.427	0.127	-0.122					
<i>total_abv_thr</i>	0.413	-0.316	-0.179	-0.155	-0.376	-0.232						
<i>area_abv_thr</i>	-0.274	-0.219	0.100	-0.116	-0.256							
<i>max_lens_frame_bg</i>	-0.239	0.169	0.270	-0.306	-0.184							0.556
<i>Attenuation_10MHz_dB_mm</i>	0.289	-0.152	0.126	0.218	-0.209	-0.184					0.113	

7.3.3 Automatic classification of cataract severity

The classifiers performance for the different cataract degrees is shown in Table 7-9 and Table 7-10.

All classifiers presented a good performance when classifying lenses into healthy and cataractous (incipient, moderate, and severe).

Considering the 27 extracted features, the F-measure for the 4 classifiers ranged from 0.946 for the Naive Bayes to 0.997 for the SVM. Since the performance of the different classifiers is similar, the relative absolute error, *i.e.*, the error of the classifiers when considering the *prior* probability of the observed classes, was also used to compare the classifiers performance (Chokkalingam 2013). The SVM was the one that showed higher performance with a sensitivity and specificity of 0.997, and a relative absolute error of 0.4% (Table 7-9).

For the 12 components obtained by PCA the F-measure ranged from 0.803 to 0.992 for the Naive Bayes and SVM classifiers, respectively. Again, the SVM was the one that showed higher performance with a sensitivity and specificity both of 0.992, and a relative absolute error of 1.1% (Table 7-10).

TABLE 7-9. PERFORMANCE OF THE DIFFERENT CLASSIFIERS USING THE 27 SELECTED FEATURES (RAE – RELATIVE ABSOLUTE ERROR) (Caixinha *et al.* 2016).

	RAE	F-Measure	Accuracy	Precision	Sensitivity	Specificity
SVM	0.4%	0.997	0.997	0.997	0.997	0.997
Naive Bayes	8.0%	0.946	0.946	0.947	0.946	0.946
Random Forest	6.5%	0.996	0.996	0.996	0.996	0.996
Multilayer Perceptron	5.9%	0.967	0.967	0.967	0.967	0.967

TABLE 7-10. PERFORMANCE OF THE DIFFERENT CLASSIFIERS USING THE 12 COMPONENTS OBTAINED BY PCA (RAE – RELATIVE ABSOLUTE ERROR) (Caixinha *et al.* 2016).

	RAE	F-Measure	Accuracy	Precision	Sensitivity	Specificity
SVM	1.1%	0.992	0.992	0.992	0.992	0.992
Naive Bayes	33.3%	0.803	0.804	0.806	0.804	0.804
Random Forest	11.2%	0.988	0.988	0.989	0.988	0.988
Multilayer Perceptron	14.3%	0.916	0.916	0.917	0.916	0.916

The results of the grid-search approach for the optimization of the *C* and Gamma parameters of the SVM classifiers are shown in Table 7-11 and Table 7-12.

TABLE 7-11. ACCURACY OF THE SVM CLASSIFIER FOR THE 27 FEATURES CONSIDERING DIFFERENT OPTIMIZATION PARAMETERS (* VALUES CHOSEN FOR THE C AND GAMMA PARAMETERS).

		Gamma			
		0.1	0.2	0.5	1
C	1	0.856	0.917	0.988	0.998
	10	0.980	0.998	0.999	1.000
	100	0.998	0.999*	0.999	1.000
	1000	0.997	0.999	0.999	1.000

TABLE 7-12. ACCURACY OF THE SVM CLASSIFIER FOR THE 12 COMPONENTS OBTAINED BY PCA CONSIDERING DIFFERENT OPTIMIZATION PARAMETERS (* VALUES CHOSEN FOR THE C AND GAMMA PARAMETERS).

		Gamma			
		0.1	0.2	0.5	1
C	1	0.998*	0.998	0.988	0.983
	10	0.998	0.998	0.990	0.983
	100	0.998	0.998	0.990	0.983
	1000	0.998	0.998	0.990	0.983

7.4 Discussion and conclusions

7.4.1 Animal model and lens characterization

In this study, the hypothesis that the administration of different concentrations of sodium selenite in rats with different eye maturation periods (before and after eyes opening) produces different nuclear cataract degrees was tested and experimentally confirmed. The animal model considered for cataract induction is identified in the literature as the model that better mimics what happens in humans for age-related cataract (Kyselova 2010; Shearer *et al.* 1997). The model used in this study for nuclear cataract induction produced, as expected, different nuclear cataract degrees classified in three different degrees of severity: incipient, moderate and severe. The obtained results showed that when high doses of sodium selenite are administrated over longer periods of maturation, after eyes opening and having already been exposed to light, the rats do not develop severe nuclear cataracts. On the other hand, when sodium selenite is administered over short periods of maturation, before eyes opening and not been exposed to light, severe

degrees of nuclear cataract developed, even with lower concentrations. However, to scientifically support and explain these findings more studies are needed.

Currently there is no reference in the literature to the objective measurement of the lens hardness or Young's modulus, two of the biomechanical properties of the lens' tissue. This study, reports for the first time the hardness and the Young's modulus of lens' tissue in two regions (nucleus and cortex) for healthy lens and for different degrees of nuclear cataract. It was objectively showed that the nucleus hardness is higher than the cortex in healthy lenses, a result which is in agreement with the microanatomy of vertebrate lenses. The lens fiber cells organization and compaction in vertebrates are common (Shi *et al.* 2009). In rats and humans, the cells of the nucleus are deprived of long organelles, more fibrous, and with a cellular arrangement/structure more compact but less organized (Augusteyn 2010; Kuwabara 1975; Shi *et al.* 2009), explaining that the nucleus from a healthy lens is harder than the cortex region where the cellular compaction is lower. The cataractogenic process promotes the increase of the lens hardness both in the nucleus and cortex regions. When the cataract forms, the hardness of these two regions increases when compared to healthy lenses. This variation is higher as the severity of the nuclear cataract increases. Lenses with severe cataract present higher hardness in the nucleus and in the cortex regions, being this increase higher in the nucleus than in the cortex ($p = 0.049$).

The results showed an increase of the lens Young's modulus with cataract progression in both regions of the lens (cortex and nucleus). This increase is in agreement with the hardness increase verified with cataract progression. Moreover, the Young's modulus showed a strong correlation with the hardness, in the two regions of the lens.

In the healthy lenses, the Young's modulus was found to be higher in the cortex than in the nucleus region, a finding in agreement with the results obtained in human lenses by Fisher (Fisher 1971) and by Michael and Bron (Michael and Bron 2011). In human young adult healthy lens tissue, the nucleus has a higher elasticity than the cortex region. The nucleus is deformable and its elastic modulus is lower than the cortex (Michael and Bron 2011). With age or with the cataractogenic process, the elastic properties of the lens change and there is a continuous decrease in lens elasticity, greater in the nucleus than in the cortex (Fisher 1971; Michael and Bron 2011), in large part due to the age-related changes in the lens proteins and the elasticity of the lens capsule (Michael and Bron 2011). These changes promote the decrease of the elasticity of the nucleus compared to the cortex and also the increase of the nucleus hardness, with age and with the cataractogenic process (Beebe *et al.* 2010; Michael and Bron 2011). In our study, it was found that the Young's modulus for the incipient and moderate cataract severity levels is higher in the nucleus than in the cortex region, indicating that the elasticity of the nucleus reduces with cataract progression. Moreover, this decrease is more pronounced in the nucleus than in the cortex, probably due to the cataract model used in this study. On the other hand, in the severe nuclear cataract it

was found that the Young's modulus of the nucleus is slightly lower than in the cortex region (2.9%). Several factors may influence this result. In this work it was assumed that the cortex and the nucleus regions of the lens were both linearly elastic and isotropic (Bocskai and Bojtár 2013; Burd *et al.* 2002; Fisher 1971; Gefen *et al.* 2009; Hermans *et al.* 2007; Hermans *et al.* 2008; Hollman *et al.* 2007; Hozic *et al.* 2012; McKee *et al.* 2011; Uchio *et al.* 1999; Weeber *et al.* 2005; Weeber *et al.* 2007; Weeber and van der Heijde 2008), and that the Poisson's ratio in both regions, and for healthy and cataractous lenses, was the same 0.49 (Burd *et al.* 2002; Schumacher *et al.* 2007). Due to the induced cataract process, that promotes mainly changes in the nucleus region, in the severe nuclear cataract condition the biomechanical changes in the nucleus are more apparent than in the cortex, and the assumption that these two regions of the lens tissue have the same Poisson's ratio is no longer correct. Since the lens tissue biomechanical properties change with age, and particularly with the cataract formation, more studies are needed to determine the correct Poisson's ratio for the lens tissue in different cataract conditions. In this study, by considering a Poisson's ratio of 0.46, instead of 0.49, for the severe nuclear cataract condition the Young's modulus in the nucleus is higher than in the cortex by 3.7%. So the correct Poisson's ratio in cataractous lenses, for the nucleus and cortex regions, needs to be confirmed.

7.4.2 Automatic detection of ocular interfaces

Algorithms were developed for automatic detection of the ocular interfaces, using the signals collected from the eye. Such allowed determining the eyeball axial length, lens thickness, the corneal thickness and the anterior and vitreous chambers' axial lengths. Several authors reported difficulties in the lens thickness estimation, related to the posterior capsule echo location (Guggenheim *et al.* 2004; Lozano and Twa 2013; Paunksnis *et al.* 2007). In this work, a new two-stage method for posterior capsule echo location was proposed, that comprises peaks detection in posterior lens region, followed by signal excursion evaluation on the vicinity of the marked peaks.

The values found for the anteroposterior lens and eye diameters are in agreement with those measured with a calliper as well as with the ones published by Hughes (Hughes 1979). The estimated values for the corneal thickness and for the anteroposterior diameters of the anterior and vitreous chambers, are also in agreement with the ones published in (Hughes 1979).

The strategy followed over the developed work makes possible the use of high frequencies for biometric evaluation of ocular structures.

7.4.3 Agreement between *in vivo*, *ex vivo* and *post mortem* acquisitions

It was demonstrated that the developed methodology for *in vivo* automatic cataract classification is reliable, since the majority of the extracted features have an excellent agreement between the *in vivo*, *post*

mortem and *ex vivo* acquisitions. This proves that *in vivo* cataract detection and classification is not affected by the ocular movements and probe free-hand misalignment. The features that showed a weak agreement between the *in vivo* and the *ex vivo* acquisitions were related to the reflection coefficient and the signal amplitude. So, in practice, it is important that the acquisitions are made in such a way that the amplitude of the signal received by the probe is maximized.

7.4.4 *In vivo* features extraction

All the 27 extracted features showed a statistically significant difference between the cataract severity levels. Particularly, acoustical parameters as velocity (propagation time) and attenuation (Huang *et al.* 2007a; Huang *et al.* 2007b; Paunksnis *et al.* 2007; Raitelaitienė and Paunksnis 2005; Tabandeh *et al.* 2000), presented a significant increase with nuclear cataract progression, in accordance with the proof-of-concept study results (Caixinha *et al.* 2014a). The frequency downshift demonstrated also to be a relevant feature for cataract severity evaluation. It was observed a frequency shifting of 1.04 ± 0.51 MHz for the healthy lenses and 1.97 ± 0.62 MHz for the lenses with severe cataract, indicating that the higher frequencies are heavily attenuated with cataract progression.

A moderate to good correlation was found between the nucleus hardness, for the different cataract severity levels, and the selected features, demonstrating that the extracted features can be used to estimate *in vivo* and noninvasively the nuclear cataract hardness.

7.4.5 Automatic cataract classification

All the tested classifiers showed a performance higher than 0.950 for the automatic classification of the cataract severity. The SVM was the classifier with the lowest classification error (0.4%), and better performance, with a sensitivity and specificity of 0.997. For the 12 components obtained by the PCA the SVM showed also the best performance with a sensitivity and specificity of 0.992, and a relative absolute error of 1.1%. The data dimensionality reduction provided by the PCA did not improve the classification performance.

7.5 Eye Scan Ultrasound System (ESUS)

Based on the developed methodology and the obtained results, a prototype of a medical device using noninvasive ultrasound technology, named ESUS (Eye Scan Ultrasound System), was developed for early and automatic cataract detection, classification, and hardness estimation in real time. The prototype is currently protected under patent provision application PPP108836 (Santos *et al.* 2015).

This section presents the ESUS, its design concept and former prototype. This thesis has contributed for the main aspects of the system.

7.5.1 ESUS description

The main characteristics of the ESUS are to:

- perform in real time the detection, characterization and evaluation of a cataract and its hardness estimation, noninvasively, using ultrasound technology;
- perform in real time axial A-scan and B-scan imaging of the eye, with automatic identification of eye's structures and cataract location;
- provide real time results in a display (*e.g.* tablet, computer) through a secure wireless communication channel;
- be reconfigurable and having learning capabilities.

The key component blocks that form ESUS are presented in Figure 7-30.

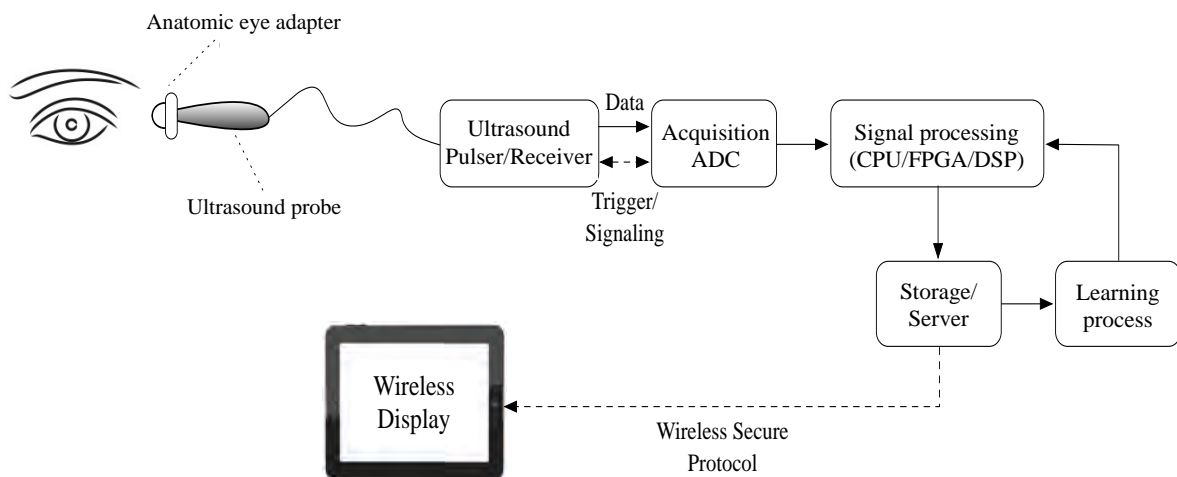


FIGURE 7-30. ESUS KEY COMPONENTS BLOCKS.

The system is composed by an ultrasound pulser/receiver that excites an ophthalmologic ultrasound probe, and detects and amplifies ultrasound echo signals. The probe sensing terminal has attached an adapter for anatomic eye coupling. Pulse-echo signal is provided to the acquisition analog-to-digital converter (ADC) system that digitizes it and feeds it to the signal processing unit. Trigger and signalling between ultrasound pulse/receiver and acquisition ADC is made through a dedicated connection and controlled by either system (acting as master or slave) according to user specifications.

Details of the enclosed operations performed at the signal processing unit are presented in Figure 7-31. Either in A-scan or B-scan mode, signal conditioning and denoising is carried out for each new received A-scan signal. A linear phase passband filter is applied to the signal, in order to select the frequencies of interest and minimize the noise, followed by a moving average filter to improve the SNR. This is followed by the detection of the ocular interfaces, enabling to identify the regions where time domain, statistical time domain, and frequency derived features are extracted. These last type of features imply to perform the DFT of a given identified segment of the signal (as described previously in section 7.2.2.4.2). These features are provided to the classifier that identifies the existence of a cataract and provides information about its location and hardness. Graphical visualization of the results, including eye's structure measures, can be made on a wireless device, through a secure connection to a host server where the results are stored.

The classification system uses one of the state-of-the-art methods, *e.g.* SVM, random forest, and decision trees, according to the processing unit computing capabilities. The system detects the presence and the location of cataract, classifies its severity and estimates its hardness. The classifier is regularly trained with a reference database that may grow with new clinical data, acquired by the system after validation by the physician. This adds a learning capability to the system given new acquired signals. Therefore, ESUS encompasses an effortless learning, reconfiguration and reprogramming capabilities, leveraged by the use of a reconfigurable hardware system.

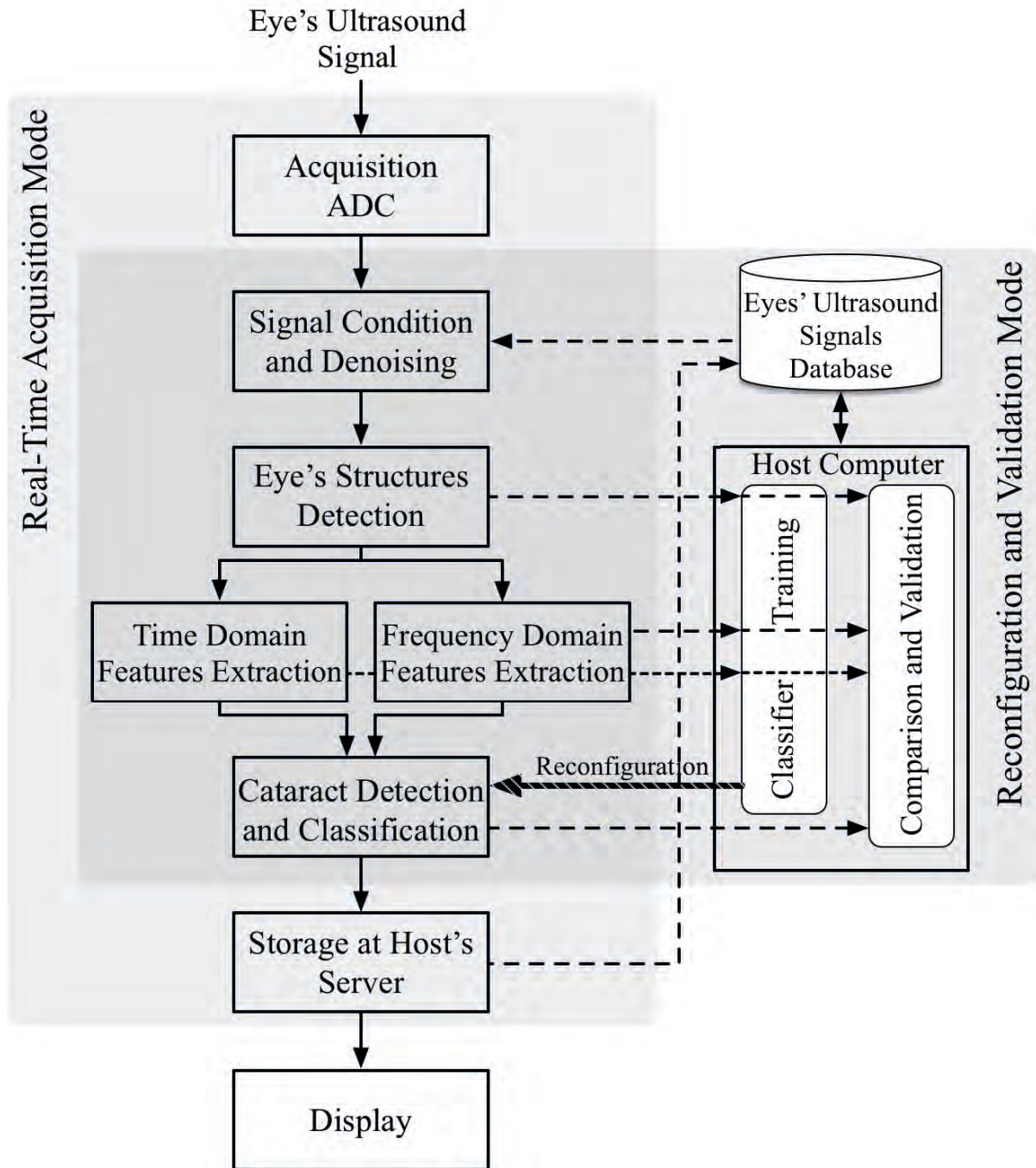


FIGURE 7-31. ESUS BLOCK DIAGRAM.

7.5.2 ESUS prototype

The prototype developed to demonstrate the system concept (Figure 7-32), is composed by a 20 MHz ophthalmic ultrasonic probe (Imasonic, SAS, France), a pulser/receiver (model Compact Pulser, Ultratek, CA, USA), an analog-to-digital acquisition board with 2 channels, 14 bits and sampling rate of 100 MHz (model FCM 150, 4DSP LLCTM, TX, USA). The signal processing unit is build up on a ZeadBoard, a low-cost, and easy reprogrammable development board based in the System-on-Chip (SoC) Zynq- 7000 architecture of Xilinx. Taking advantage of the SoC architecture, that combines an industry-standard Advanced RISC (Reduced Instruction Set Computing) Machine (ARM) dual- core CortexTM-A9 MPCore processor subsystem (PS) with Xilinx 28 nm programmable logic (PL) (also known as, field programmable gate array (FPGA)), and by exploring the FPGA and the ARM joined cooperative and parallel operation with dedicated communication channels between them, it was possible to implement in an efficient way, for real time operation, the diverse ESUS's subsystems namely: signal conditioning and denoising of the A-scan acquired signal; eyes's structures detection and features extraction; and cataract detection and classification (Ferreira 2015).

Produced results are saved to a computer that works as server. An android application (app) has been developed to visualize in real time the produced results, enabling the use of unwired displays such as tablets.

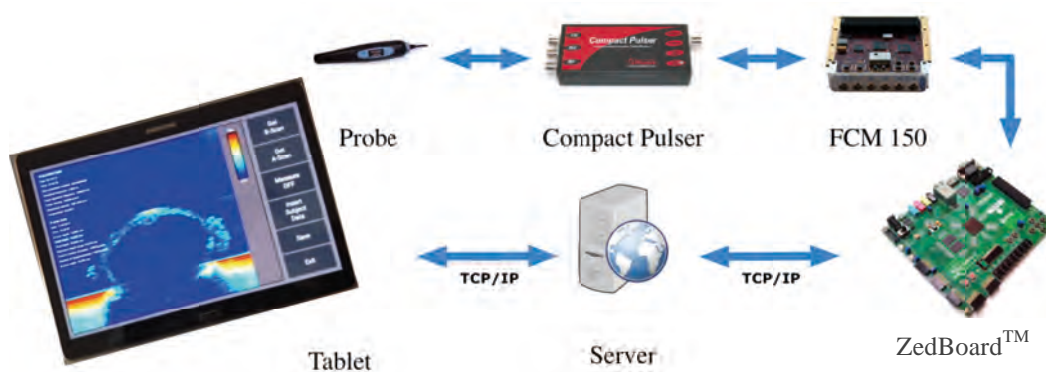


FIGURE 7-32. SCHEME OF THE ESUS PROTOTYPE (A B-SCAN FOR A RAT' LENS IS SHOWN BASED ON *EX VIVO* ACQUISITIONS).

The prototype also supports a testing mode able to process previously acquired signals stored in a database. This was used for validation of all developed blocks and for calibration/training of the classification algorithm implemented on the prototype. An accuracy, specificity and sensitivity for cataract classification over 0.950 was obtained based on the signals acquired *in vivo*, in 50 rats.

The ESUS display was designed to be user-friendly. Several options are available such as the visualization of the acquired A-scan signals, the B-scans images, and of some features, as shown in Figure 7-33. The ESUS display also allows to measure some anatomical structures directly from the visualized images. Figure 7-33 (c) and (d) a B-scan image constructed based on the *ex vivo* acquisitions performed in this work is shown.

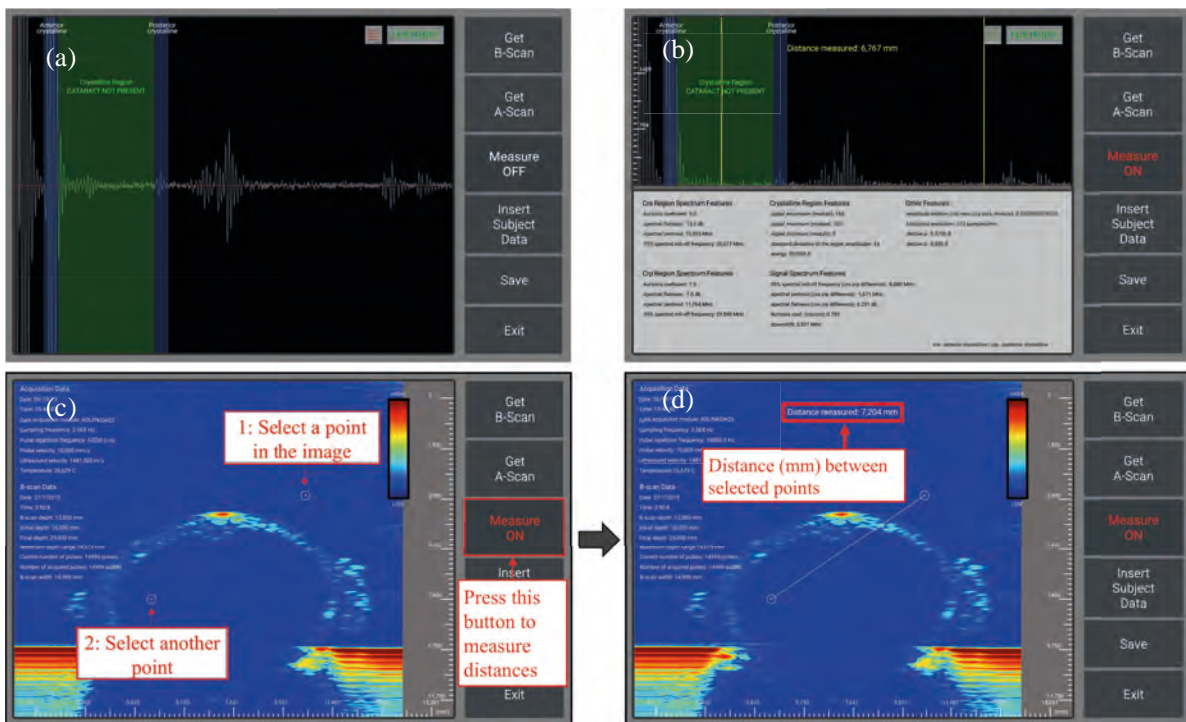


FIGURE 7-33. LAYOUT OF THE ESUS PROTOTYPE (A B-SCAN FOR A RAT'S LENS IS SHOWN BASED ON *EX VIVO* ACQUISITIONS).

The following patent was registered:

- J. Santos, M. Gomes, M. Santos, F. Perdigão, A. Morgado, L. Duarte (M. Caixinha), J. Amaro and J. Ferreira, "ESUS – Eye Scan Ultrasound System", Pedido de Patente PPP108836, September, 2015.

7.6 Resulting publications

The following paper was published (section PUBLICATIONS):

- *In vivo* Automatic Nuclear Cataract Detection and Classification in an Animal Model by Ultrasounds. Caixinha, M.; Amaro, J.; Santos, M.; Perdigão, F.; Gomes, M.; Santos, J. IEEE Transactions on Biomedical Engineering. 2016; 63(11): 2326-2335 (DOI: 10.1109/TBME.2016.2527787).

The following review paper on machine learning techniques was also published (section PUBLICATIONS):

- Machine Learning Techniques in Clinical Vision Sciences. Caixinha M. and Nunes S. Current Eye Research. 2016; (DOI: 10.1080/02713683.2016.1175019)

8 CONCLUSIONS AND FUTURE WORKS

8.1 Conclusions

This work aimed to evaluate the potential of the ultrasound technique application for *in vivo* early cataract detection and hardness estimation as well as cataract classification using machine learning techniques.

Before doing the *in vivo* experiments, in an animal model for nuclear cataract, a proof-of-concept study was performed *ex vivo*, in porcine lenses.

The conclusions of the *ex vivo* study are:

- The ultrasound velocity and attenuation increases significantly with cataract progression.
- The analysis of backscattering signals through envelope statistics allows to evaluate the scattering distribution along the cataract formation process. It was demonstrated that the scatterers arrangement evolves from a pre-Rayleigh to a Rayleigh distribution with cataract progression, showing that the opacification process is characterized by increasing concentration of regularly distributed scatterers.
- The velocity, attenuation, frequency downshift, and the parameters extracted from the backscattering signal analysis, proved to be important features for the objective characterization of cataract.
- It was demonstrated that the B-scan images are a useful tool for cataract evaluation by characterizing the echogenicity of protein aggregation and fibres compaction regions, resulting from the cataractogenic process, as confirmed by the correlations with the images of lens histological slices.
- The Nakagami parametric images can also be used to characterize the cataract formation process providing quantitative information through the m parameter. This is an indicator of the scatterers

distribution and concentration in the lens. This finding was supported by the correlations between the Nakagami m parameter and the images of lens histological slices.

- The CRT identified predictive factors for the presence of cataract, with a sensitivity of 1.000, and allowed to discriminate between different cataract severity levels, with a sensitivity of 0.784.
- The CRT showed that the Nakagami m parameter is a relevant factor for the discrimination of the cataract severity levels.
- The multiclass SVM can be used for the automatic classification of the cataract severity.
 - The cataract classification by multiclass SVM showed a sensitivity and specificity of 0.846 and 0.923, respectively.
 - The acoustical parameters combined with the analysis of the backscattering signal (B-scan and Nakagami imaging) allow a good discrimination of the different cataract degrees.
- The used machine learning techniques, and the developed methodology, can detect and classify automatically the cataract severity.

The conclusions of the *in vivo* study are:

- The developed animal model for nuclear cataract allowed obtaining *in vivo* different cataract degrees, including its early stage (incipient cataract).
- The hypothesis that the administration of different sodium selenite concentrations in rats with different eye maturation periods (before and after eyes opening) produces different nuclear cataract degrees was experimentally confirmed.
- The hardness and the elasticity (Young's modulus) of the crystalline lens were objectively measured for the first time in healthy and in cataractous lenses (with different degrees of cataract severity). It was found that: the cataractogenic process promotes the increase of the hardness and the decrease of the elasticity in both regions of the lens (nucleus and cortex); the nucleus hardness is higher than the cortex hardness, for healthy and cataractous lenses; the hardness increase in the nucleus, along the cataract progression, is higher than in the cortex; for healthy lenses, the nucleus elasticity is higher than the cortex elasticity.
- Algorithms were developed for automatic detection of the ocular interfaces, overcoming difficulties reported in the posterior capsule echo location.
- The use of high frequency ultrasounds allowed *in vivo* biometry of the ocular structures, enabling the estimation of the eyeball axial length, corneal and lens thicknesses, and anterior and vitreous chambers' axial lengths.

- Machine learning techniques were able to classify cataract severity with a performance higher than 0.950.
- The SVM was the classifier with the lowest classification error (0.4%), and the better performance (0.997), with sensitivity and specificity of 0.997.
- The agreement between the *in vivo*, *ex vivo* and *post mortem* acquisitions, showed that the *in vivo* acquisitions are reliable. The cataract detection and classification are not affected by the ocular movements or by the angle of incidence of the probe in the eye.
- The correlations obtained between the nucleus hardness and the extracted features demonstrate that the cataract hardness can be estimated *in vivo* noninvasively.
- The use of the ultrasound technique and machine learning enables cataract detection in its early stages, automatic cataract classification of its severity and noninvasive cataract hardness estimation.
- The developed classification method, represents a potential tool for the automatic cataract classification, and may contribute for a new classification system, alternative to the current classification system used in clinical practice, the LOCS III, which is based on a subjective evaluation. Due to the automatic and objective nature of the developed classification method, it represents a promising tool for use in clinic, or, for example, in large-scale epidemiological studies.

8.2 Future works

The developed prototype uses an ophthalmic ultrasound probe with CE marking, complying with the safety levels for use in humans. This prototype represents the basis for the development of a medical device for cataract surgery support. For this purpose, and before conducting a clinical trial, some works are needed.

1. In order to optimize the energy level in the phacoemulsification procedure, experimental surgeries will be performed in rats with different cataract severity degrees, using the cataract classification and hardness estimation obtained with ESUS. For verifying the safety of the selected energy levels in the posterior lens capsule preservation and in the corneal endothelial cells loss, the rats will be sacrificed and the eyes enucleated to assess the lens capsule integrity and to measure the endothelial cells loss using confocal microscopy. The ultrasound parameters will be correlated with the phacoemulsification energy level and with the surgical complications, to demonstrate that the information provided by the developed prototype reduces the risks of energy level overestimation, making the cataract surgery safer.

2. Two clinical trials will be designed to validate the prototype for use in humans. In the first one, patients with different types and cataract severity levels will be included to train the classifiers for human cataract detection, automatic classification and hardness estimation. This trial will be also used for CE (Conformité Européene) marking application. The second clinical trial will be performed to validate the prototype in a representative group of patients, according to the most frequent types of cataract in the clinical practice. The ISO (International Organization for Standardization) 13485, the European directives and the national legislations on medical devices will be followed for the design and conduction of these two clinical trials.

REFERENCES

- Abdelkader H, Alany RG, Pierscionek B. Age-related cataract and drug therapy: opportunities and challenges for topical antioxidant delivery to the lens. *J Pharm Pharmacol* 2015;67:537–50.
- Abell R, Kerr N, Howie A, Mustaffa Kamal M, Allen P, Vote B. Effect of femtosecond laser-assisted cataract surgery on the corneal endothelium. *J Cataract Refract Surg* 2014;40:1777–1783.
- Abell RG, Darian-Smith E, Kan JB, Allen PL, Ewe SYP, Vote BJ. Femtosecond laser-assisted cataract surgery versus standard phacoemulsification cataract surgery: Outcomes and safety in more than 4000 cases at a single center. *J Cataract Refract Surg* 2015;41:47–52.
- Abu El Einen KG, Shalaby MH, El Shiwly HT. Immersion B-guided versus contact A-mode biometry for accurate measurement of axial length and intraocular lens power calculation in siliconized eyes. *Retina* 2011;31:262–5.
- Ai Y, Zheng Z, O'Brien-Jenkins A, Bernard DJ, Wynshaw-Boris T, Ning C, Reynolds R, Segal S, Huang K, Stambolian D. A mouse model of galactose-induced cataracts. *Hum Mol Genet* 2000;9:1821–7.
- Alió JL, Kady B El. Control of corneal astigmatism and aberrations. *Minimizing Incisions Maximizing Outcomes Cataract Surg Berlin, Heidelberg: Springer Berlin Heidelberg, 2010.* pp. 286–291.
- American Academy of Ophthalmology. Preferred practice pattern guidelines. *Cataract in the adult eye.* Am. Acad. Ophthalmol. San Francisco, CA, 2011.
- American Institute for Ultrasound in Medicine - AIUM and National Electrical Manufacturers Association - NEMA. Standard for real-time display of thermal and mechanical acoustic

- output indices on diagnostic ultrasound equipment. Assoc. Electr. Equip. Med. Imaging Manuf. 2010.
- American Institute of Ultrasound in Medicine (AIUM). Bioeffects and safety of diagnostic ultrasound. 1st ed. American Institute of Ultrasound in Medicine, 1993.
- American Optometric Association. Care of the Adult Patient with Cataract. St Louis, MO, 2004.
- Anand R, Ma D, Alizadeh H, Comerford SA, Sambrook JF, Gething MJ, McLean IW, Niederkorn JY. Characterization of intraocular tumors arising in transgenic mice. *Invest Ophthalmol Vis Sci* 1994;35:3533–9.
- Anderson MG, Smith RS, Hawes NL, Zabaleta A, Chang B, Wiggs JL, John SWM. Mutations in genes encoding melanosomal proteins cause pigmentary glaucoma in DBA/2J mice. *Nat Genet* 2002;30:81–5.
- Aptel F, Charrel T, Lafon C, Romano F, Chapelon J-Y, Blumen-Ohana E, Nordmann J-P, Denis P. Miniaturized high-intensity focused ultrasound device in patients with glaucoma: a clinical pilot study. *Invest Ophthalmol Vis Sci* 2011;52:8747–53.
- Artzén D, Lundström M, Behndig A, Stenevi U, Lydahl E, Montan P. Capsule complication during cataract surgery: Case-control study of preoperative and intraoperative risk factors. Swedish Capsule Rupture Study Group report 2. *J Cataract Refract Surg* 2009;35:1688–1693.
- Augusteyn RC. On the growth and internal structure of the human lens. *Exp Eye Res* 2010;90:643–654.
- Babizhayev MA, Vishnyakova KS, Yegorov YE. Oxidative damage impact on aging and age-related diseases: drug targeting of telomere attrition and dynamic telomerase activity flirting with imidazole-containing dipeptides. *Recent Pat Drug Deliv Formul* 2014;8:163–92.
- Babizhayev MA, Yegorov YE. Biomarkers of oxidative stress and cataract. Novel drug delivery therapeutic strategies targeting telomere reduction and the expression of telomerase activity in the lens epithelial cells with N-acetylcarnosine lubricant eye drops: anti-cataract which hel. *Curr Drug Deliv* 2014;11:24–61.
- Babizhayev MA, Yegorov YE. Telomere attrition in human lens epithelial cells associated with oxidative stress provide a new therapeutic target for the treatment, dissolving and prevention of cataract with N-Acetylcarnosine lubricant eye drops. Kinetic, pharmacological and activity-. *Recent Pat Drug Deliv Formul* 2016;10:82–129.
- Bankman IN. Handbook of Medical Imaging. Brody W, ed. Academic Press, 2000.
- Battaglioli JL, Kamm RD. Measurements of the compressive properties of scleral tissue. *Invest Ophthalmol Vis Sci* 1984;25:59–65.

- Baum G, Greenwood I. The application of ultrasonic locating techniques to ophthalmology, part I: Reflective properties. *Am J Ophthalmol* 1958;46:319–329.
- Beake B, Goodes S, Jones S, Parkinson R, Pickford N, Roberts L, Smith J. *NanoTest User Manual* (version 2.0). Wrexham, 2002.
- Beebe DC, Holekamp NM, Shui Y-B. Oxidative damage and the prevention of age-related cataracts. *Ophthalmic Res* 2010;44:155–65.
- Bencić G, Zorić-Geber M, Sarić D, Corak M, Mandić Z. Clinical importance of the lens opacities classification system III (LOCS III) in phacoemulsification. *Coll Antropol* 2005;29 Suppl 1:91–94.
- Berthoud VM, Beyer EC. Oxidative stress, lens gap junctions, and cataracts. *Antioxid Redox Signal* 2009;11:339–53.
- Bland J, Altman DG. Statistical methods for assessing agreement between two methods of clinical measurement. *Lancet* 1986;1:307–310.
- Bochow TW, West SK, Azar A, Munoz B, Sommer A, Taylor HR. Ultraviolet light exposure and risk of posterior subcapsular cataracts. *Arch Ophthalmol* 1989;107:369–72.
- Bocskai Z, Bojtár I. Biomechanical modelling of the accommodation problem of human eye. *Period Polytech Civ Eng* 2013;57:3–9.
- Boscia F, Grattagliano I, Vendemiale G, Micelli-Ferrari T, Altomare E. Protein oxidation and lens opacity in humans. *Investig Ophthalmol Vis Sci* 2000;41:2461–2465.
- Bouckaert RR. *Bayesian Network Classifiers in Weka*. Tech. Rep. 14/2004. Department of Computer Science, The University of Waikato, 2004.
- Bouhleb N, Sevestre-Ghalila S, Graffigne C. New Markov random field model based on Nakagami distribution for modeling ultrasound RF envelope. 14th European Signal Processing Conference 2006. p. 1568982397.
- Bourne RRA, Jonas JB, Flaxman SR, Keeffe J, Leasher J, Naidoo K, Parodi MB, Pesudovs K, Price H, White RA, Wong TY, Resnikoff S, Taylor HR. Prevalence and causes of vision loss in high-income countries and in Eastern and Central Europe: 1990-2010. *Br J Ophthalmol* 2014;98:629–38.
- Boyd LS, Boyd BF, Aleman CF. Preparing for the transition to phacoemulsification. In: Amar A, Athiya A, Soosan J, eds. *Phacoemulsification* 4th ed. Jaypee Medical Publishers, 2012. p. 12.
- Boyers LN, Karimkhani C, Hilton J, Richheimer W, Dellavalle RP. Global burden of eye and vision disease as reflected in the Cochrane database of systematic reviews. *JAMA*

- Ophthalmol 2015;133:25–31.
- Brand S, Weiss EC, Lemor RM, Kolios MC. High frequency ultrasound tissue characterization and acoustic microscopy of intracellular changes. *Ultrasound Med Biol* 2008;34:1396–407.
- British Institute of Radiology B. The safe use of ultrasound in medical diagnosis. Gail ter H. London: The British Institute of Radiology, 2000.
- Burd HJ, Judge SJ, Cross JA. Numerical modelling of the accommodating lens. *Vision Res* 2002;42:2235–2251.
- Caixinha M. Técnicas não invasivas por ultrassons para visualização e caracterização objetiva da catarata. determinação da energia ótima para facoemulsificação. (Proposta de tese de Doutoramento em Engenharia Biomédica). Departamento de Física e Departamento de Engenharia Electrotécnica e de Computadores da Faculdade de Ciências e Tecnologia, e IBILI – Instituto Biomédico de Investigação em Luz e Imagem da Faculdade de Medicina; Universidade de Coimbra, 2012.
- Caixinha M, Amaro J, Santos M, Perdigão F, Gomes M, Santos J. In-vivo automatic nuclear cataract detection and classification in an animal model by ultrasounds. *IEEE Trans Biomed Eng* 2016;63:2326–2335.
- Caixinha M, Jesus D, Velte E, Santos M, Santos J. Using ultrasound backscattering signals and Nakagami statistical distribution to assess regional cataract hardness. *IEEE Trans Biomed Eng* 2014a;61:2921–2929.
- Caixinha M, Nunes S. Machine learning techniques in clinical vision sciences. *Curr Eye Res* Taylor & Francis, 2016;30:1–15.
- Caixinha M, Santos M, Santos J. Automatic cataract hardness classification ex vivo by ultrasound techniques. *Ultrasound Med Biol* 2015a;.
- Caixinha M, Velte E, Santos M, Perdigão F, Amaro J, Gomes M, Santos J. Automatic cataract classification based on ultrasound technique using machine learning: A comparative study. *Phys Procedia* 2015b;70:1221–1224.
- Caixinha M, Velte E, Santos M, Santos JB. New approach for objective cataract classification based on ultrasound techniques using multiclass SVM classifiers. 2014 IEEE International Ultrasonics Symposium IEEE, 2014b. pp. 2402–2405.
- Cameron J. Physical properties of tissue. A comprehensive reference book, edited by Francis A. Duck. *Med Phys* 1991;18:834.
- Camparini M, Macaluso C, Reggiani L, Maraini G. Retroillumination versus reflected-light images in the photographic assessment of posterior capsule opacification. *Invest Ophthalmol Vis Sci* 2000;41:3074–9.

- Cardiff R, Miller C, Munn R. Manual hematoxylin and eosin staining of mouse tissue sections. *Cold Spring Harb Protoc* 2014;2014:655–658.
- Chang B, Smith RS, Hawes NL, Anderson MG, Zabaleta A, Savinova O, Roderick TH, Heckenlively JR, Davisson MT, John SW. Interacting loci cause severe iris atrophy and glaucoma in DBA/2J mice. *Nat Genet* 1999;21:405–9.
- Chang C-C, Lin C-J. LIBSVM. *ACM Trans. Intell. Syst. Technol.* 2011a. pp. 1–27.
- Chang C-C, Lin C-J. LIBSVM: A Library for Support Vector Machines. *ACM Trans Intell Syst Technol* 2011b;2:27:1–27:27.
- Chaudhari HD, Thakkar GN, Gandhi VS, Darji PJ. Role of ultrasonography in evaluation of orbital lesions. 2013;68.
- Chen EJ, Novakofski J, Jenkins WK, Brien WDO. Young's modulus measurements of soft tissues with application to elasticity imaging. *IEEE Trans Ultrason Ferroelectr Freq Control* 1996;43:191–194.
- Chen M, Anderson E, Hill G, Chen JJ, Patrianakos T. Comparison of cumulative dissipated energy between the Infiniti and Centurion phacoemulsification systems. *Clin Ophthalmol* 2015;9:1367–72.
- Cheung CYL, Li H, Lamoureux EL, Mitchell P, Wang JJ, Tan AG, Johari LK, Liu J, Lim JH, Aung T, Wong TY. Validity of a new computer-aided diagnosis imaging program to quantify nuclear cataract from slit-lamp photographs. *Investig Ophthalmol Vis Sci* 2011;52:1314–9.
- Chokkalingam SP. Comparison of different classifier in WEKA for rheumatoid arthritis. *ICHCI* 2013;1–6.
- Christensen D. *Ultrasonic Bioinstrumentation*. Wiley, 1988.
- Christopher KL, Pedler MG, Shieh B, Ammar DA, Petrash JM, Mueller NH. Alpha-crystallin-mediated protection of lens cells against heat and oxidative stress-induced cell death. *Biochim Biophys Acta* 2014;1843:309–15.
- Church CC, Barnett SB. *Ultrasound-induced heating and its biological consequences. safe use ultrasound Med diagnosis* Gail ter H. London: The British Institute of Radiology, 2000. pp. 46–68.
- Chylack LT, Leske MC, McCarthy D, Khu P, Kashiwagi T, Sperduto R. Lens opacities classification system II (LOCS II). *Arch Ophthalmol* 1989;107:991–7.
- Chylack LT, Wolfe JK, Singer DM, Leske MC, Bullimore MA, Bailey IL, Friend J, McCarthy D, Wu SY. The Lens Opacities Classification System III. The Longitudinal Study of

- Cataract Study Group. *Arch Ophthalmol* 1993;111:831–6.
- Cobbold RSC. *Foundations of Biomedical Ultrasound*. Oxford University Press, USA, 2006.
- Coleman DJ, Lizzi FL, Franzen LA, Abramson DH. A determination of the velocity of ultrasound in cataractous lenses. *Bibl Ophthalmol* 1975;246–51.
- Coombes A, Gartry D. *Fundamentals of clinical ophthalmology: Cataract surgery*. Coster D, Hitchins R, Acheson J, Riordan-Eva P, Moore A, Collin R, Rose G, McCluskey P, Billson F, Lightman S, Towler H, eds. London: BMJ Books, 2003.
- Cumming RG, Mitchell P. Alcohol, smoking, and cataracts: the Blue Mountains Eye Study. *Arch Ophthalmol* 1997;115:1296–303.
- Cumming RG, Mitchell P, Leeder SR. Use of inhaled corticosteroids and the risk of cataracts. *N Engl J Med* 1997;337:8–14.
- Dalecki D. Mechanical bioeffects of ultrasound. *Annu Rev Biomed Eng* 2004;6:229–248.
- Dantas RG, Costa ET, Leeman S. Ultrasound speckle and equivalent scatterers. *Ultrasonics* 2005;43:405–20.
- Datiles M, Edwards P, Trus B, Green S. In vivo studies on cataract using the Scheimpflug slit lamp camera. *Invest Ophthalmol Vis Sci* 1987;1707–1713.
- Datiles MB, Ansari RR. *Clinical evaluation of cataracts*. Duane's Ophthalmol Revised Ed. Lippincott Williams & Wilkins, 2006.
- Davignon F, Deprez J-F, Basset O. A parametric imaging approach for the segmentation of ultrasound data. *Ultrasonics* 2005;43:789–801.
- Davison JA, Chylack LT. Clinical application of the lens opacities classification system III in the performance of phacoemulsification. *J Cataract Refract Surg* 2003;29:138–145.
- de Korte CL, van der Steen AF, Thijssen JM. Acoustic velocity and attenuation of eye tissues at 20 MHz. *Ultrasound Med Biol* 1994;20:471–80.
- de la Rosa-Fox N, Morales-Florez V, Toledo-Fernandez JA, Pinero M, Mendoza-Serna R, Esquivias L. Nanoindentation on hybrid organic/inorganic silica aerogels. *J Eur Ceram Soc* 2007;27:3311–3316.
- Deane C, Lees C. Doppler obstetric ultrasound: a graphical display of temporal changes in safety indices. *Ultrasound Obstet Gynecol* 2000;15:418–23.
- Dick HB. *Corneal endothelium and other safety issues. Minimizing incisions maximizing outcomes* *Cataract Surg Berlin, Heidelberg: Springer Berlin Heidelberg*, 2010. pp. 292–296.
- Dick HB, Kohnen T, Jacobi FK, Jacobi KW. Long-term endothelial cell loss following

- phacoemulsification through a temporal clear corneal incision. *J Cataract Refract Surg* 1996;22:63–71.
- Dierks K, Dieckmann M, Niederstrasser D, Schwartz R, Wegener A. Protein size resolution in human eye lenses by dynamic light scattering after in vivo measurements. *Graefe's Arch Clin Exp Ophthalmol* 1998;236:18–23.
- Donaldson KE, Braga-Mele R, Cabot F, Davidson R, Dhaliwal DK, Hamilton R, Jackson M, Patterson L, Stonecipher K, Yoo SH. Femtosecond laser-assisted cataract surgery. *J Cataract Refract Surg ASCRS and ESCRS*, 2013;39:1753–1763.
- Ederer F, Hiller R, Taylor HR. Senile lens changes and diabetes in two population studies. *Am J Ophthalmol* 1981;91:381–95.
- El-Brawany M. Ultrasound-based noninvasive measurement of cataract hardness. *Online J Electron Electr Eng* 2009;246–249.
- El-Naqa I, Member S, Yang Y, Wernick MN, Member S, Galatsanos NP, Nishikawa RM. A Support Vector Machine Approach for Detection of Microcalcifications. *IEEE Trans Med Imaging* 2002;21:1552–1563.
- European Union. Council Directive 93/42/EEC of 14 June 1993 concerning medical devices.
- Eyben F, Wöllmer M, Schuller B. openSMILE - The Munich versatile and fast open-source audio feature extractor. *ACM Multimed Florence, Italy*, 2010. pp. 1459–1462.
- Fakhry MA, El Shazly MI. Torsional ultrasound mode versus combined torsional and conventional ultrasound mode phacoemulsification for eyes with hard cataract. *Clin Ophthalmol* 2011;5:973–8.
- Fan X, Thompson B, Wang L. Effects of sample size, estimation methods, and model specification on structural equation modeling fit indexes. *Struct Equ Model Psychology Press*, 1999;6:56–83.
- Faul F, Erdfelder E, Albert-george, Buchner A. *G*Power 3 : A flexible statistical power analysis program for the social , behavioral, and biomedical sciences*. *Behav Res Methods* 2007;39:175–191.
- Faul F, Erdfelder E, Buchner A, Lang A-G. Statistical power analyses using G*Power 3.1: tests for correlation and regression analyses. *Behav Res Methods* 2009;41:1149–60.
- Ferreira JS. Sistema de aquisição ecográfica para oftalmologia usando uma arquitetura SoC Zynq-7000. Master Thesis. University of Coimbra, 2015.
- Filgueira CP, Sánchez RF, Issolio LA, Elisa M, Paz C, Sánchez RF, Issolio LA, Colombo EM. Straylight and visual quality on early nuclear and posterior subcapsular cataracts. *Curr Eye*

- Res 2016;3683:1460–2202.
- Findl O. Biometry and intraocular lens power calculation. *Curr Opin Ophthalmol* 2005;16:61–4.
- Fine I, Packer M, Hoffman R. Power modulations in new phacoemulsification technology: Improved outcomes. *J Cataract Refract Surg* 2004;30:1014–1019.
- Fine IH, Packer M, Hoffman RS. Use of power modulations in phacoemulsification Choo-choo chop and flip phacoemulsification. *J Refract Surgery* 2001;27.
- Fine IH, Packer M, Hoffman RS. New phacoemulsification technologies. *J Cataract Refract Surg* 2002;28:1054–60.
- Fischer A, Jacobson K, Rose J, Zeller R. Hematoxylin and eosin staining of tissue and cell sections. *CSH Protoc* 2008;2008:pdb.prot4986.
- Fischer-Cripps AC. Nanoindentation. *Mech. Eng. Ser.* Springer New York, 2011.
- Fisher RF. Elastic constants of the human lens capsule. *J Physiol* 1969;201:1–19.
- Fisher RF. The elastic constants of the human lens. *J Physiol* 1971;212:147–80.
- Foster S, Zhang M, Duckett AS, Cucevic V, Pavlin CJ. In vivo imaging of embryonic development in the mouse eye by ultrasound biomicroscopy. *Invest Ophthalmol Vis Sci* 2003;44:2361–2366.
- Gao X, Wong DWK, Ng T-T, Cheung CYL, Cheng C-Y, Wong TY. Automatic grading of cortical and PSC cataracts using retroillumination lens images. Lee KM, Matsushita Y, Rehg JM, Hu Z, eds. *Comput Vis – ACCV 2012 Berlin, Heidelberg*: Springer Berlin Heidelberg, 2013;7725:256–267.
- Garbe E, Suissa S, LeLorier J. Association of inhaled corticosteroid use with cataract extraction in elderly patients. *JAMA* 1998;280:539–43.
- Gefen A, Shalom R, Elad D, Mandel Y. Biomechanical analysis of the keratoconic cornea. *J Mech Behav Biomed Mater* 2009;2:224–36.
- Goswami S, Sheets N, Zavadil J. Spectrum and range of oxidative stress responses of human lens epithelial cells to H₂O₂ Insult. *Invest Ophthalmol Vis Sci* 2003;44:2084–2093.
- Guggenheim JA, Creer RC, Qin X-J. Postnatal refractive development in the Brown Norway rat: Limitations of standard refractive and ocular component dimension measurement techniques. *Curr Eye Res* 2004;29:369–376.
- Gupta M, Ram J, Jain A, Sukhija J, Chaudhary M. Correlation of nuclear density using the Lens Opacity Classification System III versus Scheimpflug imaging with phacoemulsification parameters. *J Cataract Refract Surg* 2013;39:1818–1823.

- Guyon I, Elisseeff A. An introduction to variable and feature selection. *J Mach Learn Res MIT Press*, 2003;3:1157–1182.
- Haar G. Ultrasonic imaging: safety considerations. *Interface Focus* 2011;1:686–697.
- Haidekker M. *Advanced biomedical image analysis*. John Wiley & Sons, 2011.
- Hall M, Frank E, Holmes G, Pfahringer B, Reutemann P, Witten IH. The WEKA data mining software. *ACM SIGKDD Explor* 2009;11:10–18.
- Hammond CJ, Duncan DD, Snieder H, de Lange M, West SK, Spector TD, Gilbert CE. The heritability of age-related cortical cataract: the twin eye study. *Invest Ophthalmol Vis Sci* 2001;42:601–5.
- Hammond CJ, Snieder H, Spector TD, Gilbert CE. Genetic and environmental factors in age-related nuclear cataracts in monozygotic and dizygotic twins. *N Engl J Med* 2000;342:1786–90.
- Haralick RM, Shanmugam K, Dinstein I. Textural features for image classification. *IEEE Trans Syst Man Cybern IEEE*, 1973;3:610–621.
- Harding JJ, van Heyningen R. Drugs, including alcohol, that act as risk factors for cataract, and possible protection against cataract by aspirin-like analgesics and cyclopentiazide. *Br J Ophthalmol* 1988;72:809–14.
- Haripriya A, Chang DF, Reena M, Shekhar M. Complication rates of phacoemulsification and manual small-incision cataract surgery at Aravind Eye Hospital. *J Cataract Refract Surg* 2012;38:1360–1369.
- Hashim Z, Zarina S. Osmotic stress induced oxidative damage: possible mechanism of cataract formation in diabetes. *J Diabetes Complications* 2012;26:275–9.
- Hatch KM, Schultz T, Talamo JH, Dick HB. Femtosecond laser-assisted compared with standard cataract surgery for removal of advanced cataracts. *J Cataract Refract Surg ASCRS and ESCRS*, 2015;41:1833–1838.
- Hawes NL, Chang B, Hageman GS, Nusinowitz S, Nishina PM, Schneider BS, Smith RS, Roderick TH, Davisson MT, Heckenlively JR. Retinal degeneration 6 (rd6): a new mouse model for human retinitis punctata albescens. *Invest Ophthalmol Vis Sci* 2000;41:3149–57.
- Hayashi K, Hayashi H, Nakao F, Hayashi F. Risk factors for corneal endothelial injury during phacoemulsification. *J Cataract Refract Surg* 1996;22:1079–84.
- Hayashi K, Nakao F, Hayashi F. Corneal endothelial cell loss following phacoemulsification using the Small-Port Phaco. *Ophthalmic Surg* 1994;25:510–513.
- He X, Liu J. A quantitative ultrasonic spectroscopy method for noninvasive determination of

- corneal biomechanical properties. *Invest Ophthalmol Vis Sci* 2009;50:5148–54.
- He X, Liu J. Correlation of corneal acoustic and elastic properties in a canine eye model. *Invest Ophthalmol Vis Sci* 2011;1–26.
- Heiba IM, Elston RC, Klein BE, Klein R. Genetic etiology of nuclear cataract: evidence for a major gene. *Am J Med Genet* 1993;47:1208–14.
- Heiba IM, Elston RC, Klein BE, Klein R. Evidence for a major gene for cortical cataract. *Invest Ophthalmol Vis Sci* 1995;36:227–35.
- Hejtmancik FJ. Cataracts dissolved. *Nature* 2015;1–2.
- Herman B a, Harris GR. Theoretical study of steady-state temperature rise within the eye due to ultrasound insonation. *IEEE Trans Ultrason Ferroelectr Freq Control* 1999;46:1566–74.
- Hermans E, Dubbelman M, van der Heijde R, Heethaar R. The shape of the human lens nucleus with accommodation. *J Vis* 2007;7:16.1–10.
- Hermans EA, Dubbelman M, van der Heijde GL, Heethaar RM. Change in the accommodative force on the lens of the human eye with age. *Vision Res* 2008;48:119–126.
- Hlinomazová Z, Hrazdira I. ALARA – principle and safety problems of diagnostic ultrasound. *Scr Med (Brno)* 2005;78:341–346.
- Ho MC, Lee YH, Jeng YM, Chen CN, Chang KJ, Tsui PH. Relationship between ultrasound backscattered statistics and the concentration of fatty droplets in livers: An animal study. *PLoS One* 2013;8.
- Ho MC, Lin JJ, Shu YC, Chen CN, Chang KJ, Chang CC, Tsui PH. Using ultrasound Nakagami imaging to assess liver fibrosis in rats. *Ultrasonics* 2012;52:215–22.
- Hodge WG, Witcher JP, Satariano W. Risk factors for age-related cataracts. *Epidemiol Rev* 1995;17:336–46.
- Hollman KW, O'Donnell M, Erpelding TN. Mapping elasticity in human lenses using bubble-based acoustic radiation force. *Exp Eye Res* 2007;85:890–893.
- Order MM, Barnett SB, Vella GJ, Edwards MJ, Wood AKW. In vivo heating of the guinea-pig fetal brain by pulsed ultrasound and estimates of thermal index. *Ultrasound Med Biol* 1998;24:1467–1474.
- Horwitz J, Bova M, Ding L, Haley D, Stewart P. Lens alpha-crystallin: function and structure. *Eye (Lond)* 1999;13 (Pt 3b:403–408.
- Hozic A, Rico F, Colom A, Buzhynskyy N, Scheuring S. Nanomechanical characterization of the stiffness of eye lens cells: a pilot study. *Invest Ophthalmol Vis Sci* 2012;53:2151–2156.

- Hsu C-W, Chang C-C, Lin C-J. A practical guide to Support Vector Classification. Taipei, Taiwan, 2010. Report No.: April 15, 2010 (last updated).
- Huang C, Ameri H, Deboer C, Rowley A, Xu X, Sun L, Wang S, Humayun M, Shung K. Evaluation of lens hardness in cataract surgery using high-frequency ultrasonic parameters in vitro. *Ultrasound Med Biol* 2007a;33:1609–16.
- Huang C, Chen R, Tsui P. Measurements of attenuation coefficient for evaluating the hardness of a cataract lens by a high-frequency ultrasonic needle transducer. *Phys Med Biol* 2009a;54:5981–5994.
- Huang C, Zhou Q, Ameri H, Wu W, Sun L, Wang S, Humayun M, Shung K. Determining the acoustic properties of the lens using a high-frequency ultrasonic needle transducer. *Ultrasound Med Biol* 2007b;33:1971–7.
- Huang C-C, Tsui P-H, Zhou Q, Humayun MS, Shung KK. In situ measurements of attenuation coefficient for evaluating the hardness of cataract lens by a high frequency ultrasonic needle transducer. 2009 IEEE International Ultrasonics Symposium Ieee, 2009b;:240–243.
- Hughes A. A schematic eye for the rat. *Vision Res* 1979;
- Ikeda S, Shiva N, Ikeda A, Smith RS, Nusinowitz S, Yan G, Lin TR, Chu S, Heckenlively JR, North MA, Naggert JK, Nishina PM, Duyao MP. Retinal degeneration but not obesity is observed in null mutants of the tubby-like protein 1 gene. *Hum Mol Genet* 2000;9:155–63.
- Ilavská M, Kardos L. Phacoemulsification of mature and hard nuclear cataracts. *Bratislava Med J* 2010;111:93–96.
- International Electrotechnical Commission. IEC 61157 - Requirements for the declaration of the acoustic output of medical diagnostic ultrasonic equipment. 1992.
- International Electrotechnical Commission. IEC 60601-2-37 - Medical electrical equipment – Part 2-37: Particular requirements for the safety of ultrasonic medical diagnostic and monitoring equipment. 2005.
- Jain A, Duin R, Mao J. Statistical pattern recognition: A review. *IEEE Trans Pattern Anal Mach Intell* 2000;22:4–37.
- Jesus D, Caixinha M, Santos M, Santos J. Ultrasound techniques for lens hardness characterization: A comparison study. 2012 IEEE International Ultrasonics Symposium Ieee, 2012. pp. 2376–2379.
- Jesus D, Velte E, Caixinha M, Santos M, Santos J. Using of the ultrasound frequency dependent attenuation and Nakagami distribution for cataract evaluation. 2013 IEEE 3rd Portuguese Meeting in Bioengineering (ENBENG) Ieee, 2013. pp. 1–4.

- Jin H, Randazzo J, Zhang P, Kador PF. Multifunctional antioxidants for the treatment of age-related diseases. *J Med Chem* 2010;53:1117–27.
- Johansson B, Lundström M, Montan P, Stenevi U, Behndig A. Capsule complication during cataract surgery: Long-term outcomes. Swedish Capsule Rupture Study Group report 3. *J Cataract Refract Surg* 2009;35:1694–1698.
- Kalisz A. Statistical framework for ultrasonic spectral parameter imaging. 1997;13.
- Kambhatla N, Leen T. Dimension reduction by local principal component analysis. *Neural Comput* 1997;9:1493–1516.
- Kanski JJ, Bowling B. *Clinical Ophthalmology: A Systematic Approach*. 6th ed. Butterworth-Heinemann: Elsevier Science Limited, 2006.
- Kedzierski W, Nusinowitz S, Birch D, Clarke G, McInnes RR, Bok D, Travis GH. Deficiency of rds/peripherin causes photoreceptor death in mouse models of digenic and dominant retinitis pigmentosa. *National Academy of Sciences of the United States of America* 2001. pp. 7718–23.
- Keenan J, Orr DF, Pierscionek BK. Patterns of crystallin distribution in porcine eye lenses. *Mol Vis* 2008;14:1245–53.
- Kim HK. Decrease and conquer: Phacoemulsification technique for hard nucleus cataracts. *J Cataract Refract Surg* 2009;35:1665–1670.
- Kim K-B, Hsu DK, Barnard DJ. Estimation of porosity content of composite materials by applying discrete wavelet transform to ultrasonic backscattered signal. *NDT E Int* 2013;56:10–16.
- Kirwan J, Venter L, Stulting A, Murdoch I. LOCS III examination at the slit lamp, do settings matter? *Ophthalmic Epidemiol*. 2003. pp. 259–266.
- Klein BE, Klein R, Linton KL. Prevalence of age-related lens opacities in a population. The Beaver Dam Eye Study. *Ophthalmology* 1992;99:546–52.
- Klein BE, Klein R, Linton KL, Franke T. Cigarette smoking and lens opacities: the Beaver Dam Eye Study. *Am J Prev Med* 1993;9:27–30.
- Klein BE, Magli Y, Neider MW, Klein R. Wisconsin system for classification of cataracts from photographs. University of Wisconsin, 1989.
- Kolar R, Jirik R, Jan J. Estimator comparison of the Nakagami-m parameter and its application in echocardiography. *Radioengineering* 2004;8–12.
- Kolhe S, Guru S. Cataract classification and grading: A survey. *IJIRCCE* 2015;3:8093–8100.

- Konstantopoulos A, Hossain P, Anderson DF. Recent advances in ophthalmic anterior segment imaging: a new era for ophthalmic diagnosis? *Br J Ophthalmol* 2007;91:551–7.
- Kruk J, Kubasik-Kladna K, Aboul-Enein HY. The role oxidative stress in the pathogenesis of eye diseases: Current status and a dual role of physical activity. *Mini Rev Med Chem* 2015;16:241–57.
- Kuwabara T. The maturation of the lens cell: a morphologic study. *Exp Eye Res* 1975;20:427–443.
- Kyselova Z. Different experimental approaches in modelling cataractogenesis: An overview of selenite-induced nuclear cataract in rats. *Interdiscip Toxicol* 2010;3:3–14.
- Langner S, Martin H, Terwee T, Koopmans S a, Krüger PC, Hosten N, Schmitz K-P, Guthoff RF, Stachs O. 7.1 T MRI to assess the anterior segment of the eye. *Invest Ophthalmol Vis Sci* 2010;51:6575–81.
- Lee W, Garra B. AIUM Technical Bulletin. How to interpret the ultrasound output display standard for higher acoustic output diagnostic ultrasound devices: version 2. *J Ultrasound Med* 2004;23:723–6.
- Lenhart PD, Hutchinson AK, Lynn MJ, Lambert SR. Partial coherence interferometry versus immersion ultrasonography for axial length measurement in children. *J Cataract Refract Surg ASCRS and ESCRS*, 2010;36:2100–4.
- Leon P, Umari I, Mangogna A, Zanei A, Tognetto D. An evaluation of intraoperative and postoperative outcomes of torsional mode versus longitudinal ultrasound mode phacoemulsification: A meta-analysis. *Int J Ophthalmol* 2016;9:890–7.
- Leong T, Ashokkumar M, Kentish S. The fundamentals of power ultrasound – A review. *Acoust Aust* 2011;39:54–63.
- Leske MC, Chylack LT, Sperduto R, Khu P, Wu SY, McCarthy D. Evaluation of a Lens Opacities Classification System. *Arch Ophthalmol* 1988;106:327–9.
- Li L, Cheng C, Xia C, White TW, Fletcher D a, Gong X. Connexin mediated cataract prevention in mice. *PLoS One* 2010;5:1–8.
- Liao Y-Y, Li C-H, Tsui P-H, Chang C-C, Kuo W-H, Chang K-J, Yeh C-K. Strain-compounding technique with ultrasound Nakagami imaging for distinguishing between benign and malignant breast tumors. *Med Phys* 2012;39:2325.
- Lin Y-H, Huang C-C, Wang S-H. Quantitative assessments of burn degree by high-frequency ultrasonic backscattering and statistical model. *Phys Med Biol* 2011;56:757–73.
- Liu Y, Zeng M, Liu X, Luo L, Yuan Z, Dia Y, Zeng Y. Torsional mode versus conventional

- ultrasound mode phacoemulsification: randomized comparative clinical study. *J Cataract Refract Surg* 2007;33:287–92.
- Lizzi F, Feleppa E, Kaiser A, Deng C. Ultrasonic spectrum analysis for tissue evaluation. *Pattern Recognit Lett* 2003;24:637–658.
- Lizzi FL, Coleman DJ. History of Ophthalmic Ultrasound. *J ultrasound Med* 2004;23:1255–1266.
- Lozano DC, Twa MD. Development of a rat schematic eye from in vivo biometry and the correction of lateral magnification in SD-OCT imaging. *Invest Ophthalmol Vis Sci* 2013;54:6446–55.
- Lundström M, Barry P, Henry Y, Rosen P, Stenevi U. Evidence-based guidelines for cataract surgery: Guidelines based on data in the European Registry of Quality Outcomes for Cataract and Refractive Surgery database. *J Cataract Refract Surg* 2012;38:1086–1093.
- Machado CB, Pereira WCDA, Meziri M, Laugier P. Characterization of in vitro healthy and pathological human liver tissue periodicity using backscattered ultrasound signals. *Ultrasound Med Biol* 2006;32:649–57.
- Magalhães FP, Costa EF, Cariello AJ, Rodrigues EB, Hofling-Lima AL. Comparative analysis of the nuclear lens opalescence by the lens opacities classification system III with nuclear density values provided by oculus pentacam: A cross-section study using pentacam nucleus staging software. *Arq Bras Oftalmol* 2011;74:110–113.
- Magno B, Datiles M, Lasa S. Senile cataract progression studies using the Lens Opacities Classification System II. *Invest Ophthalmol Vis Sci* 1993;34:2138–2141.
- Malhotra R. *Eye Essentials Cataract Assessment Classification and Management*. Butterworth Heinemann, ed. Elsevier, 2008.
- Mamou J, Oelze ML. Quantitative ultrasound in soft tissues. Mamou J, Oelze ML, eds. London: Springer, 2013.
- Manikandan R, Thiagarajan R. Anti-cataractogenic effect of curcumin and aminoguanidine against selenium-induced oxidative stress in the eye lens of Wistar rat pups: An in vitro study using isolated lens. *Chem Biol Interact* 2009;181:202–209.
- Massof RW, Chang FW. A revision of the rat schematic eye. *Vision Res* 1972;12:793–796.
- MathWorks Inc. Signal Processing Toolbox™ User's Guide R2015b. MathWorks Inc. 2015. p. Overview. Available from: <http://www.mathworks.co.uk/products/signal/index.html>
- McCarty CA, Mukesh BN, Fu CL, Taylor HR. The epidemiology of cataract in Australia. *Am J Ophthalmol* 1999;128:446–65.

- McKee CT, Last J a, Russell P, Murphy CJ. Indentation versus tensile measurements of Young's modulus for soft biological tissues. *Tissue Eng Part B Rev* 2011;17:155–164.
- Meyers LS, Gamst G, Guarino AJ. *Applied multivariate research: Design and interpretation*. J. Oper. Res. Soc. 2006.
- Michael R, Bron AJ. The ageing lens and cataract: a model of normal and pathological ageing. *Philos Trans R Soc Lond B Biol Sci* 2011;366:1278–92.
- Moeini H, Eslami F. Comparison of ultrasound and optic biometry with respect to eye refractive errors after phacoemulsification. *J Res Med Sci* 2008;13:43–47.
- Muhtaseb M, Kalhoro A, Ionides A. A system for preoperative stratification of cataract patients according to risk of intraoperative complications: A prospective analysis of 1441 cases. *Br J Ophthalmol* 2004;88:1242–6.
- Mundt G, Hughes W. Ultrasonics in ocular diagnosis. *Am J Ophthalmol* 1956;41:488–489.
- Muñoz B, Tajchman U, Bochow T, West S. Alcohol use and risk of posterior subcapsular opacities. *Arch Ophthalmol* 1993;111:110–2.
- Nakajima K, Kudo N, Yamamoto K, Mikami T, Kitabatake A. A study on frequency dependence of ultrasound attenuation of biological tissue in the frequency range of 2-40 MHz. *IEEE Ultrasonics Symposium* 1999;1381–1384.
- Nakajima T, Nakajima E, Fukiage C, Azuma M, Shearer TR. Differential gene expression in the lens epithelial cells from selenite injected rats. *Exp Eye Res* 2002;74:231–6.
- Narayana PA, Ophir J. On the validity of the linear approximation in the parametric measurement of attenuation in tissues. *Ultrasound Med Biol* 1983;9:357–61.
- Needles A, Arditì M, Rognin NG, Mehi J, Coulthard T, Bilan-Tracey C, Gaud E, Frinking P, Hirson D, Foster FS. Nonlinear contrast imaging with an array-based micro-ultrasound system. *Ultrasound Med Biol* 2010;36:2097–106.
- Njie-Mbye YF, Kulkarni-Chitnis M, Opere CA, Barrett A, Ohia SE. Lipid peroxidation: pathophysiological and pharmacological implications in the eye. *Front Physiol* 2013;4:366.
- Noble J, Wells P. Ultrasound image segmentation and tissue characterization. *Institution of Mechanical Engineers Part H, Journal of engineering in medicine* 2010;224:307–16.
- O'Brien WD. Ultrasound-biophysics mechanisms. *Prog Biophys Mol Biol* 2007;93:212–55.
- Oelze ML, O'Brien WD. Frequency-dependent attenuation-compensation functions for ultrasonic signals backscattered from random media. *J Acoust Soc Am* 2002;111:2308.
- Oguchi Y, van Marle GW, Eijsskoot F, Henkes HE. Study of the ultrasonic characteristics of the

- lens. *Bibl Ophthalmol* 1975;252–8.
- Oksala A, Lehtinen A. Measurement of the velocity of sound in some parts of the eye. *Acta Ophthalmol* 1958;633–639.
- Oliver W, Pharr G. An improved technique for determining hardness and elastic modulus using load and displacement sensing indentation experiments. *J Mater Res* 1992;7:1564–1583.
- Ošťádalová I, Babický A, Obenberger J. Cataract induced by administration of a single dose of sodium selenite to suckling rats. *Experientia* 1977;34:222–223.
- Pal SK, Mitra S. Multilayer perceptron, fuzzy sets, and classification. *IEEE Trans Neural Networks* 1992;3:683–697.
- Palte HD, Gayer S, Arrieta E, Scot Shaw E, Nose I, Lee E, Arheart KL, Dubovy S, Birnback DJ, Parel J-M. Are ultrasound-guided ophthalmic blocks injurious to the eye? A comparative rabbit model study of two ultrasound devices evaluating intraorbital thermal and structural changes. *Anesth Analg* 2012;115:194–201.
- Panchapakesan J, Cumming RG, Mitchell P. Reproducibility of the Wisconsin cataract grading system in the Blue Mountains Eye Study. *Ophthalmic Epidemiol* 1997;4:119–126.
- Panich N, Yong S. Improved method to determine the hardness and elastic modulus using nanoindentation. *KMITL Sci J* 2005;5:483–492.
- Parker KJ, Lerner RM, Waag RC. Comparison of techniques for in vivo attenuation measurements. *IEEE Trans Biomed Eng* 1988;35:1064–8.
- Paunksnis A, Kurapkienė S, Mačiulis A. Ultrasound quantitative evaluation of human eye cataract. *Informatika* 2007;18:267–278.
- Paunksnis A, Kurapkienė S, Mačiulis A, Raitelaitienė R, Jurkonis R, Lukoševičius A. Estimation of ultrasound attenuation coefficient of human diabetic cataract. *Ultragarsas* 2003;46:37–40.
- Pavlin CJ, Foster FS. *Ultrasound biomicroscopy of the eye*. Springer Science & Business Media, 2012.
- Pershing S, Kumar A. Phacoemulsification versus extracapsular cataract extraction: where do we stand? *Curr Opin Ophthalmol* 2011;22:37–42.
- Phaniendra A, Jestadi DB, Periyasamy L. Free radicals: properties, sources, targets, and their implication in various diseases. *Indian J Clin Biochem* 2015;30:11–26.
- Piñero DP, Plaza AB, Alió JL. Anterior segment biometry with 2 imaging technologies: very-high-frequency ultrasound scanning versus optical coherence tomography. *J Cataract Refract Surg* 2008;34:95–102.

- Prokofyeva E, Wegener A, Zrenner E. Cataract prevalence and prevention in Europe: A literature review. *Acta Ophthalmol* 2013;91:395–405.
- Quinlan J. Learning decision tree classifiers. *ACM Comput Surv* 1996;28:71–72.
- Raitelaitienė R, Paunksnis A. Ultrasonic and biochemical evaluation of human diabetic lens. *Med* 2005;41.
- Ray S, Behari J. Ultrasound attenuation in biological tissues using a bone transducer. *Med Biol Eng Comput* 1987;25:689–692.
- Realini T, Lovelace K. Measuring central corneal thickness with ultrasound pachymetry. *Optom Vis Sci* 2003;80:437–439.
- Rokach L, Maimon O. Top-down induction of decision trees classifiers - a survey. *IEEE Trans Syst Man, Cybern Part C (Applications Rev)* 2005;35.
- Sajda P. Machine learning for detection and diagnosis of disease. *Annu Rev Biomed Eng* 2006;8:537–65.
- Santos J, Gomes M, Santos M, Perdigão F, Morgado A, Caixinha M, Amaro J, Ferreira J. ESUS – Eye Scan Ultrasound System (PPP108836). Portugal, 2015.
- Santos JB. The power of ultrasonic spectroscopy in the complete characterisation of materials. *Insight Non-Destructive Test Cond Monit* 1998;40:855–859.
- Santosa S, Jones PJH. Oxidative stress in ocular disease: does lutein play a protective role? *CMAJ* 2005;173:861–2.
- Schafer ME, Arbisser LB. Quantification of acoustic exposure during cataract surgery. *IEEE Ultrason Symp 2004 IEEE*, 2004. pp. 1828–1831.
- Schumacher S, Fromm M, Lakharia R, Schaefer M, Oberheide U, Ripken T, Breitenfeld P, Gerten G, Ertmer W, Lubatschowski H. Fs-laser induced flexibility increase in the crystalline lens. *Ophthalmic Technol XVII* 2007;6426:C4261.
- Shankar H, Pagel P. Potential adverse ultrasound-related biological effects - A critical review. *Anesthesiology* 2011;115:1109–1124.
- Shankar P. A general statistical model for ultrasonic backscattering from tissues. *IEEE Trans Ultrason Ferroelectr Freq Control* 2000;47:727–36.
- Shankar PM, Dumane VA, George T, Piccoli CW, Reid JM, Forsberg F, Goldberg BB. Classification of breast masses in ultrasonic B scans using Nakagami and K distributions. *Phys Med Biol* 2003;48:2229–2240.
- Shankar PM, Dumane VA, Reid JM, Genis V, Forsberg F, Piccoli CW, Goldberg BB.

- Classification of ultrasonic B-mode images of breast masses using Nakagami distribution. *IEEE Trans Ultrason Ferroelectr Freq Control* 2001;48:569–80.
- Shearer TR, Ma H, Fukiage C, Azuma M. Selenite nuclear cataract: Review of the model. *Mol Vis* 1997;3:8.
- Shi Y, Barton K, De Maria A, Petrash JM, Shiels A, Bassnett S. The stratified syncytium of the vertebrate lens. *J Cell Sci* 2009;122:1607–1615.
- Shin H, Markey MK. A machine learning perspective on the development of clinical decision support systems utilizing mass spectra of blood samples. *J Biomed Inform* 2006;39:227–248.
- Siddiqui K. Heuristics for sample size determination in multivariate statistical techniques. *World Appl Sci J* 2013;27:285–287.
- Siddiqui M a R, Awan MA, Fairhead A, Atta H. Ultrasound velocity in heavy ocular tamponade agents and implications for biometry. *Br J Ophthalmol* 2011;95:142–4.
- Silverman RH. High-resolution ultrasound imaging of the eye - a review. *Clin Experiment Ophthalmol* 2009;37:54–67.
- Smadja D, Krueger RR. Femtosecond Laser Lens Fragmentation. In: Afshari NA, Copeland JR., eds. *Copel Afshari's Princ Pract Cornea Jaypee-Highlights Medical Publishers, Inc*, 2013. p. 7.
- Smith JMA, El-Brawany M, Nassiri D, Tabandeh H, Thompson GM. The relationship between nuclear colour and opalescence on the LOCSIII scale and physical characteristics of cataract nuclei. *Eye (Lond)* 2002;16:543–51.
- Smith RS, John SWM, Nishina PM, Sundberg JP. Systematic evaluation of the mouse eye: Anatomy, pathology, and biomethods. Richard S. Smith, Simon W. M. John, Patsy M. Nishina JPS, ed. Boca Raton: CRC Press Book, 2001.
- Smith RS, Sundberg JP, Linder CC. Mouse mutations as models for studying cataracts. *Pathobiology* 1997;65:146–54.
- Smolíková R, Wachowiak MPMP, Zurada JMJM. An information-theoretic approach to estimating ultrasound backscatter characteristics. *Comput Biol Med* 2004;34:355–70.
- Solberg Y, Rosner M, Belkin M. The association between cigarette smoking and ocular diseases. *Surv Ophthalmol* 1998;42:535–47.
- Sparrow JM, Bron AJ, Brown NA, Ayliffe W, Hill AR. The Oxford Clinical Cataract Classification and Grading System. *Int Ophthalmol* 1986;9:207–25.
- Spurrier JD. On the null distribution of the Kruskal–Wallis statistic. *J Nonparametr Stat Taylor*

- & Francis, 2003;15:685–691.
- Sugata Y, Murakami K, Ito M, Shiina T, Yamamoto Y. An application of ultrasonic tissue characterization to the diagnosis of cataract. *Acta Ophthalmol Suppl (Oxf)* 1992;35–9.
- Sugiura T, Kurosaka D, Uezuki Y. Creating cataract in a pig eye. *J Cataract Refract Surg* 1999;25:615–621.
- Syed NA, Windle JJ, Darjatmoko SR, Lokken JM, Steeves RA, Chappell R, Wallow IH, Koop BA, Mangold G, Howes KA, Albert DM. Transgenic mice with pigmented intraocular tumors: tissue of origin and treatment. *Invest Ophthalmol Vis Sci* 1998;39:2800–5.
- Tabandeh H, Thompson GM, Heyworth P. Lens hardness in mature cataracts. *Eye (Lond)* 1994;8:453–5.
- Tabandeh H, Wilkins M, Thompson G, Nassiri D, Karim A. Hardness and ultrasonic characteristics of the human crystalline lens. *J Cataract Refract Surg* 2000;26:838–41.
- Tabin G, Chen M, Espandar L. Cataract surgery for the developing world. *Curr Opin Ophthalmol* 2008;19:55–59.
- Tang X. Texture information in run-length matrices. *IEEE Trans Image Process* 1998;7:1602–9.
- Taylor A, Jacques PF, Epstein EM. Relations among aging, antioxidant status, and cataract. *Am J Clin Nutr* 1995;62:1439S–1447S.
- Taylor HR. Epidemiology of age-related cataract. *Eye (Lond)* 1999;13:445–8.
- Taylor HR, West SK, Rosenthal FS, Muñoz B, Newland HS, Abbey H, Emmett EA. Effect of ultraviolet radiation on cataract formation. *N Engl J Med* 1988;319:1429–33.
- Thakur A, Anand R. Image quality based comparative evaluation of wavelet filters in ultrasound speckle reduction. *Digit Signal Process* 2005;15:455–465.
- The Royal College of Ophthalmologists. *Cataract surgery guidelines*. London, 2010.
- The Royal College of Ophthalmologists. *Cataract surgery*. London, 2015.
- Thylefors B, Chylack LT, Konyama K, Sasaki K, Sperduto R, Taylor HR, West S. A simplified cataract grading system. *Ophthalmic Epidemiol*. 2002. pp. 83–95.
- Tournoy KG, Bolly A, Aerts JG, Pierard P, De Pauw R, Leduc D, Leloup A, Pieters T, Slabbynck H, Janssens A, Carron K, Schrevels L, Pat K, De Keukeleire T, Doms C. The value of endoscopic ultrasound after bronchoscopy to diagnose thoracic sarcoidosis. *Eur Respir J* 2010;35:1329–35.
- Tsui P, Chang C. Imaging local scatterer concentrations by the Nakagami statistical model. *Ultrasound Med Biol* 2007;33:608–19.

- Tsui P, Chang C, Ho M, Lee Y, Chen Y, Huang N, Wu Z, Chang K. Use of Nakagami statistics and empirical mode decomposition for ultrasound tissue characterization by a nonfocused transducer. *Ultrasound Med Biol* 2009;35:2055–68.
- Tsui P hsiang, Yeh CK, Chang C cheng. Noise Effect on the Performance of Nakagami Image in Ultrasound Tissue Characterization. *J Med Biol Eng* 2008;28:197–202.
- Tsui P, Huang C, Chang C, Wang S, Shung K. Feasibility study of using high-frequency ultrasonic Nakagami imaging for characterizing the cataract lens in vitro. *Phys Med Biol* 2007;52:6413–6425.
- Tsui P, Huang C, Wang S. Use of Nakagami distribution and logarithmic compression in ultrasonic tissue characterization. *J Med Biol Eng* 2006;26:69–73.
- Tsui P, Huang C, Zhou Q, Shung K. Cataract measurement by estimating the ultrasonic statistical parameter using an ultrasound needle transducer: An in vitro study. *Physiol Meas* 2011;32:513–522.
- Tsui P, Wan Y, Chien Y. Dependency of Ultrasonic Nakagami Image on The Mechanical Properties of Scattering Medium. *J Med Biol Eng* 2013;33:95–102.
- Tsui P, Wan Y, Huang C, Wang M. Effect of adaptive threshold filtering on ultrasonic Nakagami parameter to detect variation in scatterer concentration. *Ultrason Imaging* 2010a;32:229–242.
- Tsui P, Yeh C, Huang C. Noise-assisted correlation algorithm for suppressing noise-induced artifacts in ultrasonic Nakagami images. *IEEE Trans Inf Technol Biomed* 2012;16:314–22.
- Tsui PH, Liao YY, Chang CC, Kuo WH, Chang KJ, Yeh CK. Classification of benign and malignant breast tumors by 2-D analysis based on contour description and scatterer characterization. *IEEE Trans Med Imaging* 2010b;29:513–522.
- Tsui PH, Wan YL, Tai DI, Shu YC. Effects of estimators on ultrasound Nakagami imaging in visualizing the change in the backscattered statistics from a Rayleigh distribution to a Pre-Rayleigh distribution. *Ultrasound Med Biol* 2014;1–12.
- U RA, Ng YKE, Suri JS. *Image modeling of the human eye*. Artech House, 2008.
- U.S Department of Health and Human Services, FDA Food and Drug Administration, CDRH Center for Devices and Radiological Health. *Guidance for industry and FDA staff - Information for manufacturers seeking marketing clearance of diagnostic ultrasound systems and transducers*. 2008.
- Uchio E, Ohno S, Kudoh J. Simulation model of an eyeball based on finite element analysis on a supercomputer. *Br J Ophthalmol* 1999;1106–1111.

- van Oterendorp C, Diaz-Santana L, Bull N, Biermann J, Jordan JF, Lagrèze W a, Martin KR. Light scattering and wavefront aberrations in in vivo imaging of the rat eye: A comparison study. *Invest Ophthalmol Vis Sci* 2011;52:4551–9.
- Venkatesh R, Tan CSH, Sengupta S, Ravindran RD, Krishnan KT, Chang DF. Phacoemulsification versus manual small-incision cataract surgery for white cataract. *J Cataract Refract Surg* 2010;36:1849–1854.
- Wagner RF, Smith SW, Sandrik JM, Lopez H. Statistics of speckle in ultrasound B-scans. *IEEE Trans Sonics Ultrason IEEE*, 1983;30:156–163.
- Walkow T, Anders N, Klebe S. Endothelial cell loss after phacoemulsification: Relation to preoperative and intraoperative parameters. *J Cataract Refract Surg* 2000;26:727–32.
- Wang C, Geng X, Yeh T-S, Liu H-L, Tsui P-H. Monitoring radiofrequency ablation with ultrasound Nakagami imaging. *Med Phys* 2013;40:072901.
- Wang W, Zhang Z, Wang J, Wang H. An experimental study on the effects of curcumin on posterior capsule opacification in young rabbit eyes. *Chinese Med Journal-Beijing* 2011;124:3527–3531.
- Weeber HA, Eckert G, Pechhold W, van der Heijde RGL. Stiffness gradient in the crystalline lens. *Graefe's Arch Clin Exp Ophthalmol* 2007;245:1357–1366.
- Weeber HA, Eckert G, Soergel F, Meyer CH, Pechhold W, Van Der Heijde RGL. Dynamic mechanical properties of human lenses. *Exp Eye Res* 2005;80:425–434.
- Weeber HA, van der Heijde RGL. Internal deformation of the human crystalline lens during accommodation. *Acta Ophthalmol* 2008;86:642–647.
- West SK, Duncan DD, Muñoz B, Rubin GS, Fried LP, Bandeen-Roche K, Schein OD. Sunlight exposure and risk of lens opacities in a population-based study: the Salisbury Eye Evaluation project. *JAMA* 1998;280:714–8.
- West SK, Rosenthal F, Newland HS, Taylor HR. Use of photographic techniques to grade nuclear cataracts. *Invest Ophthalmol Vis Sci* 1988;29:73–7.
- West SK, Valmadrid CT. Epidemiology of risk factors for age-related cataract. *Surv Ophthalmol* 39:323–34.
- WHO Study Group. Training in diagnostic ultrasound: essentials, principles and standards. Report of a WHO Study Group. *World Health Organ Tech Rep Ser* 1998;875:i–46; back cover.
- Wilson M, Trivedi R, S. P, eds. Pediatric cataract surgery: Techniques, complications, and management. Lippincott Williams & Wilkins, 2005.

- Windle JJ, Albert DM, O'Brien JM, Marcus DM, Distche CM, Bernards R, Mellon PL. Retinoblastoma in transgenic mice. *Nature* 1990;343:665–9.
- Wong WL, Li X, Li J, Cheng C-Y, Lamoureux EL, Wang JJ, Cheung CY, Wong TY. Cataract conversion assessment using lens opacity classification system III and Wisconsin cataract grading system. *Invest Ophthalmol Vis Sci* 2013;54:280–7.
- World Health Organization. The effects of solar UV radiation on the eye: Report of an informal consultation, Geneva, 30 August - 3 September 1993. Geneva, Switzerland: Geneva : World Health Organization, 1994.
- World Health Organization. State of the world's sight VISION 2020: The Right to Sight 1999-2005. 2005.
- World Health Organization. Universal eye health: A global action plan 2014-2019. 2013.
- Wormstone IM, Wride MA. The ocular lens: A classic model for development, physiology and disease. *Philos Trans R Soc Lond B Biol Sci* 2011;366:1190–2.
- Xu Y, Gao X, Lin S, Wong DWK, Liu J, Xu D, Cheng C-Y, Cheung CY, Wong TY. Automatic grading of nuclear cataracts from slit-lamp lens images using group sparsity regression. *Med Image Comput Comput Assist Interv* 2013;16:468–75.
- Yang X, Tridandapani S, Beitler JJ, Yu DS, Wu N, Wang Y, Bruner DW, Curran WJ, Liu T. Ultrasonic Nakagami-parameter characterization of parotid-gland injury following head-and-neck radiotherapy: a feasibility study of late toxicity. *Med Phys* 2014;41:022903.
- Yang X, Yoshida E, Cassidy RJ, Beitler JJ, Yu DS, Curran WJ, Liu T. Quantitative ultrasonic Nakagami imaging of neck fibrosis after head and neck radiation therapy. *Int J Radiat Oncol Biol Phys Elsevier Inc.*, 2015;92:407–414.
- Yap EY, Heng WJ. Visual outcome and complications after posterior capsule rupture during phacoemulsification surgery. *Int Ophthalmol* 1999;23:57–60.
- Yeoh R. Practical differences between 3 femtosecond phaco laser platforms. *J Cataract Refract Surg* 2014;40:510.
- Yu X, Lee W. Characterization of the heart muscle anisotropy using ultrasound Nakagami imaging. 2014 IEEE International Ultrasonics Symposium Proceedings 2014. pp. 2367–2370.
- Zeng Y, Liu Y, Liu X, Chen C, Xia Y, Lu M, He M. Comparison of lens thickness measurements using the anterior segment optical coherence tomography and A-scan ultrasonography. *Invest Ophthalmol Vis Sci* 2009;50:290–4.
- Zhang J, Feng Y, Cai J. Phacoemulsification versus manual small-incision cataract surgery for

age-related cataract: Meta-analysis of randomized controlled trials. *Clin Exp Ophthalmol* 2013;41:379–386.

Zhang Q, Yang H, Kang SJ, Wang Y, Wang GD, Coulthard T, Grossniklaus HE. In vivo high-frequency, contrast-enhanced ultrasonography of uveal melanoma in mice: imaging features and histopathologic correlations. *Invest Ophthalmol Vis Sci* 2011;52:2662–8.

Zhou Z, Huang C-C, Shung KK, Tsui P-H, Fang J, Ma H-Y, Wu S, Lin C-C. Entropic imaging of cataract lens: An in vitro study. *PLoS One* 2014;9:e96195.

PUBLICATIONS

Ex vivo exploratory study

The following papers were published:

- Ultrasound techniques for lens hardness characterization: A comparison study. Jesus, D.; Caixinha, M.; Santos, M.; Santos, J. Ultrasonics Symposium (IUS), 2012 IEEE International. 2012; 2376-2379 (DOI: 10.1109/ ULTSYM.2012.0594).
- Using of the ultrasound frequency-dependent attenuation and Nakagami distribution for cataract evaluation Jesus, D.; Velte, E.; Caixinha, M.; Santos, M.; Santos, J. Bioengineering (ENBENG), 2013 IEEE 3rd Portuguese Meeting. 2013; 1-4 (DOI: 10.1109/ ENBENG.2013.6518388).

Ex vivo study

The following papers were published:

- Characterization of scatterers concentration in cataractous lens using Nakagami distribution by ultrasounds. Caixinha, M.; Jesus, D.; Santos, M.; Santos, J.; Velte, E. Ultrasonics Symposium (IUS), 2013 IEEE International. 2013; 425-428 (DOI: 10.1109/ULTSYM.2013.0110).

- Using ultrasound backscattering signals and Nakagami statistical distribution to assess regional cataract hardness. Caixinha, M.; Jesus, D.; Velte, E.; Santos, M.; Santos, J. IEEE Transactions on Biomedical Engineering. 2014; 61(12): 2921-2929: 1 (DOI: 10.1109/TBME.2014.2335739).
- New approach for objective cataract classification based on ultrasound techniques using multiclass SVM classifiers. Caixinha, M.; Velte, E.; Santos, M.; Santos, J. Ultrasonics Symposium (IUS), 2014 IEEE International. 2014; 2402-2405 (DOI: 10.1109/ULTSYM.2014.0599).
- Automatic Cataract Classification based on Ultrasound Techniques using Machine Learning: A comparative Study. Caixinha, M.; Velte, E.; Santos, M.; Perdigão, F.; Amaro, J.; Gomes M.; Santos, J. 2015 ICU Physics Procedia Elsevier vol. 70 p. 1221-1224 (DOI: 10.1016/j.phpro.2015.08.263).
- Automatic cataract hardness classification *ex vivo* by ultrasound techniques. Caixinha, M.; Santos, M.; Santos J. Ultrasound in Medicine and Biology. 2015; 1-10 (DOI: 10.1016/j.ultrasmedbio.2015.11.021).

***In vivo* study**

The following paper was published:

- *In vivo* Automatic Nuclear Cataract Detection and Classification in an Animal Model by Ultrasounds. Caixinha, M.; Amaro, J.; Santos, M.; Perdigão, F.; Gomes, M.; Santos, J. IEEE Transactions on Biomedical Engineering. 2016; 63(11): 2326-2335 (DOI: 10.1109/TBME.2016.2527787).
- Machine Learning Techniques in Clinical Vision Sciences. Caixinha, M. and Nunes, S., Current Eye Research. 2016; (DOI: 10.1080/02713683.2016.1175019)

Ultrasound Techniques for Lens Hardness Characterization: A comparison Study

Danilo Jesus
Department of Physics
University of Coimbra
Coimbra, Portugal

Miguel Caixinha, Mário Santos, Jaime Santos
Department of Electrical and Computers Eng.
University of Coimbra, Portugal
jaime@deec.uc.pt

Abstract— Cataract affects more than 20 million people worldwide and is the leading cause of vision loss. Currently, the phacoemulsification is the most used procedure to extract cataract and recover visual acuity. Optimal phacoemulsification energy is demanded for safety cataract removal. It is well established that the energy value is determined by the cataract hardness. In this study twenty porcine eyes were used as experimental samples. Cataract was induced by an ethanol:2-propanol:formalin solution. A 25 MHz focused transducer has been used to estimate the ultrasound velocity and attenuation. Statistical analysis was performed to compare the different used methodologies and to correlate the different ultrasound parameters with different stages of cataract formation (lens hardness).

Keywords-ultrasounds; lens hardness; statistical analysis.

I. INTRODUCTION

A cataract is a clouding or opacity of the normally transparent crystalline lens of the eye. It affects more than 20 million people worldwide and it is the leading cause of vision loss. Generally, cataracts are a natural result of aging, but some eye injuries, medications and diseases like alcoholism and diabetes can also cause cataracts [1]. Currently, the phacoemulsification is the most used procedure to extract cataract and recover visual acuity. However, the use of an inadequate phacoemulsification energy can disrupt the posterior lens capsule, and among other complications, cause a significant loss of the corneal endothelial cells [2,3]. Thus, optimal phacoemulsification energy is demanded for safety cataract removal. It is well established that the energy value is determined by the cataract hardness. The current method used to classify the cataract is the LOCSIII, which consists in comparing the picture observed by slit lamp biomicroscopy (for nuclear cataract) or examined using retroillumination images (for cortical and posterior subcapsular cataract) with a set of standard photographs [4]. These manual grading systems have a high inter and intra-observers variability [5-7].

Non-invasive ultrasound techniques have increasingly been used as an alternative approach to assess the cataract hardness and provide information about its severity and type, due essentially to their non-invasive and non-ionizing nature [8]. Studies indicate the velocity and attenuation of ultrasound waves are correlated with the lens hardness degree. In this work several approaches for lens hardness estimation are presented based on ultrasound velocity and attenuation.

II. METHODS AND MATERIALS

A. Ultrasound velocity

The ultrasound velocity (V) calculation is essentially based on two approaches. Measuring the time of flight (Δt) considering for that the anterior and posterior capsule echoes,

$$V = \frac{2d}{\Delta t} \quad (1)$$

where d is the lens thickness, or using the amplitude spectrum technique considering the lens front face and the first back face echoes by,

$$V = 2d \Delta f \quad (2)$$

where Δf is the frequency variation between two maxima (minima) of the signal spectrum. In both equations the lens thickness d is measured by a caliper. Since the lens is a soft tissue some thickness inaccuracy is expected, which also affects the velocity results. An alternative method that does not require the previous knowledge of the lens thickness, can be used [8],

$$V = c \left(\frac{t_s - t_c}{t_b - t_a} + 1 \right) \quad (3)$$

where c is the ultrasound velocity in the solution, t_c and t_s are the propagation times for the path between the transducer and a reflector with and without the lens inserted, respectively, and t_a and t_b are the propagation times for the pulses travelling from the transducer to the front and back faces of the lens, respectively. Though independent of the lens thickness, this approach requires two additional acquisitions that are not practicable in-vivo.

B. Attenuation

The frequency dependent attenuation can be estimated based on three methodologies. Thus, using the front and back capsule echoes as shown in Fig. 1a the frequency dependent attenuation is expressed as

$$\alpha(f) = \frac{20}{2d} \log_{10} \left(\frac{A_1(f)}{A_2(f)} \frac{R_{12}}{R_{21}} T_{12} T_{21} \right), \quad (4)$$

where $A_1(f)$ and $A_2(f)$ are the amplitude spectra of the lens echoes, T_{12} and T_{21} are the transmission coefficients, and R_{12}

and R_{2l} are the reflection coefficients observed in the lens boundaries (see Fig. 1a). A second methodology makes use of a planar reflector as illustrated in Fig. 1b.

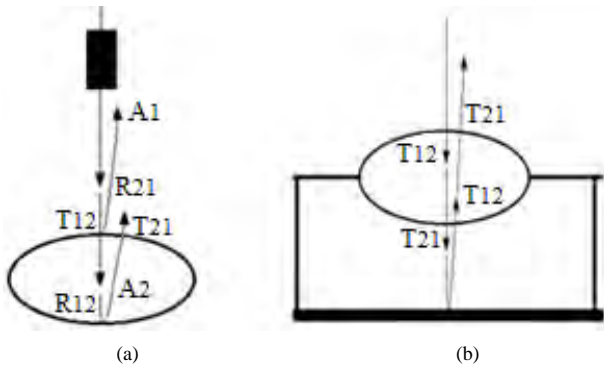


Figure 1. Experimental setup for the attenuation calculation: (a) for (4), (b) for (5).

The frequency dependent attenuation coefficient is given by

$$\alpha(f) = \frac{20}{2d} \log_{10} \left(\frac{A_3(f)}{A_4(f)} (T_{12} T_{21})^2 \right) - \alpha_s, \quad (5)$$

where $A_3(f)$ and $A_4(f)$ are the amplitude spectra from the echoes received from the reflector in the solution and the reflector with crystalline lens inserted, respectively, and α_s is the attenuation in the solution path corresponding the lens thickness. The transmission and reflection coefficients as well as the α_s factor are important attenuation correction parameters that in general are neglected in most evaluations [8]. A third methodology consists of analyzing the frequency downshift from the backscattering signal [10]. The expression for the attenuation coefficient (β) is given by,

$$\beta = \frac{\Delta f(z)}{\Delta z 4 \sigma^2} \quad (6)$$

where $\Delta f(z) / \Delta z$ is the slope of the linear fitting applied to the center frequencies plot of the backscattered echoes versus depth z in tissue, and σ is the Gaussian bandwidth of the emission pulse.

C. Lens samples

Twenty porcine eyes were used as experimental samples. Cataract was induced by an ethanol:2-propanol:formalin solution at the ratio 3:3:4 [11]. The lens average diameter measured by a caliper was 8.3 ± 0.37 mm.

D. Experimental procedure

A 25 MHz transducer with a 3.5cm focus and 5mm active diameter was used. The lenses have been placed on a perspex holder having a circular hole suited to the lens (see Fig. 1). Both the transducer and the lens were immersed in a temperature controlled solution. The measurements were taken every 20 min ranging from 0 to 180 minutes (total cataract). A Pulser/Receiver with a 35 MHz bandwidth (PR5800, Olympus NDT Inc., Waltham, MA, USA) was used in a pulse echo configuration. The received signals were displayed by a digital oscilloscope (Tektronix TDS 3032) and transferred to the computer for processing.

E. Statistical Analysis

To compare the different methods used to compute the ultrasound velocity and the frequency dependent attenuation in lenses with and without induced cataract (i.e. with different lens hardness), several statistical analyses were performed (SPSS version 17.0, SPSS Inc, Chicago, IL, USA) [12]. To test the statistically significant differences on the two acoustical parameters, the non-parametric *Kruskal-Wallis* and *Wilcoxon* tests were used [13]. To analyze the agreement between the different methods for velocity and attenuation assessment, the *Intraclass Correlation Coefficient* (ICC) was used [14].

III. RESULTS

Considering the time of flight approach, the ultrasound velocity ranged from 1617 ± 36 m/s in normal lenses and 1694 ± 31 m/s in cataractous lenses (i.e., after an immersion of 180 minutes). Considering the amplitude spectrum technique, the ultrasound velocity ranged from 1619 ± 39 m/s in normal lenses to 1692 ± 38 m/s in cataractous lenses. As expected the values are very similar because the methods are based in the same background theory. Considering the alternative method based on a reflector, the velocity of the ultrasound ranged from 1597 ± 37 m/s in normal lenses to 1670 ± 32 m/s in cataractous lenses. The time of flight and the amplitude spectrum approaches showed an excellent agreement (ICC=0.946, $p < 0.001$), justifying the obtained similar values, while the alternative method, although in agreement with the first two methods (ICC=0.824, $p < 0.001$ and ICC=0.745, $p < 0.001$, respectively), provides lower values for the ultrasound velocity in lenses. For the three methods a statistically significant increase in the ultrasound velocity with the immersion time (i.e. lens hardness) was found ($p < 0.001$). Fig. 2 illustrates the ultrasonic velocity behavior for the amplitude spectrum technique and the alternative method that makes use of a planar reflector.

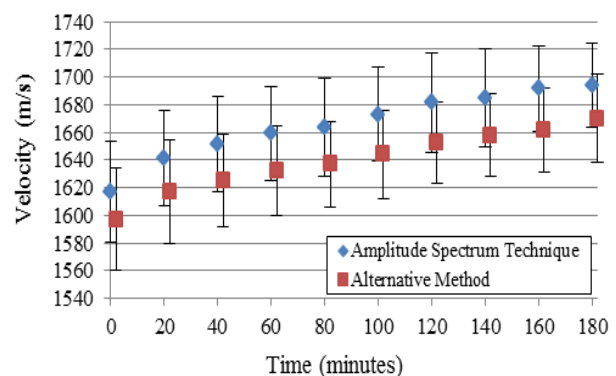


Figure 2. Ultrasound velocity for the lens characterized by the methods mentioned in the graph for immersion times ranging from 0 to 180 minutes.

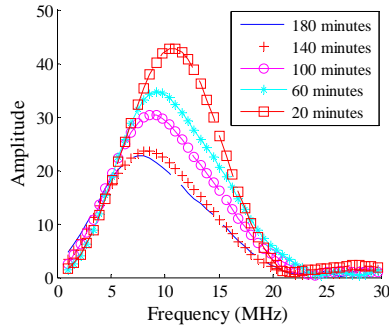


Figure 3. Signal spectra obtained using setup shown in fig. 1a.

Considering the evaluation of ultrasound frequency dependent attenuation based on the front and back capsule echoes and expressed by (4) (neglecting the coefficients of transmission and reflection), it was observed that the center frequency of the posterior capsule echo decreased 28% for the largest immersion time. Fig. 3 shows the evolution of the signal spectra for the different immersion times considered.

The second used methodology based on a planar reflector and the attenuation in the solution path occupied by the lens were previously neglected, provided a decreasing of 17% in the center frequency for the larger immersion time (see Fig. 4).

For both methods the frequency dependent attenuation increases with the immersion time ($p < 0.001$), i.e., with the increase of the lens hardness. That behavior is illustrated in Fig. 5 where the attenuation is represented versus the considered immersion times for all lens. Thus, for lens without cataract the attenuation was 0.117 ± 0.02 dB/mmMHz and 0.111 ± 0.01 dB/mmMHz, and for cataractous lenses the attenuation was 0.212 ± 0.03 dB/mmMHz and 0.18 ± 0.02 dB/mmMHz, respectively for the first and second used attenuation methodologies. The two methods showed similar performances respecting to attenuation for normal and cataractous lenses ($ICC = 0.717$ $p < 0.001$), over the times range. Notice that the attenuation assumes an almost constant value after an immersion time of 120 minutes, for both approaches. The effect in the amplitude spectrum correction to account for loss of energy due to reflections/transmissions at the lens-solution boundaries, and the effect of the geometry of the setup considering the attenuation in the solution path occupied

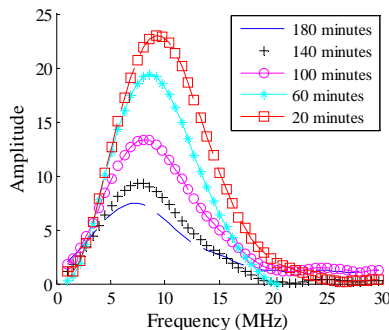


Figure 4. Signal spectra obtained using setup shown in fig. 1b.

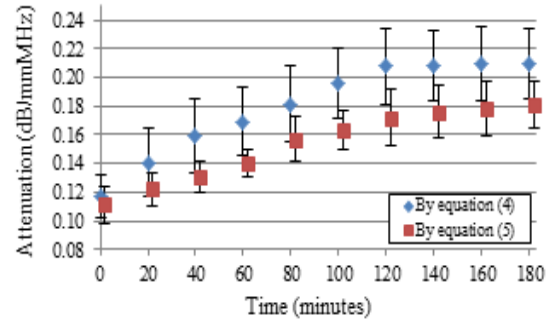


Figure 5. Frequency dependent attenuation for the used methodologies.

by the lens (see (4) and (5)), were also analyzed, leading to results showing small deviations in attenuation when compared to the simplified calculation. Thus, for the considered times those corrections produced lower attenuation values of 1.5% and 1.0% in average. From these results, it can be affirmed that the errors neglecting the corrections are meaningless.

The spectral-shift measurement approach was also used for calculating the attenuation coefficient. As the higher frequency signal components suffer increased attenuation the center frequency of the spectrum from the backscattering signal is shifted to a lower frequency with depth.

To compute the attenuation coefficient from the backscattered echoes, a tissue region was first selected with 3 mm in depth from the front lens, corresponding to the higher intensity region of backscattering. The segments of the backscattered signals were processed by using a Hanning window, which size was set to the length of incident pulse, with a 50% window overlap. Then, each segment was processed by Fourier transform to extract its spectrum, followed by a filtering using a Gaussian bandpass filter, which cutoff frequencies were set at 5 MHz and 25 MHz. The results for the center frequency against depth for the considered backscattering regions and for all lens immersed 180 minutes in the ethanol:2-propanol:formalin solution, are illustrated in Fig. 6. Also, the slope of the center frequency downshift versus depth for immersion times ranging from 20 to 180 minutes is shown in Fig. 7, which are used for the attenuation coefficient calculation, according to (6).

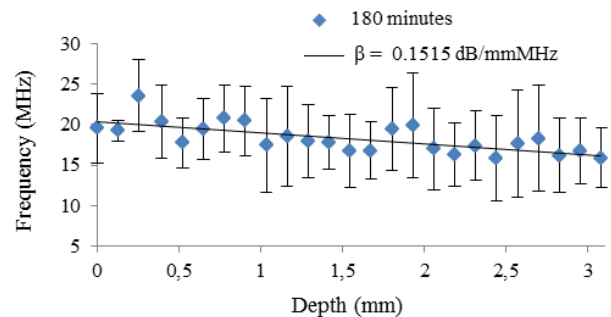


Figure 6. Center frequency downshift versus depth for all tested lens.

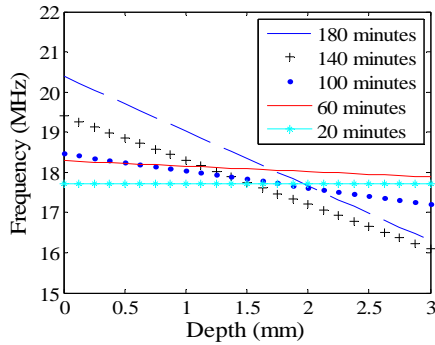


Figure 7. Slope of the center frequency downshift versus depth for all lens and times ranging from 20 to 180 minutes.

The attenuation coefficient versus the considered time range using the backscattering signals of all lenses and calculated for a sample length of 3 mm is depicted in Fig. 8. The attenuation coefficient varies from 0.0006 dB/mmMHz to 0.1515 dB/mmMHz, for immersion times of 20 and 180 minutes, respectively. Note that the attenuation for the lenses without cataract is not mentioned in the graph due to the very low amplitude of the backscattering signals as expected.

IV. DISCUSSION AND CONCLUSIONS

The results of this study confirm that the velocity and the attenuation of the ultrasounds increases with the increase of the lens hardness ($p < 0.001$).

In our study the calculated velocities are in agreement with the values published by other authors, where velocities of 1639 m/s and 1735 m/s were found in normal and cataractous porcine lenses, respectively. The first two methodologies are conceptually identical, as the only difference between them is the processing domain, that is, one uses the time domain, while the other uses the frequency domain approach. The alternative method, although in agreement with the first two ones, provides lower velocities for lenses because it uses a different approach, i.e., a reference signal from a plan reflector. As an advantage, it does not require the previous thickness knowledge. However, it cannot be used *in vivo* measurements. Three methodologies have been used to determine the attenuation. The first two showed a good agreement for the attenuation assessment in normal and cataractous lenses.

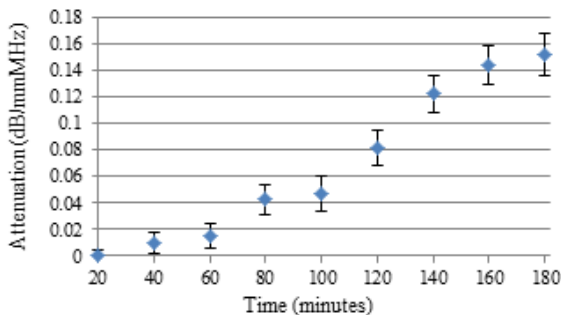


Figure 8. Attenuation coefficient versus immersion times.

Also, corrections to account for loss of energy due to reflections/transmissions at the lens-solution boundaries, and the effect of the geometry of the setup were also carried out for the two approaches. Those corrections produced lower attenuation values of 1.5% and 1.0% in average that can be relevant for the proposed goal since the selection of the optimal phacoemulsification energy depends on the lens hardness, which in turn is correlated with the attenuation. The center frequency downshift measurement approach was also used, providing the attenuation coefficient calculation along the transducer beam in the lens. The regional attenuation coefficients in lenses (near the transducer) have been characterized by selecting a small size of sample volume along the propagation depth.

REFERENCES

- [1] J. J. Kanski, *Clinical diagnosis in ophthalmology*, 1st ed. Philadelphia: Elsevier Mosby, 2006.
- [2] A. Tabatabaei et al., "Evaluation of Posterior Lens Capsule by 20-MHz Ultrasound Probe in Traumatic Cataract," *AJOPHT*, vol. 153, no. 1, pp. 51-54, 2012.
- [3] K. Hayashi, M. Yoshida, S.-ichi Manabe, and A. Hirata, "Cataract surgery in eyes with low corneal endothelial cell density.," *Journal of cataract and refractive surgery*, vol. 37, no. 8, pp. 1419-1425, 2002.
- [4] H. L. H. Li et al., "A computer-aided diagnosis system of nuclear cataract.," *IEEE Transactions on Biomedical Engineering*, vol. 57, no. 7, pp. 1690-1698, 2010.
- [5] M. Esmaeelpour Hajyar et al., "Three-Dimensional 1060-nm OCT: Choroidal Thickness Maps in Normal Subjects and Improved Posterior Segment Visualization in Cataract Patients.," *Investigative Ophthalmology & Visual Science*, vol. 51, no. 10, pp. 5260-5266, 2010.
- [6] A. C. Tan, S. C. Loon, H. Choi, and L. Thean, "Lens Opacities Classification System III: cataract grading variability between junior and senior staff at a Singapore hospital.," *Journal of cataract and refractive surgery*, vol. 34, no. 11, pp. 1948-1952, 2008.
- [7] D. R. Nixon, "Preoperative cataract grading by Scheimpflug imaging and effect on operative fluidics and phacoemulsification energy.," *Journal of cataract and refractive surgery*, vol. 36, no. 2, pp. 242-246, 2010.
- [8] C.-C. Huang et al., "Evaluation of lens hardness in cataract surgery using high-frequency ultrasonic parameters *in vitro*.," *Ultrasound in medicine biology*, vol. 33, no. 10, pp. 1609-1616, 2007.
- [9] M. A. El-brawany, "Ultrasound-Based Noninvasive Measurement of Cataract Hardness.," *The Online Journal on Electronics and Electrical Engineering*, vol. 2, no. 2, pp. 246-249, 2009.
- [10] C.-C. Huang, R. Chen, P.-H. Tsui, Q. Zhou, M. S. Humayun, and K. K. Shung, "Measurements of attenuation coefficient for evaluating the hardness of a cataract lens by a high-frequency ultrasonic needle transducer.," *Physics in medicine and biology*, vol. 54, no. 19, pp. 5981-94, Oct. 2009.
- [11] Sugiura T, Kurosaks D, Uezuki Y, Eguchi S, Obata H, Takahashi T. Creating cataract in pig eye. *J Cataract Refract Surg* 1999;25:615-621.
- [12] K. G. Tournoy et al., "The value of endoscopic ultrasound after bronchoscopy to diagnose thoracic sarcoidosis.," *The European respiratory journal : official journal of the European Society for Clinical Respiratory Physiology*, vol. 35, no. 6, pp. 1329-35, Jun. 2010.
- [13] J. D. Spurrier, "On the null distribution of the Kruskal-Wallis statistic.," *Journal of Nonparametric Statistics*, vol. 15, no. 6, pp. 685-691, Dec. 2003.
- [14] K. Mather, "R. A. Fisher's Statistical Methods for Research Workers : An Appreciation.," *Journal of the American Statistical Association*, vol. 46, no. 253, pp. 51-54, Mar. 1951.

Using of the ultrasound frequency dependent attenuation and Nakagami distribution for cataract evaluation.

Danilo Jesus, Elena Velte
Department of Physics
University of Coimbra
Coimbra, Portugal

Miguel Caixinha, Mário Santos, Jaime Santos
Department of Electrical and Computers Eng.
University of Coimbra, Portugal
jaime@deec.uc.pt

Abstract — Cataract is a clouding or opacity of the normally transparent crystalline lens of the eye. The cataract formation is associated with the increase of both inner fiber compaction and protein aggregation, which can be characterized by ultrasound backscattering. In this study, the tissue scatterers changing with cataract formation was investigated, and their influence in the frequency dependent attenuation such as in the Nakagami distribution was analyzed. For this purpose, cataracts were induced in twenty porcine lenses. A 25 MHz focused transducer was used to estimate the ultrasound attenuation considering the spectral ratio between echo signals from a reflector with and without lenses inserted. A power-law frequency dependence model was used to study the frequency dependent attenuation. The analyzed signals showed high backscattering and also a variation of the Nakagami parameter with cataract formation, indicating a scatter size increase. This conclusion could be important to assess the cataract hardness and to provide the correct information about its type and severity.

Keywords - ultrasounds; lens hardness; scattering.

I. INTRODUCTION

Cataract affects more than 20 million people worldwide and it is the leading cause of vision loss. Generally, cataracts are a natural result of aging, or could be in some cases caused by eye injuries, medications and diseases like alcoholism and diabetes [1]. The current method used to classify the cataract hardness degree shows a high inter-observers variability [2, 3]. Ultrasound techniques have increasingly been used as an alternative approach to assess the cataract hardness and provide information about its severity and type, due essentially to their non-invasive and non-ionizing nature [4]. Acoustic parameters of biologic tissues are described by the ultrasound velocity and the attenuation coefficient. In soft tissues the attenuation is assumed to be linear with frequency – high frequency components of echoes are more attenuated than lower frequency components [5]. Ultrasound pulses are attenuated as the result of absorption (transference into thermal energy) and dispersion (due to scattering) mechanisms, as they propagate through the tissue. The scattering is related with the particle size and the ultrasound wavelength, thus the frequency dependent attenuation will be lower as the particle size increases. Normal lens is acoustically homogeneous and clear.

Its characteristics change with the cataract hardness, which is due to changes in tissue density and structure (i.e., molecular weight and size). The crystalline proteins are the main structure of the human lens, representing approximately 90% of this structure. Their structural function is to assist in maintaining the appropriate refractive index of the lens and its transparency. Their molecular weights are: α -crystallins over 200kDa; β -crystallins 40-160KDa; and γ -crystallins about 20kDa [6]. Oxidative damage of the lens proteins is the major cause of cataract formation. The aggregation of the lens proteins, randomly distributed, is thought to produce sufficient fluctuation in protein density, accounting for opacification. Protein aggregation gives rise to the development of high molecular weight aggregates of sufficient size to promote ultrasound scattering. To understand the influence of protein aggregation on the frequency dependent attenuation, the linear and a non-linear frequency dependence approaches were studied. The scatterers distribution through a probability function as Nakagami distribution was also studied.

II. METHODS AND MATERIALS

A. Attenuation

The frequency dependent attenuation has been estimated using the setup shown in Figure 1, where the signals of interest are obtained from a planar reflector. Thus, the attenuation is expressed by (1),

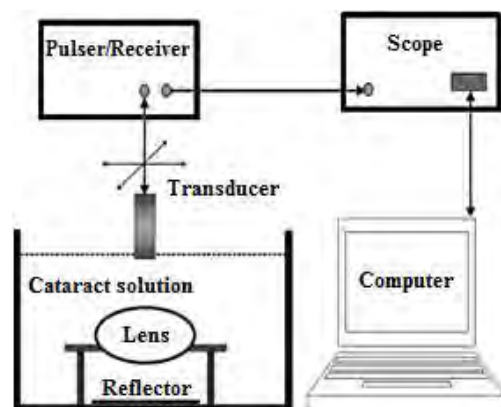


Figure 1. Experimental setup for the attenuation calculation.

$$\alpha(f) = \frac{20}{2d} \log_{10} \left(\frac{A_1(f)}{A_2(f)} (T_{12} T_{21})^2 \right) - \alpha_s \quad (1)$$

where d is the crystalline lens thickness; $A_1(f)$ and $A_2(f)$ are the amplitude spectra from the echoes received from the reflector in the solution and from the reflector with the crystalline lens inserted, respectively; T_{12} and T_{21} are the transmission coefficients observed in the lens boundaries and α_s is the attenuation in the solution path corresponding to the lens thickness. The transmission coefficients as well as the α_s factor are important attenuation correction parameters that were taken into account in this study.

B. Power-law

For biological soft tissue the pressure and temperature can be assumed to be constant and therefore the attenuation coefficient can be described by a model, which only takes the frequency into account. Some experimental methods have been used to estimate the cataract hardness by determining the attenuation coefficients [7]. A good approximation for the frequency dependent attenuation for most soft tissue is given by,

$$\alpha = \beta f^n \quad (2)$$

where β is the attenuation coefficient and n is the parameter that describe the frequency dependence attenuation. Some studies describe n as a value ranging from 1 to 2 for most soft tissues [8].

C. Nakagami Distribution

Ultrasound backscattering is essentially a random process, and therefore the statistical analysis of the ultrasound backscattered signals might provide some useful information about the scatter properties. The Nakagami parameter is related to the shape of the Nakagami distribution and determines the statistical distribution of the ultrasound backscattered envelope, as given by [9],

$$f(r, m, \Omega) = \frac{2m^m r^{2m-1}}{\Gamma(m)\Omega^m} \exp\left(-\frac{m}{\Omega} r^2\right) U(r) \quad (3)$$

where Γ and U are the gamma function and the unit step function, respectively. Let E denote the statistical mean; then the scaling parameter Ω and the Nakagami parameter m , associated with the Nakagami distribution can be respectively obtained from

$$\Omega = E(R^2) \quad (4)$$

where R is the random variable of the Nakagami distribution, and

$$m = \frac{[E(R^2)]^2}{E[R^2 - E(R^2)]^2} \quad (5)$$

The scaling parameter means the average power of the backscattered envelope. On the other hand, a variation of the Nakagami parameter from 0 to 1 means a change in the envelope statistics from a pre-Rayleigh to a Rayleigh distribution. According to previous studies, the probability density function (*pdf*) of the backscattered-signal envelope should follow a Rayleigh distribution when the resolution cell of the ultrasound transducer contains a large number of randomly distributed scatterers. If the resolution cell contains scatterers that have randomly varying scattering cross sections with a comparatively high degree of variation, the envelope statistics conforms to pre-Rayleigh distributions. If the resolution cell contains periodically located scatterers in addition to randomly distributed scatterers, the envelope statistics follow a post-Rayleigh distribution [9].

D. Lens samples

Twenty porcine eyes have been used. Cataract was induced by an ethanol:2-propanol:formalin solution at the ratio 3:3:4 [10]. The lens average thickness measured by a caliper was 8.3 ± 0.4 mm.

E. Experimental procedure

A 25 MHz transducer with a 3.5 cm focus and 5mm active diameter was used. The lenses were placed on a perspex holder having a circular hole suited to the lens (see Figure 1). Both the transducer and the lens were immersed in a temperature controlled solution. The measurements were taken every 20 min ranging from 0 to 180 minutes (total cataract). A Pulser/Receiver with a 35 MHz bandwidth (PR5800, Olympus NDT Inc., Waltham, MA, USA) was used in a pulse echo configuration. The received signals were displayed by a digital oscilloscope (Tektronix TDS 3032) and transferred to the computer for processing.

F. Statistical Analysis

To compare the different values used to analyze the frequency dependent attenuation in lenses with and without induced cataract (i.e. with different lens hardness), the non-parametric *Kruskal-Wallis* and *Wilcoxon* tests were used (SPSS version 17.0, SPSS Inc, Chicago, IL, USA). All statistical values were considered significant for p values smaller than 0.05 [11, 12].

III. RESULTS

The echo signals collected by using the setup shown in Fig.1 present a clear downshift of the central frequency of the posterior and anterior capsule echoes. In particular the central frequency of the posterior signal has decreased 17% for the immersion time ranging from baseline (0 minutes) to 180 minutes. Figure 2 shows the evolution of the signal spectra for the different immersion times considered. The attenuation calculated by (1), showed a significant increase with the immersion time ($p < 0.001$), i.e., with lens hardness. Such behavior is illustrated in Fig. 3.

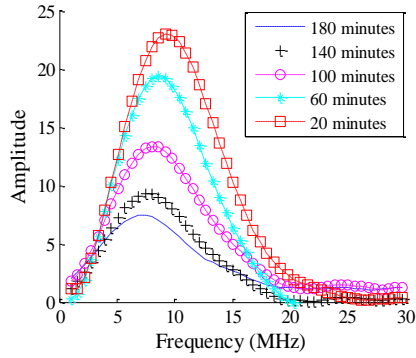


Figure 2. Signal spectra obtained using setup shown in fig.1.

Considering a linear frequency dependent attenuation ($n=1$ in Eq. 2), the attenuation coefficient was obtained by a linear regression. Fig. 4 shows the attenuation coefficient for the immersion time range. It is observed a significant increase of the attenuation till 120 minutes of immersion time. For higher times the attenuation assumes an almost constant value ($p>0.05$).

It is well known that the crystalline lens characteristics are changed by cataract formation. The cataract process is characterized by protein precipitation and aggregation, which contributes to a large variation of the scatterers size. To understand how the scatterers size affects the attenuation values, the frequency dependency was analyzed. For that, a power-law regression was applied in the range of interest (5-20MHz), and the parameter n and the attenuation coefficient β were extracted by (2). As represented in Fig. 5, the frequency dependent attenuation factor (n) ranged from 2.1 to 0.8 for lenses without and with cataracts, respectively. Also, the attenuation coefficient β increases with the immersion time, when the new calculated values for n are considered (see Fig. 6). The scatterers distribution was also analysed by the Nakagami approach. The averaged Nakagami parameter m , calculated by (5), versus the immersion time is shown in Fig. 7. It is observed that the Nakagami parameter increases from 0.63 to 0.88 for the immersion time range, corresponding to an increasing rate of 0.0013 min^{-1} .

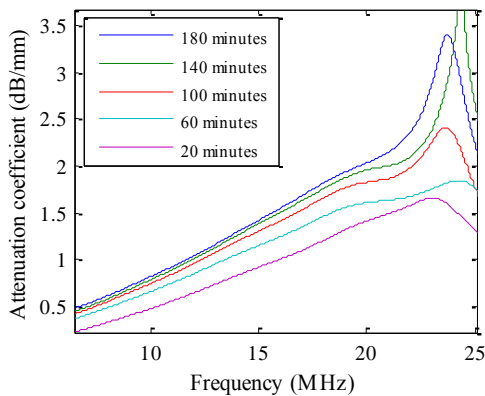


Figure 3. Attenuation for the used methodology.

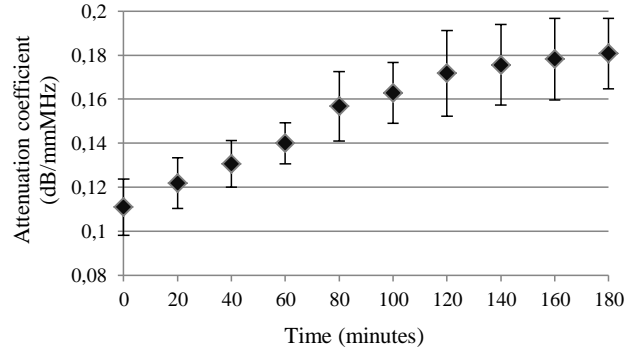


Figure 4. Frequency dependent attenuation for the used methodology.

This result indicates that the statistics of the backscattered envelope varied from a pre-Rayleigh distribution to a Rayleigh distribution as the immersion time increased. Fig. 8 shows also the scaling parameter Ω as function of immersion time. It describes how the backscattering intensity values changed with cataract formation. The results showed that the scaling parameter did not have a consistent variation along the cataract formation process, varying significantly only in the early stages of cataract formation (0 to 40 minutes). Thus, the experimental results in figure 8 showed that the intensity estimation seems to be useless for scatterers characterization. The increase in tissue hardness indicates that the tissue tends to be incompressible. However, this does not mean that the scatterers have the ability to produce stronger echoes. The results showed that the backscattered statistics with a short immersion time have a pre-Rayleigh distribution (i.e. $m<1$), suggesting that little protein aggregation and fiber compaction are present in the initial stage of cataract formation. For cataracts induced by long immersion times, the backscattered statistics gradually approached to a Rayleigh distribution (i.e. $m=1$), representing a stronger protein aggregation and fiber compaction.

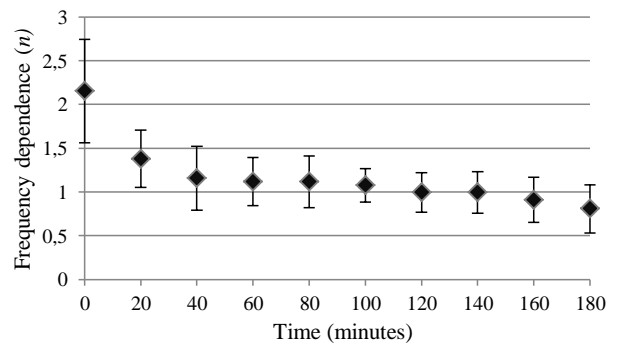


Figure 5. Parameter n for all tested lenses.

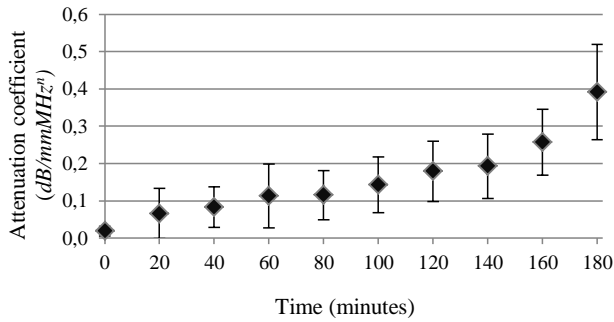


Figure 6. Attenuation coefficient (β) for all tested lenses considering a non-linear dependence.

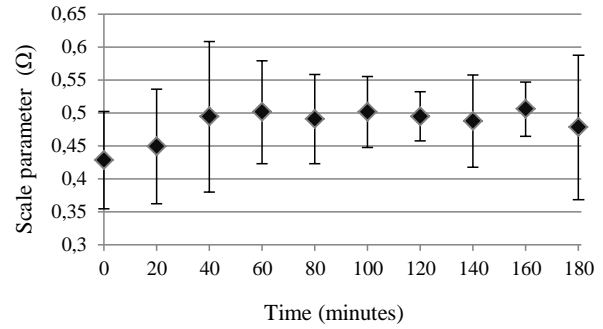


Figure 8. Nakagami scale parameter as function of immersion time.

IV. DISCUSSION AND CONCLUSIONS

In this work, we evaluated the ultrasound attenuation behavior in the cataract formation. It was observed higher attenuation values as the hardness of cataracts increased. This is due to the changing in the scatterers size. The parameter n calculated for the considered immersion time range explain that behavior. The backscattering signals were also analyzed by the Nakagami distribution. The Nakagami parameter reflected changes in the arrangement, distribution and concentration of scatterers in the lens through cataract formation. In conclusion, the process of cataract formation is associated with increasing in the hardness and opacity of the lens due to the increasing in both protein aggregation and inner fiber compaction. Thus, cataract formation may be treated as a process of change in the spatial arrangement and concentration of the scatterers, resulting from fiber compaction, proteins size and distribution, and therefore we can indirectly estimate the scatterer concentration and distribution in tissue by estimating the Nakagami parameter. The scaling parameter results suggest that the backscattering intensity measured by 25MHz focused transducer could not be used to distinguish variations in the scatterers size. However, more investigations on the frequency dependent attenuation should be carried out before using this parameter to characterize cataract hardness. Our next goal is to establish a relationship between the frequency dependence and the scatterers size using phantoms that will simulate the eye cataract formation.

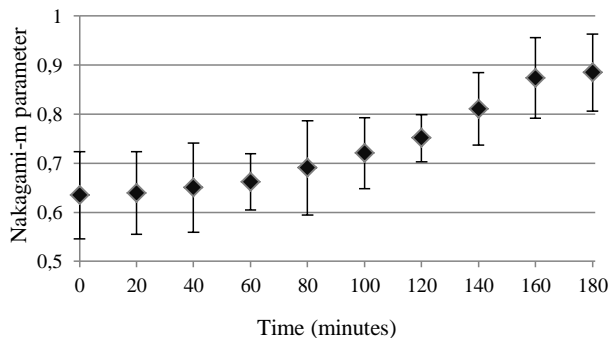


Figure 7. Nakagami-m parameter as function of immersion time.

REFERENCES

- [1] J. J. Kanski, *Clinical diagnosis in ophthalmology*, 1st ed. Philadelphia: Elsevier Mosby, 2006.
- [2] M. Esmaelpour Hajyar et al., "Three-Dimensional 1060-nm OCT: Choroidal Thickness Maps in Normal Subjects and Improved Posterior Segment Visualization in Cataract Patients," *Investigative Ophthalmology & Visual Science*, vol. 51, no. 10, pp. 5260-5266, 2010.
- [3] D. R. Nixon, "Preoperative cataract grading by Scheimpflug imaging and effect on operative fluidics and phacoemulsification energy," *Journal of cataract and refractive surgery*, vol. 36, no. 2, pp. 242-246, 2010.
- [4] C.-C. Huang et al., "Evaluation of lens hardness in cataract surgery using high-frequency ultrasonic parameters in vitro," *Ultrasound in medicine biology*, vol. 33, no. 10, pp. 1609-1616, 2007.
- [5] C.-C. Huang et al., "Determining the acoustic properties of the lens using a high-frequency ultrasonic needle transducer," *Ultrasound in medicine biology*, vol. 33, no. 12, pp. 1971-1977, 2007.
- [6] A. Paunksnis et al., "Evaluation of Ultrasound Attenuation Characteristics of Human Cataract." *Informatica*, 14(4), pp. 529-540, 2003.
- [7] C.-C. Huang et al., "Measurements of attenuation coefficient for evaluating the hardness of a cataract lens by a high-frequency ultrasonic needle transducer" *Phys Med Biol*. vol. 54, no.19, pp. 5981-5994, 2009.
- [8] Szabo T. L., and Wu J., 2000, "A model for longitudinal and shear wave propagation in viscoelastic media," *J. Acoust. Soc. Am.*, 107(5), pp. 2437-2446.
- [9] M.-C. Ho et al, "Using ultrasound Nakagami imaging to assess liver fibrosis in rats," *Ultrasonics* Vol. 52 no. 2 pp.215-222, 2012
- [10] Sugiura T, Kurosaks D, Uezuki Y, Eguchi S, Obata H, Takahashi T. Creating cataract in pig eye. *J Cataract Refract Surg* 1999;25:615-621.
- [11] K. G. Tournoy et al., "The value of endoscopic ultrasound after bronchoscopy to diagnose thoracic sarcoidosis," *The European respiratory journal : official journal of the European Society for Clinical Respiratory Physiology*, vol. 35, no. 6, pp. 1329-35, Jun. 2010.
- [12] J. D. Spurrier, "On the null distribution of the Kruskal-Wallis statistic," *Journal of Nonparametric Statistics*, vol. 15, no. 6, pp. 685-691, Dec. 2003

Characterization of scatterers concentration in cataractous lens using Nakagami distribution by ultrasounds.

Miguel Caixinha, Danilo Jesus, Mário Santos, Jaime Santos
Department of Electrical and Computers Engineering
University of Coimbra, Portugal
jaime@deec.uc.pt

Elena Velte
Department of Physics
University of Coimbra
Coimbra, Portugal

Abstract — Cataract affects more than 20 million people in the world. Its formation is associated with the increase of protein aggregation in the eye lens. In the early stages the protein aggregates act as light scatterers and in the advanced stages these aggregates increase in size preventing the light propagation through the eye. This work aims to analyze the protein aggregates and its spatial distribution, for different stages of cataract formation. Cataract was induced in porcine lenses by immersion in an ethanol:2-propanol:formalin solution. Slices of 50 μm in thickness were obtained from the nucleus and the cortex, to locally analyze the frequency dependent attenuation and the Nakagami m parameter. The slices were stained and imaged with an inverted microscope. With cataract formation a significant increase was found for the ultrasound velocity ($p > 0.001$), the frequency dependent attenuation ($p < 0.001$), the backscattering signals intensity – B-Scan images and the Nakagami m parameter ($p < 0.001$). The increase of the Nakagami m parameter in the cortex was in agreement with the increasing of the protein aggregates observed in the slices in this region, for different stages of cataract formation. The same was not observed for the nucleus, due to the higher compaction of the fibers in the nucleus in the advanced stages of the cataract, leading to weak backscattering signals. The results suggest that the interpretation of backscattering signals by the Nakagami distribution, when combined with the knowledge of the physical scatter properties are challenging for obtaining a distribution map of cataract hardness by a noninvasive method.

Keywords- *ultrasound; Cataract; Nakagami distribution; backscattering.*

I. INTRODUCTION

Cataract affects more than 20 million people worldwide [1]. Its formation is associated with the increase of protein aggregation in the eye lens. The lens transparency is highly dependent on the well-ordered arrangement of the crystalline proteins, which are present in high concentration and represent

almost the entire composition of the lens. Their structural function is to assist in maintaining the appropriate lens refractive index and its transparency. The molecular weights of the α , β , and γ -crystallins are: α -crystallins over 200kDa; β -crystallins 40-160kDa; and γ -crystallins about 20kDa [2]. With cataract formation the molecular weights of the α , β , and γ -crystallins increases significantly, and in the case of α -crystallins this increase can be over 1000 kDa [3].

Since the crystalline proteins represent almost the entire composition of the lens, the disruption of crystalline protein arrangement, as a result of protein aggregation and precipitation, leads to cataract formation [2]. The protein aggregation can be described as scatterers, and then the process of cataract can be therefore considered as a three-dimensional arrangement of scatterers. Depending on the type and cataract severity, and thus the size of the protein aggregates, may cause scattering of light or prevent their passage through the eye.

Non-invasive ultrasound techniques have increasingly been used as an alternative approach to assess objectively the cataract hardness and to provide information about its severity and type [4, 5, 6]. However, most of the used methods neither allow the characterization of the regional hardness nor the establishment of a correlation with the protein aggregation in the cataractous lens. New methodologies are therefore needed to assess the regional cataract hardness and to correlate it with the protein aggregation. In the field of medical ultrasounds, the Nakagami statistical distribution has received considerable attention because the associated Nakagami m parameter can be applied to backscattered signals, making possible the scatterers characterization in biological tissues [7].

This work aims to analyze the scatterers spatial distribution, concentration, and average dimension, for different stages of cataract formation, and to explore their impact in the ultrasound attenuation. Porcine eyes were used in this work for estimating velocity and frequency dependent attenuation in crystalline lenses because they represent a good animal model [6, 8, 9, 10].

II. MATERIALS AND METHODS

A. Lens Samples

Fifty lenses from porcine eyes were collected in a slaughterhouse. The lenses were carefully extracted and prepared to clean iris remains and adhering vitreous preserving the lens capsule. The lenses mean diameter was 8.4 ± 0.4 mm. Cataract was induced by lens immersion over time in an ethanol:2-propanol:formalin solution [11] - from zero (lens without cataract), 60 min (lens with initial cataract), 120 min (lens with advanced cataract) to 180 min (lens with total cataract). Slices of 50 μ m in thickness were obtained from two different regions of the lenses (nucleus and cortex), to locally analyze the scatterers (i.e., protein aggregates), distribution and concentration.

B. Ultrasound Velocity and Attenuation

The ultrasound velocity and the frequency dependent attenuation were estimated using the setup shown in Fig. 1.

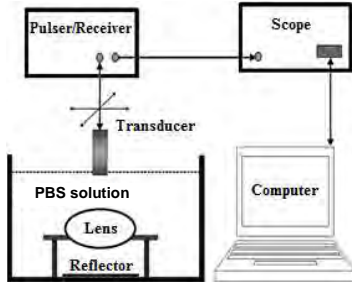


Fig. 1. Experimental setup.

The ultrasound velocity (V) was estimated based on the time of flight (Δt) considering the anterior and posterior capsule echoes, according to,

$$V = 2d/\Delta t \quad (1)$$

where d is the lens thickness and Δt is the time of flight.

The frequency dependent attenuation was estimated using a planar reflector, according to,

$$\alpha(f) = \frac{20}{2d} \log_{10} \left(\frac{A_1(f)}{A_2(f)} (T_{12} T_{21})^2 \right) - \alpha_s \quad (2)$$

where d is the lens thickness; $A_1(f)$ and $A_2(f)$ are the amplitude spectra from the echoes received from the reflector in the solution and from the reflector with the lens inserted, respectively; T_{12} and T_{21} are the transmission coefficients observed in the lens boundaries and α_s is the attenuation in the solution path corresponding to the lens thickness.

C. Nakagami Distribution

The backscattering signals from the lens tissue are essentially random, even when they result from the lens without cataract. Therefore the statistical analysis of the backscattering signals might provide useful information about the scatter properties of the tissue. The Nakagami m parameter, which is related to the shape of the Nakagami

distribution, determines the statistical distribution of the ultrasound backscattered envelope, and is given by,

$$f(r, m, \Omega) = \frac{2m^m r^{2m-1}}{\Gamma(m)\Omega^m} \exp\left(-\frac{m}{\Omega} r^2\right) U(r) \quad (3)$$

where Γ , U and Ω are the gamma function, the unit step function and the scaling parameter, respectively. Let E denote the statistical mean; then the Nakagami m parameter, associated with the Nakagami distribution can be obtained from,

$$m = \frac{[E(R^2)]^2}{E[R^2 - E(R^2)]^2} \quad (4)$$

where R is the random variable of the Nakagami distribution. The Nakagami m parameter ranges from 0 to 1 meaning a change in the envelope statistics from a pre-Rayleigh to a Rayleigh distribution [12].

D. Experimental procedure

1) *Backscattering Signals*: A 25 MHz focused (3.5 cm) transducer with a 5 mm active diameter was used in a pulse echo configuration. The lenses were placed on a perspex holder having a circular hole suited to the lens. Both the transducer and the lens were immersed in a temperature controlled phosphate buffer solution (PBS) (see Fig. 1). The measurements were taken for the referred lens immersion times (0 min – no cataract, 60 min, 120 min and 180 min – total cataract). A Pulsar/Receiver with a 35 MHz bandwidth (PR5800, Olympus NDT Inc., Waltham, MA, USA) was used. The received signals were displayed in a digital oscilloscope (Tektronix TDS 3032, Tektronix, Inc., TX, USA), and then transferred to the computer for processing. The velocity and attenuation were calculated taking the average of 10 A-Scan lines obtained over the central portion of the lens. The backscattering signals were used to estimate the frequency dependent attenuation (2), to construct B-Scan images using its intensity, and to compute the Nakagami m parameter (4).

2) *Slices of the nucleus and cortex*: Slices with 50 μ m in thickness were obtained from the different regions of the lenses. The lenses were first frozen at -40°C in an embedding resin, Cryomatrix medium (Thermo Scientific Shandon Ltd, WA, USA). Cuts were made transversally with a glass knife using a Leica Microsystems CM3350S cryostat (Leica Microsystems, Wetzlar, Germany).

3) *Tissue Staining and Imaging*: To stain the lens proteins, connective tissue and collagen, the Hematoxylin and Eosin (H&E) staining protocol was used. The stained slices from the nucleus and the cortex were imaged using an inverted microscope with a digital image capture system. The images were acquired with magnifications of 40x for the slices in the cortex and the nucleus region, and 4x for the slices of the nucleo-cortex region, and the same amounts of light and exposure times. The information provided by these images was correlated with the Nakagami and B-Scan images.

E. Statistical Analysis

To compare the ultrasound parameters in lens with and without induced cataract (i.e. with different lens hardness), the non-parametric *Kruskal-Wallis* and *Wilcoxon* tests were used (SPSS version 17.0, SPSS Inc, Chicago, IL, USA). Statistical values were considered significant for $p \leq 0.05$.

III. RESULTS

A. Ultrasound Velocity and Attenuation

The ultrasound velocity and the frequency dependent attenuation showed a statistically significant increase over cataract formation, i.e. over lens' hardness ($p < 0.001$, Fig. 2). The ultrasound velocity increased from 1600 ± 5 m/s in lens without cataract to 1652 ± 2 m/s in lens with total cataract (i.e., after 180 minutes) ($p < 0.001$; Fig. 2 (a)). The frequency dependent attenuation increased from 0.10 ± 0.01 dB/mmMHz in lenses without cataract to 0.17 ± 0.02 dB/mmMHz in lenses with total cataract ($p < 0.001$; Fig. 2 (b)).

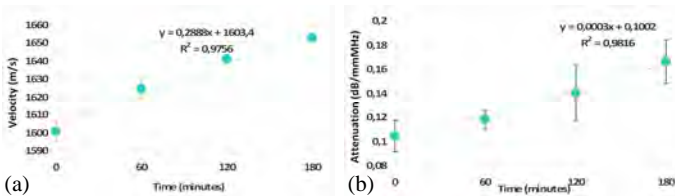


Fig. 2. Ultrasound velocity (a) and frequency dependent attenuation (b) over cataract formation.

B. B-Scan Images

The B-Scan images showed an increase of the relative echo intensity with cataract formation (Fig. 3). Also, as the cataract formation progresses the backscattering signals are collected deeper in the lens (see Fig. 3), revealing the presence of larger and dispersed protein aggregates, from the capsule to the nucleus.

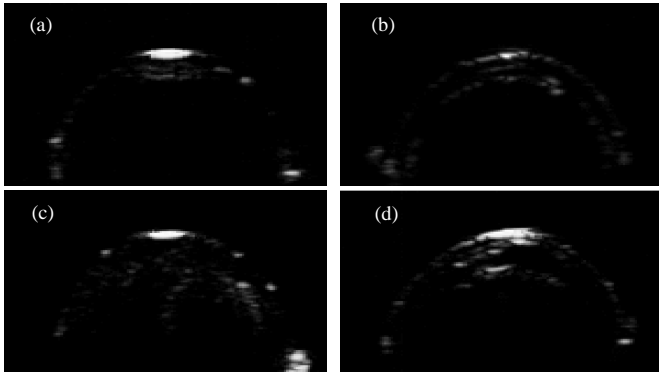


Fig. 3. B-mode images of lens: (a) without cataract; (b) 60 minutes, (c) 120 minutes, (d) and 180 minutes of immersion time.

C. Nakagami Images

The Nakagami images showed an increase of the m parameter with cataract formation (Fig. 4). With the purpose of removing the contribution of the iris, the mean Nakagami m

parameter was estimated in a region of interest. The mean value of m parameter increased from 0.32 for lenses without cataract (0 min) to 0.80 for lenses with total cataract (180 min) ($p < 0.001$). For the 60 and the 120 min the mean Nakagami m parameter was respectively: 0.48 and 0.51. No statistically differences were found between these two immersion times, $p = 0.650$. The m parameter behavior, indicates that the scatterers distribution evolves from a pre-Rayleigh to a Rayleigh distribution as the severity of the cataract increases. With cataract formation the Nakagami m parameter increases for deeper regions of the lens, as shown in Fig. 4, revealing the presence of a larger number of scatterers from the anterior capsule to the nucleus. When a total cataract is present (i.e. for an immersion of 180 min.) an increase of the Nakagami m parameter is observed between the anterior capsule of the lens and the beginning of the adult nucleus, as illustrated in Fig. 4 (d). It was also found that the Nakagami images do not identify scatterers in fetal and embryony nucleus. This is due to the larger compaction of the fibers in this region of the lens for advanced stages of cataract formation, and to the attenuation suffered in the cortex, which cause a substantial attenuation of the ultrasounds for the frequency of analysis. The result is very weak or inexistent backscattering signals coming from that depth.

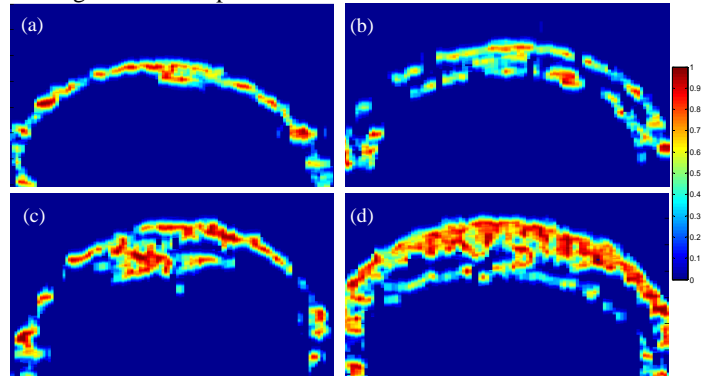


Fig. 4. Nakagami images: (a) without cataract; (b) 60 minutes; (c) 120 minutes, (d) and 180 minutes of immersion time.

D. Nucleus and Cortex protein aggregates

The $50 \mu\text{m}$ slices contain several layers of proteins in agglomerates, connective tissue and collagen fibers. Since these structures alone represent some nanometers, in accordance with the conditions of image acquisition and with the protein and connective tissue staining protocol, the darker areas of the microscopy images (Fig. 5 and Fig. 6) represent areas of higher protein aggregate concentrations. Fig. 5 shows the difference in the concentration of protein aggregates between the nucleus and cortex (from bottom to top).

For the nucleus and cortex regions (see Fig. 6) even more marked dyeings are visible along the different immersion times denoting a clear increase in protein aggregates during the process of cataract formation. Moreover, for all immersion times the nucleus region showed a higher dyeing than the cortex one, indicating the presence of more protein aggregates in this region of the lens.

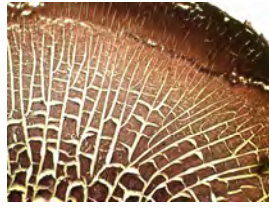


Fig. 5. Microscopy image of a transversal slice of the nucleo-cortex region.

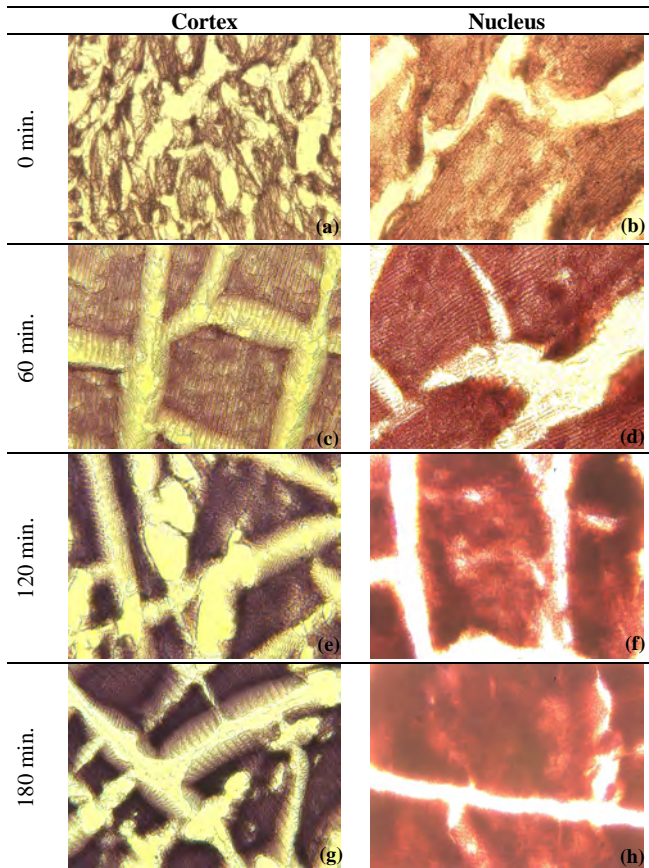


Fig. 6. Microscopy images: without cataract (cortex (a) and nucleus (b)); 60 minutes (cortex (c) and nucleus (d)); 120 minutes (cortex (e) and nucleus (f)); 180 minutes (cortex (g) and nucleus (h)).

IV. DISCUSSION AND CONCLUSIONS

It was shown in previous study that the ultrasound velocity and frequency dependent attenuation increases as the cataract hardness increase, due to changes in the scatterers size [10]. While these parameters provide cataract hardness information about the entire lens globally, the Nakagami m parameter presents as a promising parameter, capable to visualize and quantify locally the cataract formation since this parameter reflects changes in the arrangement, distribution and concentration of scatterers in the lens through cataract formation [10]. In this study it was possible to show that both the backscattering signals intensity (B-Scan) and the Nakagami m parameter vary spatially in the lens, increasing with cataract formation for deeper regions in the lens. The

images of the slices obtained for the nucleus and the cortex regions revealed the presence of protein aggregates that increased with the cataract formation. The increase of the proteins aggregates, for the different stages of cataract formation, was found to be in agreement with the increase of the Nakagami m parameter in the cortex. For the nucleus no correlation was found due to the higher compaction of the fibers in that region of the lens for the advanced stages of cataract, where the backscattering signals are very weak or inexistent. Additional study using different frequency values should be used to clarify these results. In summary, the results suggest that the interpretation of backscattering signals by the Nakagami distribution, when combined with the knowledge of the physical scatter properties are challenging. A distribution map of cataract hardness is the next goal, because it could play an important role assessing it.

ACKNOWLEDGMENT

This research is sponsored by CEMUC - Centro de Engenhariaia Mecânica da Universidade de Coimbra, FEDER/COMPETE-Programa Operacional Factores de Competitividade, and FCT - Fundação para a Ciência e a Tecnologia, under the project PTDC/DTP-PIC/0419/2012.

REFERENCES

- [1] J.J. Kanski. *Clinical Ophthalmology: A Systematic Approach*. Butterworth-Heinemann, 2006.
- [2] H. Ecrolyd and J. Carver. Crystallin proteins and amyloid fibrils. *Cellular and molecular life sciences: CMLS*, 66(1):62–68, 2009.
- [3] A.J. Kiss, A.Y. Mirarefi, S. Ramakrishnan, C.F. Zukoski, A.L. DeVries, and C.H.C. Cheng. Cold-stable eye lens crystallins of the antarctic nototheniid toothfish *dissostichus mawsoni* norman. *The Journal of Experimental Biology*, 207:4633–4649, 2004.
- [4] A. Paunksnis, S. Kurapkiene, A. Maciulis, and Paunksniene M.L. Evaluation of ultrasound attenuation characteristics of human cataract. *Informatica*, 14(4):529–540, 2003.
- [5] A. Paunksnis, S. Kurapkiene, A. Maciulis, A. Kopustinskas, and M. Paunksniene. Ultrasound quantitative evaluation of human eye cataract. *Informatica*, 18(2):267–278, 2007.
- [6] CL. de Korte, AF. van der Steen, and JM. Thijssen. Acoustic velocity and attenuation of eye tissues at 20 mhz. *Ultrasound in Medicine & Biology*, 20(5):471–480, 1994.
- [7] P.M. Shankar. A general statistical model for ultrasonic backscattering from tissues. *IEEE Transactions on Ultrasonics, Ferroelectrics and Frequency Control*, 47(3):727–736, 2000.
- [8] CC.. Huang, R. Chen, P. Tsui, Q. Zhou, MS. Humayun, and KK. Shung. Measurements of attenuation coefficient for evaluating the hardness of a cataract lens by a high-frequency ultrasonic needle transducer. *Physics in Medicine and Biology*, 54(19):5981–5994, 2009.
- [9] D. Jesus, M. Caixinha, M. Santos, and J. Santos. Ultrasound techniques for lens hardness characterization: A comparison study. In *IEEE Conference Publications*, editor, *2012 IEEE International Ultrasonics Symposium*, Dresden, 2012.
- [10] D. Jesus, E. Velte, M. Caixinha, M. Santos, and J. Santos. Using of the ultrasound frequency dependent attenuation and nakagami distribution for cataract evaluation. In *IEEE Conference Publications*, editor, *Bioengineering (ENBENG), 2013 IEEE 3rd Portuguese Meeting*, pages 1–4, 2013.
- [11] T. Sugiura, D. Kurosaka, Y. Uezuki, S. Eguchi, H. Obata, and T. Takahashi. Creating cataract in a pig eye. *Journal of Cataract and Refractive Surgery*, 25(5):615–621, 1999.
- [12] P.M. Shankar. Ultrasonic tissue characterization using a generalized nakagami model. *IEEE Transactions on Ultrasonics, Ferroelectrics and Frequency Control*, 48(6):1716–1720, 2001.

Using ultrasound backscattering signals and Nakagami statistical distribution to assess regional cataract hardness

Miguel Caixinha, Danilo Jesus, Elena Velte, Mário Santos, and Jaime B. Santos

Abstract—This study aims to analyze the protein aggregates spatial distribution for different cataract degrees, and correlate this information with the lens acoustical parameters and by this way, assess the cataract regional hardness. Different cataract degrees were induced ex-vivo in porcine lenses. A 25 MHz ultrasonic transducer was used to obtain the acoustical parameters (velocity, attenuation, and backscattering signals). B-scan and Nakagami images were constructed. Also lenses with different cataract degrees were sliced in two regions (nucleus and cortex), for fibers and collagen detection. A significant increase with cataract formation was found for the velocity, attenuation, brightness intensity of the B-Scan images, and Nakagami m parameter ($p < 0.01$). The acoustical parameters showed a good to moderate correlation with the m parameter for the different stages of cataract formation. A strong correlation was found between the protein aggregates in the cortex and the m parameter. Lenses without cataract are characterized using a Classification and Regression Tree, by a mean brightness intensity ≤ 0.351 , a variance of the B-Scan brightness intensity ≤ 0.070 , a velocity ≤ 1625 m/s and an attenuation ≤ 0.415 dB/mmMHz (sensitivity: 100% and specificity: 72.6%). To characterize different cataract degrees the m parameter should be considered. Initial stages of cataract are characterized by a mean brightness intensity > 0.351 and a variance of the m parameter > 0.110 . Advanced stages of cataract are characterized by a mean brightness intensity > 0.351 , a variance of the m parameter ≤ 0.110 and a mean m parameter > 0.374 . For initial and advanced stages of cataract, a sensitivity of 78.4% and a specificity of 86.5% are obtained.

Index Terms—Ultrasound, Backscattering, Cataract hardness, Nakagami distribution.

I. INTRODUCTION

Cataract is an opacity in the lens eye as a result of the crystalline proteins precipitation and aggregation, affecting more than 20 million people worldwide. Age-related cataract is the most frequent cause of blindness in the world being responsible for 48% of blindness, and affecting more than 10% of the working population [1]. With the increase of the elderly population, the number of persons with reduced vision or blindness secondary to cataract may reach 40 million people by the year 2020 [1]. The cataract formation seems to be the result of biochemical changes in the lens associated with aging, eye injuries, medications and diseases, but the nature and mechanisms of these changes are still under investigation [2]. The lens transparency is highly dependent on the well-ordered arrangement of the crystalline proteins and fibers, which are present in high concentration and make up almost the entire composition of the lens. Disruption of the

crystalline proteins arrangement due to the proteins aggregation leads to the impairment of light propagation in lens giving rise to cataract formation [3]. Currently surgical cataract removal is the only effective therapy for vision recovery since there is no cataract prevention or pharmacological treatment.

The phacoemulsification is the most common surgical procedure for cataract extraction. This procedure uses a hand-held ultrasonic device to fragment the cataractous lens into small pieces that are afterward aspirated [4], [5]. The posterior lens capsule remains in the eye to sustain the lens to be implanted. Integrity of the capsule is essential for reducing the risk of surgical complications and subsequent vision loss, but the choose of an inappropriate phacoemulsification energy level can disrupt the posterior capsule. Therefore, it is crucial to determine the optimal energy for the phacoemulsification probe, which value depends on the hardness of the cataract. Thus, the correct estimation of cataract hardness can minimize surgical complications. In particular, the selection of the optimal energy level for the cataract emulsification is crucial for the improvement of safety in this type of surgery. The major complications associated with this surgery, and representing approximately 5 to 10% of the postoperative complications are endothelial cells damage, and posterior capsule rupture (both related with and inadequate energy level selection, among other factors) [5]–[7]. Since every year thousands of patients are submitted to this surgery, its optimization by minimizing the complication risks and surgery time will have a significant socio-economic impact.

For the clinical prognosis and therapeutic purposes it is very important to identify the cataract type and severity, especially in its early stages [8]. Post-surgical complications can be avoided if the hardness of the cataractous lens is correctly estimated. In this context, the ultrasounds are a powerful, noninvasive and less expensive technique for biological tissue characterization [9]. The applicability of ultrasound methods for characterizing cataractous lenses has been studied in the last years [10]–[12]. In cataractous lenses, regions of higher opacity are associated with strong echoes corresponding to reflections caused by impedance variations in tissue. So, the intensity of the echo signal from a lens with cataract differs from the echo intensity obtained in a lens without cataract [11], [13], [14]. By using the amplitude of the signals it is then possible to construct a brightness image (B-Scan image) of the lens, allowing for a qualitative characterization of its structure. However, this conventional brightness image cannot be used as an indicator of lens hardness, since the amplitude of the signals are dependent on the system

settings (such as the gain or the dynamic range), the acquisition mode (angle of incidence of the ultrasound) and the user experience [13], [15]. To evaluate the hardness of the cataractous lens two important ultrasound parameters have been used, the velocity and the attenuation [4], [8], [10], [14], [16], [17]. Huang *et al.* demonstrated that the increase of the attenuation indicates an increase of the cataract hardness, and by measuring the Young modulus, established a correlation between these two parameters [10], [12].

Although some of the developed studies allow quantifying the hardness of lens based on the above-mentioned ultrasound parameters, namely the frequency dependent attenuation, they have some limitations. The most important one is related to the fact that the results only provide information about the cataract presence and respective hardness globally [10]. Thus, important information as the exact regional cataract hardness is not achieved with this methodology. Also, there is no adequate noninvasive characterization of the regional cataract hardness. In general the methods presented in the literature used to assess local cataract hardness are invasive [4], [11], [12]. By this way, it is particularly important, for cataract surgery, the correct estimation of cataract hardness in whole extension of the lens.

The ultrasound parameters used in a noninvasive way appear as the most realistic approach to assess the cataract hardness and provide information about its severity and type [4], [10]–[12]. Velocity and attenuation have been calculated using human and porcine eye lens [18]. As mentioned above an approach for visualizing cataract is based on the B-Scan image, however B-Scan describes echogenicity changes allowing only to infer about the presence or not of cataract [13]. Thus, new techniques are demanded to improve the information provided by the B-Scan imaging and to allow quantitative characterization of hardness in the human lens. For that goal, the Nakagami statistical distribution has received considerable attention because the associated Nakagami m parameter can be applied to the backscattered signals, making it possible to identify scatterers in tissue [13], [14], [19]–[22]. Concerning to cataract, the ultrasound backscattering is essentially a random process, and then the statistical analysis of the backscattered signals may provide useful information about the lens scatterers concentration and spatial distribution.

In the present work, the feasibility of the Nakagami statistical distribution to assess regional cataract hardness was evaluated. It is well established that the Nakagami distribution is a robust imaging method less sensitive to user variability and system settings. This is mainly due to the fact that the Nakagami images are based on the local statistical variation of the backscattering signals, and not only in their absolute values [13]. The Nakagami distribution allows for the characterization of different concentrations and distributions of scatterers in tissue [9], [14], [21], [23], [24], then providing the extraction of features capable to characterize the tissue properties, namely the scatterers density for subsequent correlation with the lens hardness. The Nakagami image allows then for the local estimation of the scatterers concentration in

the lens and extraction of information from backscattering regions [25]. Several studies proposed the Nakagami imaging as a complementary method to B-Scan in order to improve the information associated with the spatial arrangement and concentration of the scatterers, being useful for the identification of different degrees of the cataract hardness [11], [13], [14], [19], [20], [25].

The feasibility of using Nakagami parametric images to quantify lens hardness was explored by Tsui *et al.* [14]. Their results showed that Nakagami imaging can be used to distinguish both global and local variations in lens hardness. Tsui concluded that the scatterers concentration of the fiber compaction, which is mainly responsible for the increase in lens hardness during cataract formation, could be quantified using Nakagami images to analyze the statistical distribution of ultrasonic backscattered echoes.

In this work, Nakagami images were obtained from porcine lenses with different degrees of cataract and then compared in order to study the m parameter potential to detect the local arrangements and scatterers concentration. The images were constructed from A-Scan lines collected by a single transducer, noninvasively. In order to infer about the cataract hardness, the mean Nakagami m parameter was correlated with the acoustical parameters. Additionally, stained slices from the lens (nucleus and cortex regions) were imaged and used as a confirming method for scatterers distribution and concentration in different regions of the lenses, and for different stages of the cataract formation.

II. MATERIALS AND METHODS

A. Lens samples

Two hundred and two (202) lenses from porcine eyes were collected in a slaughterhouse. Lens were carefully extracted and prepared to clean iris remains and adhering vitreous, preserving the lens capsule. Cataract was induced in 140 lenses immersed over time in an ethanol:2-propanol:formalin solution at the ratio 3:3:4 [26]. To obtain different cataract degrees the lenses were immersed in the solution during 60, 120 and 180 minutes, corresponding to lenses with initial (52), advanced (46) and total (42) cataract, respectively. Sixty-two lenses were used as control (without cataract).

B. Experimental Setup

The ultrasound parameters as velocity and frequency dependent attenuation, and the backscattering signals were obtained using the setup shown in Fig. 1.

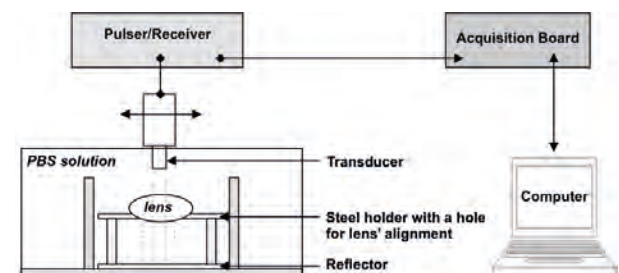


Fig. 1. Experimental setup.

A 25 MHz transducer (model JAP-F25.3.1, Krautkramer, NSW, Australia) with a 25 mm focus and 5 mm active diameter with a pulse length of 0.13 μ s at -6 dB was used. The lenses were placed on a stainless steel holder having a machined hole suited to the lens. All over the data collection the solution temperature was kept constant at 28.0 \pm 0.5 $^\circ$ C. A pulse/receiver with a 35 MHz bandwidth (model PR5800, Olympus NDT Inc., Waltham, MA, USA) was used in a pulse-echo configuration. The echo signals were recorded and digitized with a 14 bit, 200 MHz A/D card (model PCIe-9842, ADLINK Technology Inc., Taipei, Taiwan). The transducer was moved using a computer-controlled micro-positioning system.

C. Ultrasound Velocity and Attenuation

The ultrasound propagation velocity (v) in the lens was calculated as the average value of ten A-Scan lines collected over the central portion of the lens, according to the following expression [10], [14].

$$v = c \left(\frac{t_s - t_c}{t_b - t_a} + 1 \right) \quad (1)$$

where c is the ultrasound velocity in the solution, t_c and t_s are the propagation times for the path between the transducer and a reflector with and without the lens inserted, respectively, and t_a and t_b correspond to the propagation times of the waves from the transducer to the front and back faces of the lens, respectively.

The ultrasound attenuation coefficient was calculated by evaluating the frequency dependent attenuation all over the crystalline tissue, for the central frequency of the transducer, considering also the average of ten A-scan lines, by using the following expression, [12],

$$\alpha(f) = \frac{20}{2d} \log_{10} \left(\frac{A_1(f)}{A_2(f)} (T_{12} T_{21})^2 \right) - \alpha_s \quad (2)$$

where d is the lens thickness; $A_1(f)$ and $A_2(f)$ are the amplitude spectra from the echoes received from the reflector without and with the lens inserted, respectively; T_{12} and T_{21} are the transmission coefficients in the lens boundaries and α_s is the attenuation in the used solution for the path corresponding to the lens thickness.

The lens thickness value was obtained by the following expression,

$$d = \frac{vt}{2} \quad (3)$$

where v is the ultrasound velocity calculated by (1) and t is the propagation time in the lens.

D. B-Scan Imaging

Although A-Scan signals contain a large amount of information they are difficult to interpret and therefore, the ultrasound data are usually presented as brightness-modulated images (B-Scan). The construction of these images encompasses the envelope detection of the signals, followed by a logarithmic compression. Then, the signals

are converted to a scale of 256 grey levels for posterior image reconstruction by using the multiple scan lines, collected from a given region of the tissue. The envelope of the A-scan signals were obtained using the Hilbert transform [27], [28].

For each lens, the B-Scan images were constructed using 15000 A-Scan signals sampled at a 200 MHz rate, considering the envelope amplitudes of the backscattering signals and a dynamic range of 40 dB. The distance between each A-Scan line was 0.001 mm.

E. Nakagami Statistics

The probability density function of the backscattered signals envelope, $f(r, m, \Omega)$, given by the Nakagami distribution is expressed by [23],

$$f(r, m, \Omega) = \frac{2m^m r^{2m-1}}{\Gamma(m) \Omega^m} \exp\left(-\frac{m}{\Omega} r^2\right) U(r) \quad (4)$$

where Γ is the gamma function, U is the unit step function, m and Ω are the Nakagami parameters. The m parameter is the shape parameter and Ω is the scale parameter. The m parameter is expressed as,

$$m = \frac{[E(R^2)]^2}{E[R^2 - E(R^2)]^2} \quad (5)$$

where $E(\cdot)$ denotes the statistical mean.

As the statistics of the backscattered echoes vary with the scatter concentration the Nakagami image can be used to identify the scatter concentrations in the lens [21], [23]. Although Nakagami images can be seen as a reliable tool to complement B-scan images, some problems have to be solved to make it effective, namely the artifacts generated by the noise in the anechoic areas of the lenses. In order to reduce noise and improve the Nakagami m parameter performance, an adaptive threshold filter was applied to the backscattered signals before the construction of the Nakagami parametric image [29]. Having a noise level corresponding to a SNR of 17 dB, the adaptive threshold filter was based on noise-assisted empirical mode decomposition. Its performance is similar to the conventional thresholding technique based on the applying a cutoff value for rejecting small echoes. The Nakagami m parameter, calculated after adaptive threshold filtering, is also called noise-assisted Nakagami m parameter [20], [29]. Other two filtering techniques were tested in this work, noise-assisted correlation algorithm [30] and wavelet-based image denoising [31]. The results obtained were very similar to the noise-assisted empirical mode decomposition technique.

The Nakagami parametric image was constructed based on the B-mode image, and corresponds to two-dimensional representation of the m parameter values. The image construction process encompassed a sliding window selected to provide good resolution, considering that a small window improves the resolution but, on the other hand, gives rise to few envelope points, which can lead to bad estimations of the m parameter [19]. In this work, it was considered a window with three times the transducer

pulse length ($0.39\mu\text{s}$) corresponding to 78 samples, taking into account the sampling frequency of 200 MHz and 99% of overlapping. A color scale was used for the Nakagami image to facilitate the visualization and interpretation. The color scale ranges from blue to red as the values of the m parameter increase from 0 to 1, corresponding to backscattered signal envelopes changing from a pre-Rayleigh to a Rayleigh statistical distributions.

F. Region of Interest (ROI)

To correlate B-Scan brightness intensity and Nakagami m parameter with the acoustical parameters, and with the information obtained from the slices, a ROI was defined in the images.

The ROI was chosen selecting an area on the B-Scan and Nakagami images that includes only regions containing protein aggregates and collagen fibers. A ROI with 4.5 mm in width and 1.5 mm in depth was considered (Fig. 2 - left). Additionally, to exclude any contribution of the external region of the lens, a mask with the shape of the lens was used (Fig. 2 - right).



Fig. 2. ROI used to compute the mean brightness intensity and the mean m parameter.

G. Nucleus and cortex slices and Imaging

Slices with $50\mu\text{m}$ in thickness were obtained in different regions of the lenses. The lenses were first frozen at -40°C in an embedding resin, Cryomatrix Shandon medium (Thermo Scientific Shandon Ltd, WA, USA). Cuts were made transversally with a glass knife using a Leica Microsystems CM3350S cryostat (Leica Microsystems, Wetzlar, Germany).

To stain the lens proteins, connective tissue and collagen, the Hematoxylin and Eosin (H&E) staining protocol was used. The stained slices from the nucleus and the cortex were imaged using an inverted microscope with a digital image capture system. The images were acquired with the same magnification (40x for the slices in the cortex and the nucleus region, and 4x for the slices of the nucleus-cortex region) and the same amounts of light and exposure times. According to the protein staining protocol and connective tissue, the mean brightness intensity of the slice images was computed to estimate the quantity of proteins and collagen fibers. The information provided by these images was correlated with the mean Nakagami m parameter and with mean brightness intensity of the B-Scan images.

III. STATISTICAL ANALYSIS

Statistically significant differences between lens with and without induced cataract (i.e. with different hardness) were tested for the ultrasound velocity, the attenuation, the

mean brightness intensity on B-Scan images, the mean Nakagami m parameter and for the mean brightness intensity of the slice images obtained in the cortex and nucleus regions, using ANOVA and Student-t tests. Correlations between the different parameters were tested using the Spearman correlation coefficient.

To verify whether the different parameters can predict the presence of cataract, a classification and regression tree (CRT) with a 10-fold cross validation was performed. Classification and regression trees (CRT) are a supervised learning technique that creates rules to classify elements according to predefined categories [32], [33]. CRT are classifiers with a tree-like structure that splits recursively the input dataset until each data subset consists completely (or predominantly) of elements from one category. The tree grows from the parent (root) to the child nodes (leaves) and in each node a testing is performed on one or more attributes to decide how the data should be split. Data partitioning is completed when the data subset at a node is either "pure" (i.e. all cases within the node has the same target variable value) or sufficiently small (as set *a priori* by the user). CRT uses an algorithm where data partitioning is based on the maximization of the within-node homogeneity, i.e., the minimization of the number of cases with different membership in each node of the tree (minimization of the node impurity) [32]. Furthermore, to reduce the risk of overfitting, and to create a more accurate CRT, the initial tree is pruned, that is the small and/or deep nodes of the tree are removed.

The commercial statistical software IBM SPSS Statistics version 20 was used (IBM Corp., NY, USA). Statistical values were considered significant for p -values lower than 0.05.

IV. RESULTS AND DISCUSSION

A. Acoustical parameters: Ultrasound Velocity and Attenuation

The results for the propagation velocity and attenuation for the studied lenses are shown in Fig. 3. It is observed an increase of the acoustical parameters values with the cataract formation. The ultrasound velocity ranged from 1585.0 ± 31.7 m/s in normal lenses to 1652.7 ± 27.8 m/s in lenses with total cataract (after 180 minutes of immersion time). The attenuation increased from 0.406 ± 0.028 dB/mmMHz in normal lenses to 0.444 ± 0.037 dB/mmMHz in lenses with total cataract. For both acoustical parameters a statistically significant increase was found with the cataract formation ($p < 0.001$), being not statistically significant between 120 and 180 minutes of immersion time ($p > 0.834$).

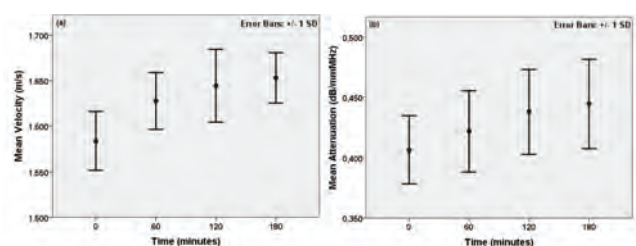


Fig. 3. Acoustical parameters versus cataract formation, i.e., lens immersion times: (a) velocity; (b) attenuation.

B. B-Scan Images

The constructed B-Scan images illustrate an increase of the backscattering signals amplitude over the cataract formation (see Fig. 4), characterized by an increased region with high scatterers concentration, from the cortex to the nucleus, which are responsible for opacity in the lens [34], as observed in the Nakagami images (see Fig. 7). The cataract formation pattern, observed in the referred B-Scan and Nakagami images is a result of the method used for cataract induction. After 60 minutes of lens immersion a separation between the cortex and the nucleus becomes visible (Fig. 4b) as a result of the different fiber compactations, originating different acoustical impedances between these two regions. The mean brightness intensity (normalized values) in the ROI, increased from 0.239 ± 0.094 for a lens without cataract (Fig. 4a and Fig. 5) to 0.753 ± 0.222 , for a lens with total cataract (Fig. 4d and Fig. 5). A statistically significant increase was found with cataract formation, i.e., over and between the different immersion times ($p < 0.01$). Moreover, the mean brightness intensity showed a good correlation with the velocity ($r = 0.605$, $p < 0.001$) and a moderate correlation with the attenuation ($r = 0.529$, $p < 0.001$).

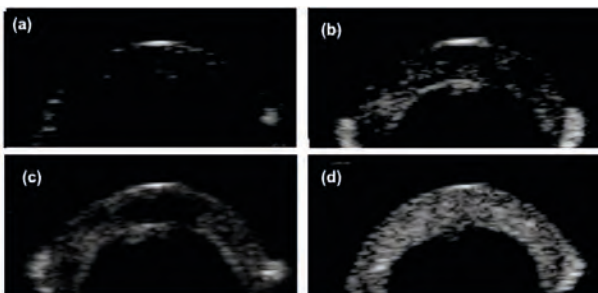


Fig. 4. B-Scan images for lenses: (a) without cataract; (b) 60 minutes; (c) 120 minutes; (d) and 180 minutes of immersion time.

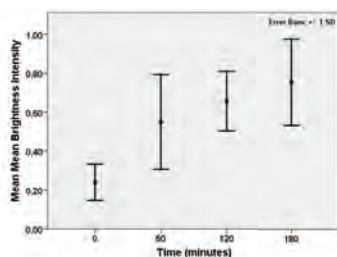


Fig. 5. Mean B-Scan brightness intensity versus cataract formation, i.e., lens immersion times.

C. Nakagami Images

The Nakagami images showed also consistent results i.e., the m parameter increases with cataract formation from the cortex to the nucleus. The mean value of the m parameter, obtained in the ROI changed from 0.272 ± 0.076 for lenses without cataract (Fig. 6 and Fig. 7a) to 0.554 ± 0.166 , for lenses with total cataract (Fig. 6 and Fig. 7d). A statistically significant increase was found with cataract formation, i.e., over and between the different immersion times ($p < 0.01$). Moreover, the mean Nakagami

m parameter showed a good correlation with the velocity ($r = 0.657$, $p < 0.001$) and a moderate correlation with the attenuation ($r = 0.471$, $p < 0.001$).

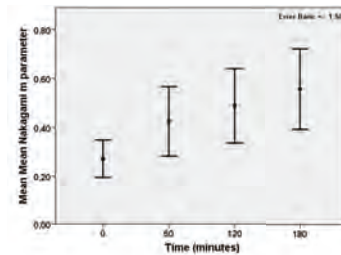


Fig. 6. Mean Nakagami m parameter versus cataract formation, i.e., lens immersion times.

In normal lenses the m parameter values are close to 0 (Fig. 7a), while for lenses with total cataract values are close to 1 (Fig. 7d). The m parameter behavior indicates that the scatterers distribution evolves from a pre-Rayleigh to a Rayleigh distribution as the cataract progresses from initial to total cataract [19], [23]. Also, with cataract formation the m parameter increases deeper in the cortex region (Fig. 7), revealing the presence of a larger number of scatterers from the cortex to the nucleus. These results are in agreement with the work carried out by Tsui *et al.* [14], where a 35 MHz ultrasonic transducer was used to characterize cataract in porcine lens. That higher frequency transducer limited the depth analysis in lenses. In this work, using a 25 MHz transducer in a noninvasive way, it is possible to obtain scatterers distribution for deeper regions in lenses, as shown in Fig. 7.

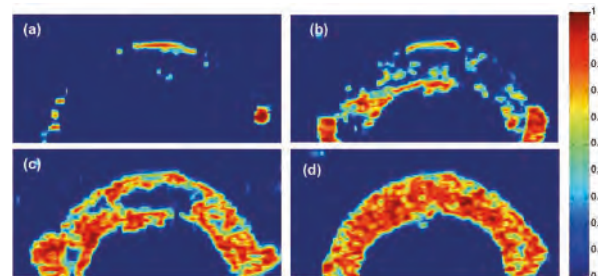


Fig. 7. Nakagami images representing the scatterers distribution for different degrees of cataract, for: lenses without cataract (a); 60 minutes of immersion time (b); 120 minutes (c); and with total cataract (d).

Tsui *et al.* [11] also performed an ex-vivo study in porcine lens using a high frequency needle transducer of 47 MHz. They calculated the acoustical parameters for normal and cataractous lenses invasively, making possible to locally estimate cataract hardness using backscattering signals and the Nakagami distribution. However, it is important to refer that Nakagami parameter estimation could be affected by the cataract hardness. This hypothesis was raised by Tsui *et al.* in a recent work [25], where they explore the relation between the features of the Nakagami images and the mechanical properties of a medium with scatterers. The study was performed in phantoms with different hardness and scatterers concentration in order to confirm which of these parameters have a higher impact on the m parameter estimation. Although no definitive

conclusion was obtained, they found that the m parameter measured in a medium with a low scatterers concentration correlated strongly with the hardness. In our work, tissues with different degrees of hardness and consequently with different scatterers concentration and fibers compaction (as evidenced by the histological images, section D.) were analyzed, and therefore, a different estimation of the m parameter for the groups of lenses considered in this work can occur. However, in the cataract formation, where the increase of the hardness is related to the increase of the fibers compaction and scatterers concentration, it is difficult to separate the contribution of these two parameters. In particular, for the type of cataract induced in this work (total cataract), it is impossible to separate hardness and scatterers concentration contributions for m parameter estimation.

D. Nucleus and Cortex protein aggregates

The difference in protein aggregate's concentration between the nucleus and cortex in a cataractous lens is shown in the microscopy image of a transversal slice of the nucleus-cortex region (see Fig. 8). The slice, with 50 μm , contains several layers of proteins in agglomerates, connective tissue and collagen fibers. Since these structures alone represent some nanometers, in accordance with the conditions of image acquisition and with the protein and connective tissue staining protocol, the darker areas in the microscopy images represent areas of higher protein aggregates concentration.

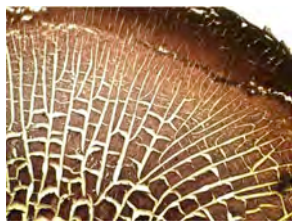


Fig. 8. Microscopy image of a transversal slice of the nucleus-cortex region.

For the nucleus and the cortex regions (Fig. 9) more pronounced dyeings are visible along the different immersion times denoting a clear increase in protein aggregates during the process of cataract formation. This is in agreement with the decrease of the brightness intensity (normalized values) of the slice images observed for the different immersion times for both cortex and nucleus regions (Fig. 10). Moreover, for all immersion times the nucleus region showed a higher dyeing than the cortex region indicating the presence of more protein aggregates in that region of the lens. The microscopy images are in agreement with the results obtained in the Nakagami images for different degrees of cataract. A strong correlation was found between the mean brightness intensity of the slice images obtained in the cortex region and the mean Nakagami m parameter ($r=-0.943$; $p=0.029$) (Fig. 11). No correlation was made for the nucleus due to the absence of backscattering signals for the whole extension of that region of the lens. Regarding the mean brightness intensity in the B-Scan images, a statistically significant correlation was also found ($r=-0.922$; $p=0.039$).

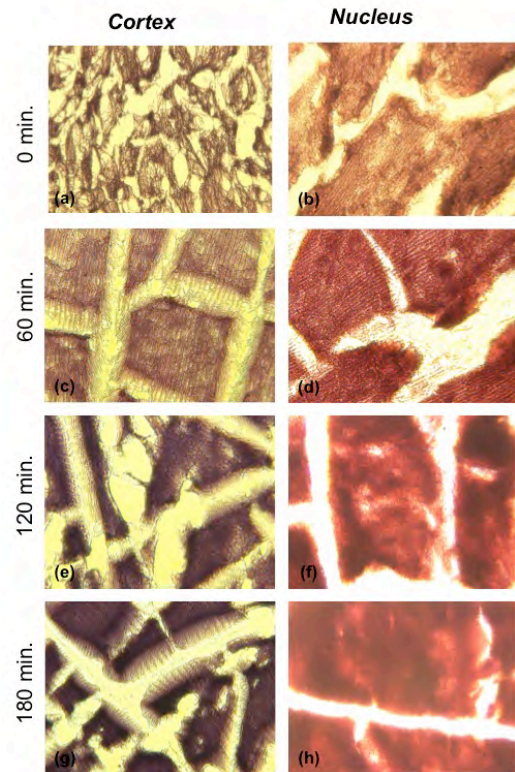


Fig. 9. Microscopy images. Left side: cortex (a - 0 minutes; c - 60 minutes; e - 120 minutes; and g - 180 minutes). Right side: nucleus (b - 0 minutes; d - 60 minutes; f - 120 minutes; and h - 180 minutes).

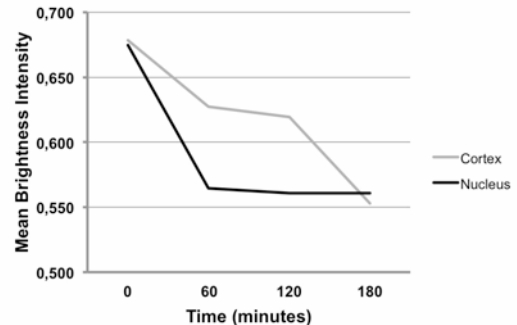


Fig. 10. Mean brightness intensity for the slice images obtained in the cortex and the nucleus for different immersion times.

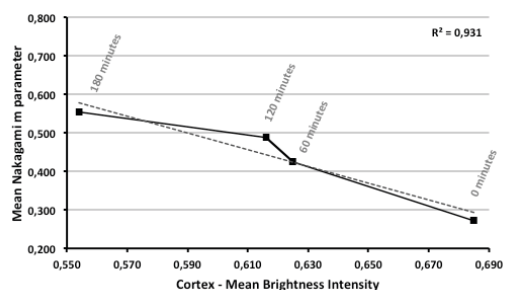


Fig. 11. Mean Nakagami m parameter versus mean brightness intensity of the slice images for the 4 immersion times.

E. Predictive parameters for cataract formation

A CRT was performed considering the two acoustical parameters (velocity and attenuation), the B-Scan mean brightness intensity and the mean Nakagami m parameter. Additionally, to account for the dispersion of the brightness intensity values in the B-Scan image and the spreading of the m parameter values in the Nakagami image, the variance of the brightness intensity and the variance of the m parameter for the same ROI were considered.

Eighty-seven percent (87.1%) of the lenses were correctly predicted by the CRT, with a risk estimate factor of 25.2% (Fig. 12). A good discrimination was found between lenses without cataract and lenses with cataract. Seventy-three percent (72.6%) of the lenses without cataract are characterized by a mean B-Scan brightness intensity ≤ 0.351 , a variance of the B-Scan brightness intensity ≤ 0.070 , a velocity ≤ 1625 m/s and an attenuation ≤ 0.415 dB/mmMHz. Lenses with cataract are characterized by a mean brightness B-Scan intensity > 0.351 , being the remaining discriminating factors the variance and the mean value of the Nakagami m parameter. Lenses with initial cataract are characterized by a variance of the m parameter in the Nakagami image > 0.110 , or when the variance is lower by a mean value of the m parameter ≤ 0.374 , while lenses with advanced cataract are characterized by a lower value of the variance of the Nakagami m parameter and a higher value of the mean value of the m parameter.

The cutoff values characterizing lenses without cataract, classify 157 lenses with cataract and 45 lenses without cataract (Table 1). The mean and variance of the

B-Scan brightness intensity, and the velocity and/or the attenuation values allow for a sensitivity of 100% for the presence of cataract (all the lenses with cataract are correctly identified) and a specificity of 72.6% (i.e., for the classification of lenses without cataract). The absence of scatters in lenses without cataract results in a low mean value and in a smaller variance of the m parameter, and therefore the m parameter does not appear as a discriminating factor for lenses without cataract.

Table 1. Classification of Cataract versus No Cataract.

	Cataract	No Cataract	TOTAL
Lenses with 60, 120 or 180 minutes of immersion times	140	0	140
Lenses without cataract (0 minutes)	17	45	62
TOTAL	157	45	202

For lenses with cataract, a variance of the m parameter in the Nakagami image (> 0.110) and a mean value of the m parameter (> 0.374) allowed for a sensitivity of 78.4% for the advanced stages of cataract formation and a specificity of 86.5% for the initial stages (Table 2).

Table 2. Classification of advanced versus initial stages of cataract formation.

	Severe Cataract	Initial Cataract	TOTAL
Lenses with immersion times of 120 and 180 minutes (Advanced Cataract)	69	19	88
Lenses with 60 minutes of immersion time (Initial Cataract)	7	45	52
TOTAL	64	76	140

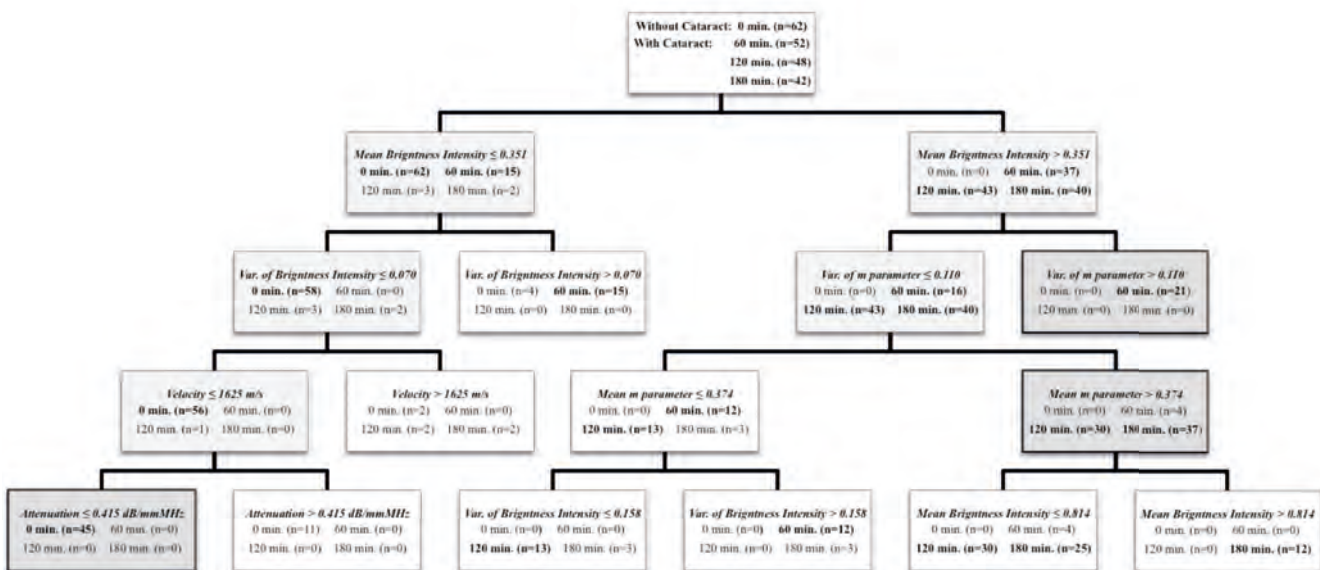


Fig. 12. Principal nodes of the CRT.

V. CONCLUSIONS

In this work, the cataract hardness was characterized noninvasively by assessing the acoustical parameters, the brightness intensity of the B-Scan images and the Nakagami m parameter. It was shown that the velocity and attenuation increase with cataract formation and this increase correlates with the increase of the mean Nakagami m parameter, i.e. with the increase of the protein aggregates, confirmed by the slice images obtained for different immersion times. For lenses with advanced stages of cataract, it was shown that none of the global parameters, velocity and attenuation, showed statistically significant differences. Using machine learning techniques (CRT) it was demonstrated that the acoustical parameters and the mean brightness intensity of the B-Scan images have a good sensitivity to discriminate lenses without cataract. When cataract is present, the acoustical parameters do not allow for a good discrimination of the different stages of cataract. Here the Nakagami m parameter, combined with the B-Scan images brightness intensity should be used to characterize the different degrees of cataract. The obtained results showed that the Nakagami image complements the information provided by the B-Scan image and the acoustical parameters for cataract characterization.

Our results show that the ultrasound scanning of eye lenses through Nakagami image is a potential imaging tool to noninvasively assess cataract hardness. The methodology developed in this work represents a technological basis for the development of a medical device for patient-oriented cataract surgery.

ACKNOWLEDGMENT

This research is sponsored by CEMUC – Center of Mechanical Engineering, University of Coimbra, FEDER funds through the program COMPETE – Operational Program for Competitiveness Factors – and by national funds through FCT – Foundation for Science and Technology, under the project PTDC/DTP-PIC/0419/2012.

REFERENCES

- [1] World Health Organization, “Vision 2020 The right to sight - Global initiative for the elimination of avoidable blindness: action plan 2006-2011,” Switzerland, 2008.
- [2] J. Kanski, *Clinical diagnosis in ophthalmology*, 1st ed. Philadelphia: Elsevier Mosby, 2007.
- [3] H. Ecroyd and J. Carver, “Crystallin proteins and amyloid fibrils,” *Cell. Mol. Life Sci.*, vol. 66, no. 1, pp. 62–81, Jan. 2009.
- [4] C. Huang, Q. Zhou, H. Ameri, W. Wu, L. Sun, S. Wang, M. Humayun, and K. Shung, “Determining the acoustic properties of the lens using a high-frequency ultrasonic needle transducer,” *Ultrasound Med. Biol.*, vol. 33, no. 12, pp. 1971–7, Dec. 2007.
- [5] S. Wilson, R. Trivedi, Ed., *Pediatric Cataract Surgery: Techniques, Complications, and*

- Management*. Lippincott Williams & Wilkins, 2005, p. 320.
- [6] M. Muhtaseb, A. Kalhor, and A. Ionides, “A system for preoperative stratification of cataract patients according to risk of intraoperative complications: a prospective analysis of 1441 cases.,” *Br. J. Ophthalmol.*, vol. 88, no. 10, pp. 1242–6, Oct. 2004.
- [7] P. Carricondo and A. Fortes, “Senior resident phacoemulsification learning curve,” *Arq. Bras. Oftalmol.*, vol. 73, no. 4, pp. 7–10, 2010.
- [8] A. Paunksnis, S. Kurapkienė, and A. Mačiulis, “Ultrasound quantitative evaluation of human eye cataract,” *Informatika*, vol. 18, no. 2, pp. 267–278, 2007.
- [9] M. Ho, J. Lin, Y. Shu, C. Chen, K. Chang, C. Chang, and P. Tsui, “Using ultrasound Nakagami imaging to assess liver fibrosis in rats.,” *Ultrasonics*, vol. 52, no. 2, pp. 215–22, Feb. 2012.
- [10] C. Huang, H. Ameri, C. Deboer, A. Rowley, X. Xu, L. Sun, S. Wang, M. Humayun, and K. Shung, “Evaluation of lens hardness in cataract surgery using high-frequency ultrasonic parameters in vitro.,” *Ultrasound Med. Biol.*, vol. 33, no. 10, pp. 1609–16, Oct. 2007.
- [11] P. Tsui, C. Huang, Q. Zhou, and K. Shung, “Cataract measurement by estimating the ultrasonic statistical parameter using an ultrasound needle transducer: an in vitro study,” *Physiol. Meas.*, vol. 32, no. 5, pp. 513–522, May 2011.
- [12] C. Huang, R. Chen, and P. Tsui, “Measurements of attenuation coefficient for evaluating the hardness of a cataract lens by a high-frequency ultrasonic needle transducer,” *Phys. Med. Biol.*, vol. 54, no. 19, pp. 5981–5994, 2009.
- [13] P. Tsui and C. Chang, “Imaging local scatterer concentrations by the Nakagami statistical model.,” *Ultrasound Med. Biol.*, vol. 33, no. 4, pp. 608–19, Apr. 2007.
- [14] P. Tsui, C. Huang, C. Chang, S. Wang, and K. Shung, “Feasibility study of using high-frequency ultrasonic Nakagami imaging for characterizing the cataract lens in vitro,” *Phys. Med. Biol.*, vol. 52, no. 21, pp. 6413–6425, Nov. 2007.
- [15] P. Tsui, C. Yeh, and C. Chang, “Noise Effect on the Performance of Nakagami Image in Ultrasound Tissue Characterization,” *J. Med. Biol. Eng.*, pp. 3–8, 2008.
- [16] H. Tabandeh, M. Wilkins, G. Thompson, D. Nassiri, and A. Karim, “Hardness and ultrasonic characteristics of the human crystalline lens,” *J. Cataract Refract. Surg.*, vol. 26, pp. 838–841, 2000.
- [17] R. Raitelaitienė and A. Paunksnis, “Ultrasonic and biochemical evaluation of human diabetic lens,” *Med.*, vol. 41, no. 8, 2005.
- [18] C. de Korte, A. van der Steen, J. Thijssen, J. Duindam, C. Otto, and G. Puppels, “Relation between local acoustic parameters and protein distribution in human and porcine eye lenses,” *Exp. Eye Res.*, vol. 59, no. 5, pp. 617–27, Nov. 1994.

- [19] P. Tsui, C. Huang, and S. Wang, "Use of Nakagami distribution and logarithmic compression in ultrasonic tissue characterization," *J. Med. Biol. Eng.*, vol. 26, no. 2, pp. 69–73, 2006.
- [20] P. Tsui, C. Chang, M. Ho, Y. Lee, Y. Chen, N. Huang, Z. Wu, and K. Chang, "Use of nakagami statistics and empirical mode decomposition for ultrasound tissue characterization by a nonfocused transducer.," *Ultrasound Med. Biol.*, vol. 35, no. 12, pp. 2055–68, Dec. 2009.
- [21] P. Tsui, C. Yeh, Y. Liao, C. Chang, W. Kuo, K. Chang, and C. Chen, "Ultrasonic Nakagami imaging: a strategy to visualize the scatterer properties of benign and malignant breast tumors.," *Ultrasound Med. Biol.*, vol. 36, no. 2, pp. 209–17, Feb. 2010.
- [22] G. Pinton, J. Aubry, E. Bossy, M. Muller, M. Pernot, and M. Tanter, "Attenuation, scattering, and absorption of ultrasound in the skull bone.," *Med. Phys.*, vol. 39, no. 1, pp. 299–307, Jan. 2012.
- [23] P. Shankar, "A general statistical model for ultrasonic backscattering from tissues.," *IEEE Trans. Ultrason. Ferroelectr. Freq. Control*, vol. 47, no. 3, pp. 727–36, Jan. 2000.
- [24] P. Shankar, "Ultrasonic tissue characterization using a generalized Nakagami model," *IEEE Trans Ultrason Ferroelectr Freq Control*, vol. 48, no. 6, pp. 1716–1720, 2001.
- [25] P. Tsui, Y. Wan, and Y. Chien, "Dependency of Ultrasonic Nakagami Image on The Mechanical Properties of Scattering Medium," *J. Med. Biol. Eng.*, vol. 33, no. 1, pp. 95–102, 2013.
- [26] T. Sugiura, D. Kurosaka, and Y. Uezuki, "Creating cataract in a pig eye," *J. Cataract Refract. Surg.*, vol. 25, no. 5, pp. 615–621, May 1999.
- [27] J. Noble and P. Wells, "Ultrasound image segmentation and tissue characterization.," *Proc. Inst. Mech. Eng. H.*, vol. 224, no. 2, pp. 307–16, Jan. 2010.
- [28] F. Lizzi, E. Feleppa, A. Kaiser, and C. Deng, "Ultrasonic spectrum analysis for tissue evaluation," *Pattern Recognit. Lett.*, vol. 24, no. 4, pp. 637–658, 2003.
- [29] P. Tsui, Y. Wan, C. Huang, and M. Wang, "Effect of adaptive threshold filtering on ultrasonic Nakagami parameter to detect variation in scatterer concentration," *Ultrason. Imaging*, vol. 32, no. 4, pp. 229–242, Oct. 2010.
- [30] P. Tsui, C. Yeh, and C. Huang, "Noise-assisted correlation algorithm for suppressing noise-induced artifacts in ultrasonic Nakagami images.," *IEEE Trans. Inf. Technol. Biomed.*, vol. 16, no. 3, pp. 314–22, May 2012.
- [31] A. Thakur and R. Anand, "Image quality based comparative evaluation of wavelet filters in ultrasound speckle reduction," *Digit. Signal Process.*, vol. 15, no. 5, pp. 455–465, Sep. 2005.
- [32] L. Rokach and O. Maimon, "Top-down induction of decision trees classifiers - a survey," *IEEE Trans. Syst. Man, Cybern. Part C (Applications Rev.)*, vol. 35, no. 4, 2005.

- [33] Quinlan J, "Learning Decision Tree Classifiers," *ACM Comput. Surv.*, vol. 28, no. 1, pp. 71–72, 1996.
- [34] K. Sharma and P. Santhoshkumar, "Lens Aging: Effects of Crystallins," *Biochim. Biophys. Acta*, vol. 1790, no. 10, pp. 1095–1108, 2009.



Miguel Caixinha received the B.Sc. in Applied Physics and Optics, specialization in Optometry in 2000 from the University of Beira Interior, Portugal. In 2006 he received the M.Sc. in Vision Sciences from the Faculty of Medicine of the University of Coimbra, Portugal, and in 2012 the Diploma of Advanced Studies in Biomedical Engineering from the University of Coimbra. He is currently Ph.D. student in Biomedical Engineering in the University of Coimbra, and researcher in the CEMUC research group from the University of Coimbra. His research interests are in the field of Optometry and Vision Sciences namely in the anterior segment of the eye.



Danilo A. Jesus graduated his Integrated Master degree in Biomedical Engineering, Biomedical Instrumentation and Biomaterials in 2012 at University of Coimbra, Portugal. From August of 2013 to January of 2014, he was a research fellow in the Centre for Mechanical Engineering, University of Coimbra. In February of 2014 he joined to BioMediTech, a joint institute of Tampere University of Technology and University of Tampere, Finland. Currently, he is Ph.D. Student in Wrocław University of Technology through the project AGEYE (Ageing Eye), a Marie Curie Initial Training Network action, funded by the 7th EU framework program, to foster research training in Vision Sciences.



Elena Velte is a young researcher who has recently obtained her Integrated Master degree in Biomedical Engineering from the University of Coimbra. Her thesis was focused on the study of new methods for objective assessment of cataracts. Specialized in image processing and analysis, she is currently working in the field of biometric recognition.



Mário J. Santos received the B.Sc., M.Sc. and Ph.D. degrees in Electrical Engineering from Department of Electrical and Computer Engineering, University of Coimbra, Portugal in 1990, 1997 and 2004, respectively. He is currently an Assistant Professor in Department of Electrical and Computer Engineering in Coimbra University. His research interests are related with ultrasonic non-destructive testing. Actually, he is investigating applications of ultrasonic guided waves in the inspection of plate and plate-like structures and biologic tissue characterization using conventional ultrasonic bulk waves.



Jaime B. Santos received the M.Sc. degree in Electrical Engineering in 1985, from the University of Coimbra, and the Ph.D. degree in Electrical Engineering from the University of Coimbra, Portugal, in 1994. He is currently Associate Professor at Faculty of Science and Technology, University of Coimbra. His research interests include ultrasounds namely NDT&E and image processing.

New approach for objective cataract classification based on ultrasound techniques using multiclass SVM classifiers

Miguel Caixinha, Elena Velte, Mário Santos, and Jaime B. Santos
 Department of Electrical and Computers Engineering
 University of Coimbra,
 Coimbra, Portugal
 jaime@deec.uc.pt

Abstract— In the present work, ultrasound A-scan signals were acquired from healthy and cataractous porcine lenses. B-mode images were reconstructed from the collected signals. The parametric Nakagami images were subsequently constructed from the B-mode images. Acoustical and spectral parameters were obtained from the central region of the lens. Image textural parameters were extracted from the B-scan and Nakagami images. Ninety-seven parameters were extracted from a total of 75 healthy and 135 cataractous lenses. Lenses with cataract were split in two groups: incipient and advanced cataract, corresponding to a 60 and 120 minutes of immersion time in a cataract induction solution, respectively. The obtained parameters were subjected to feature selection with Principal Component Analysis (PCA) and used for classification through a multiclass Support Vector Machine (SVM). This paper shows that multiclass SVM can perform effectively the classification of the cataract severity, with an overall performance of 89%, classifying correctly 93% of the features.

Keywords— *cataract, ultrasound, classification, Support Vector Machine.*

I. INTRODUCTION

Cataract is an opacity in the lens eye as a result of the crystalline proteins precipitation and aggregation, affecting more than 20 million people worldwide. Age-related cataract is the most frequent cause of blindness in the world being responsible for 48% of blindness, and affecting more than 10% of the working population [1]. With the increase of the elderly population, the number of persons with reduced vision or blindness secondary to cataract may reach 40 million people by the year 2020 [1]. Currently surgical cataract removal is the only effective therapy for vision recovery since there is no cataract prevention or pharmacological treatment.

The phacoemulsification is the most common surgical procedure for cataract extraction. This procedure uses a hand-held ultrasonic device to fragment the cataractous lens into small pieces that are afterward aspirated [2], [3]. The posterior lens capsule remains in the eye to sustain the lens to be implanted. Integrity of the posterior capsule is essential for reducing the risk of surgical complications and subsequent vision loss, however the selection of an inappropriate phacoemulsification energy level can disrupt the posterior capsule. Therefore, it is crucial to determine the optimal phacoemulsification energy level, which value depends on the hardness of the cataract. The correct estimation of cataract hardness is then critical to minimize surgical complications.

For the clinical prognosis and therapeutic purposes it is very important identify the cataract type and severity, especially in its early stages [4]. The post-surgical complications can be avoided if the hardness of the cataractous lens is correctly estimated. In this context, ultrasounds are a powerful, noninvasive and less expensive techniques for biological tissue characterization [5]. In a recent work, our research group showed that the backscattering signals and the Nakagami statistical distribution, correlates with the protein aggregates formation in the lens, and that the ultrasound parameters can be used to objectively assess the regional cataract hardness [6].

In this work multiclass Support Vector Machine (SVM) classifier is investigated for the cataract automatic classification using ultrasound parameters obtained from porcine lenses with different cataract degrees. Currently the classification of cataract severity is performed by human examiners making use of retroillumination and/or slit-lamp images. The current cataract classification systems rely therefore on a subjective evaluation that depends on the exam settings, and the examiners expertise [7], [8]. Some approaches have been used for the automatic classification of the cataract severity, however these approaches rely also on retroillumination and/or slit-lamp images [8], [9]. In this work an extensive extraction and selection of acoustical parameters, i.e., velocity, attenuation and backscattering signals (B-Scan and Nakagami images), is performed in order to classify objectively and automatically the cataract severity. To extract features from the B-Scan and Nakagami images, a textural analysis was performed [10][11][12]. The examination of medical images requires often interpretation of the tissue appearance, which is in usually described in terms of its smoothness, grain, regularity or homogeneity. These features translate into variations of image intensity, which represent tissue echogenicity and can be quantified using textural analysis metrics. For the backscattering characterization through signal analysis, two major approaches can be followed: modeling by statistical distributions and spectral analysis [10][11],[12]. In this work both approaches were used. The amplitude of the backscattering signal (envelope) was modeled by the Nakagami statistical distribution. The parameters of this distribution provide features such as density (the number of scatterers within the resolution cell of the transducer) and the amplitude of the scatter, which is related to the scatterers size [11]. On the other hand, spectral analysis of ultrasound signals, provide information about acoustical and structural tissue properties such as the backscattering and the effective scatter size [10],[12].

II. MATERIALS AND METHODS

A. Lens samples

Two hundred and twenty (220) lenses from porcine eyes were collected in a slaughterhouse. Lens were carefully extracted and prepared to clean iris remains and adhering vitreous, preserving the lens capsule. Ten lenses were excluded from the study because they presented some degree of cataract after enucleated.

Cataract was induced in 135 lenses immersed over time in an ethanol:2-propanol:formalin solution at the ratio 3:3:4 [13]. To obtain different cataract degrees the lenses were immersed in the solution over 60 and 120 minutes, corresponding to lenses with initial (64) and advanced (71) cataract, respectively. Seventy-five lenses (75) were used as control (without cataract).

B. Experimental Setup

The ultrasound parameters as velocity, frequency dependent attenuation, and the backscattering signals were obtained using the setup shown in Fig. 1.

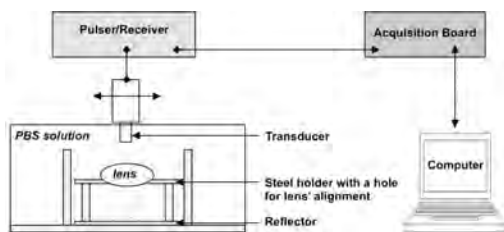


Fig. 1. Experimental setup.

A 25 MHz center frequency transducer (model JAP-F25.3.1, Krautkramer, NSW, Australia) with a 25 mm focus and 5 mm active diameter with a pulse length of 0.13 μ s at -6 dB was used. The lenses were placed on a stainless steel holder having a machined hole suited to the lens. Both the transducer and the lens were immersed in a phosphate buffered saline solution (PBS), with temperature controlled. All over the data collection the solution temperature was kept constant at $28.0 \pm 0.5^\circ\text{C}$. A pulse/receiver with a 35 MHz bandwidth (model PR5800, Olympus NDT Inc., Waltham, MA, USA) was used in a pulse-echo configuration. The echo signals were recorded and digitized with a 14 bit, 200 MHz A/D card (model PCIe-9842, ADLINK Technology Inc., Taipei, Taiwan). The transducer was moved using a computer-controlled micro-positioning system.

C. Data acquisition

In order to characterize cataract formation 97 parameters were extracted from the collected A-Scan signals.

i) Ultrasound Velocity and Attenuation: The ultrasound propagation velocity in the lens was calculated as the average value of ten A-Scan lines collected over the central portion of the lens, according to [6], [14], [15]. The ultrasound attenuation coefficient was calculated by evaluating the frequency dependent attenuation all over the lens tissue, for the central frequency of the transducer, considering also the average of ten A-scan lines as described in [6], [16],

The mean and variance values for the ultrasound velocity and attenuation were computed.

ii) Time-frequency distribution – Hilbert and Fourier transforms: The A-Scan time-frequency distribution characteristics were extracted from the Hilbert spectrum [17]. When compared to the Fourier transform power spectrum, the Hilbert spectrum not only shows constraints defining a more precise representation of particular events in time-frequency space, but also provide a more physically meaningful interpretation of the underlying dynamic processes [18]. The use of time-frequency distributions for analysis of biomedical signals, which takes into account the nonstationarity of these signals, are useful for many applications, including the medical abnormalities diagnosis [19].

The Hilbert and Fourier spectra were obtained from the A-scan signals acquired from the central region of the lens. The signals were analyzed using linear regression techniques to compute the spectral slope (dB/MHz), intercept (dB, extrapolation to zero frequency) and midband fit (dB value of the regression line at the center frequency). Spectral slope is affected by intervening attenuation and is related to the effective sizes of tissue scatterers. Spectral intercept is unaffected by intervening attenuation that is linearly dependent on frequency; it is related to the effective sizes, concentrations and relative acoustic impedances of tissue scatterers. The midband fit is affected by attenuation and is related to the above tissue properties [20]. The mean frequency, frequency downshift, frequency at maximal amplitude and backscattering coefficient were also computed.

iii) B-Scan Imaging: The ultrasound data are usually presented as brightness-modulated images (B-Scan). The construction of these images encompasses the signal envelope detection followed by a logarithmic compression. Then, the signal is converted to a 256 grey levels scale for posterior image reconstruction by using the multiple A-Scan lines collected from a given region of the tissue.

The B-Scan images were constructed using 15000 A-Scan lines sampled at a 200 MHz rate, considering the backscattering envelope amplitude, obtained by the Hilbert transform [21], [22], and a dynamic range of 40 dB (Fig. 2). The distance between each A-Scan line was 0.001 mm.



Fig. 2. B-scan images: (a) control lenses; (b) lenses with 60 minutes of immersion time; (c) lenses with 120 minutes of immersion time. Red line: region of interest for the texture analysis.

Spectral analysis of the B-Scan images through Discrete Fourier Transform (DFT) was performed. The predominant and global periodicity, the predominant and global orientation, the variance of the periodicity function, the variance of the orientation function, and the amplitude of the DFT were extracted.

To obtain parameters from the B-Scan images a texture analysis was also performed in order to discriminate different tissue properties [23]. The following parameters were extracted in a region of interest selected from the B-Scan (Fig. 2 (c)):

- First order statistic parameters from the image histogram, i.e. mean, variance, kurtosis, skewness, standard deviation, mode and median.

- Grey Level Co-occurrence Matrix (GLCM) parameters for 0°, 45°, 90° and 135°, i.e., energy, inertia, entropy correlation and homogeneity, [24], [25].
- Grey Level Run Length Matrix (GLRLM) parameters, i.e., Short and Long Run Emphasis (SRE and LRE), Grey Level Non-Uniformity (GLNU), Run Percentage (RP), Rung Length Non-Uniformity (RLNU), Low and High Grey Level Run Emphasis (LGLRE and HGLRE), [24]–[27].
- Fractal Dimension (Hausdorff dimension) [24].

iv) Nakagami Statistics and Imaging: The backscattered signals envelope was analyzed in order to obtain statistical parameters that could discriminate different cataract degrees. For this purpose the Nakagami distribution was used as described in [6], [28].

The Nakagami parametric image was constructed based on the B-mode image, and corresponds to a 2D representation of the m parameter values (i.e., the Nakagami shape parameter). The image construction process encompassed a sliding window selected to provide good resolution [29]. In this work, it was considered a window with three times the transducer pulse length (0.39 μ s) corresponding to 78 samples, taking into account the sampling frequency of 200 MHz and 99% of overlapping. A color scale was used for the Nakagami image to facilitate the visualization and interpretation. The color scale ranges from blue to red as the m parameter increases from 0 to 1, corresponding to backscattered signal envelopes changing from a pre-Rayleigh to a Rayleigh statistical distribution (Fig. 3).

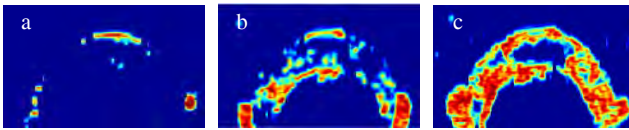


Fig. 3. Nakagami images: a) control lenses; b) lenses with 60 minutes of immersion time; c) lenses with 120 minutes of immersion time.

The Nakagami parameters m and Ω (shape and scale, respectively) were used in this work. To extract additional features from the Nakagami images, a texture analysis was also performed. The following parameters were extracted: first order statistic parameters; GLCM parameters for 0°, 45°, 90° and 135°, [24], [25]; GLRLM parameters, [24]–[27]; and fractal Dimension (Hausdorff dimension) [24].

D. Features selection and dimensionality reduction using Principal Component Analysis (PCA)

A dimensionality reduction was performed in order to obtain a parsimonious description of the multivariate data, reducing or eliminating statistically correlated components, obtaining a compact, accurate, and representative sample of the data [30]. Given the small data set (210) compared to the dimensionality of the features (97), the selection of the most discriminative features was performed using principal component analysis (PCA). PCA is the most used technique for linear dimensionality reduction. PCA, performs an orthogonal transformation of the data converting a set of correlated variables into a set of functions linearly uncorrelated, i.e., components. The first principal component has the largest possible variance, corresponding to the largest eigenvalue [31], [32][30].

To identify the best set of components, the classifier performance was computed using the F-measure for different sets.

E. Cataract degree Classification using multiclass SVM

The most discriminative set of components, corresponding to the features set with the highest F-measure, was used in a multiclass SVM classifier [33]. The one-against-all approach was used to classify the features into one of the three lens categories, i.e. normal lens, incipient cataract and advanced cataract. A k-fold cross-validation with k=10 was performed to train and test the multiclass SVM classifier. The multiclass SVM classifier was tested 200 times with the same features. The performance of the multiclass SVM was assessed based on the average performance of the multiclass SVM classification considering the following measures: F-measure; accuracy; sensibility and specificity (based on the number of True Positive (TP), True Negative (TN), False Positives (FP) and False Negative (FN)).

III. RESULTS AND DISCUSSION

Fifteen components were selected by PCA, corresponding to the highest F-measure (F-measure = 95%). A total of 3150 features (15 components for each lens), classified into one of the three categories (normal, incipient and advanced cataract) were used in the multiclass SVM classification. The precision of the classifier was 89%, i.e., 89% of the features were classified in the same category in the 200 tests performed with the classifier.

The overall performance of the multiclass SVM was of 93%, i.e., features correctly classified in the respective group of cataract severity (Table 1 and Table 2). The overall sensibility was of 89% and the overall specificity was of 94%.

TABLE 1. AVERAGE MULTICLASS SVM CLASSIFICATION FOR THE THREE GROUPS OF LENSES.

Predicted Group	True Group			TOTAL
	Cataract	Normal	Incipient	
Normal		972	4	1078
Incipient		15	855	997
Advanced		138	101	836
TOTAL		1125	960	1065

Ninety two percent (92%) of the extracted features from normal lenses were correctly classified (the sensitivity was 86% and the specificity 95%, Table 2). Ninety two percent (92%) of the extracted features from lenses with incipient cataract were correctly classified (the sensitivity was 89% and the specificity 94%, Table 2). Eighty five percent (85%) of the extracted features from lenses with advanced cataract were correctly classified (the sensitivity was 79% and the specificity 89%, Table 2).

TABLE 2. AVERAGE PERFORMANCE MEASURES FOR THE MULTICLASS SVM CLASSIFICATION.

	Normal Lens	Incipient Cataract	Advanced Cataract	Overall
TP	972	855	836	--
FP	106	142	239	--
FN	153	105	229	--
TN	1919	2048	1846	--
Sensitivity	0.86	0.89	0.79	0.89
Specificity	0.95	0.94	0.89	0.94
Accuracy	0.92	0.92	0.85	0.93
F-measure	0.88	0.87	0.78	0.89

IV. CONCLUSIONS

Previous works showed that the cataract hardness can be characterized noninvasively using ultrasound features. In this work, a good performance of multiclass SVM for the cataract classification was obtained confirming the existence of an association between the ultrasound parameters (velocity, attenuation and backscattering signals) and the cataract degree, allowing therefore for the objective discrimination of the cataract severity.

Our results showed that multiclass SVM can be used as a computer-aided diagnosis (CAD) system for the cataract classification based on the ultrasound analysis. The velocity and attenuation combined with the backscattering signal analysis in terms of B-Scan and Nakagami imaging allow for a good discrimination of the different cataract degrees and appear as a good alternative to the clinical classification system currently used.

ACKNOWLEDGMENT

This research is sponsored by CEMUC - Centro de Engenharia Mecânica da Universidade de Coimbra, FEDER funds through the program COMPETE - Programa Operacional Factores de Competitividade - and by national funds through FCT - *Foundation for Science and Technology*, under the project PTDC/DTP-PIC/0419/2012.

REFERENCES

- [1] World Health Organization, "Vision 2020 The right to sight - Global initiative for the elimination of avoidable blindness: action plan 2006-2011," Switzerland, 2008.
- [2] J. Kanski, *Clinical diagnosis in ophthalmology*, 1st ed. Philadelphia: Elsevier Mosby, 2007.
- [3] S. P. M. Wilson, R. Trivedi, Ed., *Pediatric Cataract Surgery: Techniques, Complications, and Management*. Lippincott Williams & Wilkins, 2005, p. 320.
- [4] A. Paunsknis, S. Kurapkienė, and A. Mačiulis, "Ultrasound quantitative evaluation of human eye cataract," *Informatica*, vol. 18, no. 2, pp. 267-278, 2007.
- [5] M. Ho, J. Lin, Y. Shu, C. Chen, K. Chang, C. Chang, and P. Tsui, "Using ultrasound Nakagami imaging to assess liver fibrosis in rats," *Ultrasonics*, vol. 52, no. 2, pp. 215-222, Feb. 2012.
- [6] M. Caixinha, D. Jesus, E. Velte, M. Santos, and J. Santos, "Using ultrasound backscattering signals and Nakagami statistical distribution to assess regional cataract hardness," *IEEE Trans. Biomed. Eng.*, vol. PP, no. 99, 2014.
- [7] J. Kirwan, L. Venter, A. Stulting, and I. Murdoch, "LOCS III examination at the slit lamp, do settings matter?," *Ophthalmic Epidemiology*, Oct-2003.
- [8] X. Gao, D. W. K. Wong, T.-T. Ng, C. Y. L. Cheung, C.-Y. Cheng, and T. Y. Wong, "Automatic grading of cortical and PSC cataracts using retroillumination lens images," *Comput. Vis. - ACCV 2012*, vol. 7725, pp. 256-267, Nov. 2013.
- [9] Y. Xu, X. Gao, S. Lin, D. W. K. Wong, J. Liu, D. Xu, C.-Y. Cheng, C. Y. Cheung, and T. Y. Wong, "Automatic grading of nuclear cataracts from slit-lamp lens images using group sparsity regression," *Med. Image Comput. Comput. Assist. Interv.*, vol. 16, no. Pt 2, pp. 468-75, Jan. 2013.
- [10] S. Brand, E. C. Weiss, R. M. Lemor, and M. C. Kolios, "High frequency ultrasound tissue characterization and acoustic microscopy of intracellular changes," *Ultrasound Med. Biol.*, vol. 34, no. 9, pp. 1396-407, Sep. 2008.
- [11] R. Smolíková, M. P. M. P. Wachowiak, and J. M. J. M. Zurada, "An information-theoretic approach to estimating ultrasound backscatter characteristics," *Comput. Biol. Med.*, vol. 34, no. 4, pp. 355-70, Jun. 2004.
- [12] C. B. Machado, W. C. D. A. Pereira, M. Meziri, and P. Laugier, "Characterization of in vitro healthy and pathological human liver tissue periodicity using backscattered ultrasound signals," *Ultrasound Med. Biol.*, vol. 32, no. 5, pp. 649-57, May 2006.
- [13] T. Sugiura, D. Kurosaka, and Y. Uezuki, "Creating cataract in a pig eye," *J. Cataract Refract. Surg.*, vol. 25, no. 5, pp. 615-621, May 1999.
- [14] P. Tsui, C. Huang, C. Chang, S. Wang, and K. Shung, "Feasibility study of using high-frequency ultrasonic Nakagami imaging for characterizing the cataract lens in vitro," *Phys. Med. Biol.*, vol. 52, no. 21, pp. 6413-6425, Nov. 2007.
- [15] C. Huang, H. Ameri, C. Deboer, A. Rowley, X. Xu, L. Sun, S. Wang, M. Humayun, and K. Shung, "Evaluation of lens hardness in cataract surgery using high-frequency ultrasonic parameters in vitro," *Ultrasound Med. Biol.*, vol. 33, no. 10, pp. 1609-16, Oct. 2007.
- [16] C. Huang, R. Chen, and P. Tsui, "Measurements of attenuation coefficient for evaluating the hardness of a cataract lens by a high-frequency ultrasonic needle transducer," *Phys. Med. Biol.*, vol. 54, no. 19, pp. 5981-5994, 2009.
- [17] N. E. Huang, Z. Shen, S. R. Long, M. C. Wu, H. H. Shih, Q. Zheng, N.-C. Yen, C. C. Tung, and H. H. Liu, "The empirical mode decomposition and the Hilbert spectrum for nonlinear and non-stationary time series analysis," *Proc. R. Soc. A Math. Phys. Eng. Sci.*, vol. 454, no. 1971, pp. 903-995, Mar. 1998.
- [18] T. Schlurmann, "The empirical mode decomposition and the Hilbert spectra to analyse embedded characteristic oscillations of extreme waves," *Rogue Waves*, 2000.
- [19] a Andrade, P. Kyberd, and S. Nasuto, "The application of the Hilbert spectrum to the analysis of electromyographic signals," *Inf. Sci. (Ny)*, vol. 178, no. 9, pp. 2176-2193, May 2008.
- [20] A. Kalisz, "Statistical framework for ultrasonic spectral parameter imaging," vol. 13, no. 9, 1997.
- [21] J. Noble and P. Wells, "Ultrasound image segmentation and tissue characterization," *Proc. Inst. Mech. Eng. H.*, vol. 224, no. 2, pp. 307-16, Jan. 2010.
- [22] F. Lizzi, E. Feleppa, A. Kaiser, and C. Deng, "Ultrasonic spectrum analysis for tissue evaluation," *Pattern Recognit. Lett.*, vol. 24, no. 4, pp. 637-658, 2003.
- [23] K. D. D. Onohue, L. H. Uang, T. B. Urks, F. F. Orsberg, and C. W. P. Iccoli, "Tissue classification with generalized spectrum parameters," vol. 27, no. 11, pp. 1505-1514, 2001.
- [24] I. N. Bankman, *Handbook of Medical Imaging*. Academic Press, 2000, pp. 215-230.
- [25] R. M. Haralick, K. Shanmugam, and I. Dinstein, "Textural Features for Image Classification," *IEEE Trans. Syst. Man. Cybern.*, vol. 3, no. 6, pp. 610-621, Nov. 1973.
- [26] M. Haidekker, *Advanced Biomedical Image Analysis (Google eBook)*. John Wiley & Sons, 2011, p. 528.
- [27] X. Tang, "Texture information in run-length matrices," *IEEE Trans. Image Process.*, vol. 7, no. 11, pp. 1602-9, Jan. 1998.
- [28] P. Shankar, "A general statistical model for ultrasonic backscattering from tissues," *IEEE Trans. Ultrason. Ferroelectr. Freq. Control*, vol. 47, no. 3, pp. 727-36, Jan. 2000.
- [29] P. Tsui, C. Huang, and S. Wang, "Use of Nakagami distribution and logarithmic compression in ultrasonic tissue characterization," *J. Med. Biol. Eng.*, vol. 26, no. 2, pp. 69-73, 2006.
- [30] N. Kambhatla and T. Leen, "Dimension reduction by local principal component analysis," *Neural Comput.*, vol. 9, no. 7, pp. 1493-1516, Oct. 1997.
- [31] P. Sajda, "Machine learning for detection and diagnosis of disease," *Annu. Rev. Biomed. Eng.*, vol. 8, pp. 537-65, Jan. 2006.
- [32] H. Shin and M. K. Markey, "A machine learning perspective on the development of clinical decision support systems utilizing mass spectra of blood samples," *J. Biomed. Inform.*, vol. 39, no. 2, pp. 227-48, Apr. 2006.
- [33] I. El-naqa, S. Member, Y. Yang, M. N. Wernick, S. Member, N. P. Galatsanos, and R. M. Nishikawa, "A Support Vector Machine Approach for Detection of Microcalcifications," *IEEE Trans. Med. Imaging*, vol. 21, no. 12, pp. 1552-1563, 2002.



● *Original Contribution*

AUTOMATIC CATARACT HARDNESS CLASSIFICATION *EX VIVO* BY ULTRASOUND TECHNIQUES

MIGUEL CAIXINHA,^{*†} MÁRIO SANTOS,^{*} and JAIME SANTOS^{*}

^{*}Department of Physics, University of Coimbra, PT-3030-290 Coimbra, Portugal; and [†]Department of Electrical and Computer Engineering, University of Coimbra, Coimbra, Portugal

(Received 30 June 2015; revised 16 November 2015; in final form 23 November 2015)

Abstract—To demonstrate the feasibility of a new methodology for cataract hardness characterization and automatic classification using ultrasound techniques, different cataract degrees were induced in 210 porcine lenses. A 25-MHz ultrasound transducer was used to obtain acoustical parameters (velocity and attenuation) and backscattering signals. B-Scan and parametric Nakagami images were constructed. Ninety-seven parameters were extracted and subjected to a Principal Component Analysis. Bayes, K-Nearest-Neighbours, Fisher Linear Discriminant and Support Vector Machine (SVM) classifiers were used to automatically classify the different cataract severities. Statistically significant increases with cataract formation were found for velocity, attenuation, mean brightness intensity of the B-Scan images and mean Nakagami m parameter ($p < 0.01$). The four classifiers showed a good performance for healthy versus cataractous lenses (F-measure $\geq 92.68\%$), while for initial versus severe cataracts the SVM classifier showed the higher performance (90.62%). The results showed that ultrasound techniques can be used for non-invasive cataract hardness characterization and automatic classification. (E-mail: miguel.caixinha@gmail.com) © 2015 World Federation for Ultrasound in Medicine & Biology.

Key Words: Ultrasound, Cataract, Classification, Phacoemulsification, SVM.

INTRODUCTION

Age-related cataracts are responsible for 48% of cases of blindness worldwide, affecting more than 10% of the working population (World Health Organization 2008). With the increase of the elderly population, vision impairment or blindness secondary to cataract may reach 40 million people by the year 2020 (Kanski 2007; World Health Organization 2008). Cataract formation results from the disruption of the crystalline lens proteins' arrangement because of protein aggregation and fiber compaction, which leads to the increase in the lens's hardness and the impairment of light propagation through the eye (Ecroyd and Carver 2009; Kanski 2007). Currently, surgical cataract removal is the only effective therapy for vision recovery as there is no cataract preventative or pharmacologic treatment.

Phacoemulsification is the most common surgical procedure for cataract extraction (Huang et al. 2007b; Wilson and Trivedi 2005). The integrity of the

lens capsule is essential for reducing the risk of surgical complications and subsequent vision loss, but an inappropriate phacoemulsification energy level selection, which depends on the cataract hardness, may result in the disruption of the posterior capsule and endothelial cells loss. Thus the correct estimation of cataract hardness can minimize surgical complications (Carricondo and Fortes 2010; Muhtaseb et al. 2004; Wilson and Trivedi 2005).

Ultrasound appears as a promising non-invasive technique for cataract characterization using the information provided by the interaction of the waves with the tissue structural elements. Important tissue physical properties can be inferred from ultrasound scattering, reflection and absorption (Moradi et al. 2007; Shung and Thieme 1992). In particular, the ultrasound backscattering signals contain important information about tissues' internal scattering structures and absorption properties (Huang et al. 2007a; 2009; Onohue et al. 2001; Tsui et al. 2011). The most common representation for the backscattering signals is the B-Scan image (Szabo 2014). This technique uses the envelope of the ultrasound echoes from a region of interest (ROI) to create gray-scale images as an intensity

Address correspondence to: Miguel Caixinha, Department of Electrical and Computer Engineering, University of Coimbra, PT-3030-290 Coimbra, Portugal. E-mail: miguel.caixinha@gmail.com

mapping (Brand et al. 2008; Huang et al. 2007a; 2007b; Paunksnis et al. 2007; Raitelaitienė and Paunksnis 2005; Tabandeh et al. 2000; Tsui and Chang 2007; Tsui et al. 2007; 2008; 2011). However, due to the processing complexity, B-Scan images commonly used in medical diagnosis contain less information than the original signals (Brand et al. 2008; Despotovic et al. 2008). An alternative way to represent the backscattering signals information is by the parametric Nakagami image (Tsui 2013), which is based on the envelope statistics of the A-scan signals (Caixinha et al. 2013; 2014; Ho et al. 2012; Tsui and Chang 2007).

The Nakagami distribution allows for the characterization of the scatterers' concentration and distribution in tissues (Ho et al. 2012; Shankar 2000; 2001; Tsui et al. 2007; 2010b). This approach appears as a complementary method to the B-Scan providing improved information about the spatial arrangement and scatterers' concentration, which is useful for the identification of cataract hardness degree (Caixinha et al. 2014; Tsui and Chang 2007; Tsui et al. 2006; 2007; 2009; 2011; 2013). The parametric Nakagami images have a different physical meaning in the tissue characterization: they provide information associated with scatterers' distribution and concentration by reflecting the statistical distribution of the backscattered signals. The Nakagami distribution provides a good fit to the probability density function (pdf) of the envelope statistics of the ultrasonic backscattered echoes from tissues (Shankar 2004; Shankar et al. 2003). The primary parameter to determine the backscattered statistics in the Nakagami distribution is the m parameter, which is estimated from the statistical moments of the backscattered signal envelope, (Shankar 2000; Tsui and Wang 2004). The Nakagami m parameter has already been used to characterize scatterers' properties in biological tissues (Cloutier et al. 2004; Raju and Srinivasan 2002; Shankar et al. 2001; 2003; Wang and Tasi 2001).

In this work, porcine lenses with different cataract degrees were used for the extraction of the acoustical parameters velocity and attenuation and the backscattering in order to objectively characterize the cataract hardness and also to provide its automatic classification using machine-learning techniques. To demonstrate the correlation between ultrasound parameters and cataract hardness, and to prove that the used cataract induction method promotes an increase in the protein aggregation and fiber compaction, stained slices from the nucleus and the cortex regions were obtained and analyzed. The slices were imaged to show the scatterers' distribution and concentration in different regions of the lenses for the different cataract formation stages.

This work aims to demonstrate the feasibility of a new methodology for cataract hardness characterization and classification using ultrasound and machine learning, and by this way creating the bases for the development of a medical device capable of classifying cataracts automatically.

MATERIALS AND METHODS

Lens samples

Two hundred and twenty (220) porcine eyes were collected from a slaughterhouse. The lenses were extracted from the eyes and carefully prepared, cleaning iris remains and adhering vitreous and preserving the capsule. Ten lenses were excluded due to the presence of opacities. The mean anteroposterior and equatorial diameters were 8.2 ± 0.2 mm and 12.3 ± 0.2 mm, respectively.

Cataract was induced in 135 lenses by immersion in an ethanol:2-propanol:formalin solution at the ratio 3:3:4 (Sugiura et al. 1999) over 60 or 120 min in order to obtain two different degrees of cataract. Sixty-four lenses with initial cataract and 71 with severe cataract were obtained. Seventy-five healthy lenses (without cataract) were used as control.

Experimental setup

The ultrasound characterization of lenses was made using the setup shown in Figure 1. The velocity- and frequency-dependent attenuation and the backscattering signals were obtained (Caixinha et al. 2014). For that goal, a 25-MHz ultrasound transducer (model IAP-F25.3.1, Krautkramer, NSW, Australia) with a 25-mm focus, - mm active diameter, focal diameter of 0.3 mm and pulse length of $0.13 \mu\text{s}$ (-6 dB) was used. The transducer and the lens (placed at the transducer focus) were immersed in a phosphate-buffered saline solution (PBS) at $28.0 \pm 0.5^\circ\text{C}$. A 35-MHz bandwidth pulse/receiver (model PR5800, Olympus NDT Inc., Waltham, MA, USA) was used to excite the transducer in a pulse-echo configuration (Caixinha et al. 2014). A computer-controlled micro-positioning system allowed a precise transducer movement over the lens.

Data acquisition

Ultrasound velocity and attenuation. The propagation velocity (v) in the lens was calculated considering the average value of 10 A-Scan lines collected from its center portion, according to Huang et al. (2007a) and Tsui et al. (2007).

$$v = c \left(\frac{t_s - t_c}{t_b - t_a} + 1 \right) \quad (1)$$

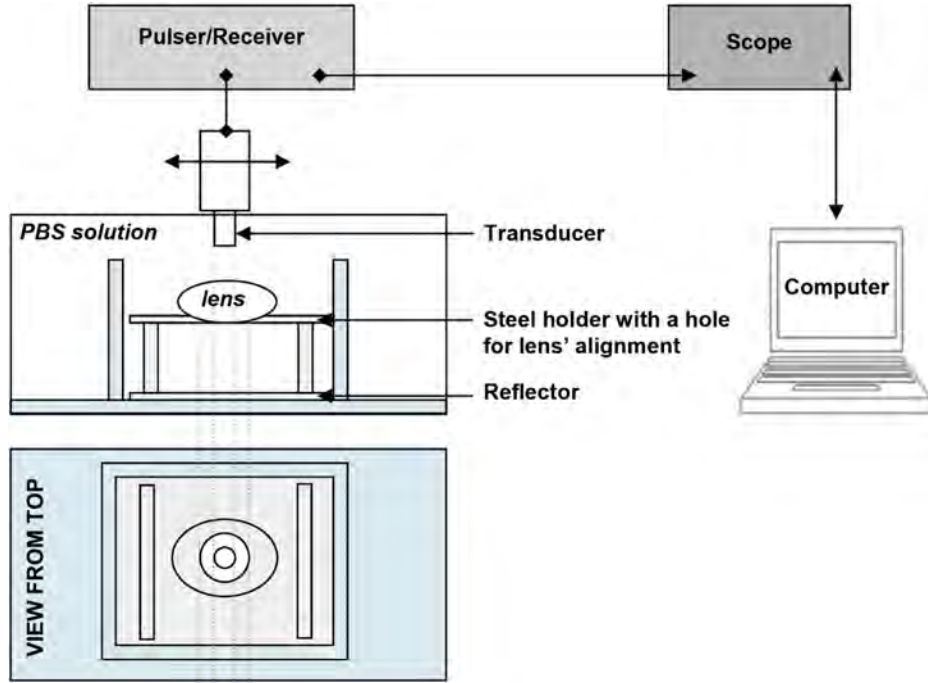


Fig. 1. Experimental setup.

where c is the propagation velocity in the solution; t_c and t_s are the propagation times for the path between the transducer and a plane reflector with and without the lens inserted, respectively; and t_a and t_b are the propagation times between the transducer and the lens boundaries, as illustrated in Figure 2.

The ultrasound attenuation coefficient was calculated by evaluating the frequency-dependent attenuation for the transducer center frequency, considering also the average of 10 A-Scan lines, according to, (Huang *et al.* 2009).

$$\alpha(f) = \frac{20}{2d} \log_{10} \left(\frac{A_1(f)}{A_2(f)} (T_{12} T_{21})^2 \right) - \alpha_s \quad (2)$$

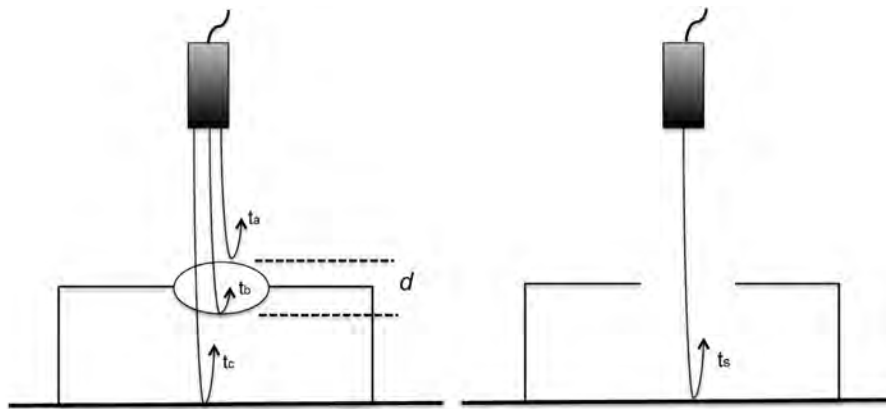


Fig. 2. Illustration for the ultrasound velocity calculation.

where d is the lens thickness; $A_1(f)$ and $A_2(f)$ are the amplitude spectra of the signals from the reflector without and with the lens inserted, respectively; T_{12} and T_{21} are the transmission coefficients in the lens boundaries; and α_s is the attenuation in the solution for the path (d) occupied by the lens, as illustrated in Figure 3.

B-Scan imaging. The B-Scan image, or brightness-modulated image, encompasses the signal envelope detection followed by a logarithmic compression. For the backscattering signals, the envelope was obtained using the Hilbert transform (Lizzi *et al.* 2003; Noble and Wells 2010) and a dynamic range of 40 dB. For the image construction, 15,000 A-Scan

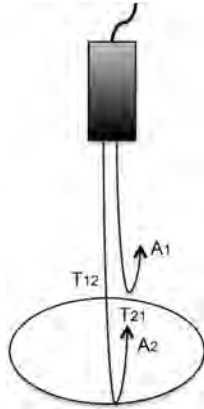


Fig. 3. Illustration for the attenuation calculation.

lines, sampled at a 200-MHz rate and spaced by 0.001 mm, were used.

Nakagami statistics and imaging. The probability density function of the backscattering signal envelope, $f(r, m, \Omega)$, given by the Nakagami distribution is expressed by Caixinha et al. (2014) and Shankar (2000).

$$f(r, m, \Omega) = \frac{2m^m r^{2m-1}}{\Gamma(m)\Omega^m} \exp\left(-\frac{m}{\Omega}r^2\right) U(r) \quad (3)$$

where Γ is the gamma function, U is the unit step function and m and Ω are the Nakagami shape and scale parameters, respectively. The m parameter is expressed by

$$m = \frac{[E(R^2)]^2}{E[R^2 - E(R^2)]^2} \quad (4)$$

where $E(\cdot)$ denotes the statistical mean.

As the statistics of the backscattered echoes vary with the scatter concentration, the Nakagami image can be used to identify the scatter concentrations in the lens (Shankar 2000; Tsui et al. 2010b). The Nakagami parametric image is a 2-D representation of the m values, where a sliding window with width three times the transducer pulse length ($0.39 \mu\text{s}$) was selected in order to provide good resolution (Tsui et al. 2006), which corresponds to 78 samples for the used sampling frequency (200 MHz) and 99% overlapping. To reduce the noise, an adaptive threshold filter was applied to the backscattered signals before the Nakagami parametric image construction (Tsui et al. 2010a).

Features extraction

Ninety-seven parameters were extracted from the collected signals, namely 18 from the A-Scans and 79 from the backscattering of the signals, using Matlab (MathWorks Inc., Natick, MA, USA).

Features from the A-Scan signals. For the A-Scan signals, the following features were extracted: the mean and variance values of the ultrasound velocity and attenuation coefficient and the Hilbert and Fourier spectra (Andrade et al. 2008; Caixinha et al. 2014; Huang et al. 1998; Schlurmann 2000) acquired on the center portion of the lens. Concerning to the referred spectra, linear regression techniques were used to compute slope, intercept and mid-band (Kalisz 1997). The mean frequency, frequency downshift, frequency at maximal amplitude and backscattering coefficient were also extracted.

Features from the backscattering signals. As the backscattering signals can provide useful information about acoustical and structural properties of tissue micro-structure (Brand et al. 2008; Machado et al. 2006), spectral analysis was performed on these signals and the following features were extracted: the predominant and global periodicity, the pre-dominant and global orientation, the variance of the periodicity function, the variance of the orientation function and the amplitude of the Discrete Fourier Transform (FT).

To extract features from the B-Scan images, a textural analysis was performed (Brand et al. 2008; Machado et al. 2006; Onohue et al. 2001; Smolíková et al. 2004). The following features were extracted: first-order statistics from the image histogram (such as mean, variance, kurtosis, skewness, standard deviation, mode and median); Grey Level Co-occurrence Matrix (GLCM) for 0° , 45° , 90° and 135° (energy, inertia, entropy, correlation and homogeneity; Bankman 2000; Haralick et al. 1973); Grey Level Run Length Matrix (GLRLM; Short and Long Run Emphasis [SRE and LRE]), Grey Level Non-Uniformity (GLNU), Run Percentage (RP), Run Length Non-Uniformity (RLNU), Low and High Grey Level Run Emphasis (LGLRE and HGLRE; Bankman 2000; Haidekker 2011; Haralick et al. 1973; Tang 1998); and Fractal Dimension (Hausdorff dimension; Bankman 2000).

The Nakagami shape, m , and scale, Ω , parameters were extracted from the Nakagami distribution. Also from the textural analysis of Nakagami images, similar features based on the first order statistics, GLCM, GLRLM and Fractal Dimension, were extracted.

Region of interest (ROI). For features extraction from the B-Scan and the Nakagami images, a ROI was defined including only the anterior lens hemisphere, excluding the anterior capsule, therefore including only regions containing protein aggregates and collagen fibers. A ROI 4.5 mm in width and 1.5 mm in depth was considered (Fig. 4, left). Additionally, a mask with the lens shape was used in order to exclude the surrounding regions of the lens (Fig. 4, right).

Nucleus and cortex histologic slices

To prove that the used cataract induction method promoted an increase in protein aggregation and fiber compaction, and also to correlate the lens hardness with the information obtained from the B-Scan and the Nakagami images, slices 50 μm thick were obtained from 15 lenses, considering different regions (five healthy, five with initial cataract and five with severe cataract). The lenses were frozen at -40°C in an embedding resin, Cryomatrix Shandon medium (Thermo Scientific Shandon Ltd, Manor Park, WA, USA), and then cuts were transversally made with a glass knife using a Leica Microsystems CM3350 S cryostat (Leica Microsystems, Wetzlar, Germany).

To stain the lens proteins, connective tissue and collagen, the Hematoxylin and Eosin (H&E) staining protocol was used (Cardiff *et al.* 2014; Fischer *et al.* 2008). The stained slices from the nucleus and the cortex were imaged using an inverted microscope with a digital image capture system calibrated for brightness intensity. The images were acquired with the same magnification (40 for the slices), light and exposure time. To compare the amount of proteins and collagen fibers in the different lens regions, and to compare between healthy and cataractous lenses, the mean brightness intensity of each image was computed. The mean brightness intensity obtained in these images was correlated with the mean brightness intensity of the B-Scan images as well as with the mean of the Nakagami m parameter.

Data analysis

Correlations and statistically significant differences between healthy and cataractous lenses. Statistically significant differences between healthy and cataractous lenses were tested for in the ultrasound velocity, frequency-dependent attenuation, mean brightness intensity of B-Scan images and mean Nakagami m parameter using ANOVA and Student t -tests. The correlations between the different features were tested using the Spearman correlation coefficient. Values were considered to be statistically significant for $p < 0.05$.

Features selection. To identify features with statistically significant differences between healthy and catarac-

tous lenses, and between initial and severe cataract, an exploratory univariate analysis was performed using the Wilcoxon Rank Sum test.

In order to reduce the features number to 20 maximum (considering the 210 cases and the 97 features under analysis [Siddiqui 2013]), a principal component analysis (PCA) was performed (Guyon and Elisseeff 2003; Kambhatla and Leen 1997; Sajda 2006; Shin and Markey 2006). PCA is a multivariate statistical method that generates a new set of features, which is a linear combination of the original features. The composition of each new component is determined by the information provided by each feature and its correlation with other features. Mathematically, the principal components are found by calculating the eigenvectors and eigenvalues of the covariance matrix. This process is equivalent to finding the axis system in which the covariance matrix is diagonal. The eigenvector with the largest eigenvalue is the direction of greatest variation; the one with the second largest eigenvalue is the (orthogonal) direction with the next highest variation. To select the best set of components provided by the PCA, a stepwise approach was used. The selected number of components was based on the set that achieved the highest average F-measure value.

Cataract classification. The following classifiers were used for cataract classification: the Bayes and K Nearest-Neighbour (KNN), based on a probabilistic approach, and the Fisher Linear Discriminant (FLD) and Support Vector Machines (SVM), based on the construction of decision boundaries (Jain *et al.* 2000).

The selected components from the PCA that simultaneously reduce the data dimension and explain the observed variance in the data were used to train and test the four classifiers. A k -fold cross-validation was performed with $k = 10$. The performance of the different classifiers was assessed based on the F-measure, accuracy, precision, sensitivity and specificity.

Results

Lens characterization. The propagation velocity increased from 1585.0 ± 31.7 m/s in healthy lenses to

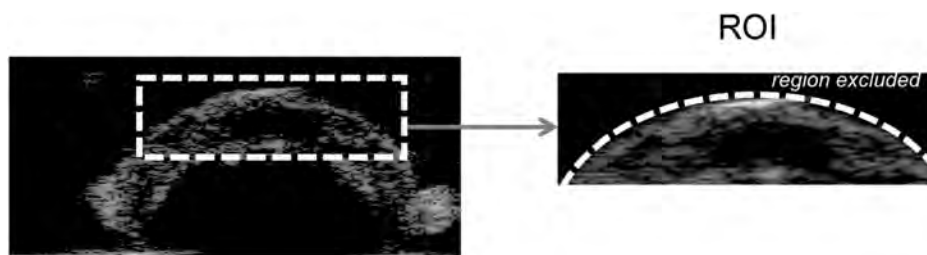


Fig. 4. Selected region of interest for features extraction from the B-Scan and the Nakagami images.

1627.3 \pm 31.4 m/s and 1644.2 \pm 27.8 m/s for initial and severe cataractous lenses, respectively ($p < 0.001$). The frequency dependent attenuation increased from 0.406 \pm 0.028 dB/mm MHz in healthy lenses to 0.422 \pm 0.033 dB/mm MHz and to 0.438 \pm 0.035 dB/mm MHz for initial and severe cataractous lenses, respectively ($p < 0.001$).

The B-Scan images showed a brightness intensity increase over the cataract formation in the considered ROI (Fig. 5, first column). The mean brightness intensity (normalized values) increased from 0.239 \pm 0.094 for healthy lenses to 0.549 \pm 0.243 and 0.656 \pm 0.153 for initial and severe cataractous lenses, respectively ($p < 0.01$).

The Nakagami m parameter increased with cataract formation. The mean value of the m parameter increased from 0.272 \pm 0.076 for healthy lenses to 0.424 \pm 0.142 and 0.488 \pm 0.152 for initial and severe cataractous lenses, respectively ($p < 0.01$), as illustrated in Figure 5 (second column).

The m parameter behavior indicates that the scatterers' distribution evolves from a pre-Rayleigh to a Rayleigh distribution as the cataract progresses from initial to severe (values close to 1; Shankar 2000; Tsui et al. 2006). Also, with cataract formation the m parameter increases deeper in the cortex region, revealing the presence of a larger number of scatterers from the cortex to the nucleus.

Correlations with the protein aggregates

The 50- μ m lens slices contained several protein layers in agglomerates, connective tissue and collagen fi-

bers. As these structures alone represent some nanometers, in accordance with the conditions of image acquisition and with the protein and connective tissue staining protocol, the darker areas in the microscopy images are associated with higher protein aggregates concentration (Fig. 3, third and fourth columns).

For nucleus and cortex regions (Fig. 3, third and fourth columns), more pronounced dyeing is visible over the two different immersion times, indicating an increase in protein aggregates during the cataract formation process. Moreover, for the two immersion times, the nucleus showed higher dyeing areas than the cortex, indicating the presence of more protein aggregates and fiber compaction. A strong correlation was found between the mean brightness intensity of the slice images obtained in the cortex region and both the mean brightness intensity in the B-Scan images ($R = -0.922$; $p = 0.039$) and the mean of the Nakagami m parameter ($R = -0.943$; $p = 0.029$). No correlation was made for the nucleus due to the signal's low amplitude in that region of the lens.

Features selected

The univariate analysis showed that most of the 97 extracted features presented a statistically significant difference between healthy and cataractous lenses and between initial and severe cataract (Fig. 6).

The average F-measure values for the four classifiers demonstrated that two components allow the highest discrimination between healthy and cataractous lenses (F-measure = 0.95), while nine components are needed

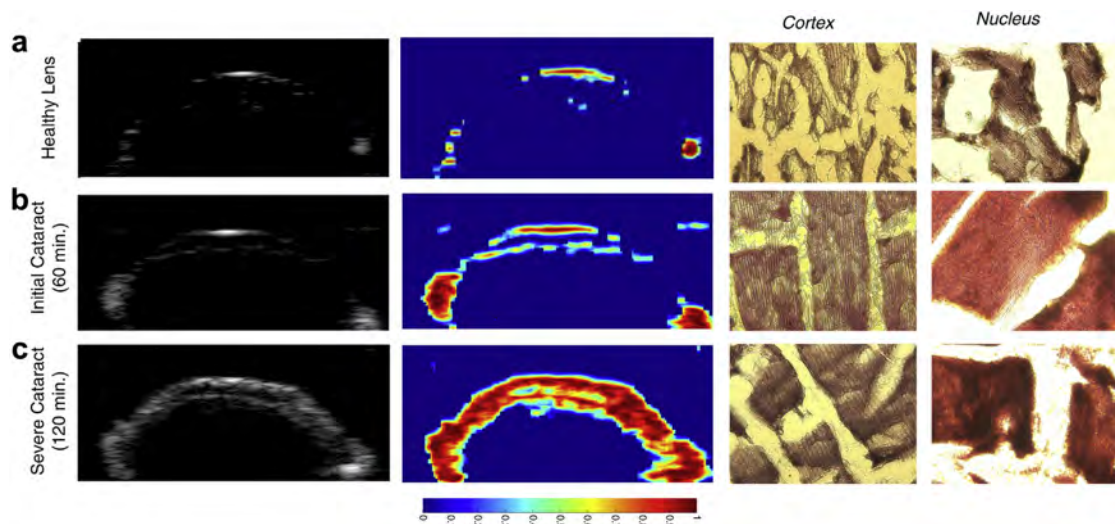


Fig. 5. B-Scan images (first column), Nakagami images (second column, blue and red colors correspond respectively to m values of 0 and 1) and histologic images for the cortex (third column) and the nucleus (fourth column): (a) healthy lenses [without cataract], (b) lenses with initial cataract [60 min of immersion time] and (c) lenses with severe cataract [120 min of immersion time].

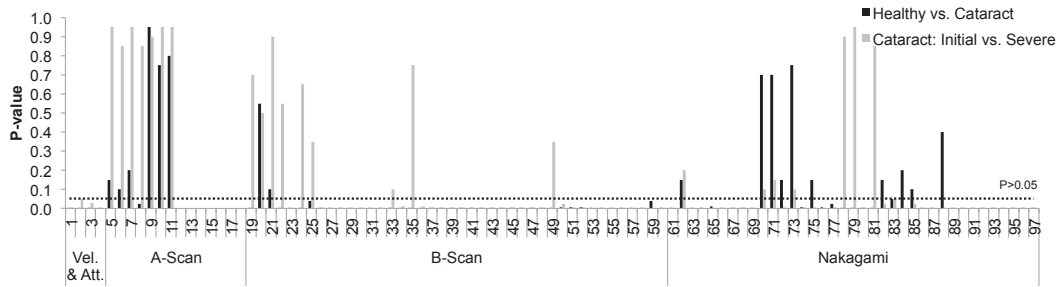


Fig. 6. p values for the 97 features extracted from the A-Scan and backscattering signals (statistically significant features had a p value < 0.05).

to reach the highest discrimination between initial and severe cataract (F-measure = 0.91; Fig. 7).

Classification performance

For the classification into healthy and cataractous lenses, all the classifiers showed a good performance (F-measure $\geq 92.68\%$, Fig. 8). The sensitivity was higher for the KNN and SVM classifiers (95.71% and 94.99%, respectively), while the specificity was higher for the KNN and FLD classifiers (85.55% and 85.14%, respectively).

For the classification into initial and severe cataractous lenses, only the SVM classifier reached a good performance (F-measure = 90.62%, Fig. 9), while the other classifiers performed below 80%. The sensitivity and specificity for the SVM were 98.30% and 80.59%, respectively. For the others classifiers (Bayes, KNN and FLD), the performance was lower than 79.81% (FLD), with sensitivities and specificities lower than 81.40% and 78.26%, respectively (FLD).

DISCUSSION AND CONCLUSION

For clinical prognosis and therapeutic purposes, the correct classification of the cataract type and severity is very important to avoid or minimize surgical or post-surgical complications (Paunksnis *et al.* 2007). In this

context, ultrasound appears as a promising non-invasive technique for cataract hardness characterization (Ho *et al.* 2012).

During the cataractogenic process, there is an increase of light-scatter particles caused by protein aggregation and fiber compaction, which contributes to lens hardness and therefore to the impairment of light propagation through the eye (Ecroyd and Carver 2009; Kanski 2007; Michael and Bron 2011). These changes in the lens tissue structure impact their acoustical properties. Thus, it is expected that the ultrasound waves suffer higher attenuation associated with the absorption and scattering phenomena as they propagate through the cataractous lens (Tsui and Chang 2007; Tsui *et al.* 2011). Also, it is expected that the propagation velocity increases with tissue density and hardness as a result of the protein aggregation and fibers compaction, justifying the observed evolution of velocity in cataractous lenses in this work. The attenuation of ultrasound waves in biological tissues is largely influenced by the presence of high-molecular-weight compounds, tissue density and scatterers (Paunksnis *et al.* 2003). In an *ex-vivo* study, Tabandeh *et al.* (2000) demonstrated that the attenuation of ultrasound waves in human lenses correlates with its hardness. It was also demonstrated by Huang *et al.* (2007a; 2009) that the attenuation increase indicates an increase of cataract hardness. By measuring the Young

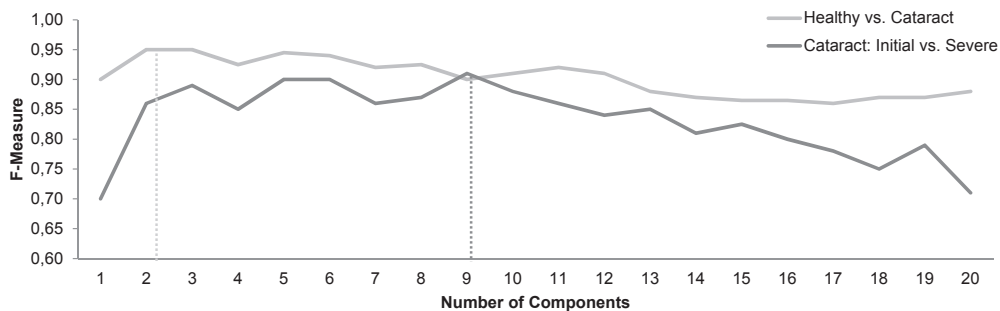


Fig. 7. F-measure for the first 20 components obtained by principal components analysis (average value for the four classifiers).

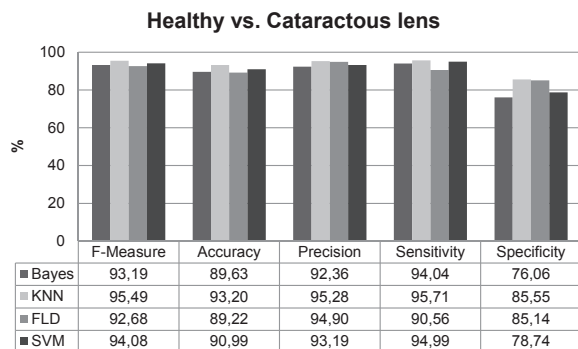


Fig. 8. Performance for the classification into healthy or cataractous lenses (Bayes, K Nearest-Neighbour, Fisher Linear Discriminant and Support Vector Machines classifiers).

modulus, a correlation between these two parameters was established, showing that the frequency dependent attenuation can be used to globally estimate the cataractous lens hardness (Huang et al. 2007a; 2007b; Korte et al. 1994; Paunksnis et al. 2007; Raitelaitienė and Paunksnis 2005; Tabandeh et al. 2000; Tsui et al. 2007).

In this work it was shown that cataract hardness can be characterized non-invasively and classified automatically using acoustical parameters, B-Scan and Nakagami images. It was also shown that the propagation velocity and frequency dependent attenuation increase significantly with cataract formation.

Regarding the B-Scan images, in cataractous lenses, regions of opacity are associated with backscattering signals of higher intensity, which is not observed in the signals from the normal lens (Tsui and Chang 2007; Tsui et al. 2011). Thus, the brightness images describe the echogenicity changes in the tissues, allowing for a qualitative characterization of lens structure. In cataract formation more areas of echogenicity appear, and therefore the brightness intensity of B-Scan images increases (Tsui and Chang 2007). In this work, the B-

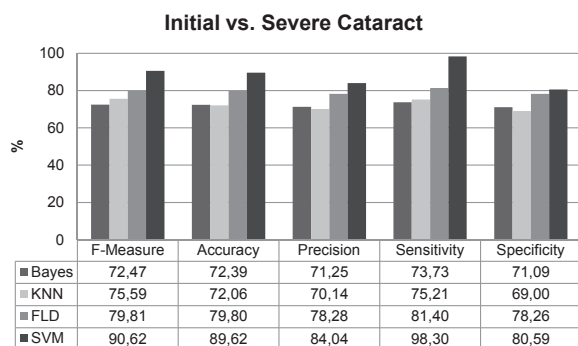


Fig. 9. Performance for the classification into initial or severe cataractous lenses (Bayes, K Nearest-Neighbour, Fisher Linear Discriminant and Support Vector Machines classifiers).

Scan images showed a brightness intensity increase over the cataract formation as a result of the increased region of high scatterers' concentration, from the cortex to the nucleus, which is responsible for lens opacity (Sharma and Santhoshkumar 2009). That was also demonstrated by the m parameter, which also showed an increase over the cataract formation as observed in the Nakagami images. The cataract formation pattern observed in the B-Scan and Nakagami images is a result of the used method for cataract induction. After 60 min of lens immersion, a separation between the cortex and the nucleus becomes visible due to the different fiber compactations between these two regions, which is confirmed by the histologic images. Moreover, the m parameter behavior indicates that the scatterers' distribution evolves from a pre-Rayleigh to a Rayleigh distribution as the cataract progresses from initial to severe cataract (Shankar 2000; Tsui et al. 2006). Also, with cataract formation, the m parameter increases deeper in the cortex region, revealing the presence of a larger number of scatterers from the cortex to the nucleus. These results are in agreement with the work carried out by Tsui et al. (2007), where a 35-MHz ultrasound transducer was used to characterize cataract in a porcine lens invasively. In this work, the use of a 25-MHz transducer has made non-invasively obtaining scatterer distributions in deeper regions of the lenses possible.

It should be noticed that the Nakagami m parameter estimation is affected by two components, the hardness of the tissue and the scatterers' concentration (Tsui et al. 2013). In cataract formation, where the increase of the hardness is related to the increase of fiber compaction and scatterers' concentration, the separation between hardness and scatterers components is difficult for the used cataract induction model.

Different cataract classification systems have been developed. The most frequently used is the Lens Opacity Classification System version III (LOCSIII; Chylack et al. 1993) and Wisconsin Cataract Grading System (WCGS; Panchapakesan et al. 1997). These systems are based on retro-illumination and slit-lamp images and rely on subjective data, depending on the examination settings and examiner's expertise (Gao et al. 2013; Kirwan et al. 2003). In this work, it was shown that SVM can be a useful tool for the automatic classification of the cataract severity, based on the ultrasound technique.

It is recognized that the image textural features are influenced not only by the intrinsic ultrasound properties of the porcine lens tissue, but also by the properties of the ultrasound system. For a different ultrasonic measurement configuration, the measured textural features must be influenced in a similar manner as those reported in this work, although with potentially different values.

Therefore, in a clinical implementation, the classifiers will need to be trained using the textural features associated with the used ultrasound imaging system configuration.

In conclusion, it was demonstrated in this work that propagation velocity and attenuation, when combined with the backscattering signals, represented in terms of B-Scan and Nakagami images, allow for a good discrimination of the different cataract degrees. The developed methodology combined with machine-learning techniques has great potential for the automatic classification of cataract and for the monitoring of its formation. Also, the proposed methodology allows estimation of the cataract hardness, knowledge of which is very important for the selection of the optimal ultrasound phacoemulsification or laser energy levels, thus reducing the risks of the energy level over-estimation and making the cataract surgery safer.

Acknowledgments—This research is sponsored by CEMUC—Mechanical Engineering Center of Coimbra University, FEDER funds through the program COMPETE—Operational Program for Competitiveness Factors—and by national funds through FCT—Foundation for Science and Technology, under the project PTDC/DTP-PIC/0419/2012.

REFERENCES

- Andrade AO, Kyberd P, Nasuto S. The application of the Hilbert spectrum to the analysis of electromyographic signals. *Inf Sci (Ny)* 2008;178:2176–2193.
- Bankman IN. Chapter 14: Two-dimensional shape and texture quantification. *Handbook of medical imaging*. Brody W, ed. Academic Press, San Diego, CA, 2000, 215–230.
- Brand S, Weiss EC, Lemor RM, Kolios MC. High frequency ultrasound tissue characterization and acoustic microscopy of intracellular changes. *Ultrasound Med Biol* 2008;34:1396–1407.
- Caixinha M, Jesus D, Santos M, Santos J, Velte E. Characterization of scatterers concentration in cataractous lens using Nakagami distribution by ultrasounds. *IEEE Int Ultrason Symp Prague*, 2013;425–428.
- Caixinha M, Jesus D, Velte E, Santos M, Santos J. Using ultrasound backscattering signals and Nakagami statistical distribution to assess regional cataract hardness. *IEEE Trans Biomed Eng* 2014;61:2921–2929.
- Cardiff R, Miller C, Munn R. Manual hematoxylin and eosin staining of mouse tissue sections. *Cold Spring Harb Protoc* 2014;2014:655–658.
- Carricondo P, Fortes A. Senior resident phacoemulsification learning curve. *Arq Bras Oftalmol* 2010;73:7–10.
- Chylack LT, Wolfe JK, Singer DM, Leske MC, Bullimore MA, Bailey IL, Friend J, McCarthy D, Wu SY. The Lens Opacities Classification System III. The Longitudinal Study of Cataract Study Group. *Arch Ophthalmol* 1993;111:831–836.
- Cloutier G, Daronatand M, Savery D, Garcia D, Durand L, Foster F. Non-Gaussian statistics and temporal variations of the ultrasound signal backscattered by blood at frequencies between 10 and 58 MHz. *J Acoust Soc Am* 2004;116:566–577.
- Despotovic I, Goossens B, Vansteenkiste E, Pizurica A, Philips W. Using phase information in ultrasound RF-signals for tissue characterization. *Annu Work Circuits, Syst Signal Process. 19th Proceedings* 2008;314–317.
- Ecroyd H, Carver J. Crystallin proteins and amyloid fibrils. *Cell Mol Life Sci* 2009;66:62–81.
- Fischer A, Jacobson K, Rose J, Zeller R. Hematoxylin and eosin staining of tissue and cell sections. *CSH Protoc* 2008;2008. pdb.prot4986.
- Gao X, Wong DW, Ng T-T, Cheung CYL, Cheng C-Y, Wong TY. Automatic grading of cortical and PSC cataracts using retroillumination lens images. In: Lee KM, Matsushita Y, Rehg JM, Hu Z, (eds). *Comput Vis – ACCV 2012*. Berlin, Heidelberg: Springer Berlin Heidelberg; 2013.
- Guyon I, Elisseeff A. An introduction to variable and feature selection. *J Mach Learn Res* 2003;3:1157–1182. MIT Press.
- Haidekker M. *Advanced biomedical image analysis* (Google eBook). John Wiley & Sons; 2011.
- Haralick RM, Shanmugam K, Dinstein I. Textural features for image classification. *IEEE Trans Syst Man Cybern IEEE* 1973;3:610–621.
- Ho MC, Lin JJ, Shu YC, Chen CN, Chang KJ, Chang CC, Tsui PH. Using ultrasound Nakagami imaging to assess liver fibrosis in rats. *Ultrasonics* 2012;52:215–222. Elsevier BV.
- Huang C, Ameri H, Deboer C, Rowley A, Xu X, Sun L, Wang S, Humayun M, Shung K. Evaluation of lens hardness in cataract surgery using high-frequency ultrasonic parameters *in vitro*. *Ultrasound Med Biol* 2007a;33:1609–1616.
- Huang C, Chen R, Tsui P. Measurements of attenuation coefficient for evaluating the hardness of a cataract lens by a high-frequency ultrasonic needle transducer. *Phys Med Biol* 2009;54:5981–5994.
- Huang C, Zhou Q, Ameri H, Wu W, Sun L, Wang S, Humayun M, Shung K. Determining the acoustic properties of the lens using a high-frequency ultrasonic needle transducer. *Ultrasound Med Biol* 2007b;33:1971–1977.
- Huang NE, Shen Z, Long SR, Wu MC, Shih HH, Zheng Q, Yen N-C, Tung CC, Liu HH. The empirical mode decomposition and the Hilbert spectrum for nonlinear and non-stationary time series analysis. *Proc R Soc A Math Phys Eng Sci* 1998;454:903–995.
- Jain A, Duin R, Mao J. Statistical pattern recognition: a review. *IEEE Trans Pattern Anal Mach Intell* 2000;22:4–37.
- Kalisz A. Statistical framework for ultrasonic spectral parameter imaging. *Ultrasound Med Biol* 1997;13:1371–1382.
- Kambhatla N, Leen T. Dimension reduction by local principal component analysis. *Neural Comput* 1997;9:1493–1516.
- Kanski J. *Clinical diagnosis in ophthalmology*. (1st ed). Philadelphia, PA: Elsevier Mosby; 2007.
- Kirwan J, Venter L, Stulting A, Murdoch I. LOCS III examination at the slit lamp, do settings matter? *Ophthalmic Epidemiol* 2003;10:259–266.
- de Korte C, van der Steen A, Thijssen J, Duindam J, Otto C, Puppels G. Relation between local acoustic parameters and protein distribution in human and porcine eye lenses. *Exp Eye Res* 1994;59:617–627.
- Lizzi F, Feleppa E, Kaiser A, Deng C. Ultrasonic spectrum analysis for tissue evaluation. *Pattern Recognit Lett* 2003;24:637–658.
- Machado CB, Pereira WC, Meziri M, Laugier P. Characterization of *in vitro* healthy and pathological human liver tissue periodicity using backscattered ultrasound signals. *Ultrasound Med Biol* 2006;32:649–657.
- Michael R, Bron AJ. The ageing lens and cataract: a model of normal and pathological ageing. *Philos Trans R Soc Lond B Biol Sci* 2011;366:1278–1292.
- Moradi M, Mousavi P, Isotalo PA, Siemens DR, Sauerbrei EE, Abolmaesumi P. A new approach to analysis of RF ultrasound echo signals for tissue characterization: animal studies. *Proc SPIE Spie* 2007;6513:65130.
- Muhtaseb M, Kalhor A, Ionides A. A system for preoperative stratification of cataract patients according to risk of intraoperative complications: a prospective analysis of 1441 cases. *Br J Ophthalmol* 2004;88:1242–1246.
- Noble J, Wells P. Ultrasound image segmentation and tissue characterization. *Proc Inst Mech Eng H* 2010;224:307–316.
- Onohue KD, Uang L, Urks T, Orsberg F, Iccoli CW. Tissue classification with generalized spectrum parameters. *Ultrasound Med Biol* 2001;27:1505–1514.
- Panchapakesan J, Cumming RG, Mitchell P. Reproducibility of the Wisconsin cataract grading system in the Blue Mountains Eye Study. *Ophthalmic Epidemiol* 1997;4:119–126.
- Paunksnis A, Kurapkiene S, Maciulis A. Ultrasound quantitative evaluation of human eye cataract. *Informatica* 2007;18:267–278.

- Paunksnis A, Kurapkienė S, Mačiulis A, Raitelaitienė R, Jurkonis R, Lukoševičius A. Estimation of ultrasound attenuation coefficient of human diabetic cataract. *Ultrasonics* 2003;46:37–40.
- Raitelaitienė R, Paunksnis A. Ultrasonic and biochemical evaluation of human diabetic lens. *Medicina* 2005;41:641–648.
- Raju BI, Srinivasan MA. Statistics of envelope of high-frequency ultrasonic backscatter from human skin *in vivo*. *Ultrason Ferroelectr Freq Control IEEE Trans* 2002;49:871–882.
- Sajda P. Machine learning for detection and diagnosis of disease. *Annu Rev Biomed Eng* 2006;8:537–565.
- Schlurmann T. The empirical mode decomposition and the Hilbert spectra to analyse embedded characteristic oscillations of extreme waves [Abstract]. *Rogue Waves 2000 Workshop, Brest, France*.
- Shankar P. A general statistical model for ultrasonic backscattering from tissues. *IEEE Trans Ultrason Ferroelectr Freq Control* 2000;47:727–736.
- Shankar P. The use of the compounding probability density function in ultrasonic tissue characterization. *Phys Med Biol* 2004;49:1007–1015.
- Shankar P. Ultrasonic tissue characterization using a generalized Nakagami model. *IEEE Trans Ultrason Ferroelectr Freq Control* 2001;48:1716–1720.
- Shankar PM, Dumane VA, George T, Piccoli CW, Reid JM, Forsberg F, Goldberg BB. Classification of breast masses in ultrasonic B scans using Nakagami and K distributions. *Phys Med Biol* 2003;48:2229–2240.
- Shankar PM, Dumane VA, Reid JM, Genis V, Forsberg F, Piccoli CW, Goldberg BB. Classification of ultrasonic B-mode images of breast masses using Nakagami distribution. *IEEE Trans Ultrason Ferroelectr Freq Control* 2001;48:569–580.
- Sharma K, Santhoshkumar P. Lens Aging: Effects of crystallins. *Biochim Biophys Acta* 2009;1790:1095–1108.
- Shin H, Markey MK. A machine learning perspective on the development of clinical decision support systems utilizing mass spectra of blood samples. *J Biomed Inform* 2006;39:227–248.
- Shung KK, Thieme GA. *Ultrasonic scattering in biological tissues*. Boca Raton, Florida: CRC Press; 1992.
- Siddiqui K. Heuristics for sample size determination in multivariate statistical techniques. *World Appl Sci J* 2013;27:285–287.
- Smolíková R, Wachowiak MP, Zurada JM. An information-theoretic approach to estimating ultrasound backscatter characteristics. *Comput Biol Med* 2004;34:355–370.
- Sugiura T, Kurosaka D, Uezuki Y. Creating cataract in a pig eye. *J Cataract Refract Surg* 1999;25:615–621.
- Szabo TL. *Diagnostic ultrasound imaging: inside out*. Oxford, UK: Elsevier; 2014.
- Tabandeh H, Wilkins M, Thompson G, Nassiri D, Karim A. Hardness and ultrasonic characteristics of the human crystalline lens. *J Cataract Refract Surg* 2000;26:838–841.
- Tang X. Texture information in run-length matrices. *IEEE Trans Image Process* 1998;7:1602–1609.
- Tsui P, Chang C. Imaging local scatterer concentrations by the Nakagami statistical model. *Ultrasound Med Biol* 2007;33:608–619.
- Tsui P, Chang C, Ho M, Lee Y, Chen Y, Huang N, Wu Z, Chang K. Use of Nakagami statistics and empirical mode decomposition for ultrasound tissue characterization by a nonfocused transducer. *Ultrasound Med Biol* 2009;35:2055–2068.
- Tsui P, Huang C, Chang C, Wang S, Shung K. Feasibility study of using high-frequency ultrasonic Nakagami imaging for characterizing the cataract lens *in vitro*. *Phys Med Biol* 2007;52:6413–6425.
- Tsui P, Huang C, Wang S. Use of Nakagami distribution and logarithmic compression in ultrasonic tissue characterization. *J Med Biol Eng* 2006;26:69–73.
- Tsui P, Huang C, Zhou Q, Shung K. Cataract measurement by estimating the ultrasonic statistical parameter using an ultrasound needle transducer: an *in vitro* study. *Physiol Meas* 2011;32:513–522.
- Tsui P, Wan Y, Chien Y. Dependency of ultrasonic Nakagami image on the mechanical properties of scattering medium. *J Med Biol Eng* 2013;33:95–102.
- Tsui P, Wan Y, Huang C, Wang M. Effect of adaptive threshold filtering on ultrasonic Nakagami parameter to detect variation in scatterer concentration. *Ultrason Imaging* 2010a;32:229–242.
- Tsui P, Wang S. The effect of the transducer characteristics on the estimation of Nakagami parameter as a function of scatterer concentration. *Ultrasound Med Biol* 2004;30:1345–1353.
- Tsui P, Yeh CK, Chang C. Noise effect on the performance of Nakagami image in ultrasound tissue characterization. *J Med Biol Eng* 2008a;28:197–202.
- Tsui P, Yeh C, Liao Y, Chang C, Kuo W, Chang K, Chen C. Ultrasonic Nakagami imaging: a strategy to visualize the scatterer properties of benign and malignant breast tumors. *Ultrasound Med Biol* 2010b;36:209–217.
- Tsui PH. Potential of ultrasound Nakagami imaging in clinical tissue characterization. *J Med Ultrasound* 2013;21:51–53.
- Wang S, Tasi F. Characterization of bony tissues from ultrasonic backscattering using statistical models. *IEEE Ultrason Symp* 2001;2:1205–1208.
- Wilson ME, Trivedi RH, (eds). *Pediatric Cataract Surgery: Techniques, Complications, and Management*. Philadelphia: Lippincott Williams & Wilkins; 2005.
- World Health Organization. *Vision 2020 The right to sight - Global initiative for the elimination of avoidable blindness: action plan 2006-2011*. Vasa, Switzerland: Author; 2008.



Available online at www.sciencedirect.com

ScienceDirect

Physics Procedia 70 (2015) 1221 – 1224

Physics

Procedia

2015 International Congress on Ultrasonics, 2015 ICU Metz

Automatic Cataract Classification based on Ultrasound Technique using Machine Learning: A comparative Study

Miguel Caixinha^{a*}, Elena Velte^b, Mário Santos^a, Fernando Perdigão^{a,c}, João Amaro^{a,c}, Marco Gomes^{a,c} and Jaime Santos^a

^a Department of Electrical and Computer Engineering, University of Coimbra, PT-3030-290 Coimbra, Portugal

^b Department of Physics, University of Coimbra PT-3030-290 Coimbra, Portugal

^c Instituto de Telecomunicações, PT-3030-290 Coimbra, Portugal

Abstract

This paper addresses the use of computer-aided diagnosis (CAD) system for the cataract classification based on ultrasound technique. Ultrasound A-scan signals were acquired in 220 porcine lenses. B-mode and Nakagami images were constructed. Ninety-seven parameters were extracted from acoustical, spectral and image textural analyses and were subjected to feature selection by Principal Component Analysis (PCA). Bayes, K Nearest-Neighbors (KNN), Fisher Linear Discriminant (FLD) and Support Vector Machine (SVM) classifiers were tested. The classification of healthy and cataractous lenses shows a good performance for the four classifiers (F-measure $\geq 92.68\%$) with SVM showing the highest performance (90.62%) for initial versus severe cataract classification.

© 2015 The Authors. Published by Elsevier B.V. This is an open access article under the CC BY-NC-ND license (<http://creativecommons.org/licenses/by-nc-nd/4.0/>).

Peer-review under responsibility of the Scientific Committee of ICU 2015

Keywords: cataract, classification, machine learning

1. Introduction

Age-related cataract is the most frequent cause of blindness in the world being responsible for 48% of blindness, and affecting more than 10% of the working population. Phacoemulsification is the most common surgical procedure to recover vision. Integrity of the lens capsule is essential for reducing the risk of surgical complications and subsequent vision loss; the selection of an inappropriate phacoemulsification energy level can

* Corresponding author. Tel.: +351.239.796285; fax: +351.239.796247.

E-mail address: miguel.caixinha@gmail.com

disrupt the posterior lens capsule. Therefore, it is crucial to determine the optimal phacoemulsification energy level, which value depends on the lens hardness [1].

For clinical prognosis and therapeutic purposes it is very important to identify the cataract type and severity, especially in its early stages [2]. Recently, Caixinha *et al*, demonstrated that the ultrasound techniques can be used to objectively characterize cataract hardness [3]. In this work the acoustical parameters and backscattering signals obtained from porcine lenses with different cataract degrees are used for objective and automatic cataract classification. Several approaches have been used for classification of cataract severity based on retroillumination and/or slit-lamp images. However, the classification of these images relies on subjective data, depending on the examination settings, and on the examiners expertise [4], [5]. To characterize and classify the different stages of cataract formation, based on the acoustical parameters and in the backscattering signals, information was extracted and then used for automatic classification using machine learning techniques.

2. Materials and Methods

2.1. Lens samples

Two hundred and twenty (220) porcine lenses were collected in a slaughterhouse. Lens were extracted and prepared to clean iris remains and adhering vitreous, preserving the lens capsule. Ten (10) lenses were excluded due to the presence of lens opacities. Cataract was induced in 135 lenses immersed over time in an ethanol:2-propanol:formalin solution at the ratio 3:3:4 [6]. To obtain different cataract degrees the lenses were immersed in the solution during 60 or 120 minutes, corresponding to lenses with initial (64) or severe (71) cataract, respectively. Seventy-five (75) lenses were used as control (without cataract).

2.2. Experimental Setup

The ultrasound parameters as velocity, frequency dependent attenuation, and backscattering signals were obtained using a 25 MHz central frequency transducer (model JAP-F25.3.1, Krautkramer, NSW, Australia) with a 25 mm focus and 5 mm active diameter. The pulse length used was 0.13 μ s at -6 dB. The setup description can be found in [3] (Fig. 1).

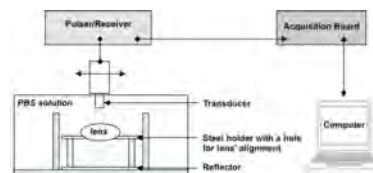


Fig. 1. Experimental setup.

2.3. Data acquisition

To characterize different degrees of cataract formation 97 parameters were extracted from the A-Scan and backscattering signals.

2.3.1. Features extracted from the A-Scan signals

Ten (10) A-Scan lines were collected over the central portion of the lens to compute the mean and variance values of the ultrasound velocity, v , and attenuation coefficient $\alpha(f)$, according to [3]. Additionally, the Hilbert and Fourier spectra were obtained. The signals were analyzed using linear regression techniques to compute the spectral slope (dB/MHz), intercept (dB, extrapolation to zero frequency), and midband fit (dB value of the regression line at the center frequency) [7]. The mean frequency, frequency downshift, frequency at maximal amplitude and backscattering coefficient were also calculated.

2.3.2. Features extracted from the backscattering signals: B-Scan Imaging

B-Scan images were constructed for each lens using 15000 A-Scan lines sampled at a 200 MHz rate, considering the envelope amplitudes of the backscattering signals, obtained using the Hilbert transform, and a dynamic range of 40 dB. The distance between each A-Scan line was 0.001 mm (Fig. 2 – top row).

A spectral analysis through 2D Fourier Transform (FT) was performed. The predominant and global periodicity, the predominant and global orientation, the variance of the periodicity function, the variance of the orientation function, and the amplitude of the Discrete FT were extracted. To extract features from the B-Scan images a textural analysis was performed. The following parameters were extracted: First order statistic parameters from the image histogram, i.e. mean, variance, kurtosis, skewness, standard deviation, mode and median; Grey Level Co-occurrence Matrix (GLCM) parameters for 0°, 45°, 90° and 135°, i.e., energy, inertia, entropy correlation and homogeneity; Grey Level Run Length Matrix (GLRLM) parameters, i.e., Short and Long Run Emphasis (SRE and LRE), Grey Level Non-Uniformity (GLNU), Run Percentage (RP), Rung Length Non-Uniformity (RLNU), Low and High Grey Level Run Emphasis (LGLRE and HGLRE); and Fractal Dimension (Hausdorff dimension).

2.3.3. Features extracted from the backscattering signals: Nakagami Statistics and Imaging

To extract statistical parameters that could discriminate different cataract degrees the probability density function of the backscattered signals envelope was estimated using the Nakagami distribution [3], [8] (Fig. 2 – bottom row). In this work the Nakagami shape and scale parameters, m and Ω respectively, were used. Additionally, the following features were extracted from the Nakagami images based on a textural analysis: First order statistic parameters; GLCM parameters for 0°, 45°, 90° and 135°; GLRLM parameters; and Fractal Dimension (Hausdorff dimension).

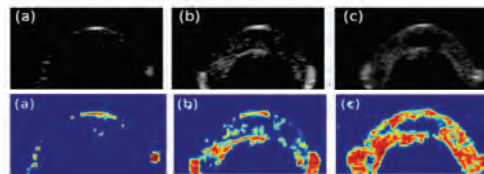


Fig. 2. B-scan images (top row) and Nakagami images (bottom row) for the 3 types of lenses: (a) healthy; (b) initial cataract (60 minutes of immersion time); and (c) severe cataract (120 minutes of immersion time) [3].

2.4. Features selection and Classification

Given the small data set (210) compared to the dimensionality of the features (97), the selection of the most discriminative features was essential [9]. For this purpose, a principal component analysis (PCA) was performed [9] [10]. To select the best set of components a stepwise approach was used, i.e., the 4 classifiers were tested with different numbers of components, from 1 to 20. The selected number of components was based on the set of components that achieved the highest average F-measure.

Four (4) different classifiers were considered: Bayes, K Nearest-Neighbor (KNN), Fisher Linear Discriminant (FLD) and Support Vector Machines (SVM) classifiers [11]. A k -fold cross-validation was performed with $k=10$; i.e., the classifiers were trained with $k-1$ samples selected at random and tested with the remaining sample. To reduce bias the cross-validation was performed 200 times. The performance of the different classifiers was assessed based on the average performance of the 4 classifiers using the F-measure, accuracy, precision, sensibility and specificity.

3. Results

Two (2) components allows for the highest discrimination between healthy and cataractous lenses (average F-measure = 0.95), while 9 components are needed to reach the highest discrimination between initial and severe cataract (F-measure = 0.91).

Considering the classification between healthy and cataractous lenses, all the classifiers showed a good performance (F-measure $\geq 92.68\%$, Table 1). The sensitivity was higher for KNN and SVM classifiers (95.71% and

94.99%, respectively), while the specificity was higher for KNN and FLD classifiers (85.55% and 85.14% respectively).

Considering the classification between initial and severe cataractous lenses, only the SVM classifier reached a good performance (F-measure = 90.62%, Table 1). The sensitivity and specificity for SVM classification was 98.30% and 80.59%, respectively. For the remaining classifiers (Bayes, KNN and FLD) the performance was lower than 79.81% (FLD), being the sensitivities and specificities lower than 81.40% and 78.26%, respectively (FLD).

Table 1. Performance of the 4 classifiers for the classification into Healthy or Cataractous lens and for Initial or Severe cataract.

	Healthy vs Cataractous lens					Initial or Severe cataract				
	Precision	Specificity	Sensitivity	Accuracy	F-Measure	Precision	Specificity	Sensitivity	Accuracy	F-Measure
Bayes	92.36	76.06	94.04	89.63	93.19	71.25	71.09	73.73	72.39	72.47
KNN	95.28	85.55	95.71	93.20	95.49	70.14	69.00	75.21	72.06	75.59
FLD	94.90	85.14	90.56	89.22	92.68	78.28	78.26	81.40	79.80	79.81
SVM	93.19	78.74	94.99	90.99	94.08	84.04	80.59	98.30	89.62	90.62

4. Conclusion

Ultrasound scanning of the eye lens through B-Scan and Nakagami images is a potential tool to noninvasively characterize and automatically classify the cataract hardness. Our results showed that SVM could be used as a computer-aided diagnosis (CAD) system for cataract classification based on ultrasound techniques. The velocity and attenuation combined with the backscattering signals analysis in terms of B-Scan and Nakagami imaging allow for a good discrimination of the different cataract degrees and appear as a good alternative for the subjective classification systems currently used.

The methodology developed in this work represents a technological basis for the development of a medical device for patient-oriented cataract surgery. A centralized classification database may improve classification accuracy as the classification algorithm "learns" from the growing database. Thus, the acquisition of robust data from different types and stages of cataract formation will take an increasing importance.

In the future, clinical trials will be required to determine how to best integrate the diagnosis with the classification results and patient care.

Acknowledgements

This research is sponsored by FEDER through COMPETE – Programa Operacional de Factores de Competitividade; and by FCT – Fundação para a Ciência e Tecnologia (project PTDC/DTP-PIC/0419/2012).

References

- [1] M. Muhtaseb, A. Kalhor, and A. Ionides, "A system for preoperative stratification of cataract patients according to risk of intraoperative complications: a prospective analysis of 1441 cases.," *Br. J. Ophthalmol.*, vol. 88, no. 10, pp. 1242–6, Oct. 2004.
- [2] A. Paunksnis, S. Kurapkienė, and A. Mačiulis, "Ultrasound quantitative evaluation of human eye cataract," *Informatica*, vol. 18, no. 2, pp. 267–278, 2007.
- [3] M. Caxinha, D. Jesus, E. Velte, M. Santos, and J. Santos, "Using ultrasound backscattering signals and Nakagami statistical distribution to assess regional cataract hardness," *IEEE Trans. Biomed. Eng.*, vol. PP, no. 99, 2014.
- [4] J. Kirwan, L. Venter, A. Stulting, and I. Murdoch, "LOCS III examination at the slit lamp, do settings matter?," *Ophthalmic Epidemiology*, Oct-2003.
- [5] X. Gao, D. W. K. Wong, T.-T. Ng, C. Y. L. Cheung, C.-Y. Cheng, and T. Y. Wong, "Automatic grading of cortical and PSC cataracts using retroillumination lens images," *Comput. Vis. – ACCV 2012*, vol. 7725, pp. 256–267, Nov. 2013.
- [6] T. Sugiura, D. Kurosaka, and Y. Uezuki, "Creating cataract in a pig eye," *J. Cataract Refract. Surg.*, vol. 25, no. 5, pp. 615–621, May 1999.
- [7] A. Kalisz, "Statistical framework for ultrasonic spectral parameter imaging," vol. 13, no. 9, 1997.
- [8] P. Shankar, "A general statistical model for ultrasonic backscattering from tissues.," *IEEE Trans. Ultrason. Ferroelectr. Freq. Control*, vol. 47, no. 3, pp. 727–36, Jan. 2000.
- [9] K. Siddiqui, "Heuristics for Sample Size Determination in Multivariate Statistical Techniques," *World Appl. Sci. J.*, vol. 27, no. 2, pp. 285–287, 2013.
- [10] P. Sajda, "Machine learning for detection and diagnosis of disease.," *Annu. Rev. Biomed. Eng.*, vol. 8, pp. 537–65, Jan. 2006.
- [11] A. Jain, R. Duin, and J. Mao, "Statistical Pattern Recognition: A Review," *IEEE Trans. Pattern Anal. Mach. Intell.*, vol. 22, no. 1, pp. 4–37, 2000.

In-vivo Automatic Nuclear Cataract Detection and Classification in an Animal Model by Ultrasounds

Miguel Caixinha, *Graduate Student member, IEEE*, João Amaro, *Graduate Student member, IEEE*, Mário Santos, Fernando Perdigão, Marco Gomes, and Jaime Santos

Abstract— Objective: To early detect nuclear cataract *in vivo* and automatically classify its severity degree, based on the ultrasound technique, using machine learning. **Methods:** A 20 MHz ophthalmic ultrasound probe with a focal length of 8.9 mm, and active diameter of 3 mm was used. Twenty-seven features in time and frequency domain were extracted for cataract detection and classification with Support Vector Machine (SVM), Bayes, Multilayer Perceptron and Random Forest classifiers. Fifty rats were used: fourteen as control and thirty-six as study group. An animal model for nuclear cataract was developed. Twelve rats with incipient, 13 with moderate, and 11 with severe cataract were obtained. The hardness of the nucleus and the cortex regions was objectively measured in 12 rats using the NanoTest™. **Results:** Velocity, attenuation and frequency downshift significantly increased with cataract formation ($P < 0.001$). The SVM classifier showed the higher performance for the automatic classification of cataract severity, with a precision, sensitivity and specificity of 99.7% (relative absolute error of 0.4%). A statistically significant difference was found for the hardness of the different cataract degrees ($P = 0.016$). The nucleus showed a higher hardness increase with cataract formation ($P = 0.049$). A moderate to good correlation between the features and the nucleus hardness was found in 23 out of the 27 features. **Conclusion:** The developed methodology made possible detecting the nuclear cataract *in-vivo* in early stages, classifying automatically its severity degree and estimating its hardness. **Significance:** Based on this work a medical prototype will be developed for early cataract detection, classification and hardness estimation.

Index Terms—Cataract, Classification, Hardness, Machine Learning, Ultrasound.

I. INTRODUCTION

Cataract is an opacity in the lens eye that results from the disruption of the crystalline lens proteins arrangement due to the proteins aggregation and fiber compaction [1], [2]. Since there is no cataract prevention or pharmacological treatment, the surgical cataract removal is the only effective therapy to recover vision loss. Phacoemulsification is the most common surgical technique used in the developed countries for cataract removal. This technique involves the use of ultrasound energy to fragment the cataractous lenses into small pieces that are afterward aspirated [3]–[5].

Recently, the laser assisted cataract surgery uses laser radiation energy to fragment the cataractous lenses, [6], [7]. In the cataract surgery the posterior lens capsule remains in the eye to sustain the intraocular lens to be implanted. The overestimation of the phacoemulsification energy level can disrupt the posterior lens capsule, which integrity is essential for reducing the risk of surgical complications. It is well established that the phacoemulsification energy levels are directly related with the cataract hardness [7]–[9]. Therefore, it is of great clinical importance the objective classification of cataract, and the estimation of its hardness, namely in dense or nuclear cataracts, in order to minimize the surgical complications, and avoid vision loss, [10]–[12].

For clinical purposes it is very important to identify the cataract type and severity, especially in its early stages. Currently, cataract is classified using the Lens Opacities Classification System, Version III (LOCS III) [13]–[15]. This system and others used for cataract classification [13], [14], [16]–[21], rely on a subjective comparison between an image database and the acquired images that depends on the exam settings and graders [22]–[25]. In this context, the ultrasound technique appears as a powerful non-invasive alternative for objective cataract characterization and classification [26]–[28].

This work aims to demonstrate that the ultrasound technique can be used to early detect nuclear cataract *in-vivo*, classify its severity degree, and estimate its hardness. Features were extracted from the eyes' collected signals and then used to train and test different classifiers in order to accurately identify the healthy and cataractous lenses, as well as automatically classify the nuclear cataract according to the following degrees: incipient, moderate, and severe. For that purpose, an animal model was developed. Fifty rats were used in the study: fourteen as control and thirty-six as study group. From the animal model twelve rats with incipient cataract, thirteen with moderate, and eleven with severe cataract were obtained.

To validate the setup for *in-vivo* cataract detection and classification, three different approaches for signals collection were considered: *in-vivo*, *post-mortem* and *ex-vivo*. The authors intended to demonstrate that the eye movements' *in-vivo* and the probe misalignment with the free-hand acquisition do not affect the classification results.

II. MATERIALS AND METHODS

A. Animal model for nuclear cataract

Wistar rats were used for nuclear cataract induction by sodium selenite (Na_2SeO_3). This animal model is currently used in cataract research since that type of induced cataract mimics well human age-related cataract [29], [30]. Cataract by selenite-overdose is an extremely rapid and convenient model for nuclear cataract [31]. It is well established that oxidative damage plays an important role in the opacification process and the redox cycles are mandatory for the maintenance of lens transparency. Oxidative stress induced by free radicals has also been identified as one of the major triggering factors for senile cataract formation [32]–[34]. Both morphological and biochemical properties of this model have been comprehensively investigated [35]. The cataract is produced by a single subcutaneous injection of 19 to 30 $\mu\text{moles/kg}$ body weight of sodium selenite into suckling rats of 10 to 14 days of age, since selenite is cataractogenic only when administered in rats before completion of the critical maturation period of the lens, *i.e.*, approximately 16 days of age [29], [30].

In order to obtain different nuclear cataract degrees, the authors modified the animal model created by Ostadalova *et al.* [31], and conducted a pilot study in six rats. The rats were injected with three different concentrations of sodium selenite and at different periods of eyes' maturation (before or after eyes opening, *i.e.*, at day 11 or day 15). All the rats were examined at the fourth month with a modified slit-lamp. As expected, different cataract severity levels were obtained.

In this work, 36 rats were used as study group, with ages ranging from 4 to 10 months, with a mean age of 4.8 ± 2.5 months. The rats were firstly split in six groups with six rats each. Then, three groups were injected before eyes opening with 20, 25 and 30 $\mu\text{mol/kg}$ (at day 11), while the other three groups were injected after eyes opening with 20, 25 and 30 $\mu\text{mol/kg}$ (at day 15). With this procedure, the authors obtained the intended cataract severity levels.

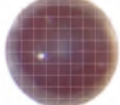


B. Experimental procedure

1) Samples characterization

All the rats' eyes were tracked for changes in the transparent media and other type of lens opacities, with a modified slit lamp. The images from the induced cataract were acquired with a digital camera keeping the magnification and the focal length fixed. The severity of the produced cataracts was thereafter classified in three types, according to the transparency and the area occupied by the opacity in the entire lens: incipient, moderate, and severe. A standardized grid was projected onto the images to assist the manual classification. The approach consisted of counting the squares occupied by the opacity. Thus, based on the area occupied by the opacity, its appearance and shape, the cataract was labeled as incipient when a small and diffuse opacity was observed; moderate when a diffuse opacity with well-defined borders occupying approximately half of the lens was observed; and severe when a well-

defined opacity, occupying approximately half of the lens was observed. Table I illustrates the images of the different cataract degrees obtained from three representative eyes.

TABLE I
CLASSIFICATION CRITERIA FOR THE 3 LEVELS OF CATARACT SEVERITY

Incipient cataract	Moderate cataract	Severe cataract
		
Small and diffuse opacity	Diffuse opacity with well-defined borders occupying approximately half of the lens	Well-defined opacity, occupying approximately half of the lens

To demonstrate that the different induced cataract have different hardness, twelve lenses (three without cataract, three with incipient cataract, three with moderate cataract, and three with severe cataract), were submitted to hardness tests, using the NanoTestTM (Micro Materials Ltd, Wrexham, UK) [36]. For the tests, the lenses were firstly frozen at -40°C in an embedding resin, Cryomatrix Shandon medium (Thermo Scientific Shandon Ltd, WA, USA) and then cut transversally with a glass knife using a Leica Microsystems CM3350S cryostat (Leica Microsystems, Wetzlar, Germany). The sample nanohardness measurement requires that the tissue has a regular surface and a thickness such that the penetration depth of the indentation does not have a radius less than 10% of the total tissue thickness to avoid the substrate effect. Experimentally, and after analyzing the samples with the optical microscope, it was found that the most regular surfaces of the lens tissue were obtained when cuts were made with 50 μm in thickness at -20°C . Based on this result, several slices were made in two regions of the lens (cortex and nucleus). Six indentations were performed in each analyzed region and the average value was considered as the mean hardness of the lens in that region.

Three different approaches for ultrasound signal collection were considered: *in-vivo*, *post-mortem* and *ex-vivo* as shown in Fig. 1 and Fig. 2. With the *post-mortem* and the *ex-vivo* acquisitions, the authors intended demonstrating that the eye movements, and the eventual probe misalignment in relation to the ocular surface that can happen *in-vivo*, do not affect the classification results.

All the experiments were carried out in accordance with the European regulation on the protection of animals used for scientific purposes (Directive 2010/63/EU). The experiments were approved by the national Directorate General of Food and Veterinary Medicine, and by the Animal Welfare Office of the University of Coimbra. The animal experiments were made with care to minimize its suffering.

2) Ultrasound signal acquisition

A 20 MHz ophthalmic probe (Imasonic, SAS, France) with a focal length of 8.9 mm, and an active diameter of 3 mm was used. The probe was excited using a pulser/receiver (model Compact Pulser, Ultratek, USA) with a 1 kHz pulse repetition frequency (PRF). The A-Scan

signals were sampled using a high speed ADLINK DAQ PCIe board (model PCIe-9842, ADLINK Technology Inc., Taipei, Taiwan) with a sampling rate of 200 MS/s. A digital oscilloscope (model TDS 3032, Tektronix Inc., TX, USA) was used to display the signals during the acquisitions (see Fig. 3). Data processing was carried out in Matlab (MathWorkds Inc., MA, USA).

Before the *in-vivo* acquisitions, the rats were anesthetized with an intraperitoneal ketamine hydrochloride injection (75 mg/kg), and their pupils were dilated with 10% phenylephrine hydrochloride eye drops. Then, the rats were sacrificed with cervical dislocation and *post-mortem* signal acquisitions were carried out. For the *in-vivo* and *post-mortem* acquisitions, a custom-made buffer, filled with an isotonic PBS solution, was used for the eye probe coupling (Fig. 1). For the *ex-vivo* signals acquisition, the eyes were enucleated from the orbital cavity and placed on a holder, with a machined hole suited to the lens, immersed in the PBS solution with the temperature kept constant during the acquisitions (at $28.0 \pm 0.5^\circ\text{C}$). The probe was attached to a micropositioning system, allowing its precise positioning over the eye surface, then improving the collected signals (Fig. 2).



Fig. 1. Setup for *in-vivo* and *post-mortem* acquisitions.

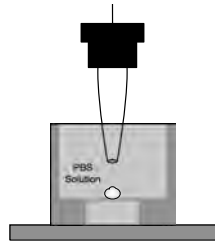


Fig. 2. Setup for *ex-vivo* acquisitions.

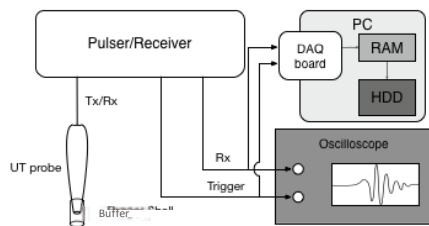


Fig. 3. Setup for data acquisition.

An A-scan signal illustrating the ultrasound propagation over the ocular boundaries is shown in Fig. 4. High amplitude reflections are observed at the anterior and posterior cornea as well as at the anterior lens capsule. A strong echo is also observed when cataract is present. The echo originated from the posterior lens capsule is of low amplitude as the ones from the retina, choroid, and the periorbital fat.

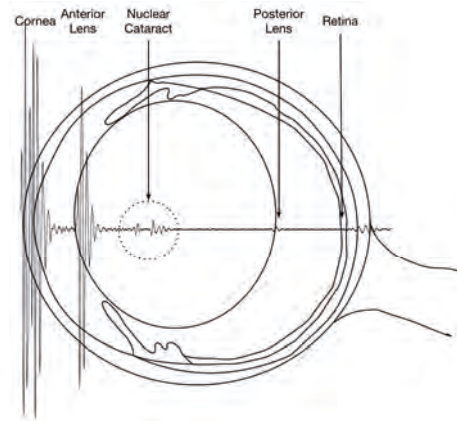


Fig. 4. Illustration of an A-Scan signal for a cataractous lens through the ocular structures.

C. Signal Processing

1) Automatic detection of ocular interfaces

Before the detection of the ocular interfaces, signal conditioning and denoising was carried out. A linear phase passband filter with cut-off frequencies of 1 MHz and 50 MHz was applied to the signal, in order to select the frequencies of interest, and minimize the noise. Then, to improve the signal-to-noise ratio (SNR), a moving average of 20 A-scans was performed, corresponding to an averaging period of 20 ms (according to the PRF).

Several algorithms were developed for the automatic detection of the ocular interfaces, which are described in pseudo-code in Fig. 5 along with an illustration of their implementation over the signal waveform. The propagation time was used for the definition of the different regions of the ocular interfaces searching, assuming the distances knowledge between the corneal and lens interfaces [37], and considering a mean propagation velocity of 1600 m/s and 1650 m/s, for healthy and cataractous lenses, respectively [26]. Therefore, the anterior cornea interface's time instant on A-scan, *i.e.*, t_C , is used as a relative reference for the determination of the time instants of the remaining ocular interfaces.

In order to find t_C , a search window was considered taking as reference the emission pulse, t_p , which is located in the time instant corresponding to highest absolute amplitude value of the A-scan. The search region for t_C starts at $t_p + 3 \mu\text{s}$ (with $3 \mu\text{s}$ being a safe margin to avoid any disturbance by the emission pulse) until the A-scan ends, enabling successful detection for both setups of Fig. 1 and Fig. 2, where $t_C - t_p$ may differ due to the different distances between the probe and the eye. The anterior cornea interface detection comprises two steps: first, the position of the maximum absolute value of the signal in the search region is located, max_pos ; second, starting at sample $\text{max_pos} - 20$ (20 samples correspond to $0.1 \mu\text{s}$) the first sample that is above a threshold defined as the signal's standard deviation (std) is searched.

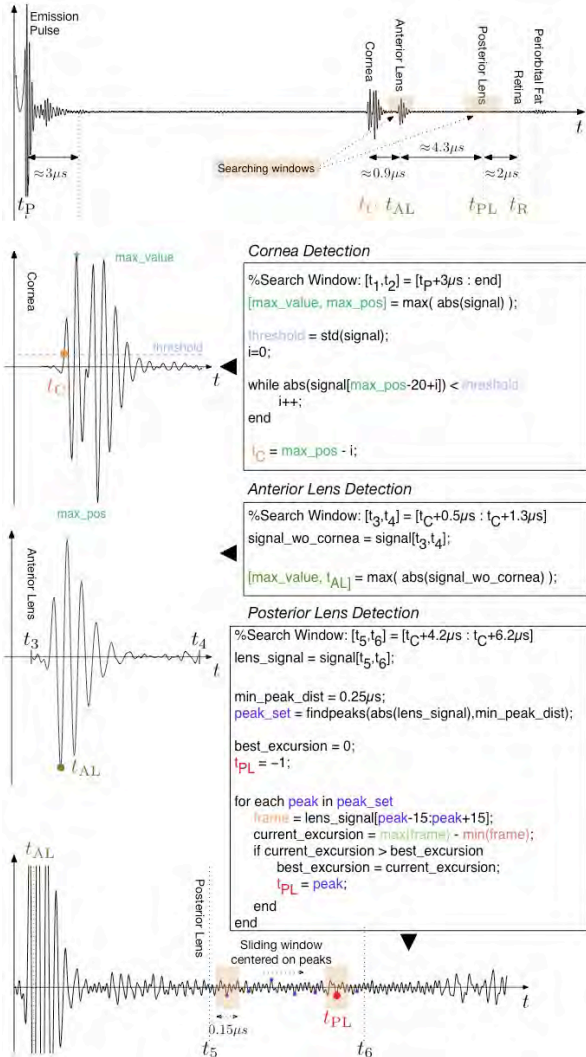


Fig. 5. Procedure for automatic detection of ocular interfaces in pseudo-code.

Taking t_C , the anterior lens interface detection is straightforward, being defined by the position of the maximum absolute value of the signal in the region $[t_C + 0.5 \mu s; t_C + 1.3 \mu s]$, which corresponds to a range of $0.9 \pm 0.4 \mu s$ (Fig. 5).

The posterior lens capsule echo presented low amplitude mainly due to attenuation, in some cases this amplitude is of the same order of magnitude of the noise. Therefore, a more elaborated searching method was developed. Thus, considering the search window $[t_C + 4.2 \mu s; t_C + 6.2 \mu s]$, according to [26] and [34], the signal peaks spaced at least by $0.25 \mu s$ were determined, where $0.25 \mu s$ relates to the length of the echo pulses, which are characterized by 5 cycles (20 MHz excitation signal). To apply this constraint, the `findpeaks` function, [38] chooses the taller peak (absolute value) of the search window and eliminates all peaks within $0.25 \mu s$ of it. Then, the function repeats the procedure for the tallest remaining peak and iterates until it runs out of peaks to consider. Next, a window with $0.15 \mu s$

(corresponding to 30 samples of the digitized A-scan signal) centered in each peak is set, and the signal excursion (difference between maximum and minimum) inside the window is calculated. The position of the peak whose window presents the highest signal excursion provided good estimation of the posterior lens capsule location. The algorithm here proposed, to automatically detect the low amplitude echoes from the posterior lens capsule addresses the challenge reported by several authors in the literature [39]–[41].

The developed methods allow the estimation of the corneal thickness, anterior and posterior chamber axial lengths, and lens thickness. The echoes originating from retina, choroid, and periorbital fat can be used to assess the eyeball axial length.

2) Features extraction

After signal filtering and automatic detection of the ocular interfaces, 27 features were extracted from the A-scan signals for each acquisition approach, in order to identify the presence of cataract and classify its severity.

Three types of features were extracted, listed in Table II: time domain features (f1 to f10); statistical time domain features (f11 to f19) and frequency derived features (f20 to f27). The time domain features were extracted directly from the A-scan signal and are explained in Fig. 6 and Table II. The statistical time domain features were extracted by applying a sliding rectangular window of $0.30 \mu s$ (60 samples) to the lens signal. The sliding window procedure was applied throughout the entire lens signal, excluding the anterior and posterior lens echoes (variable running time depending on lens size). Some measures, such as energy (f14), sample standard deviation (f15), RMS (f16), and SFM (Spectral Flatness Measure; the ratio of the geometric mean to the arithmetic mean of the frame samples), (f19), are taken from the signal frame that has the highest amplitude excursion, characterized by feature f12. The spectral centroid (f21) and 95% roll-off (f20) are measures usually taken for audio signals [42] and are evaluated through a Discrete Fourier Transform (DFT) of a frame. They represent the center of the spectral samples distribution, and the frequency below which 95% of the magnitude distribution is concentrated, respectively. The ratios described in f18-f21 are taken from the highest excursion frames in the anterior and posterior lens reflections. The frequency downshift (f22) and feature f27 are standard in ultrasound quantitative evaluation [43]. For their evaluation, the DFT was applied to the anterior and posterior lens frames and their peak spectral frequencies (f_{CA} and f_{CP} , respectively) were extracted. The frequency downshift is the difference of the peak values ($f_{CA} - f_{CP}$). To account for variations in lens size, feature f23 represents the frequency downshift (f22) divided by the lens propagation time (f1). The ratio of the anterior and posterior lens spectra represents the transfer function, from which the linear and quadratic fitting parameters (f24 to f26) are extracted. From the linear fitted slope, the attenuation (f27) can be computed according to [43].

To classify the cataract severity levels based on the 27 extracted features, for each averaged A-scan (the averaging buffer holds 20 A-scans) a feature vector was produced. For every 50 feature vectors, a final vector was computed by calculating the median value for each feature.

To optimize the classification performance the extracted features were subjected to a Principal Component Analysis (PCA) [44]. The PCA generates a new set of features, which is a linear combination of the original features. The number of generated components was defined such that 95% of the variance of the original data was explained.

TABLE II
EXTRACTED FEATURES DESCRIPTION

f1. Propagation time in the lens path, (d_5).
f2. Maximum absolute amplitude of the signal inside the lens, ($global_lens_max$).
f3. Propagation time until maximum absolute amplitude (f2) signal inside the lens, (max_idx).
f4. Normalized propagation time, f_3/f_1 , (max_idx_nor).
f5. Decaying time with a threshold of 80% of maximum amplitude, ($last_idx_abv_thr$).
f6. Maximum duration of an excursion of the absolute amplitude above the threshold, ($longest_seq_abv_thr$).
f7. The starting instant where feature f6 occurs, ($idx_longest_seq_abv_thr$).
f8. The cumulative duration of all excursions above the threshold, f6 included, ($total_abv_thr$).
f9. The area of the envelope above the threshold, ($area_abv_thr$).
f10. Maximum excursion of the signal inside the lens, ($global_lens_minmax$).
f11. Ratio of the standard deviation of the absolute value of the signal inside the lens by the standard deviation of the absolute value of the anterior lens reflection, ($global_lens_std$).
f12. Maximum signal excursion of the signal of all frames along the lens, (max_lens_minmax).
f13. Initial position (time) of the frame where f12 occurs, ($max_lens_frame_bg$).
f14. Energy of the frame where f12 occurs, (max_lens_energy).
f15. Standard deviation of the frame where f12 occurs, ($max_lens_standard_deviation$).
f16. Root-mean-square value of the frame where f12 occurs, (max_lens_RMS).
f17. The anterior to posterior lens amplitude ratio ($ a_1/a_2 $, see figure 6), ($Maximum_Lens_Amplitude_Ratio$).
f18. The ratio of kurtosis coefficients of the anterior and posterior lens reflections, (KC_Ratio).
f19. The ratio of spectral flatness measures of the posterior and anterior lens, (SFM_Ratio).
f20. The ratio of Roll-off 95% bandwidths of the anterior and posterior lens reflections, ($RO95_ratio$).
f21. The ratio of spectral centroids of the anterior and posterior lens reflections, ($Spectral_centroid_Ratio$).
f22. Frequency downshift from anterior to posterior lens reflections, ($Frequency_Downshift$).
f23. Central frequency deviation (f_{22}/f_1). This normalization factor eliminates the variations in the downshift induced by the natural variability in lens sizes, ($Norm_Freq_downshift$).
f24. The y-intercept value of the linear fitted transfer function, ($Linear_Fitting_Coefficient_a0$).
f25. The slope of the linear fitted transfer function, ($Linear_Fitting_Coefficient_a1$).
f26. Quadratic Fitting Coefficient (second order coefficient of the quadratic fitting of the transfer function), ($Quadratic_Fit_Coef_b2$).
f27. Attenuation coefficient value in the lens for 10 MHz, calculated according to the method defined in [43], ($Attenuation_db_mm_10MHz$).

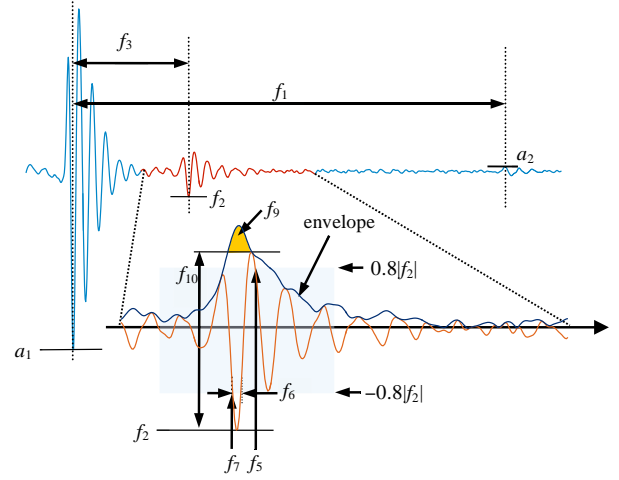


Fig. 6. Temporal features extraction from a lens echo signal. The signal in red indicates the presence of cataract. The labels f_i indicate features listed in Table II.

D. Machine learning techniques for automatic cataract classification

1) Classifiers

The 27 extracted features were used to train and test different classifiers in order to classify cataract into healthy, incipient, moderate, and severe. The following classifiers were tested: Bayes Network [45], Multilayer Perceptron (Neural Network) [46], Support Vector Machines (SVM) with a Radial Basis Function (RBF) kernel [47], and Random Forest [48]. For the SVM classifier a grid-search approach was used to optimize simultaneously the cost function C and the RBF Gamma parameter establishing a trade-off between the accuracy and the total number of support vectors [49].

For classifiers' training, a k -fold cross-validation was used with $k=10$; *i.e.*, the sample pool was divided into $k-1$ balanced sets, and at each iteration $k-1$ sets were used for training and the last set was used for testing. Afterwards, the performance of the classifiers was calculated taking the average performance of each fold. The metrics used to assess classifiers performance were the F-measure, accuracy, precision, sensibility and specificity.

2) Data analysis

A Spearman correlation was used to assess correlations between the lens thickness and the rats' age, and for correlations between the nucleus hardness and the extracted features.

To assess the agreement between acquisitions performed *in-vivo*, *post-mortem*, and *ex-vivo*, the Intraclass Correlation Coefficient (ICC) for these 3 acquisitions was computed for the extracted features.

Statistically significant differences between lenses without cataract (controls), and lenses with cataract (incipient, moderate and severe) were tested for the extracted features using ANOVA. For statistically significant differences between lenses hardness measured

by NanoTest™ [36] and the cataract severity, the Kruskal-Wallis test was used.

PCA and classification were performed with the Waikato Environment for Knowledge Analysis (WEKA) software [50], and the statistical analyses were performed in IBM SPSS Statistics version 22.0 (IBM Corp. in Armonk, NY).

Results were considered statistically significant for P-values < 0.05.

III. RESULTS

A. Animal model for nuclear cataract

The three different nuclear cataract degrees (incipient, moderate, and severe) were observed in the 36 rats injected before eyes opening, however most of them developed moderate or severe cataract. Thus, for the rats injected with low concentration of sodium selenite (20 $\mu\text{mol/kg}$), only one developed incipient cataract, and the other five presented moderate cataract. Concerning to the 25 $\mu\text{mol/kg}$ concentration, five rats developed severe cataract and only one presented moderate cataract. All the rats injected with high concentration of sodium selenite (30 $\mu\text{mol/kg}$) developed severe cataract. Only incipient and moderate cataracts were observed in the rats injected after eye opening. In particular, for low concentration of sodium selenite (20 $\mu\text{mol/kg}$), the rats developed incipient cataract. For the 25 $\mu\text{mol/kg}$ concentration, five rats developed also incipient cataract and one developed moderate cataract. All the rats injected with 30 $\mu\text{mol/kg}$ developed moderate cataract.

The used cataract induction model produced 12 rats with incipient cataract, 13 rats with moderate cataract, and 11 rats with severe cataract.

No statistically significant differences were found between the different cataract degrees and age ($P=0.050$).

B. Rats' eye characterization

The 50 rats (14 healthy and 36 with nuclear cataract) lens thickness ranged from 3.06 mm to 4.28 mm (mean \pm standard-deviation: 3.52 ± 0.49 , Table III), which is in accordance with the results found in the literature [37], where a 3.71 mm mean value was proposed for rats with a mean age of 4.2 months. An association between lens thickness and rats age over 2 months was proposed by [39]. In this study only a weak correlation was found between the lens thickness and the rats' age ($R=0.397$; $P<0.001$).

The rat's eye axial length, the corneal thickness, the anterior and posterior chambers' axial lengths and the lens thickness were estimated *in-vivo* using the ultrasound pulse-echo signals. A mean velocity of 1600 m/s for healthy lenses and 1650 m/s for cataractous lenses was considered based on the results obtained in porcine eyes by Caixinha *et al.*, [26]. The results for the eye axial length measured *ex-vivo* and estimated *in-vivo*, using the propagation time and velocity, are presented in Table III. It was not possible *ex-vivo* obtaining accurate measurements for the corneal thickness, as well as for the anterior and posterior chambers' axial lengths, (values missing in Table III).

TABLE III
RAT'S EYE DIMENSIONS

	Measured <i>ex-vivo</i>	Estimated <i>in-vivo</i>	Hughes [37]
Corneal thickness (mm)	-	0.20 ± 0.02	0.26 ± 0.002
Lens thickness (mm)	3.52 ± 0.49	3.54 ± 0.01	3.71 ± 0.05
Axial length (mm)			
Anterior chamber	-	0.74 ± 0.09	0.62
Posterior chamber	-	1.69 ± 0.19	1.39
Eye	5.88 ± 0.45	6.23 ± 0.20	6.29 ± 0.04

C. Lens hardness measurement

The hardness of the cortex and nucleus regions was measured for the different cataract degrees using the NanoTest™. To confirm that the indentations were carried out in the correct region of the lens, each slice was previously observed with optical microscopy (LEICA DM 400 M LED, 2013). After the tests, the indentation images were acquired with the same equipment (Fig. 7).

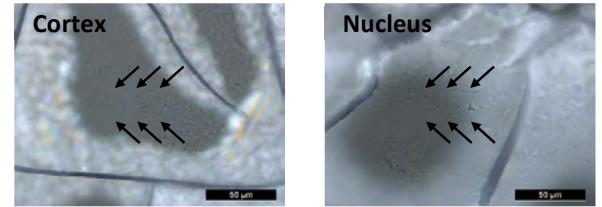


Fig. 7. Slice images of lenses with severe cataract. The arrows identify the indentation locations.

A statistically significant difference was found for the hardness of the different nuclear cataracts in the cortex and the nucleus regions ($P=0.016$; Table IV). The results showed an increase of the lens hardness with cataract formation in the cortex and the nucleus regions. Also, as expected the nucleus region presented higher hardness than the cortex region for all nuclear cataract degrees. The nucleus region showed a higher hardness increase with the cataract severity ($P=0.049$). Moreover, even for the healthy lenses (without cataract), the nucleus region presented a higher hardness than the cortex (Table IV).

A moderate correlation was found between the lens hardness and the rats mean age ($R=0.597$, $P=0.003$ for the nucleus, and $R=0.474$, $P=0.022$ for the cortex).

TABLE IV
HARDNESS MEASURED BY NANOTEST™ FOR HEALTHY LENSES AND LENSES WITH DIFFERENT CATARACT DEGREES

	Cortex	Nucleus
Healthy (GPa)	0.136 ± 0.003	0.156 ± 0.005
Incipient (GPa)	0.159 ± 0.004	0.195 ± 0.009
Moderate (GPa)	0.183 ± 0.004	0.228 ± 0.014
Severe (GPa)	0.199 ± 0.004	0.264 ± 0.009

D. Features analysis

1) Agreement between acquisitions

Overall, a good agreement was found between the extracted features obtained *in-vivo*, *post-mortem* and *ex-vivo*. Twenty-six out of the 27 features showed a fair to excellent agreement ($ICC \geq 0.400$) between the *in-vivo* and *post-mortem* acquisitions. The agreement between the *in-*

vivo and *ex-vivo* extracted features was fair to excellent ($ICC \geq 0.400$) in 24 out of the 27 features. Since the eye movements and probe misalignment do not significantly affect the features extracted *in-vivo* only *in-vivo* results are presented hereinafter.

2) *In-vivo* results

All the 27 *in-vivo* extracted features showed a statistically significant difference between healthy and different nuclear cataract degrees, and between different cataract degrees (incipient, moderate and severe cataract), ($P < 0.01$).

In particular, for the acoustical parameters frequently used in tissue characterization as the propagation velocity and attenuation [28], [41], [51]–[53], it was verified that the wave propagation time decreased from $4.31 \pm 0.02 \mu s$ to $3.93 \pm 0.11 \mu s$ in healthy and severe cataract lenses, respectively ($P < 0.001$; Fig. 8), meaning that the velocity increases with the cataract severity, in spite of the lens thickness variation ($3.52 \pm 0.49 \text{ mm}$). Concerning to the attenuation, it increased from $2.78 \pm 0.60 \text{ dB/mm}$ to $5.50 \pm 2.25 \text{ dB/mm}$ in healthy and severe cataract lenses, respectively, ($P < 0.001$; Fig. 9).

The observed increase in the propagation velocity and frequency dependent attenuation with the cataract severity is in accordance with the results obtained in a previous study carried out in porcine lenses [26].

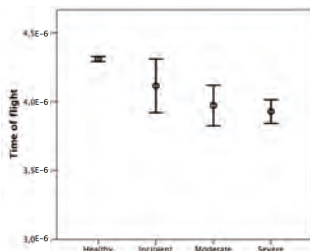


Fig. 8. Wave propagation time in lenses with different cataract degrees (mean±1SD).

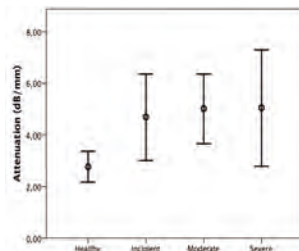


Fig. 9. Attenuation coefficient in lenses with different cataract degrees (mean±1SD).

An interesting parameter to infer about the tissue microstructure changing is the frequency downshift of signals. It was observed a frequency shifting of $1.04 \pm 0.51 \text{ MHz}$ for the healthy lenses and $1.97 \pm 0.62 \text{ MHz}$ for the lenses with severe cataract ($P < 0.001$; Fig. 10).

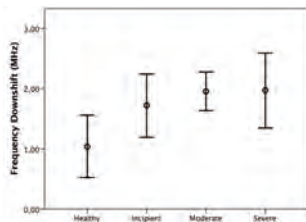


Fig. 10. Frequency downshift in healthy and cataractous lenses (mean±1SD).

Moreover, a moderate to good correlation between the selected features and the nucleus hardness for the different

cataract severity levels was found in 23 out of the 27 features (Fig. 11).

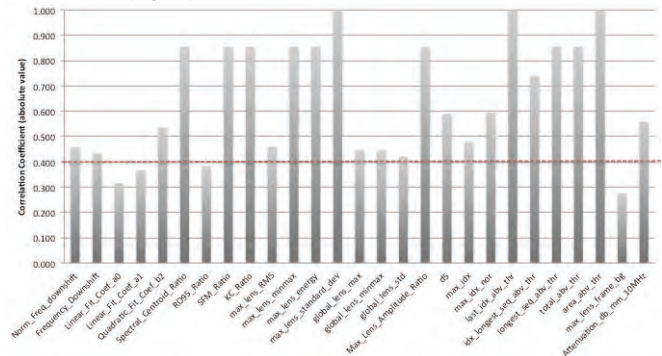


Fig. 11. Correlation coefficient between the nucleus hardness and the extracted features *in-vivo*.

E. Automatic classification of cataract severity

The classifiers performance for the different cataract degrees is shown in Table V and Table VI. All classifiers presented a good performance when classifying lenses into healthy and cataractous (incipient, moderate, and severe). Considering the 27 extracted features the F-measure ranged from 0.946 to 0.997 for the Bayes and SVM classifiers, respectively. The SVM is the one that showed higher performance with a sensitivity and specificity both of 0.997, and with a relative absolute error of 0.4% (Table V).

The features optimization process using the PCA led to 12 components, which accounted for 95.1% of the cumulative variance of the features. For those 12 components the F-measure ranged from 0.803 to 0.992 for the Bayes and SVM classifiers, respectively. Again, the SVM is the one that showed higher performance with a sensitivity and specificity both of 0.992, and with a relative absolute error of 1.1% (Table VI).

TABLE V
PERFORMANCE OF THE DIFFERENT CLASSIFIERS USING THE SELECTED 27 FEATURES (RAE – RELATIVE ABSOLUTE ERROR, RF – RANDOM FOREST, MP - MULTILAYER PERCEPTRON)

	F-		Precision	Sensitivity	Specificity
	RAE	Measure			
SVM	0.4%	0.997	0.997	0.997	0.997
Bayes	8.0%	0.946	0.946	0.946	0.946
RF	6.5%	0.996	0.996	0.996	0.996
MP	5.9%	0.967	0.967	0.967	0.967

TABLE VI
PERFORMANCE OF THE DIFFERENT CLASSIFIERS USING THE 12 COMPONENTS OBTAINED BY PCA (RAE – RELATIVE ABSOLUTE ERROR, RF – RANDOM FOREST, MP - MULTILAYER PERCEPTRON)

	F-		Precision	Sensitivity	Specificity
	RAE	Measure			
SVM	1.1%	0.992	0.992	0.992	0.992
Bayes	33.3%	0.803	0.804	0.804	0.804
RF	11.2%	0.988	0.988	0.988	0.988
MP	14.3%	0.916	0.916	0.916	0.916

IV. DISCUSSION

A. Animal model

In this study the hypothesis that the administration of different concentrations of sodium selenite in rats with

different eye maturation periods (before and after eyes opening) produces different nuclear cataract degrees was tested and experimentally confirmed. The animal model considered for cataract induction is identified in the literature as the model that better mimics what happens in humans for age related cataract [29], [30]. The modified model presented in this study proved to be the most appropriated one, since it allowed obtaining different severity degrees of nuclear cataract. The produced cataract hardness as well as the healthy lens hardness were objectively measured in two regions (nucleus and cortex) by using the NanoTest™, for the first time. The authors, objectively showed that the nucleus hardness is higher than the cortex, which is in agreement with the microanatomy of vertebrate lenses [54]. As the nuclear cataract severity increased it was also observed a hardness increase in the cortical region, being that increase more pronounced in the nucleus region ($P=0.049$).

B. Automatic detection of ocular interfaces.

Algorithms were developed for the automatic detection of the ocular boundaries using the eye collected signals. Such allowed determining the eyeball axial length, lens thickness, the corneal thickness and the anterior and posterior chambers' axial lengths. Several authors reported difficulties in lens thickness estimation namely in the posterior capsule echo location [39]–[41]. To overcome this challenge, a new two-stage method has been proposed in section II.C-1), that comprises peak detection in posterior lens region, followed by signal excursion evaluation on the vicinity of the marked peaks. The diameter values found for the anteroposterior lens and for the anteroposterior eye are in agreement with those measured experimentally with a caliper as well as with the ones published by Hughes *et al.* [37]. The estimated values for the corneal thickness and for the anteroposterior diameters (front and rear chambers) are also in agreement with the ones published in [37]. Thus, the strategy followed by the authors makes possible the use of high frequencies for biometric evaluation of ocular structures with improved resolution.

C. Extracted features

All the 27 features showed a statistically significant difference between the different cataract severity levels. Particularly, the acoustical parameters frequently used in tissue characterization, velocity (propagation time) and attenuation [28], [41], [51]–[53], both presented a remarkable increase with nuclear cataract formation in accordance with a recent study carried out by the authors using *ex-vivo* porcine lenses (with cataract induced by lens immersion in an ethanol:2-propanol:formalin solution) [26]. The frequency downshift of signals demonstrated also to be a good metric for severity cataract evaluation. It was observed a frequency shifting of 1.04 ± 0.51 MHz for the healthy lenses and 1.97 ± 0.62 MHz for the lenses with severe cataract indicating that the higher frequencies are heavily attenuated with cataract formation.

A moderate to good correlation was found between the nucleus hardness for the different cataract severity levels

and the selected features, demonstrating that the extracted features can be used to estimate *in-vivo* and noninvasively the nuclear cataract hardness.

D. Automatic cataract classification

All the tested classifiers showed a performance higher than 95% for the automatic classification of the cataract severity. The SVM should be chosen because is the one with the lowest classification error (0.4%), and the better performance, with a sensitivity and specificity both of 0.997. For the 12 components obtained by the PCA the SVM showed also the best performance with a sensitivity and specificity both of 0.992, and a relative absolute error of 1.1%. However, the data dimensionality reduction provided by the PCA did not improve the classification performance.

V. CONCLUSIONS

In this study, an animal model was developed for nuclear cataract induction, which allowed obtaining different cataract degrees *in-vivo*. Furthermore, this model allowed for the objective hardness measurement of the lens tissue in the different conditions of cataract severity.

New methodologies were also developed and tested for the characterization of hardness in healthy and pathological stages of the nuclear cataract formation, as an important biomechanical property of the lens tissue.

Experimental measurements carried out in the lens tissue showed that the hardness of the nucleus is higher than the cortex and its value increases with the severity of the cataract in those two regions.

The objective assessment of hardness in different regions of healthy and cataractous lens is presented for the first time.

The correlation results between the acoustical parameters and the measured hardness demonstrated that the lens hardness can be estimated noninvasively.

The agreement between the acquired data *in-vivo* and *post-mortem* showed that the fluctuations induced by eye movements, do not significantly affect the classification results. Concerning to the *in-vivo* and *ex-vivo* signal acquisitions it was shown that the *in-vivo* signals are not significantly affected by the probe free-hand, indicating that the developed setup for the *in-vivo* cataract detection and classification is valid.

The authors also demonstrated that the use of high frequency ultrasounds with accurate processing signal methodologies enables the early nuclear cataract detection and classification. The application of machine learning techniques allowed for the classification of cataract severity with a performance of 99.7%.

As future work, the authors intend to develop a medical prototype for early cataract detection, classification and respective hardness estimation, using the results of this work.

ACKNOWLEDGMENT

This work was supported by FEDER funds through the program COMPETE—Operational Program for

Competitiveness Factors—by national funds through Foundation for Science and Technology (FCT), under the Project PTDC/DTP-PIC/0419/2012—and by Instituto de Telecomunicações PEst-UID/EEA/50008/2013 (pluriannual funding)—and under the Project PEst-C/EME/UI0285/2013.

References

- [1] H. Ecroyd and J. Carver, "Crystallin proteins and amyloid fibrils," *Cell. Mol. Life Sci.*, vol. 66, no. 1, pp. 62–81, Jan. 2009.
- [2] J. Kanski, *Clinical diagnosis in ophthalmology*, 1st ed. Philadelphia: Elsevier Mosby, 2007.
- [3] A. Coombes and D. Gartry, *Fundamentals of Clinical Ophthalmology: Cataract Surgery*, BMJ Publis. London, 2003.
- [4] American Academy of Ophthalmology Cataract and Anterior Segment Panel, "Preferred Practice Pattern Guidelines. Cataract in the Adult Eye.," San Francisco, CA, 2011.
- [5] American Optometric Association, "Care of the Adult Patient with Cataract," St Louis, MO, 2004.
- [6] R. Yeoh, "Practical differences between 3 femtosecond phaco laser platforms," *J. Cataract Refract. Surg.*, vol. 40, no. 3, p. 510, 2014.
- [7] I. H. Fine, M. Packer, and R. S. Hoffman, "New phacoemulsification technologies," *J. Cataract Refract. Surg.*, vol. 28, no. 6, pp. 1054–60, Jun. 2002.
- [8] R. Venkatesh, C. S. H. Tan, S. Sengupta, R. D. Ravindran, K. T. Krishnan, and D. F. Chang, "Phacoemulsification versus manual small-incision cataract surgery for white cataract," *J. Cataract Refract. Surg.*, vol. 36, no. 11, pp. 1849–1854, 2010.
- [9] I. Fine, M. Packer, and R. Hoffman, "Power modulations in new phacoemulsification technology: Improved outcomes," *J. Cataract Refract. Surg.*, vol. 30, pp. 1014–1019, 2004.
- [10] I. H. Fine, M. Packer, and R. S. Hoffman, "Use of power modulations in phacoemulsification Choo-choo chop and flip phacoemulsification," in *Symposium on Cataract, IOL and Refractive Surgery*, 1998, vol. 3350, no. 00.
- [11] M. Wilson, R. Trivedi, and P. S., Eds., *Pediatric Cataract Surgery: Techniques, Complications, and Management*. Lippincott Williams & Wilkins, 2005.
- [12] R. Abell, N. Kerr, A. Howie, M. Mustafa Kamal, P. Allen, and B. Vote, "Effect of femtosecond laser-assisted cataract surgery on the corneal endothelium," *J. Cataract Refract. Surg.*, vol. 40, no. 11, pp. 1777–1783, 2014.
- [13] M. C. Leske, L. T. Chylack, R. Sperduto, P. Khu, S. Y. Wu, and D. McCarthy, "Evaluation of a Lens Opacities Classification System.," *Arch. Ophthalmol.*, vol. 106, no. 3, pp. 327–9, Mar. 1988.
- [14] L. T. Chylack, M. C. Leske, D. McCarthy, P. Khu, T. Kashiwagi, and R. Sperduto, "Lens opacities classification system II (LOCS II)," *Arch. Ophthalmol.*, vol. 107, no. 7, pp. 991–7, Jul. 1989.
- [15] L. Chylack and J. Wolfe, "The lens opacities classification system III," *Arch.*, vol. 111, pp. 831–836, 1993.
- [16] J. M. Sparrow, A. J. Bron, N. A. Brown, W. Ayliffe, and A. R. Hill, "The Oxford Clinical Cataract Classification and Grading System.," *Int. Ophthalmol.*, vol. 9, no. 4, pp. 207–25, Dec. 1986.
- [17] S. K. West, F. Rosenthal, H. S. Newland, and H. R. Taylor, "Use of photographic techniques to grade nuclear cataracts.," *Invest. Ophthalmol. Vis. Sci.*, vol. 29, no. 1, pp. 73–7, Jan. 1988.
- [18] B. E. Klein, Y. Magli, M. W. Neider, and R. Klein, "Wisconsin system for classification of cataracts from photographs," 1989.
- [19] B. E. Klein, R. Klein, and K. L. Linton, "Prevalence of age-related lens opacities in a population. The Beaver Dam Eye Study.," *Ophthalmology*, vol. 99, no. 4, pp. 546–52, Apr. 1992.
- [20] B. Thylefors, L. T. Chylack, K. Konyama, K. Sasaki, R. Sperduto, H. R. Taylor, and S. West, "A simplified cataract grading system.," *Ophthalmic epidemiology*, vol. 9, no. 2, pp. 83–95, Apr-2002.
- [21] L. T. Chylack, J. K. Wolfe, D. M. Singer, M. C. Leske, M. A. Bullimore, I. L. Bailey, J. Friend, D. McCarthy, and S. Y. Wu, "The Lens Opacities Classification System III. The Longitudinal Study of Cataract Study Group.," *Arch. Ophthalmol.*, vol. 111, no. 6, pp. 831–6, Jun. 1993.
- [22] J. Panchapakesan, R. G. Cumming, and P. Mitchell, "Reproducibility of the Wisconsin cataract grading system in the Blue Mountains Eye Study," *Ophthalmic Epidemiol.*, vol. 4, no. 3, pp. 119–126, 1997.
- [23] J. a Davison and L. T. Chylack, "Clinical application of the lens opacities classification system III in the performance of phacoemulsification," *J. Cataract Refract. Surg.*, vol. 29, no. 1, pp. 138–145, Jan. 2003.
- [24] X. Gao, D. W. K. Wong, T.-T. Ng, C. Y. L. Cheung, C.-Y. Cheng, and T. Y. Wong, "Automatic grading of cortical and PSC cataracts using retroillumination lens images," *Comput. Vis. – ACCV 2012*, vol. 7725, pp. 256–267, Nov. 2013.
- [25] J. Kirwan, L. Venter, A. Stulting, and I. Murdoch, "LOCS III examination at the slit lamp, do settings matter?," *Ophthalmic Epidemiology*, pp. 259–266, Oct-2003.
- [26] M. Caixinha, D. Jesus, E. Velte, M. Santos, and J. Santos, "Using ultrasound backscattering signals and Nakagami statistical distribution to assess regional cataract hardness," *IEEE Trans. Biomed. Eng.*, vol. PP, no. 99, 2014.
- [27] M. Caixinha, E. Velte, M. Santos, and J. B. Santos, "New approach for objective cataract classification based on ultrasound techniques using multiclass SVM classifiers," in *2014 IEEE International Ultrasonics Symposium*, 2014, pp. 2402–2405.
- [28] C. Huang, H. Ameri, C. Deboer, A. Rowley, X. Xu, L. Sun, S. Wang, M. Humayun, and K. Shung, "Evaluation of lens hardness in cataract surgery using high-frequency ultrasonic parameters in vitro.," *Ultrasound Med. Biol.*, vol. 33, no. 10, pp. 1609–16, Oct. 2007.
- [29] T. R. Shearer, H. Ma, C. Fukiage, and M. Azuma, "Selenite nuclear cataract: review of the model.," *Mol. Vis.*, vol. 3, no. June, p. 8, Jul. 1997.
- [30] Z. Kyselova, "Different experimental approaches in modelling cataractogenesis: An overview of selenite-induced nuclear cataract in rats.," *Interdiscip. Toxicol.*, vol. 3, no. 1, pp. 3–14, Mar. 2010.
- [31] I. Ošťádalová, a. Babický, and J. Obenberger, "Cataract induced by administration of a single dose of sodium selenite to suckling rats," *Experientia*, vol. 34, no. 2, pp. 222–223, 1978.
- [32] V. M. Berthoud and E. C. Beyer, "Oxidative stress, lens gap junctions, and cataracts.," *Antioxid. Redox Signal.*, vol. 11, no. 2, pp. 339–53, Feb. 2009.
- [33] D. C. Beebe, N. M. Holekamp, and Y.-B. Shui, "Oxidative damage and the prevention of age-related cataracts.," *Ophthalmic Res.*, vol. 44, no. 3, pp. 155–65, Jan. 2010.
- [34] L. Li, J. Duker, Y. Yoshida, and E. Niki, "Oxidative stress and antioxidant status in older adults with early cataract," *Eye*, vol. 23, no. 6, pp. 1464–1468, 2008.
- [35] R. Yağcı, B. Aydın, M. Erdurmuş, R. Karadağ, A. Gürel, M. Durmuş, and R. Yiğitoğlu, "Use of melatonin to prevent selenite-induced cataract formation in rat eyes.," *Curr. Eye Res.*, vol. 31, no. 10, pp. 845–850, 2006.
- [36] N. Panich and S. Yong, "Improved method to determine the hardness and elastic modulus using nanoindentation," *KMITL Sci. J.*, vol. 5, no. 2, pp. 483–492, 2005.
- [37] A. Hughes, "A schematic eye for the rat," *Vision Res.*, 1979.
- [38] MathWorks Inc, "Signal Processing Toolbox™ User's Guide R2015b," *MathWorks Inc*, 2015. [Online]. Available: <http://www.mathworks.co.uk/products/signal/index.html>.
- [39] D. C. Lozano and M. D. Twa, "Development of a rat schematic eye from in vivo biometry and the correction of lateral magnification in SD-OCT imaging.," *Invest. Ophthalmol. Vis. Sci.*, vol. 54, no. 9, pp. 6446–55, Sep. 2013.
- [40] J. A. Guggenheim, R. C. Creer, and X.-J. Qin, "Postnatal refractive development in the Brown Norway rat: Limitations of standard refractive and ocular component dimension measurement techniques," *Curr. Eye Res.*, vol. 29, no. 4–5, pp. 369–376, 2004.
- [41] A. Paunksnis, S. Kurapkienė, and A. Mačiulis, "Ultrasound quantitative evaluation of human eye cataract," *Informatika*, vol. 18, no. 2, pp. 267–278, 2007.

- [42] F. Eyben, M. Wöllmer, and B. Schuller, "openSMILE - The Munich Versatile and Fast Open-Source Audio Feature Extractor," in *ACM Multimedia (MM)*, 2010, pp. 1459–1462.
- [43] J. B. Santos, "The power of ultrasonic spectroscopy in the complete characterisation of materials," *Insight Non-Destructive Test. Cond. Monit.*, vol. 40, no. 12, pp. 855–859, 1998.
- [44] I. Guyon and A. Elisseeff, "An introduction to variable and feature selection," *J. Mach. Learn. Res.*, vol. 3, pp. 1157–1182, 2003.
- [45] R. R. Bouckaert, "Bayesian Network Classifiers in Weka," Department of Computer Science, The University of Waikato, 2004.
- [46] S. K. Pal and S. Mitra, "Multilayer perceptron, fuzzy sets, and classification," *IEEE Trans. Neural Networks*, vol. 3, no. 5, pp. 683–697, 1992.
- [47] C.-C. Chang and C.-J. Lin, "LIBSVM: A Library for Support Vector Machines," *ACM Trans. Intell. Syst. Technol.*, vol. 2, pp. 27:1–27:27, 2011.
- [48] A. Jain, R. Duin, and J. Mao, "Statistical Pattern Recognition: A Review," *IEEE Trans. Pattern Anal. Mach. Intell.*, vol. 22, no. 1, pp. 4–37, 2000.
- [49] C.-W. Hsu, C.-C. Chang, and C.-J. Lin, "A Practical Guide to Support Vector Classification," Taipei, Taiwan, 2010.
- [50] M. Hall, E. Frank, G. Holmes, B. Pfahringer, P. Reutemann, and I. H. Witten, "The WEKA data mining software," *ACM SIGKDD Explor.*, vol. 11, no. 1, pp. 10–18, 2009.
- [51] C. Huang, Q. Zhou, H. Ameri, W. Wu, L. Sun, S. Wang, M. Humayun, and K. Shung, "Determining the acoustic properties of the lens using a high-frequency ultrasonic needle transducer," *Ultrasound Med. Biol.*, vol. 33, no. 12, pp. 1971–7, Dec. 2007.
- [52] H. Tabandeh, M. Wilkins, G. Thompson, D. Nassiri, and A. Karim, "Hardness and ultrasonic characteristics of the human crystalline lens," *J. Cataract Refract. Surg.*, vol. 26, no. 6, pp. 838–41, Jun. 2000.
- [53] R. Raitelaitienė and A. Paunksnis, "Ultrasonic and biochemical evaluation of human diabetic lens," *Med.*, vol. 41, no. 8, 2005.
- [54] Y. Shi, K. Barton, A. De Maria, J. M. Petrash, A. Shiels, and S. Bassnett, "The stratified syncytium of the vertebrate lens," *J. Cell Sci.*, vol. 122, no. Pt 10, pp. 1607–1615, 2009.



Machine Learning Techniques in Clinical Vision Sciences

Miguel Caixinha & Sandrina Nunes

To cite this article: Miguel Caixinha & Sandrina Nunes (2016): Machine Learning Techniques in Clinical Vision Sciences, Current Eye Research

To link to this article: <http://dx.doi.org/10.1080/02713683.2016.1175019>



Published online: 30 Jun 2016.



Submit your article to this journal [↗](#)



View related articles [↗](#)



View Crossmark data [↗](#)

Machine Learning Techniques in Clinical Vision Sciences

Miguel Caixinha^{a,b} and Sandrina Nunes^{c,d}

^aDepartment of Physics, Faculty of Sciences and Technology, University of Coimbra, Coimbra, Portugal; ^bDepartment of Electrical and Computer Engineering, Faculty of Sciences and Technology, University of Coimbra, Coimbra, Portugal; ^cFaculty of Medicine, University of Coimbra, Coimbra, Portugal; ^dCoimbra Coordinating Centre for Clinical Research, Association for Innovation and Biomedical Research on Light and Image, Coimbra, Portugal

ABSTRACT

This review presents and discusses the contribution of machine learning techniques for diagnosis and disease monitoring in the context of clinical vision science. Many ocular diseases leading to blindness can be halted or delayed when detected and treated at its earliest stages. With the recent developments in diagnostic devices, imaging and genomics, new sources of data for early disease detection and patients' management are now available. Machine learning techniques emerged in the biomedical sciences as clinical decision-support techniques to improve sensitivity and specificity of disease detection and monitoring, increasing objectively the clinical decision-making process. This manuscript presents a review in multimodal ocular disease diagnosis and monitoring based on machine learning approaches. In the first section, the technical issues related to the different machine learning approaches will be present. Machine learning techniques are used to automatically recognize complex patterns in a given dataset. These techniques allows creating homogeneous groups (unsupervised learning), or creating a classifier predicting group membership of new cases (supervised learning), when a group label is available for each case. To ensure a good performance of the machine learning techniques in a given dataset, all possible sources of bias should be removed or minimized. For that, the representativeness of the input dataset for the true population should be confirmed, the noise should be removed, the missing data should be treated and the data dimensionally (i.e., the number of parameters/features and the number of cases in the dataset) should be adjusted. The application of machine learning techniques in ocular disease diagnosis and monitoring will be presented and discussed in the second section of this manuscript. To show the clinical benefits of machine learning in clinical vision sciences, several examples will be presented in glaucoma, age-related macular degeneration, and diabetic retinopathy, these ocular pathologies being the major causes of irreversible visual impairment.

ARTICLE HISTORY

Received 20 October 2015
Revised 14 March 2016
Accepted 24 March 2016

KEYWORDS

Automated diagnosis;
clinical research; machine
learning; pattern
recognition; vision sciences

Introduction

Many ocular diseases leading to blindness, such as glaucoma, age-related macular degeneration (AMD), and diabetic retinopathy (DR) can be halted or delayed when detected and treated in its earliest stages.¹

With the recent developments in diagnostic devices, imaging, and genomics, new sources of data for early disease detection and patients' management are now available.

However, to handle the amount of multimodal data for clinical decisions' support, new strategies such as machine learning are required.

Machine learning emerged in the biomedical sciences as a clinical decision-support technique to improve sensitivity and specificity of disease detection and monitoring, increasing objectively the clinical decision-making process.

Machine learning techniques represents a tool to analyze high-dimensional and high-complex medical datasets, allowing incorporation of multimodal data, prior knowledge, and noise reduction.^{2,3}

This manuscript is a review of the literature in multimodal ocular disease diagnosis and monitoring, based on machine learning approaches. Data pre-processing, learning

algorithms, and performance assessment are discussed. The applications of these approaches for diagnosis and monitoring are presented in different ocular diseases. Special attention will be given to glaucoma, AMD, and DR, these three ocular diseases being the major causes of irreversible visual impairment in the World.⁴

Machine learning approaches

The purpose of machine learning techniques is to automatically recognize complex patterns in a given dataset, allowing therefore for inference or prediction in new datasets.⁵

Machine learning techniques allow for the identification of homogeneous groups in the input dataset (unsupervised learning). When a group or category label is available for each case (supervised learning), machine learning techniques allow for the creation of a classifier, or a regression function, predicting the category membership of new cases (Figure 1). In order to ensure a good performance of the machine learning techniques in a given dataset, all possible sources of bias should be identified, removed or minimized. Therefore, before any machine learning process, the representativeness

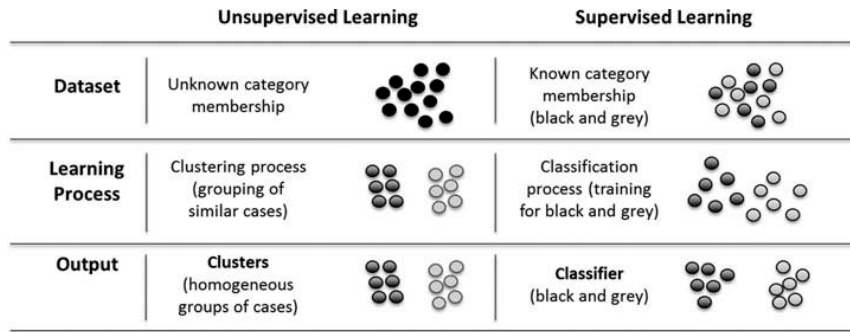


Figure 1. Illustration of the two machine learning approaches, the unsupervised approach, when the category membership is unknown, and the supervised approach, when the category membership is known.

of the input dataset for the true population (i.e., the population under study) should be confirmed, the noise should be removed, the missing data should be treated, and the data dimensionally (i.e., the number of parameters/features and the number of cases in the dataset) should be adjusted.

Data pre-processing

Noise and highly correlated data, or spurious data, which raise from high-dimensional and high-complex datasets, may impair the machine learning performance. To reduce bias, the input dataset should undergo through a “cleaning process”, or data pre-processing, to remove noise, normalize data, treat missing data, and select, or extract relevant data (features).⁶⁻⁸ Figure 2 illustrates the different data pre-processing steps.

Noise reduction: Noise reduction should be performed in data where noise is expected, such as data generated by procedures in which the acquisition processes are prone to noise, e.g., images obtained by Optical Coherence Tomography (OCT).⁹ Presently, most of the manufacturers already apply a noise

reduction algorithm in their equipment to reduce noise. Two approaches are proposed in the literature for noise reduction, the model-based and the heuristic approaches. In the model-based approaches, a noise model is created, requiring therefore an *a priori* knowledge of the noise characteristics, e.g., noise sources and signals. Heuristic approaches, on the other hand, do not require an *a priori* noise model, being therefore the more frequently used approaches. Heuristic approaches are usually based on filters, examples are:^{2,6}

- moving average filters (smoothen the data by averaging sub-samples of the dataset);
- median filters (smoothen the data by considering the median value of sub-samples of the dataset);
- Gaussian filters (modified the input data by performing a convolution, i.e., a mathematical operation between two functions, with a Gaussian function);
- wavelet filters (modified the input data by performing a convolution with a wavelet series); and
- deconvolution filters (modifies the input data based on prior knowledge of the acquisition systems’ characteristics, for example, point spread function and noise statistics).

Data normalization: When analyzing data collected from different sources, the data measured on different scales should be adjusted to a common scale (e.g., if we want to consider simultaneously the age in years and the height in cm, both parameters need to have a similar order of magnitude). Data normalization can be achieved using statistical metrics such as the average, median, maximal value, range, or standard-deviation of the data, or by performing a data transformation using for example, a mathematical function, such as the logarithm function. The data transformation will depend on the nature and the behavior of the data under analysis.

Missing data: Missing data occur due mainly to acquisition failures, non-answers, or incorrect data entry. Missing data randomness should be first specified, namely, if data are missing completely at random, just missing at random or missing not at random.^{10,11} Two approaches can be followed to handle missing data, one based on data deletion, and another based on data imputation. Deletion approaches can be listwise, i.e., omitting completely from the analyses the cases with missing values

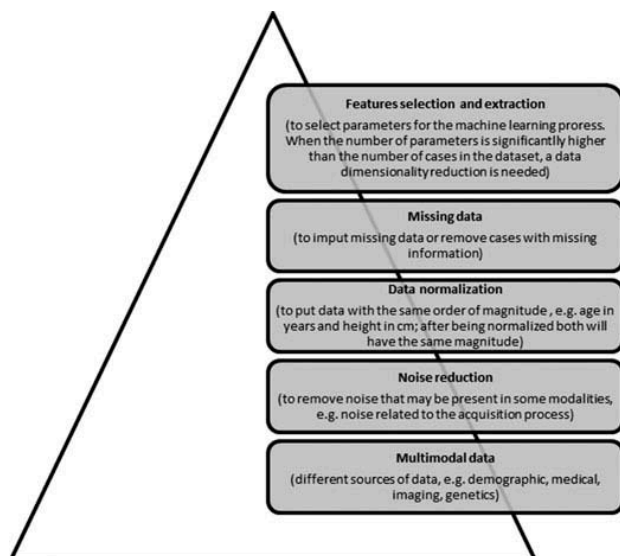


Figure 2. Steps of the data pre-processing (data cleaning process).

(reducing the sample size), or pairwise when only the missing values are omitted from the analysis (keeping the sample size, but creating different sets for data analyses). In the imputation approaches, missing values are replaced by the mean values, or by other estimated values obtained by a regression analysis, or by a maximum likelihood estimation approach.

Feature selection and extraction: To select the most relevant features reducing the data dimensionality, features are usually selected, and in some cases extracted (i.e., the transformation of the features set into a smaller and relevant set), improving therefore the learning process performance.^{2,3,6,7,7,12-14} The ratio of the number of cases/elements in the dataset (n) to the number of parameters/features (f) is frequently used to estimate the risk of bias by overtraining. A n/f ratio over 10 is usually recommended.^{6,8,15} In order to reduce data dimensionality and obtain a new dataset corrected, ordered, and/or simplified that kept the meaningful information of the original dataset, different methods can be applied. The methods most frequently used are:⁵

- principal component analysis (PCA) (that is based on the covariance of the dataset, which allows identifying the principal directions in which the data varies and therefore the identification of strong patterns in a dataset);
- factor analysis (FA) (that is also based on the dataset variability and on the correlation between data. FA creates latent variables, i.e., new variables that are not directly observed, and that reflect the variations of two or more variables of the original dataset);
- independent component analysis (ICA) (that separates the data into components statistically independent from each other by maximizing the statistical independence of the estimated components);
- wavelet transform (WT) (that consists of the transformation of the data through the decomposition of the dataset into wavelets); and
- singular value decomposition (SVD) (that is a method for identifying and ordering the dimensions along which the data exhibit the highest variation. After identifying the data dimensions with the highest variation, an approximation to the original dataset is made using a smaller number of dimensions).

Learning algorithms

Based on the desired outcome of the learning process, learning algorithms can be classified into two major types: supervised or unsupervised.^{5,8,13,16,17}

Supervised learning is usually used to diagnose or predict disease outcomes. In supervised learning, each case in the input dataset is characterized by a category label. The system generates a function that maps the dataset to the existing categories by minimizing the classification error.

Unsupervised learning is usually used to identify patterns of diseases. In unsupervised learning, or clustering, no information is provided *a priori* on the cases' category membership. The system generates a model forming natural clusters

with the input dataset. The clusters are formed based on specific similarity criteria between cases.

Supervised and unsupervised learning processes can be combined for disease detection and prediction.¹⁸

Supervised learning: In supervised learning, each case n_i in the input dataset ($i = 1, N$) is characterized by x_j parameters or features ($j = 1, P$) plus one additional parameter k_l that identifies the category membership ($l = 1, K$).

The purpose of the supervised learning is to create a function, or rules, based on a training dataset that maps data into the existing categories allowing for the prediction of new cases. This function is a classifier when the category is discrete, or a regression function when the category is continuous.

The supervised learning techniques most frequently used are: linear discriminant analysis (LDA), support vector machines (SVMs), neural networks (NNs), Bayesian classifiers, k-Nearest Neighbor (kNN), and decision and classification trees (DCTs).

- LDA creates predictive functions that maximize the discrimination between previously established categories.¹⁹ Based on the category membership, discriminant functions, which are linear combinations of the predictive parameters/features, are computed to maximize dissimilarities between categories.
- While LDA separate linearly data from different categories, SVM allows for non-linear separation by mapping non-linearly the input data to a high-dimensional space (feature space), where optimal hyper-planes are formed minimizing the classification error.^{8,20,21} The constraints imposed on the construction of the separating surfaces result in sub-sets of data that are involved in the decision function called support vectors. By using non-linear kernels (such as spline function, Gaussian function, polynomial function, and radial basis function), SVM can model complex separation hyper-planes.²²
- The NN technique is a different approach of supervised learning. The NN architecture consists of several nodes (neurons) connected each other into different layers: one input layer to input data, one output layer to produce the category estimation (guess), and one or more hidden layers with different node connection weights. The NN is trained with the input dataset, and the output guess is compared to the known category. If classification errors occur, the weights are adjusted, and the process is repeated.^{8,20}
- Bayesian classifiers are based on a probabilistic approach. The classification is based on decision rules that assign data to the category with the maximum posterior probability. The rules will depend on the given prior probability, cost function (a function that attributes a cost, or risk number, for the classification in each category), and category conditional density. Therefore, the Bayesian decision rule can be modified taking into account different misclassification costs to minimize the probability of misclassification. Different estimates for the category densities can be used being parametric or nonparametric.¹³

- kNNs are nonparametric decision rules that depend on the similarity measure between cases and the number of nearest cases, k . This method classifies data according to the similarity measure (or distance) of the new data to the existing ones, i.e., based on the training dataset. New cases are classified according to the majority vote of its neighbours.¹³
- DCTs create rules to classify cases according to the k_l categories.^{23,24} DCTs are classifiers with a tree-like structure that splits recursively the input dataset until each data sub-set consists completely (or predominantly) of cases from one category. The tree grows from the parent (root) to the child nodes (leafs), and in each node a test on one or more attributes is performed to decide how the data should be split. Data partitioning is completed when the sub-set at a node is either “pure” (i.e., all cases within the node has the same target variable value), or sufficiently small (as set *a priori* by the user).^{23,25,26} Furthermore, to reduce the risk of overfitting and to create a more accurate DCT, the initial tree can be pruned, i.e., the small and/or deep nodes of the tree can be removed.

DCTs are easier to interpret and easier to use in clinical practice than LDA, SVM, NN, Bayes or kNN approaches since each category is characterized by a set of rules.

Unsupervised learning: In unsupervised learning, it is assumed that each case n_i ($i = 1, N$), characterized by x_j ($j = 1, P$) parameters/features, can be grouped into k_l ($l = 1, K$) homogeneous clusters, and that no information is available on the cases’ group membership. Unsupervised learning is usually referred to as cluster analysis (CA).²⁷

Cluster analysis aims to group data sharing some similarity measure (e.g., distance) or feature (e.g., correlation). Given the distance, or correlation measure chosen, the cases in the dataset are combined according to specific grouping criteria that will depend on the CA approach to be used. The grouping process can be either hierarchical, when the number of underlying clusters in the dataset is unknown *a priori*, or non-hierarchical when the number of underlying clusters is known.⁵

In hierarchical cluster analysis (HCA), the clustering process can be agglomerative or divisive. In the agglomerative HCA, the clustering process starts with N clusters, each one composed of one single case, and in the next iterations the process will merge the closest clusters until achieving one single cluster composed by the entire dataset. In the divisive HCA, the clustering process starts in the opposite way. Along the HCA processes, coefficients are computed which indicate the dissimilarity between the grouped or split clusters. The analysis of these coefficients allows the number of homogeneous clusters in the dataset to be identified.

Clusters can be merged when the distance between clusters obtained using a specific criterion is reached, such as the clusters’ centroids are minimized (centroid algorithm); when the mean distance between each pair of cases is minimized (average linkage algorithm); when the distance between pairs of cases in different clusters is minimized (nearest neighbor algorithm), or maximized (farthest neighbor algorithm); or

when the within-cluster variance is minimized (Ward’s method algorithm).^{5,17}

In non-hierarchical cluster analysis (non-HCA), on the other hand, an *a priori* number of groups (clusters) underlying the dataset are required. This clustering technique tries to create a dataset partition that better groups the data into the predefined K clusters, i.e., in which the cases in a given cluster are similar, and the cases from different clusters are dissimilar. This clustering technique assumes that each case belongs to one cluster only, and that each cluster is composed of at least one case (with the exception of the fuzzy clustering approaches where each case has a different probability of belonging to different clusters).

To create K clusters, K representative cases are chosen in the dataset by the user (e.g., chosen at random or estimated from a previous analysis). These cases (seeds) are used as the initial clusters’ centroids. The clustering process starts by assigning each case from the dataset to the nearest centroid (based on the similarity metric chosen), then clusters’ centroids are recomputed and the cases reassigned to the nearest centroid. The process iterates until convergence is achieved, i.e., until centroids remain stable in consecutive iterations, thus being considered the solution sought.

The *a priori* K number of clusters, and the initial clusters’ centroids, can also be estimated using HCA, improving therefore the final clustering solution.²⁸

Since clustering processes depend on the similarity measure, the clustering criteria, and the representative cases, different clustering algorithms, or even a specific clustering algorithm run several times, may produce different clustering solutions. If homogenous (natural) clusters exist in the dataset, different clustering processes may result in similar solutions. Otherwise, the clustering solutions may differ. In order to be able to identify and characterize clusters (patterns) in the input dataset, it is frequently recommended to perform different clustering algorithms and/or to repeat the clustering processes.¹⁷

Machine learning performance

The performance of the different machine learning processes will depend on the input dataset, and on the approaches and algorithms chosen. In supervised machine learning, the input dataset is crucial because predictive functions, or rules, are learned from the input dataset. To achieve a good performance, the dataset is usually split into three independent sub-sets, one for training (to establish the predictive functions/rules); one for testing (to assess the performance of the established functions/rules, i.e., the error in the classification); and another for validation (to assess the performance of the learning process within the training phase).

To assess machine learning performance, the known category membership and the category predicted by the learning algorithm are compared. For two categories, the sensitivity and specificity can be computed, such as the AUC – Area Under the ROC (Receiver Operating Characteristic) Curve, i.e., the area under the curve obtained by representing the sensitivity versus one minus the specificity.²⁹

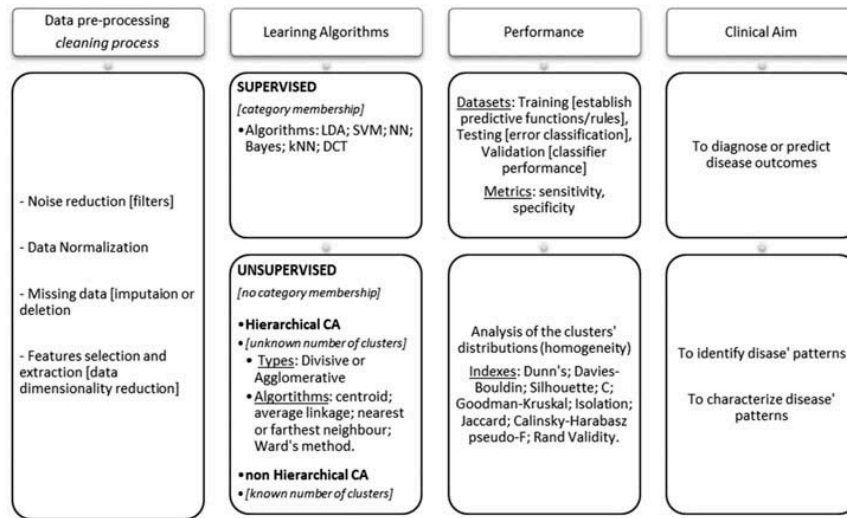


Figure 3. Machine learning steps.

For unsupervised processes, heuristic methods are used to assess the model's performance since no information on the true cases' category membership is available. For clustering, the performance is assessed based on the analysis of the clusters' distributional properties, and the clusters' homogeneity. Several indices are available in the literature to compute the clustering performance, such as: the Dunn's, the Davies-Bouldin,³⁰ the Silhouette,³¹ the C, the Goodman-Kruskal, the Isolation,³² the Jaccard,³³ the Calinsky-Harabasz pseudo-F,³⁴ and the Rand Validity Indices.

Machine learning flow chart

The different steps of the machine learning are illustrated in Figure 3.

Machine learning in clinical vision sciences

Machine learning is widely used in clinical vision sciences. Most of these techniques are used for image processing, and for computer-aided diagnosis (CAD) system development. More recently, these techniques have been used for clinical application, for disease diagnosis and monitoring. Several examples are available in the literature from general ocular diseases, for example glaucoma, retinal diseases, cataract, and ocular surface diseases.

An exhaustive search was performed in the PubMed database. Studies published until 15 September 2015 using the search terms "machine learning" and "eye" in any field of the articles were screened based on their title and abstract. Articles focused on image processing, image enhancement, eye movement or visual learning, i.e., without a direct application in clinical practice, were excluded (Figure 4).

A total of 64 articles were considered in this review. In three-quarters of the studies supervised machine learning techniques (e.g., classifiers) were used, while unsupervised techniques were used in only one-quarter of the studies.

Classifiers are widely used for the diagnosis of specific diseases. Classifiers can be used to classify medical images, for the

automatic diagnosis of diseased or non-diseased eye based on color fundus photography;³⁵ to classify or diagnose cataract based on slit-lamp photography images;^{36,37} to diagnose achromatopsia based on electroretinograms;³⁸ to detect circinate exudates based on color fundus photography;³⁹ to diagnose dry eye based on infrared meibography or based on slit-lamp photography images;⁴⁰⁻⁴² and for the diagnosis of keratoconus based on 7-order Zernike polynomial data, topographic and tomographic parameters, and Scheimpflug analyzer images.^{25,43-45}

The clinical areas where supervised techniques are most widely used are: glaucoma^{8,46-66} (based on optical coherence tomography, visual fields, scanning laser polarimetry and/or automated perimetry), AMD^{26,67-69} (based on fluorescein angiography and color fundus photography), and DR⁷⁰⁻⁷⁹ (based on color fundus photography, optical coherence tomography, survey data and/or tear fluid proteomics markers). The classifiers most frequently used for diagnosis and/or classification of AMD and DR are SVM, kNN, and DCT (Random Forest). Glaucoma is the clinical area where new machine learning algorithms have been actively developed. Bowd et al.^{8,46,47,63} provided a review of the different approaches used for glaucoma diagnosis.

Classifiers are also used to identify predictive factors for a specific disease, the most frequently used are DCT (Classification and Regression Trees, CART) and LDA.^{20,48-50,80-84} To predict disease progression, authors usually combine cluster analysis with classifiers. By identifying clusters in the data, patterns of disease progression can be identified, and afterwards characterized using classifiers.^{48-56,85-88} Other methods to predict disease progression have also been proposed such as, Gaussian kernel-based multi-class classification,⁵⁸ or longitudinal series of structural data.⁸⁵

Unsupervised methods allow for the identification of patterns, exploring data for a better understanding of the disease. The method mostly used to identify and characterize some specific disease or condition is the k-means cluster analysis, which had been used for anterior segment abnormalities in

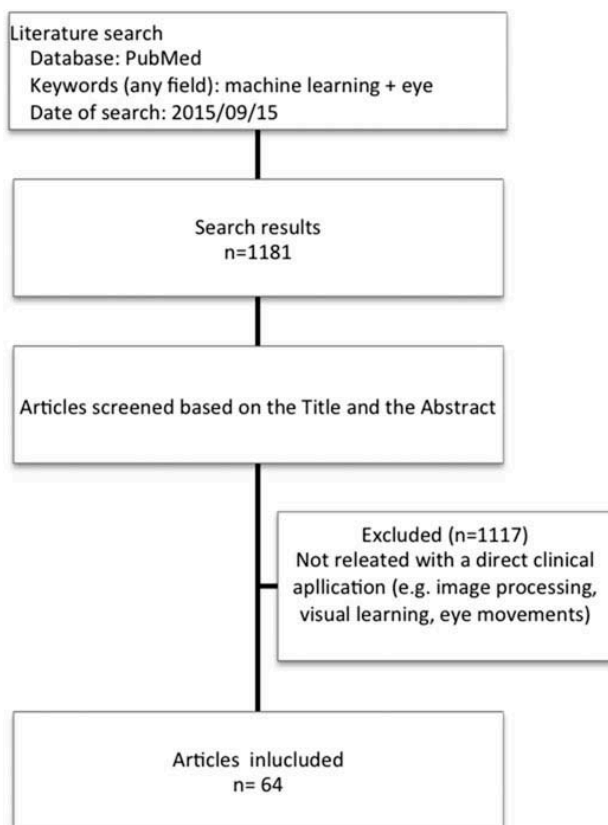


Figure 4. Flow diagram for the studies selection.

particular dry eyes and DR (based on color fundus photography, tear proteins, and magnetic resonance imaging – MRI).^{35,70,89–92}

Hierarchical cluster analysis has also been used to identify patterns within a specific disease or condition, the Wards method is the most frequently used.^{88,93} This approach was used in DR, based on color fundus photography and optical coherence tomography,⁸⁸ and in blepharitis and dry eye, based on the Schirmer test, tear volume, flow, and turnover tests, and meibomian gland lipid expression tests.⁹³

To show the clinical benefits of machine learning techniques in clinical vision sciences, three examples in a different clinical area will be presented, one in glaucoma, one in AMD and another in DR, these three ocular pathologies being the major causes of irreversible visual impairment in the world.⁴

Glaucoma is the ophthalmological condition where supervised learning approaches are most frequently used. Glaucomatous endpoints are well characterized allowing for the discrimination between glaucomatous and non-glaucomatous eyes,⁸ a review of machine learning classifiers for glaucoma detection can be found in literature studies.^{8,46,47}

Most of the published studies in the field of glaucoma used supervised machine learning techniques to improve diagnosis (Table 1). In all the studies, a good performance is obtained (Area Under the ROC Curve – AUC of approximately 0.8 is usually reported). In the majority of the studies, the results showed that the disease diagnosis can be improved when supervised machine learning techniques are used. However,

when analyzing the results of Huang et al.,^{20,84} or Bowd et al.,⁴⁷ where it was found that the nerve fiber indicator (NFI) alone,^{20,84} or the retinal nerve fiber layer (RNFL) alone,⁴⁷ showed a similar performance to the performance of the machine learning techniques with more features, we may question if, for clinical practice, machine learning techniques can effectively improve glaucoma diagnosis.

More than the machine learning itself, it is of major importance to know which parameters can be used to improve disease diagnosis and contribute to early glaucoma detection. The works performed by Goldbaum, Sample, Yousefi and Bowd et al.^{51–54,56,64–66,86,87} explore this problem, i.e., by using unsupervised machine learning techniques, these authors tried to find and characterize patterns of glaucoma progression, identifying predictive features, that can be used to automatically classify non-glaucoma from glaucoma in the earliest stages. This approach could be helpful in the clinical practice to better characterize glaucoma suspect patients, and therefore to improve the early disease detection.

The same authors, in their more recent works^{51–54,56,86,87} identified different patterns of glaucoma progression based on Standard Automated Perimetry (SAP). Three clusters were identified: one cluster characterized by two patterns of visual fields (VFs); another cluster characterized also by two other different patterns of VFs; and a last cluster characterized by five patterns of VFs. The obtained patterns were found to be associated with VF abnormalities. The first cluster was composed mainly of eyes with normal VFs, while the two other clusters were composed mainly of eyes with abnormal VFs. The model proposed by the authors allows identifying different patterns of disease progression in glaucomatous eyes, without *a priori* information about the category membership. In Raza et al.,⁶⁴ cluster analysis was used to compute a new metric that identifies abnormal structural and functional areas on OCT and SAP, respectively, allowing for the improvement of the discrimination between glaucomatous and non-glaucomatous eyes.

In AMD, the challenge when using machine learning techniques is to automatically identify AMD-related lesions to improve AMD diagnosis contributing therefore to a faster treatment (Table 2).

Most of the AMD-related lesions are manually detected by physicians, being time-consuming and prone to a high inter-observer variability. AMD-related lesions are usually graded in centralized reading centers that have trained graders, allowing therefore for the reduction of the inter-observer variability and for a more accurate lesion detection. In clinical practice, machine learning techniques can be helpful if integrated with the medical devices (e.g., angiography or color fundus photography) allowing for the automatic and accurate AMD-lesion detection. The accuracy obtained with such techniques for AMD-lesion detection is usually over 80%.^{26,39,67,69}

Also, as demonstrated by Fraccaro et al.,⁶⁸ machine learning techniques can be integrated in clinics' electronic medical record (EMR) systems allowing for an automatic and accurate AMD diagnosis of the patients followed in clinic.

In DR, supervised machine learning techniques are mainly used to improve diagnosis for screening programs (Table 3).

Table 1. Studies on glaucoma using machine learning techniques.

Authors	Aim	Procedures/examinations	Machine learning type	Machine learning techniques	Pre-processing	Performance	Conclusions
Hitzl et al. ⁵⁷	Improve diagnosis for visual field (VF) defects	Standard ophthalmoscopic examination and nerve head topographic data	Supervised	LDA, DCT (CART), NN	Yes	95% confidence interval (CI) for the correct classification (sensitivity/specificity): LDA: [88;92]% ([4;16]/[98;99]) DCT: [88;92]% ([0;3]/[99.6;100]) NN: [91.1;94.2]%([6.9;19.9]/[98.1;99.4])	Standard ophthalmoscopy data combined with optic nerve head topographic data are not enough to discriminate normal from glaucomatous visual field defects.
Mardin et al. ⁸³	Improve diagnosis	Heidelberg Retinal Tomograph (HRT)	Supervised	DCT, LDA	No	Misclassification (sensitivity/specificity): DCT: 14.8% (81.6%/88.8%) LDA: 20.4% (82.6%/76.7%)	Bagging DCT approaches allows improving the discrimination between normal and glaucomatous eyes based on standard examination.
Huang et al. ⁸⁴	Establish predictive factors	Glaucoma Diagnosis (GDx) scanning laser polarimetry with Variable Corneal Compensation (VCC) parameters	Supervised	DCT (CART)	Yes	AUC (sensitivity/specificity): NFI: 0.831 (66.2%/94.4%) Superior average: 0.807 (62.2%/98.6%) Superior maximum RNFL thickness: 0.773 (62.2%/86.1%). Remaining parameters: ≤ 0.774 (no case with a sensitivity $\geq 60\%$ and a specificity $\geq 80\%$)	The NFI, the superior average and the superior maximum RNFL thickness were found to be the best predictive factors.
Huang et al. ²⁰	Improve diagnosis	GDx VCC parameters	Supervised	LDA, NN	No	AUC: LDA: 0.950 NN: 0.970	Both LDA and NN cannot improve glaucoma diagnosis since the AUC of the NFI alone is already of 0.932.
Essock et al. ⁴⁸⁻⁵⁰	Improve diagnosis	GDx VCC parameters	Supervised	LDA	Yes	AUC: 0.928 Sensitivity: 82% Specificity: 90%	Good sensitivity and specificity for VF loss in patients with ocular hypertension.
Goldbaum et al. ⁵²⁻⁵⁴⁻⁵⁶ Sample et al. ⁵¹ Yousefi et al. ⁸⁷ Bowd et al. ⁸⁶	Improve diagnosis	SAP data	Unsupervised	CA combined with ICA (Variational Bayesian-Independent component analysis Mixture - VIM)	No	3 clusters were identified 2 axes characterize 2 clusters and 5 axes characterize 1 cluster based on the relative magnitude of the axes.	The model allow identifying disease progression in glaucomatous eyes, without <i>a priori</i> information about category membership, being identified 3 clusters of VF (patterns), one with non-glaucomatous eyes (normal VF) and two with glaucomatous eyes (abnormal VF). For each glaucomatous cluster different patterns of VF could be identified.
Yousefi et al. ⁸⁵ Bowd et al. ⁴⁷	Improve diagnosis and predict progression	Structural data extracted from Optical Coherence Tomography - OCT (RNFL) and SAP (visual functional data)	Supervised	Bayes, Lazy, Meta and Tree classifiers	Yes	Sensitivity for a specificity of 80%: For all features (RNFL and SAP): $\geq 74\%$ For RNFL only: $\geq 76\%$ For SAP only: $\geq 28\%$	Previous studies using Bayes classifiers showed that the AUC when using OCT, SAP or OCT combined with SAP data presented a similar performance (AUC: for OCT data: 0.817; for SAP data: 0.841; for OCT and SAP data: 0.869). Recently it was found that the RNFL alone provide similar diagnostic accuracy compared with classifiers that include both RNFL and SAP. Measurements of the RNFL in inferior nasal, inferior temporal, global, superior temporal, and temporal sectors provide the most discriminating power for stable or progressing glaucomatous eyes.

(Continued)

Table 1. (Continued).

Authors	Aim	Procedures/examinations	Machine learning type	Machine learning techniques	Pre-processing	Performance	Conclusions
Bowd et al. ⁶⁶	Improve diagnosis and predict progression	HRT (117 parameters) and SAP data	Supervised	Bayes (Relevance Vector Machine - RVM)	Yes	AUC for progressors and non-progressors: For all HRT parameters: 0.544 For selected HRT parameters: 0.640 For all SAP parameters: 0.669 For selected SAP parameters: 0.762 For all HRT and SAP parameters: 0.644 For selected HRT and SAP parameters: 0.805	The method used (RVM) showed that SAP parameters discriminate better progressing and non-progressing eyes, than HRT parameters. However, when combining HRT and SAP data and when selecting only relevant parameters, the discrimination between progressing and non-progressing eye improves significantly.
Racette et al. ⁶⁵	Improve diagnosis	HRT and Short-Wavelength Automated Perimetry (SWAP) data	Supervised	Bayes (RVM)	Yes	AUC for progressors and non-progressors: For all HRT parameters: 0.868 For selected HRT parameters: 0.878 For all SWAP parameters: 0.729 For selected SWAP parameters: 0.763 For all HRT and SWAP parameters: 0.898 For selected HRT and SWAP parameters: 0.925	The method used (RVM) showed that when combining relevant HRT and SWAP parameters the discrimination between glaucomatous and non-glaucomatous eyes improve, improving therefore the diagnostic accuracy of HRT and SWAP.
Raza et al. ⁶⁴	Improve diagnosis	OCT (macular retinal ganglion cell plus inner plexiform layer - mRGCP; macular and optic disc retinal nerve fiber layer - mRNFL and dRNFL) and SAP data	Unsupervised	Cluster (5-5-1 cluster criterion)		A new metric was developed based on cluster analysis to identify abnormal areas on OCT and SAP. The combination of the OCT and SAP metrics allows to identify abnormal areas on both OCT and SAP allowing improving the AUC for glaucomatous and non-glaucomatous eyes. For all OCT parameters (maximum): 0.818 For all SAP parameters (maximum): 0.797 For all OCT and SAP parameters (maximum): 0.869	OCT and SAP were first analyzed with cluster analysis to identify areas of abnormal data. Structure (OCT) and function (SAP) were combined by using the two obtained continuous cluster metrics. The combined structure-function metric allows improving the detection of glaucomatous eyes.
Kim et al. ⁵⁸	Improve diagnosis and predict progression	RNFL	Supervised	Fractal Analysis (FA) for Gaussian Kernel based multiclass classification	Yes	AUC for progressors and non-progressors: 0.82 AUC for progressors, non-progressors, and normal: 0.88	The novel FA for multiclass classification among progressors, non-progressors, and normal patients, achieve a good performance with few features and low computational complexity.
Asaoka et al. ⁵⁹	Improve diagnosis for Open Angle Glaucoma	VF	Supervised	DCT (Random Forest)	No	AUC: 0.79	The two groups of healthy VF and VF of preperimetric glaucomatous eyes VFs can be well distinguished by using the Random Forest classifier.
Sugimoto et al. ⁶⁰	Improve diagnosis for VF loss	OCT parameters; presence/absence of glaucomatous VF damage; and: age, gender, right or left eye, axial length	Supervised	DCT (Random Forest)	No	For individual OCT parameters: Circumpapillary RNFL, AUC: 0.77 Macular RNFL, AUC: 0.87 Ganglion cell layer + inner plexiform layer, AUC: 0.80 Rim area, AUC: 0.78 For combined parameters, AUC: 0.75	The Random Forest classifier applied to OCT parameters provides an accurate prediction of the presence of perimetric deterioration in glaucoma suspects, however the individual OCT parameters provides higher AUC.

(Continued)

Table 1. (Continued).

Authors	Aim	Procedures/examinations	Machine learning type	Machine learning techniques	Pre-processing	Performance	Conclusions
Xu et al. ⁶¹	Improve diagnosis	OCT parameters	Supervised	LogitBoost adaptative boosting classifier	Yes	AUC for super pixel analysis: 0.855 AUC for Circumpapillary RNFL: 0.707	The new method for 3D OCT analysis improves the discrimination between glaucoma suspect, showing a potential to improve early detection of glaucoma damage.
Oh et al. ⁶²	Improve diagnosis	Sex, age, menopause, and duration of hypertension, IOP, spherical equivalent refractive errors, vertical cup-to-disc ratio, presence of superotemporal RNFL defect, and presence of inferotemporal RNFL defect	Supervised	Multivariate logistic regression and artificial neural network (ANN)	Yes	AUC: 0.890 Accuracy: 84.0% Sensitivity: 78.3% Specificity: 85.9%	The ANN approach may be used as a screening tool for differentiating Open Angle Glaucoma patients from Glaucoma Suspect patients.
Belghith et al. ⁶³	Improve diagnosis	OCT parameters	Supervised	Bayesian (kernel-based), Fuzzy, ANN, SVM	Yes	AUC: Bayes: 0.91 Fuzzy: 0.83 ANN: 0.69 SVM: 0.60	By training the classifiers with healthy and non-progressing eyes, a high diagnostic accuracy can be achieved for detecting glaucoma progression.

Table 2. Studies in AMD using machine learning techniques.

Authors	Aim	Procedures/examinations	Type of machine learning	Techniques used	Pre-processing	Performance	Conclusions
Tsai et al. ²⁶	Improve diagnosis and quantify choroidal neovascularization (CNV)	Fluorescein angiography (fluorescence leakage – intensity changes over time)	Supervised	AdaBoost algorithm	Yes	Accuracy: 83%	The developed CAD tool for CNV quantification can be useful for the objective evaluation of CNV.
Mookiah et al. ⁶⁷	Improve diagnosis of dry AMD	Color fundus photography	Supervised	SVM, kNN, Bayes, NN	Yes	Accuracy: 93.70%, Sensitivity: 91.11% Specificity: 96.30%	An AMD Risk Index was developed based on the selected features used to classify normal and dry AMD. The proposed system can be used to assist the clinicians and also for AMD screening.
Lahmiri et al. ³⁹	Detect circinate exudate	Color fundus photography	Supervised	SVM	Yes	Perfect classification	The developed CAD tool for circinate exudates can be useful for the objective evaluation of circinate exudates.
Fraccaro et al. ⁶⁸	Improve diagnosis	Clinical signs (soft drusens, retinal pigmentation) Patients' data collected from the patient's files: demographics and presence/absence of major AMD-related clinical signs (soft drusen, retinal pigment epithelium, defects/pigment mottling, depigmentation area, subretinal hemorrhage, subretinal fluid, macula thickness, macular scar, subretinal fibrosis).	Supervised	Logistic regression, DCT (Random Forest), SVM, AdaBoost algorithm	No	AUC ≥ 0.90	All machine learning models identified soft drusen and age as the most discriminating variables that can be integrated with a EMR to provide the physicians with real time support.
Feeny et al. ⁶⁹	Improve diagnosis and detect geographic atrophy (GA)	Color fundus photography	Supervised	DCT (Random Forest)	Yes	Positive Predictive Value: 82% Negative Predictive Value: 95%	Machine learning methods can be used for the automated characterization of GA in color fundus photographs.

Table 3. Studies in DR using machine learning techniques.

Authors	Aim	Procedures/examinations	Type of machine learning	Techniques used	Pre-processing	Performance	Conclusions
Priya et al. ⁷⁰	Improve diagnosis for screening	Color fundus photography	Supervised	SVM	Yes	Sensitivity: 99.4% Specificity: 100%	The developed CAD system allows for a good discrimination between normal, non-proliferative and proliferative DR.
Agurto et al. ⁸⁹	Improve diagnosis for screening	Color fundus photography	Supervised	Partial Least Squares regression model	Yes	Sensitivity for a specificity of 50%: For sight threatening DR: 100% For non-proliferative DR: 92% For maculopathy: 94%	The developed CAD system allows for a good discrimination between normal, non-proliferative DR, sight threatening DR and maculopathy.
Nunes et al. ⁸⁸	Risk model (phenotypes of DR progression)	Color fundus photography and OCT	unsupervised and Supervised	Hierarchical CA and DCT (CART)	No	Calinsky-Harabask pseudo-F index higher for 3 clusters solution. Three different phenotypes of DR progression were identified with different risks of CSME development. Accuracy: 88.6% Risk estimate: 12.5%	Hierarchical CA identifies 3 different phenotypes of NPDR based on MA turnover and central macular thickness. Eyes/patients from phenotype C show a higher risk for the development of CSME (OR = 3.536; P < 0.001).
Ganesan et al. ⁷¹	Improve diagnosis for screening	Color fundus photography	Supervised	SVM, NN	Yes	Accuracy \geq 99.12%	The developed system allows for the early DR detection with a good accuracy.
Akram et al. ⁷³	Improve diagnosis for macular edema	Color fundus photography	Supervised	Gaussian mixture model, SVM	Yes	Accuracy: 96.8% Sensitivity: 97.3% Specificity: 95.9%	The proposed system for detection and grading of macular edema can be used to assist the ophthalmologists for the early and automated detection of DR.
Welikala et al. ⁷²	Improve diagnosis of Proliferative DR	Color fundus photography	Supervised	SVM	Yes	Sensitivity: 100% Specificity: 90.0%	The developed CAD system can be used for the detection of new vessels in retinal images with a high performance.
Oh et al. ⁷⁴	Risk model for DR	Color fundus photography for the presence of DR and variables from demographic data, medical history, blood pressure, blood tests, and urine tests	Supervised	Logistic regression models (sparse learning model), SVM, DCT (Random Forest), Bayes, kNN	No	Accuracy: 89.2% Sensitivity: 75.0% Specificity: 89.6%	The proposed method for identifying diabetic populations who are at a high risk of DR can be used in clinical practice when integrated with an EMR.
Noronha et al. ⁷⁵	Improve diagnosis for screening	Color fundus photography	Supervised	SVM	Yes	Accuracy, Sensitivity and Specificity \geq 99%	A Diabetic Retinopathy Risk Index was proposed in this work based on a features selection process which allows identifying normal and DR. This index can be used as an adjunct tool by the physicians during the eye screening to cross-check their diagnosis.

(Continued)

Table 3. (Continued).

Authors	Aim	Procedures/examinations	Type of machine learning	Techniques used	Pre-processing	Performance	Conclusions
Torok ^{76,78}	Improve diagnosis for screening	Color fundus photography (microaneurysms – MA) and Tears film markers	Supervised	SVM, Recursive Partitioning, DCT (Random Forest), Bayes, Logistic Regression, kNN	Yes	MA detection method: Sensitivity: 84% Specificity: 81% Proteomics data: Sensitivity: 87% Specificity: 68% Combined data: Sensitivity: 93% Specificity: 78%	Combining MA information (obtained from color fundus photography) and tears film data, the performance for DR diagnosis can be improved. The developed methodology could be used as a reliable screening method comparable to the requirements of DR screening programs applied in the clinical practice.
Tang et al. ⁷⁷	Improve diagnosis for screening	Color fundus photography	Supervised	Evolutionary Algorithms	Yes	Sensitivity: 92.2% Specificity: 90.4%	The results demonstrate a strong potential of machine learning techniques as an effective tool to assist grading.
Krishnamoorthy et al. ⁷⁹	Improve diagnosis for screening	Color fundus photography	Supervised	SVM	Yes	Sensitivity: 88% Specificity: 72%	The developed CAD system - Diabetic Fundus Image Recuperation (DFIR), method, allows to discriminate efficiently candidate fundus images based on Sliding Window Approach increasing the sensitivity for DR screening.

The aim is to automatically detect DR-lesions based on color fundus photography and, based on these lesions, to automatically identify the disease. For screening programs, these techniques may have a great impact since they will allow discriminating diabetic patients with or without DR, relieving the burden of the hospitals and clinics. To improve DR diagnosis, Torok et al. ^{76,78} proposed including tear film proteomics markers. They showed that by combining microaneurysm (MA) lesions and tear film markers, the performance for the classification can be improved (from a sensitivity and specificity of 84% and 81%, respectively, when considering only the MA, to 93% and 78% when considering also the tear film markers). However, when comparing the performance obtained in the work of Torok et al. (considering only MA lesions) with others' works (performed also using color fundus photography), it seems that the diagnostic performance was underestimated, and that by using other features (extracted from color fundus images) the sensitivity and specificity can be improved to almost 90%. ^{67,70–73,75,77,79,89}

A different application of machine learning in DR is the establishment of risk models for DR progression. ^{74,88} In Oh et al. ⁷⁴ supervised machine learning techniques are used to identify patients at risk for DR progression based on the patients' information registered in the EMR systems. Like in AMD, by using these techniques with an EMR system, the early detection of patients at risk for DR progression can be improved and easily implemented in hospitals and clinics. In Nunes et al., ⁸⁸ unsupervised machine learning techniques are used to identify patterns of DR progression. In this work 3 different phenotypes of DR progression were identified in patients with mild non-proliferative DR, each

one associated with a different risk of DR progression. In this work, clinically available procedures were used, namely color fundus photography and optical coherence tomography (OCT). By using a supervised machine learning technique (DCT), rules were obtained allowing better characterization of the identified phenotypes and allowing establishment of rules that can be easily used in the clinical practice. By using these rules, DR patients can be classified in one of these three phenotypes (A, B, and C). Phenotype C was characterized by a MA turnover ≥ 6 MA in a period of 6 months. Phenotype B was characterized by a MA turnover < 6 MA in a period of 6 months and a central subfield retinal thickness ≥ 220 μm . Phenotype A was characterized by a MA turnover < 6 MA in a period of 6 months and a central subfield retinal thickness < 220 μm . Phenotypes B and C were associated with a higher risk of clinically significant macular edema (CSME) development in a period of 2 years. When compared to phenotype A, phenotype C was associated with a 3.5-fold increased risk for developing CSME (Odds Ratio, OR = 3.536), and phenotype B was associated with a 2.8-fold increased risk for developing CSME (OR = 2.802).

These results may have a great importance for DR patients' management since patients identified as phenotypes B and C can be identified early and followed more closely.

Discussion

Frequently, clinicians try to combine the results obtained from the different testing and imaging devices for disease diagnose and monitoring. Machine learning techniques have

shown to be very useful, and powerful tools for supporting the clinical-decision-making task.

Machine learning techniques have been used in clinical visual sciences to integrate multimodal information, and to improve the existing testing or imaging devices for disease diagnosis, prediction, and monitoring. Presently, machine learning algorithms are already available in some commercial diagnostic devices to automatically identify diseased eyes. One of these devices is the GDx from Carl Zeiss Meditec, Inc., where NN algorithms are used to detect glaucomatous eyes.⁹⁴

More recently, Bayesian approaches have also been used with supervised and unsupervised machine learning methods, allowing creation of predictive models that include prior knowledge, e.g., predictive models with prior knowledge of the disease stage, severity or even progression. In Medeiros et al.,⁹⁵ a Bayesian Hierarchical method, integrating eye' structural and functional information, was developed. This new methodology allows for the continuous inclusion of information into the predictive model improving the model's estimates for glaucoma progression. These new methodologies are promising, however since there are no criteria to select the best machine learning method, several methods should be tested and compared. Based on the performance of the used algorithms, the computational complexity and the obtained clinical results, the researcher may select the method that best fits the dataset used and the purpose of the work.

This review presents some of the machine learning methods mostly used in vision sciences.

However, several problems still need to be solved to obtain unbiased predictive models in clinical vision sciences.

One of the major problems for the predictive models in eye diseases is related to the selection of the training sample. Predictive models should be created for patient' diagnosis, or disease prediction. However, the existing predictive models are commonly based on a training set composed of one of the patient's eyes (both eyes are considered independently), the chosen eye being normal (healthy or non-diseased) or diseased (i.e., with a specific eye condition). Most of the published works consider only one eye per patient, it being selected at random,⁸² selected based on the patient's right or left eye,⁵⁷ or selected based on the patient' worst or better eye.^{20,84} To create a predictive model able to consider eye-specific covariates within each patient, instead of considering each eye individually, new approaches need to be developed. Approaches based on clustering methods may overcome this problem. Rosner et al.,^{96,97} for example, developed a non-parametric approach that considers each eye as a sub-unit of a cluster, i.e., the patient. This approach, called the clustered Wilcoxon rank sum procedure, allows for the analysis of both patients' eyes as a whole rather than individuals.

Moreover, when using the predictive models in the true population, the patients' eyes may have a different condition, than the one that was considered for the models' training. A model for glaucoma detection, for example, used in a patient with diabetic retinopathy, may fail to consider the patient's eyes as diseased, since the model was trained only for glaucoma or non-glaucoma prediction.

The population' characteristics, and the existence of different diseases, and also the existence of different disease'

phenotypes, should be considered *a priori* when selecting the input dataset, since the selection of the training set may bias the machine learning output.⁹⁸

Other issues, which will compromise the predictive model performance, are related to the presence of noise in the input dataset; the correctness of the data used for the input dataset, such as, the data obtained from the different testing or imaging devices; the outcomes used to characterize eyes' abnormalities;^{20,84} and the short to medium periods of patients' follow-up, used for disease progression models.⁹⁵ Therefore, data pre-processing is an important step before performing a machine learning technique. It is known that most of the data have some intrinsic noise that may influence the machine learning output. This noise will be different according to the source of data, such as the imaging modality, the used device, and the device settings. When using commercial devices, the noise is considered as a systemic error. The user can improve the quality of the data and reduce noise by performing several acquisitions and averaging them. The user can also minimize other sources of bias, such as acquiring the data with the same device and under the same conditions and settings.

By overcoming these issues, unbiased predictive models may be created. Moreover, by assessing patients, based on the summation of all the major risk factors, and based on multimodal data, these predictive models will allow for the identification of patients who are most likely to benefit from treatment, and for the quantification of the combined effect of the different risk factors. These models will be a valuable decision-making tool for disease diagnosis and treatment management, contributing significantly to stratified and personalized medicine.^{99–101}

Funding

This research received no specific grant or funding.

Declaration of interests

The authors report no conflicts of interest. The authors alone are responsible for the content and writing of the paper.

References

1. Cotter SA, Varma R, Ying-Lai M, Azen SP, Klein R. Causes of low vision and blindness in adult Latinos. The Los Angeles Latino Eye Study. *Ophthalmology* 2006;113(9):1574–1582.
2. Sajda P. Machine learning for detection and diagnosis of disease. *Annu Rev Biomed Eng* 2006 Jan;8:537–565.
3. Kononenko I. Machine learning for medical diagnosis: history, state of the art and perspective. *Artif Intell Med* 2001;23(1):89–109.
4. World Health Organization. Global data on visual impairments 2010. WHO Press; 2012.
5. Duda RO, Hart PE, Stork DG. *Pattern classification*, 2nd. Ed. New York: John Wiley & Sons; 2001.
6. Shin H, Markey MK. A machine learning perspective on the development of clinical decision support systems utilizing mass spectra of blood samples. *J Biomed Inf* 2006 Apr;39(2):227–248.
7. Aburas A, Zulkurnain N. Investigation of the time-series medical data based on wavelets and K-means clustering. *ARISER* 2007;3(3):112–122.

8. Bowd C, Goldbaum MH. Machine learning classifiers in glaucoma. *Optom Vis Sci* 2008;85(6):396–405.
9. Szkulmowska A, Wojtkowski M, Gorczynska I, Bajraszewski T, Szkulmowski M, Targowski P, et al. Coherent noise-free ophthalmic imaging by spectral optical coherence tomography. *J Phys D Appl Phys* 2005;38(15):2606–2611.
10. Nakai M, Ke W. Review of the methods for handling missing data in longitudinal data analysis. *Int J Math Anal* 2011;5(1):1–13.
11. Schafer JL, Graham JW. Missing data: our view of the state of the art. *Psychol Methods* 2002;7(2):147–77.
12. Tsien CL. Event discovery in medical time-series data. *Proc AMIA Symp* 2000;858–862.
13. Jain A, Duijn R, Mao J. Statistical pattern recognition: a review. *IEEE Trans Pattern Anal Mach Intell* 2000;22(1):4–37.
14. Guyon I, Elisseeff A. An introduction to variable and feature selection. *J Mach Learn Res*. MIT Press; 2003;3:1157–1182.
15. Siddiqui K. Heuristics for sample size determination in multivariate statistical techniques. *World Appl Sci J* 2013;27(2):285–287.
16. Rosenberg D, Handler A, Furner S. A new method for classifying patterns of prenatal care utilization using cluster analysis. *Matern Child Health J* 2004;8(1):19–30.
17. Everitt BS. Commentary: classification and cluster analysis. *BMJ* 1995;311(7004):535–536.
18. Barton FB, Fong DS, Knatterud GL. Classification of Farnsworth-Munsell 100-hue test results in the early treatment diabetic retinopathy study. *Am J Ophthalmol* 2004;138(1):119–124.
19. Tatsuoka MM, Lohnes PR. Multivariate analysis (techniques for educational and psychological research). *J Educ Stat* 1989;14(1):110–114.
20. Huang ML, Chen HY, Huang WC, Tsai YY. Linear discriminant analysis and artificial neural network for glaucoma diagnosis using scanning laser polarimetry-variable cornea compensation measurements in Taiwan Chinese population. *Graefes Arch Clin Exp Ophthalmol* 2010;248(3):435–441.
21. Chang C-C, Lin C-J. LIBSVM: A Library for Support Vector Machines. *ACM Trans Intell Syst Technol* 2011;2:27:1–27:27.
22. Ivanciuc O. Applications of support vector machines in chemistry. *Rev Comput Chem* 2007;23:291–400.
23. Rokach L, Maimon O. Top-down induction of decision trees classifiers—a survey. *IEEE Trans Syst Man Cybern Part C Appl Rev* 2005;35(4):476–487.
24. Quinlan J. Learning decision tree classifiers. *ACM Comput Surv* 1996;28(1):71–72.
25. Twa MD, Parthasarathy S, Roberts C, Mahmoud AM, Raasch TW, Bullimore MA. Automated decision tree classification of corneal shape. *Optom Vis Sci* 2005;82(12):1038–1046.
26. Tsai C-L, Yang Y-L, Chen S-J, Lin K-S, Chan C-H, Lin W-Y. Automatic characterization of classic choroidal neovascularization by using adaboost for supervised learning. *Invest Ophthalmol Vis Sci* 2011;52(5):2767–2774.
27. Jiang D, Tang C, Zhang A. Cluster analysis for gene expression data: a survey. *IEEE Trans Knowl Data Eng* 2004;16(11):1370–1386.
28. Kaufman L, Rousseeuw P. Clustering large applications (Program CLARA). Finding groups in data: an introduction to cluster analysis. Hoboken, NJ: John Wiley & Sons, Inc.; 1990. p. 126–63.
29. Fawcett T. An introduction to ROC analysis. *Pattern Recognit Lett* 2006;27(8):861–874.
30. Davies DL, Bouldin DW. A cluster separation measure. *IEEE Trans Pattern Anal Mach Intell* 1979;1(2):224–227.
31. Rousseeuw PJ. Silhouettes: a graphical aid to the interpretation and validation of cluster analysis. *J Comput Appl Math* 1987;20(1):53–65.
32. Pauwels EJ, Frederix G. Finding salient regions in images: non-parametric clustering for image segmentation and grouping. *Comput Vis Image Underst* 1999;75(1–2):73–85.
33. Jaccard P. The distribution of the flora in the alpine zone. *New Phytol*. Wiley Online Library; 1912;11(2):37–50.
34. Milligan GW, Cooper MC. An examination of procedures for determining the number of clusters in a data set. *Psychometrika* 1985;50(2):159–179.
35. Acharya U R, Wong LY, Ng EYK, Suri JS. Automatic identification of anterior segment eye abnormality. *ITBM-RBM* 2007;28(1):35–41.
36. Xu Y, Gao X, Lin S, Wong DWK, Liu J, Xu D, et al. Automatic grading of nuclear cataracts from slit-lamp lens images using group sparsity regression. *Med Image Comput Comput Assist Interv* 2013 Jan;16(Pt 2):468–475.
37. Cheung CYL, Li H, Lamoureux EL, Mitchell P, Wang JJ, Tan AG, et al. Validity of a new computer-aided diagnosis imaging program to quantify nuclear cataract from slit-lamp photographs. *Investig Ophthalmol Vis Sci* 2011 Mar;52(3):1314–1319.
38. Bagheri A, Persano Adorno D, Rizzo P, Barraco R, Bellomonte L. Empirical mode decomposition and neural network for the classification of electroretinographic data. *Med Biol Eng Comput* 2014 Jul;52(7):619–628.
39. Lahmiri S, Boukadoum M. Automated detection of circinate exudates in retina digital images using empirical mode decomposition and the entropy and uniformity of the intrinsic mode functions. *Biomed Tech (Berl)* 2014 Aug;59(4):357–66.
40. Koh YW, Celik T, Lee HK, Petznick A, Tong L. Detection of meibomian glands and classification of meibography images. *J Biomed Opt* 2012 Aug;17(8):086008.
41. Remeseiro B, Penas M, Mosquera A, Novo J, Penedo MG, Yebra-Pimentel E. Statistical comparison of classifiers applied to the interferential tear film lipid layer automatic classification. *Comput Math Methods Med* 2012 Jan;2012:207315.
42. Remeseiro B, Bolon-Canedo V, Peteiro-Barral D, Alonso-Betanzos A, Guijarro-Berdiñas B, Mosquera A, et al. A methodology for improving tear film lipid layer classification. *IEEE J Biomed Heal Inf* 2014 Jul;18(4):1485–1493.
43. Marsolo K, Twa M, Bullimore MA, Parthasarathy S. Spatial modeling and classification of corneal shape. *IEEE Trans Inf Technol Biomed* 2007;11(2):203–212.
44. Saad A, Guilbert E, Gatinel D. Corneal enantiomorphism in normal and keratoconic eyes. *J Refract Surg* 2014 Aug;30(8):542–547.
45. Smadja D, Touboul D, Cohen A, Doveh E, Santhiago MR, Mello GR, et al. Detection of subclinical keratoconus using an automated decision tree classification. *Am J Ophthalmol* 2013 Aug;156(2):237–246.e1.
46. Bowd C, Chan K, Zangwill LM, Goldbaum MH, Lee T-W, Sejnowski TJ, et al. Comparing neural networks and linear discriminant functions for glaucoma detection using confocal scanning laser ophthalmoscopy of the optic disc. *Invest Ophthalmol Vis Sci* 2002;43(11):3444–3454.
47. Bowd C, Hao J, Tavares IM, Medeiros FA, Zangwill LM, Lee TW, et al. Bayesian machine learning classifiers for combining structural and functional measurements to classify healthy and glaucomatous eyes. *Investig Ophthalmol Vis Sci* 2008;49(3):945–953.
48. Essock EA, Guntant P, Zheng Y, Garway-Heath DF, Kotecha A, Spratt A. Predicting visual field loss in ocular hypertensive patients using wavelet-fourier analysis of GDx scanning laser polarimetry. *Optom Vis Sci* 2007;84(5):380–387.
49. Essock EA, Zheng Y, Guntant P. Analysis of GDx-VCC polarimetry data by wavelet-fourier analysis across glaucoma stages. *Investig Ophthalmol Vis Sci* 2005;46(8):2838–2847.
50. Essock EA, Sinai MJ, Bowd C, Zangwill LM, Weinreb RN. Fourier analysis of optical coherence tomography and scanning laser polarimetry retinal nerve fiber layer measurements in the diagnosis of glaucoma. *Arch Ophthalmol* 2003;121(9):1238–1245.
51. Sample PA, Boden C, Zhang Z, Pascual J, Lee TW, Zangwill LM, et al. Unsupervised machine learning with independent component analysis to identify areas of progression in glaucomatous visual fields. *Investig Ophthalmol Vis Sci* 2005;46(10):3684–3692.
52. Goldbaum MH, Jang G-J, Bowd C, Hao J, Zangwill LM, Liebmann J, et al. Patterns of glaucomatous visual field loss in

- sita fields automatically identified using independent component analysis. *Trans Am Ophthalmol Soc* 2009;107:136–144.
53. Goldbaum MH, Sample PA, Zhang Z, Chan K, Hao J, Lee T-W, et al. Using unsupervised learning with independent component analysis to identify patterns of glaucomatous visual field defects. *Invest Ophthalmol Vis Sci* 2005;46(10):3676–3683.
 54. Goldbaum MH. Unsupervised learning with independent component analysis can identify patterns of glaucomatous visual field defects. *Trans Am Ophthalmol Soc* 2005;103:270–280.
 55. Goldbaum MH, Sample PA, Chan K, Williams J, Lee TW, Blumenthal E, et al. Comparing machine learning classifiers for diagnosing glaucoma from standard automated perimetry. *Investig Ophthalmol Vis Sci* 2002;43(1):162–169.
 56. Goldbaum MH, Lee I, Jang G, Balasubramanian M, Sample PA, Weinreb RN, et al. Progression of patterns (POP): a machine classifier algorithm to identify glaucoma progression in visual fields. *Invest Ophthalmol Vis Sci* 2012 Oct;53(10):6557–6567.
 57. Hitzl W, Reitsamer HA, Hornykewycz K, Mistlberger A, Grabner G. Application of discriminant, classification tree and neural network analysis to differentiate between potential glaucoma suspects with and without visual field defects. *J Theor Med* 2003;5(3–4):161–170.
 58. Kim PY, Iftekharuddin KM, Davey PG, Tóth M, Garas A, Holló G, et al. Novel fractal feature-based multiclass glaucoma detection and progression prediction. *IEEE J Biomed Heal Inf* 2013 Mar;17(2):269–276.
 59. Asaoka R, Iwase A, Hirasawa K, Murata H, Araie M. Identifying “preperimetric” glaucoma in standard automated perimetry visual fields. *Invest Ophthalmol Vis Sci* 2014 Dec;55(12):7814–7820.
 60. Sugimoto K, Murata H, Hirasawa H, Aihara M, Mayama C, Asaoka R. Cross-sectional study: Does combining optical coherence tomography measurements using the “Random Forest” decision tree classifier improve the prediction of the presence of perimetric deterioration in glaucoma suspects? *BMJ Open* 2013 Jan;3(10):e003114.
 61. Xu J, Ishikawa H, Wollstein G, Bilonick RA, Folio LS, Nadler Z, et al. Three-dimensional spectral-domain optical coherence tomography data analysis for glaucoma detection. *PLoS One* 2013 Jan;8(2):e55476.
 62. Oh E, Yoo T, Hong S. Artificial neural network approach for differentiating open-angle glaucoma from glaucoma suspect without a visual field test. *Invest Ophthalmol Vis Sci* 2015;56(6):3957–3966.
 63. Belghith A, Bowd C, Medeiros FA, Balasubramanian M, Weinreb RN, Zangwill LM. Learning from healthy and stable eyes: a new approach for detection of glaucomatous progression. *Artif Intell Med* 2015;64(2):105–115.
 64. Raza AS, Zhang X, De Moraes CG V, Reisman CA, Liebmann JM, Ritch R, et al. Improving glaucoma detection using spatially correspondent clusters of damage and by combining standard automated perimetry and optical coherence tomography. *Invest Ophthalmol Vis Sci* 2014 Jan;55(1):612–624.
 65. Racette L, Chiou CY, Hao J, Bowd C, Goldbaum MH, Zangwill LM, et al. Combining functional and structural tests improves the diagnostic accuracy of relevance vector machine classifiers. *J Glaucoma* 2010 Mar;19(3):167–175.
 66. Bowd C, Lee I, Goldbaum MH, Balasubramanian M, Medeiros FA, Zangwill LM, et al. Predicting glaucomatous progression in glaucoma suspect eyes using relevance vector machine classifiers for combined structural and functional measurements. *Invest Ophthalmol Vis Sci* 2012 Apr;53(4):2382–2389.
 67. Mookiah MRK, Acharya UR, Koh JEW, Chua CK, Tan JH, Chandran V, et al. Decision support system for age-related macular degeneration using discrete wavelet transform. *Med Biol Eng Comput* 2014 Sep;52(9):781–796.
 68. Fraccaro P, Nicolo M, Bonetto M, Giacomini M, Weller P, Traverso CE, et al. Combining macula clinical signs and patient characteristics for age-related macular degeneration diagnosis: a machine learning approach. *BMC Ophthalmol* 2015 Jan 27;15(1):10.
 69. Feeny A, Tadarati M, Freund D, Bressler N, Burlina P. Automated segmentation of geographic atrophy of the retinal epithelium via random forests in AREDS color fundus images. *Comput Biol Med* 2015;65(124–136).
 70. Priya R, Aruna P. Review of automated diagnosis of diabetic retinopathy using the support vector machine. *Int J Appl Eng Res Dindigul* 2011;1(4):844–863.
 71. Ganesan K, Martis RJ, Acharya UR, Chua CK, Min LC, Ng EYK, et al. Computer-aided diabetic retinopathy detection using trace transforms on digital fundus images. *Med Biol Eng Comput* 2014 Aug;52(8):663–672.
 72. Welikala RA, Dehmeshki J, Hoppe A, Tah V, Mann S, Williamson TH, et al. Automated detection of proliferative diabetic retinopathy using a modified line operator and dual classification. *Comput Methods Programs Biomed* 2014 May;114(3):247–261.
 73. Akram MU, Tariq A, Khan SA, Javed MY. Automated detection of exudates and macula for grading of diabetic macular edema. *Comput Methods Programs Biomed* 2014 Apr;114(2):141–152.
 74. Oh E, Yoo TK, Park E-C. Diabetic retinopathy risk prediction for fundus examination using sparse learning: a cross-sectional study. *BMC Med Inf Decis Mak* 2013 Jan;13:106.
 75. Noronha K, Acharya UR, Nayak KP, Kamath S, Bhandary S V. Decision support system for diabetic retinopathy using discrete wavelet transform. *Proc Inst Mech Eng H* 2013 Mar;227(3):251–261.
 76. Torok Z, Peto T, Csoz E, Tukacs E, Molnar A, Maros-Szabo Z, et al. Tear fluid proteomics multimarkers for diabetic retinopathy screening. *BMC Ophthalmol* 2013 Jan;13(1):40.
 77. Tang HL, Goh J, Peto T, Ling BW-K, Al Turk LI, Hu Y, et al. The reading of components of diabetic retinopathy: an evolutionary approach for filtering normal digital fundus imaging in screening and population based studies. *PLoS One* 2013 Jan;8(7):e66730.
 78. Torok Z, Peto T, Csoz E, Tukacs E, Molnar A, Berta A, et al. Combined methods for diabetic retinopathy screening, using retina photographs and tear fluid proteomics biomarkers. *J Diabetes Res* 2015;1–8.
 79. Krishnamoorthy S, Alli P. A novel image recuperation approach for diagnosing and ranking retinopathy disease level using diabetic fundus image. *PLoS One* 2015;10(5):1–13.
 80. Chiang MMT, Mirkin B. Intelligent choice of the number of clusters in k-means clustering: an experimental study with different cluster spreads. *J Classif* 2010;27(1):3–40.
 81. Shekar DVC, Srinivas VS. Clinical data mining – an approach for identification of refractive errors. *Proc Int MultiConference Eng Comput Sci*. 2008;1(Vol I):19–21.
 82. Schmidt GW, Broman AT, Hindman HB, Grant MP. Vision survival after open globe injury predicted by classification and regression tree analysis. *Ophthalmology* 2008;115(1):202–209.
 83. Mardin CY, Hothorn T, Peters A, Jünemann AG, Nguyen NX, Lausen B. New glaucoma classification method based on standard Heidelberg Retina Tomograph parameters by bagging classification trees. *J Glaucoma* 2003;12(4):340–346.
 84. Huang ML, Chen HY. Glaucoma classification model based on GDx VCC measured parameters by decision tree. *J Med Syst* 2010;34(6):1141–1147.
 85. Yousefi S, Goldbaum MH, Balasubramanian M, Jung T-P, Weinreb RN, Medeiros FA, et al. Glaucoma progression detection using structural retinal nerve fiber layer measurements and functional visual field points. *IEEE Trans Biomed Eng* 2014 Apr;61(4):1143–1154.
 86. Bowd C, Weinreb RN, Balasubramanian M, Lee I, Jang G, Yousefi S, et al. Glaucomatous patterns in frequency doubling technology (FDT) perimetry data identified by unsupervised machine learning classifiers. *PLoS One* 2014 Jan;9(1):e85941.
 87. Yousefi S, Goldbaum MH, Balasubramanian M, Medeiros FA, Zangwill LM, Liebmann JM, et al. Learning from data: recognizing glaucomatous defect patterns and detecting progression from visual field measurements. *IEEE Trans Biomed Eng* 2014 Jul;61(7):2112–24.
 88. Nunes S, Ribeiro L, Lobo C, Cunha-Vaz J. Three different phenotypes of mild nonproliferative diabetic retinopathy with

- different risks for development of clinically significant macular edema. *Invest Ophthalmol Vis Sci* 2013 Jul;54(7):4595–604.
89. Agurto C, Barriga ES, Murray V, Nemeth S, Crammer R, Bauman W, et al. Automatic detection of diabetic retinopathy and age-related macular degeneration in digital fundus images. *Invest Ophthalmol Vis Sci* 2011;52(8):5862–5671.
 90. Hung W-L, Chang Y-C. A modified fuzzy C-means algorithm for differentiation in MRI of ophthalmology. *Model Decis Artif Intell Lect Notes Comput Sci Vol* 2006;3885:340–50.
 91. Wu K-L, Yang M-S. Alternative c-means clustering algorithms. *Pattern Recognit* 2002;35:2267–2278.
 92. Grus F, Augustin A. Analysis of tear protein patterns by a neural network as a diagnostic tool for the detection of dry eyes. *Electrophoresis* 1999;20(4–5):875–880.
 93. Mathers WD, Choi D. Cluster analysis of patients with ocular surface disease, blepharitis, and dry eye. *Arch Ophthalmol* 2004;122(11):1700–1704.
 94. Poinosawmy D, Tan JC, Bunce C, Hitchings RA. The ability of the GDx nerve fibre analyser neural network to diagnose glaucoma. *Graefes Arch Clin Exp Ophthalmol* 2001;239(2):122–127.
 95. Medeiros FA, Leite MT, Zangwill LM, Weinreb RN. Combining structural and functional measurements to improve detection of glaucoma progression using Bayesian hierarchical models. *Investig Ophthalmol Vis Sci* 2011;52(8):5794–5803.
 96. Rosner B, Glynn RJ. Multivariate methods for clustered ordinal data with applications to survival analysis. *Stat Med* 1997;16(4):357–372.
 97. Rosner B, Glynn R, Lee M. A nonparametric test for observational non-normally distributed ophthalmic data with eye-specific exposures and outcomes. *Ophthalmic Epidemiol* 2007;14(4):243–250.
 98. Langedger C, Wenger M, Duftner C, Dejaco C, Baldissera I, Moncayo R, et al. Use of the European preliminary criteria, the Breiman-classification tree and the American-European criteria for diagnosis of primary Sjögren's Syndrome in daily practice: a retrospective analysis. *Rheumatol Int* 2007;27(8):699–702.
 99. Weinreb RN, Friedman DS, Fechtner RD, Cioffi GA, Coleman AL, Girkin CA, et al. Risk assessment in the management of patients with ocular hypertension. *Am J Ophthalmol* 2004;138(3):458–467.
 100. Wilson PWF, D'Agostino RB, Levy D, Belanger AM, Silbershatz H, Kannel WB. Prediction of coronary heart disease using risk Factor categories. *Circulation* 1998;1837–1847.
 101. Trusheim MR, Berndt ER, Douglas FL. Stratified medicine: strategic and economic implications of combining drugs and clinical biomarkers. *Nat Rev Drug Discov* 2007;6(4):287–293.